Development of Molecular Tools for the Investigation of Arenavirus Spike Architecture

Amelia Briony Shaw

Submitted in accordance with the requirements for the degree of

Doctor of Philosophy

The University of Leeds

The Astbury Centre for Structural Molecular Biology

May 2021

The candidate confirms that the work submitted is her own and that appropriate credit has been given where reference has been made to the work of others.

Acknowledgements

Chapter 5: Dr Daniel Maskell performed the cryo-electron tomography data collection on LCMV.

First and foremost, I would like to thank John for all his support, knowledge, optimism and solutions to the many problems I encountered during this PhD. There were some difficult times, especially with COVID, and John was an excellent supervisor throughout! I also must thank Juan, my assessor turned adopted supervisor, for teaching me so much about electron microscopy and sub-tomogram averaging, for his enthusiasm and for spending so much of his time to help me. Special thank you to Jamel for your problem-solving skills and scientific discussions, even when I gate-crashed a practical session. I would like to thank the electron microscopy facility, in particular Dan, for their assistance in my electron microscopy experiments, especially when COVID tried, and failed, to put a stop to it.

To the members of Garstang 8.61 and 8.54, thank you for your entertainment, knowledge and friendliness. I would particularly like to thank past and present members of the Barr group, who welcomed me with open arms and taught me everything I know today. Special thanks to Emma for fuelling my passion in electron microscopy, to Owen for his shared enthusiasm on the arenaviruses and to Ellie for the whiteboard games and being a fabulous team-mate. Thanks also go to Ollie for being my friend since the first day of uni, and to Kate for entertaining my crazy discussions and showing me a live feed of cows when I really needed it. I also have to thank the members of Wine Wednesday, who provided support, help, (wine) and laughs when I really needed it. Kat, thank you for being my best friend, my travelling buddy and just amazing, I really miss you!

Finally, the biggest thanks has to go to the people who got me to where I am today, my Mum, my Dad, my grandparents, my aunties and my brothers. You have always been there, you always fully supported whatever I did and you always fully believed in me - I love you all. Mum, thanks for all those times you kept me going when I felt I could not do it anymore. I also cannot write my acknowledgements without mentioning my thesis-writing support buddies, Sherlock and Honey-Bee, you are the most adorable cats ever!

Abstract

The *Arenaviridae* family of segmented RNA viruses includes several important human pathogens, some of which are the causative agents of haemorrhagic fever, a disease with severe morbidity and high mortality. Currently, effective therapeutic and preventative measures for such pathogens are limited. The prototypical arenavirus is lymphocytic choriomeningitis virus (LCMV), which on account of its low pathogenicity in humans provides the opportunity to understand more about arenavirus infections under bio-safety level 2 containment.

The work described here sought to develop and exploit molecular tools for arenavirus study. Firstly, a high-affinity antibody reactive against LCMV nucleocapsid protein (NP) was generated. This LCMV NP antibody was subsequently used to investigate the intracellular localisation of the NP during the viral lifecycle and to develop a method for the titration of non-cytolytic LCMV, allowing the quantification of infectious virus.

Secondly, the LCMV NP antibody and the titration method were subsequently used to optimise a reverse genetics system, designed to recover infectious recombinant LCMV entirely from cDNAs. This system was further engineered to introduce the eGFP gene into the S segment of LCMV, permitting simple and rapid monitoring of LCMV gene expression and infection through fluorescent live cell analysis. The reverse genetics system was further engineered to successfully generate infectious LCMV carrying a C-terminal-6xHis-tagged NP, which could be utilised to purify native viral ribonucleoprotein complexes from infected cells. The successful production of both of these tagged replication-competent recombinant LCMV variants are valuable tools for the study of arenaviruses.

Using the molecular tools generated here, LCMV was highly concentrated and purified for its examination by cryo-electron tomography, alongside another arenavirus, Pichindé virus (PICV), providing a direct comparison between the two arenaviruses. Sub-tomogram averaging was then used to resolve the structures of the native glycoprotein complex (GPC) entry spikes, present on the viral surface. These results indicated structural differences of the GPC between multiple arenaviruses, which could provide information on different entry requirements and their pathogenicity.

Contents

List of Figures

List of Tables

Abbreviations

BHK baby hamster kidney
bp base pair
BSA bovine serum albumin
CASV California Academy of Sciences virus
cDNA complementary deoxyribonucleic acid
CHAPV Chapare virus
CNS central nervous system
cRNA complementary ribonucleic acid
cryo-EM cryo-electron microscopy
cryo-ET cryo-electron tomography
CSF cerebrospinal fluid
DAAs direct acting antivirals
DMEM Dulbecco's modified eagle medium
DMSO dimethyl sulfoxide
DNase deoxyribonuclease
DTT dithiothreitol
EDTA ethylenediaminetetraacetic acid
eGFP enhanced green fluorescent protein
eIF4 eukaryotic initiation factor 4
EM electron microscopy
EMDB Electron Microscopy Data Bank
ER endoplasmic reticulum
ESCRT endosomal sorting complexes required for transport
FBS foetal bovine serum
ffu focus forming unit
G3BP1 Ras-GAP SH3 domain binding protein
GA Golgi apparatus
GAPDH glyceraldehyde 3-phosphate dehydrogenase
GPC glycoprotein complex
GTOV Guanarito virus
HAZV Hazara virus
HDV Rz hepatitis delta virus ribozyme
hpi hours post infection
hpt hours post transfection
HRP horseradish peroxidase
HTAs host-targeting antivirals
ICTV International Committee on Taxonomy of Viruses
IEC ion-exchange chromatography
IF immunofluorescence
IFN interferon
IGR intergenic region
IMAC immobilised metal-affinity chromatography
IRF3 interferon regulatory factor 3
JUNV Junín virus
kDa kilodalton
L segment large segment
LACV La Crosse virus
LAMP1 lysosomal associated membrane protein
LARGE like-acetylglucosaminyltransferase
LASV Lassa virus
LB Luria-Bertani
LCMV lymphocytic choriomeningitis virus
LCMV-ARM LCMV; armstrong strain
LCMV-Cl13 LCMV; clone-13 derivative
LDS lithium dodecyl sulphate
LP L Polymerase
LUJV Lujo virus
M segment medium segment
M^7G 7-methylguanosine
MACV Machupo virus
MOI multiplicity of infection
MOPV Mopeia virus
mRNA messenger ribonucleic acid
Ni^{2+}-NTA nickel-nitrilotriacetic acid
NMR nuclear magnetic resonance
NP nucleocapsid protein
NTA nitrilotriacetic acid
OD optical density
ORF open reading frame
P2A porcine teschovirus 1 2A
PAMP pathogen-associated molecular pattern
PCR polymerase chain reaction
pfu plaque forming unit
pI isoelectric point
PI4P phosphatidylinositol-4-phosphate
PICV Pichindé virus
pol-I/II polymerase I/II
PVDF polyvinylidene fluoride
RdRp RNA-dependent RNA polymerase
RIG-I retinoic acid-inducible gene I)
rLCMV recombinant LCMV
RNase ribonuclease
RNP ribonucleoprotein
RT-PCR reverse-transcription PCR
RTCs replication-transcription complexes
S segment small segment
SBAV Sabiá virus
SDS-PAGE sodium dodecyl sulphate–polyacrylamide gel electrophoresis
SEC size-exclusion chromatography
SFM serum-free Dulbecco's modified eagle medium

SKI-1/S1P subtilisin kexin isozyme-1/Site-1 protease
SUMO small ubiquitin-related modifier
T7P T7 RNA polymerase
TAE tris-acetate-EDTA
TCRV Tacaribe virus
Tsg101 tumour susceptibility gene 101
UHV University of Helsinki virus
ULP1 ubiquitin-like-specific protease 1
UTR untranslated region
VLP virus-like particle
vRNA virion-associated ribonucleic acid
ZP Z matrix protein

Chapter 1

Introduction to the Arenaviruses

1.1 General Introduction

1.1.1 Discovery

The first arenavirus was isolated in 1933 in St. Louis (USA), during sampling to find the etiological cause of an outbreak of encephalitis (Armstrong and Lillie, 1934). It was temporarily called the virus of experimental lymphocytic choriomeningitis (Armstrong and Lillie, 1934) and was later renamed to lymphocytic choriomeningitis virus (LCMV). In 1935, it was identified as a cause of aseptic meningitis in humans (Rivers and Scott, 1936) and the natural reservoir host was identified as the common house mouse (*Mus musculus*) (Traub, 1935). The original isolated LCMV strain was named the Armstrong strain, after Charles Armstrong who had isolated it (Armstrong and Lillie, 1934). Two other LCMV strains, Traub and WE, were also isolated in the 1930s, from laboratory-infected mice and a human who had been exposed to persistently infected mice (Takagi et al., 2012; Welsh and Seedhom, 2008). The Traub strain was named after Erich Traub, who had isolated the strain, whereas the WE strain was named after the person it was isolated from (Traub, 1935; Rivers and Scott, 1936).

The next arenaviruses discovered were Tacaribe virus (TCRV; Trinidad and Tobago; 1956 (Downs et al., 1963)) and Junín virus (JUNV; Argentina; 1958 (Parodi et al., 1958, 1959)). These viruses were shown to be serologically cross-reactive in complement fixation assays and were easily distinguishable from LCMV by neutralisation assays, leading to the establishment of the Tacaribe antigenic complex (Casals et al., 1963). By the 1970s, several other arenaviruses had been discovered and were added to this grouping due to their cross-reactivity in the complement

fixation assays (Machupo (Johnson et al., 1965); Amaparí (Pinheiro et al., 1966); Latino (first mentioned in (Murphy et al., 1970)); Parana (Johnson et al., 1965); Pichindé (Trapido and Sanmartín, 1971); and Tamiami (Lord et al., 1970)). Some of these newly identified arenaviruses did not cause disease in humans, whilst others caused severe, and often fatal, human diseases, which were clinically quite similar (Radoshitzky et al., 2015).

Members of the Tacaribe antigenic complex were not serologically cross-reactive with LCMV, but there was cross-reactivity between these viruses in indirect immunofluorescence assays (Rowe et al., 1970a). Furthermore, examination by thin-section electron microscopy revealed these viruses to be morphologically indistinguishable from LCMV (Murphy et al., 1970). This led to the establishment of a new taxonomic group of viruses called the Arenaviruses (initially Arenoviruses (Rowe et al., 1970b)). The group was named as such because the electron microscopic investigation revealed the presence of electron-dense granules, proposed to be host cell ribosomes, in the viral particles, giving them a sandy (Latin; *arenosus*) appearance (Rowe et al., 1970b; Dalton et al., 1968). LCMV was made the prototypic virus of this group (Rowe et al., 1970b). In 1969, another arenavirus was discovered in patients suffering from Lassa fever in Nigeria (Frame et al., 1970). Lassa virus (LASV) was serologically cross-reactive, using the complement fixation assay, with LCMV and some members of the Tacaribe antigenic complex (Buckley et al., 1970), and shared morphological similarities with LCMV (Wood et al., 1970).

In addition to the serological and morphological similarities shared by these viruses, the viruses also shared similar biological and biochemical properties and all persisted in nature by establishing chronic infections of rodent hosts (Howard and Young, 1984; Radoshitzky et al., 2015). This provided enough evidence for the International Committee on Taxonomy of Viruses (ICTV) to establish a new taxon; the *Arenavirus* genus, which later developed into the *Arenaviridae* family (Fenner, 1976).

Over the years, serological evidence has guided the addition of newly discovered arenaviruses to the *Arenaviridae* family. During the last ten years, there has been a significant increase in the rate of discovery of arenaviruses (table 1.2). This is the result of the technological advancements in next-generation sequencing. This development has also led to an expansion of arenavirus-harbouring hosts, including shrews, reptiles (specifically snakes) and fish. This has also resulted in

the reclassification of the *Arenaviridae* family, incorporating a further three genera (Garry and Garry, 2019)).

1.1.2 Classification of the *Bunyavirales* Order

Recently, the ICTV reorganised virus taxonomy in order for the organisation to better reflect that of other biological taxonomies. This would assist the discovery of novel viruses and their taxonomic assignment. Therefore, the ICTV created the first viral realm; Riboviria, comprising all viruses with RNA as genomic material. The reorganisation of the taxonomy led to the establishment of the *Bunyavirales* order (Realm: *Riboviria* > Kingdom: *Orthornavirae* > Phylum: *Negarnaviricota* > Subphylum: *Polyploviricotina* > Class: *Ellioviricetes*), into which the *Arenaviridae* family was classified. Other families within the *Bunyavirales* order include *Cruliviridae*, *Fimoviridae*, *Hantaviridae*, *Leishbuviridae*, *Mypoviridae*, *Nairoviridae*, *Peribunyaviridae*, *Phasmaviridae*, *Phenuiviridae*, *Tospoviridae* and *Wupedeviridae*. The *Bunyavirales* order was created in order to group together related viruses, all of which have a single-stranded, segmented RNA genome in either negative-sense or ambisense orientation (Maes et al., 2018). There are 477 virus species classified within the *Bunyavirales* order, which infect a wide range of hosts, including mammals, reptiles, birds, fish, insects, plants and arthropods, reflecting the diversity of the order (figure 1.1).

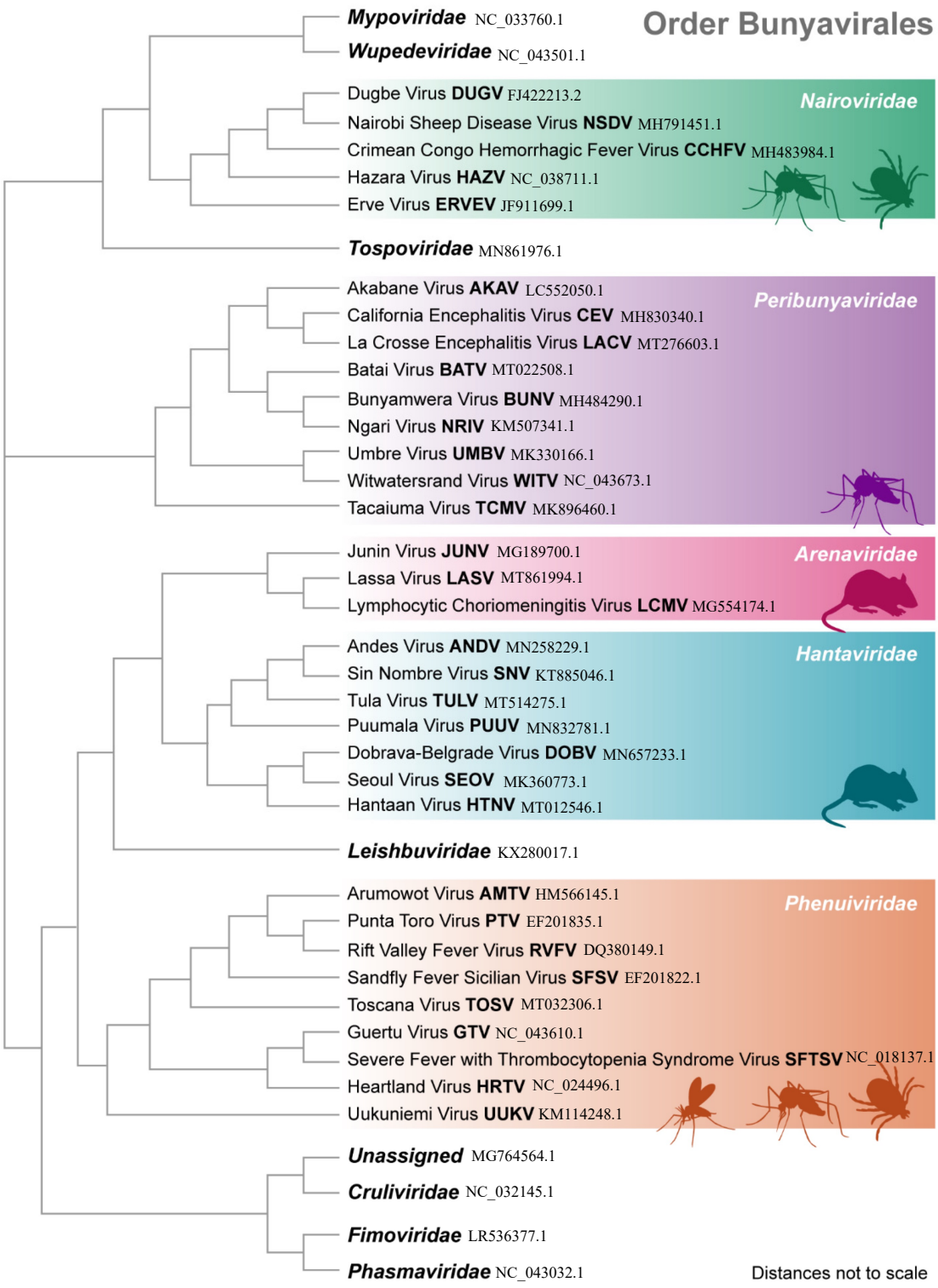

Figure 1.1: Phylogenetic Tree of the *Bunyavirales* Order The 13 families of the *Bunyavirales* Order were organised into a phylogenetic tree based on the nucleocapsid protein amino acid sequences. In families where a virus has not been specified, the type virus species was used for analysis. The vector species have been included for the *Nairoviridae* (mosquito, tick), *Peribunyaviridae* (mosquito), *Arenaviridae* (rodent), *Hantaviridae* (rodent), and *Phenuiviridae* (sandfly, mosquito, tick) families. The tree was assembled by (Leventhal et al., 2021), using Geneious Prime tree builder global alignment and the tree was transformed to make the branches equal length, therefore it is not to scale. GenBank accession numbers for sequences have been included alongside the virus name.

1.1.3 Classification of the *Arenaviridae* Family

Based on phylogenetic analysis of the sequences of the viral RNA-dependent RNA-polymerase (LP) and the nucleocapsid protein (NP), the *Arenaviridae* family has been recently organised into four genera; *Antennavirus*, *Hartmanivirus*, *Mammarenavirus* and *Reptarenavirus*, comprising a total of 50 species (as of July 2019, (Walker et al., 2019)). Table 1.1 describes the classification of all the arenavirus species within the *Arenaviridae* family, whereas the phylogeny of the arenavirus species has been shown in figure 1.2.

For a novel arenavirus to be designated as a new arenavirus species, it must fulfil the following ICTV criteria; the virus must have been isolated from a new natural host species, the virus must be present in a new distinct geographic region and the viral nucleocapsid protein (NP) sequence must be sufficiently different from others by at least 12 % (Radoshitzky et al., 2015; Salvato et al., 2005).

Table 1.1: ICTV-Accepted Taxonomic Organisation of the *Arenaviridae* Family.

Genus	Species	Viruses	Abbr.
Antennavirus	*Hairy antennavirus*	Wēnlǐng frogfish arenavirus 2	WlFAV-2
	Striated antennavirus	Wēnlǐng frogfish arenavirus 1	WlFAV-1
Hartmanivirus	***Haartman hartmanivirus***	Haartman Institute snake virus 1	HISV-1
		Haartman Institute snake virus 2	HISV-2
	Muikkunen hartmanivirus	Dante Muikkunen virus 1	DMaV-1
	Schoolhouse hartmanivirus	old schoolhouse hartmanivirus 1	OScV-1
		old schoolhouse hartmanivirus 2	OScV-2
	Zurich hartmanivirus	veterinary pathology Zurich virus 1	VPZV-1
		veterinary pathology Zurich virus 2	VPZV-2
Mammarenavirus	*Allpahuayo mammarenavirus*	Allpahuayo virus	ALLV
	Alxa mammarenavirus	Alxa virus	ALXV
	Argentinian mammarenavirus	Junín virus	JUNV
	Bear Canyon mammarenavirus	Bear Canyon virus	BCNV
	Brazilian mammarenavirus	Sabiá virus	SBAV
	Cali mammarenavirus	Pichindé virus	PICV
	Chapare mammarenavirus	Chapare virus	CHAPV
	Chevrier mammarenavirus	Lìjiāng virus	LIJV
	Cupixi mammarenavirus	Cupixi virus	CUPXV
	Flexal mammarenavirus	Flexal virus	FLEV
	Gairo mammarenavirus	Gairo virus	GAIV
	Guanarito mammarenavirus	Guanarito virus	GTOV
	Ippy mammarenavirus	Ippy virus	IPPYV
	Lassa mammarenavirus	Lassa virus	LASV
	Latino mammarenavirus	Latino virus	LATV
	Loei River mammarenavirus	Loei River virus	LORV
	Lujo mammarenavirus	Lujo virus	LUJV
	Luna mammarenavirus	Luli virus	LULV

Continuation of Table 1.1

Genus	**Species**	**Viruses**	**Abbr.**
		Luna virus	LUAV
	Lunk mammarenavirus	Lunk virus	LNKV
	Lymphocytic choriomeningitis mammarenavirus	Dandenong virus	DANV
		lymphocytic choriomeningitis virus	LCMV
	Machupo mammarenavirus	Machupo virus	MACV
	Mariental mammarenavirus	Mariental virus	MRLV
	Merino Walk mammarenavirus	Merino Walk virus	MRWV
	Mobala mammarenavirus	mobala virus	MOBV
	Mopeia mammarenavirus	Mopeia virus	MOPV
		Morogoro virus	MORV
	Okahandja mammarenavirus	Okahandja virus	OKAV
	Oliveros mammarenavirus	Oliveros virus	OLVV
	Paraguayan mammarenavirus	Paraná virus	PRAV
	Pirital mammarenavirus	Pirital virus	PIRV
	Planalto mammarenavirus	Aporé virus	APOV
	Ryukyu mammarenavirus	Ryukyu virus	RYKV
	Serra do Navio mammarenavirus	Amaparí virus	AMAV
	Solwezi mammarenavirus	Solwezi virus	SOLV
	Souris mammarenavirus	souris virus	SOUV
	Tacaribe mammarenavirus	Tacaribe virus	TCRV
	Tamiami mammarenavirus	Tamiami virus	TMMV
	Wenzhou mammarenavirus	Wēnzhōu virus	WENV
	Whitewater Arroyo mammarenavirus	Big Brushy Tank virus	BBRTV
		Catarina virus	CTNV
		Skinner Tank virus	SKTV
		Tonto Creek virus	TTCV
		Whitewater Arroyo virus	WWAV
	Xapuri mammarenavirus	Xapuri virus	XAPV
Reptarenavirus	*California reptarenavirus*	CAS virus	CASV
	Giessen reptarenavirus	University of Giessen virus 1	UGV-1
		University of Giessen virus 2	UGV-2
		University of Giessen virus 3	UGV-3
	Golden reptarenavirus	Golden Gate virus	GOGV
	Ordinary reptarenavirus	tavallinen suomalainen mies virus 2	TSMV-2
	Rotterdam reptarenavirus	ROUT virus 1	ROUTV
		University of Helsinki virus 1	UHV-1

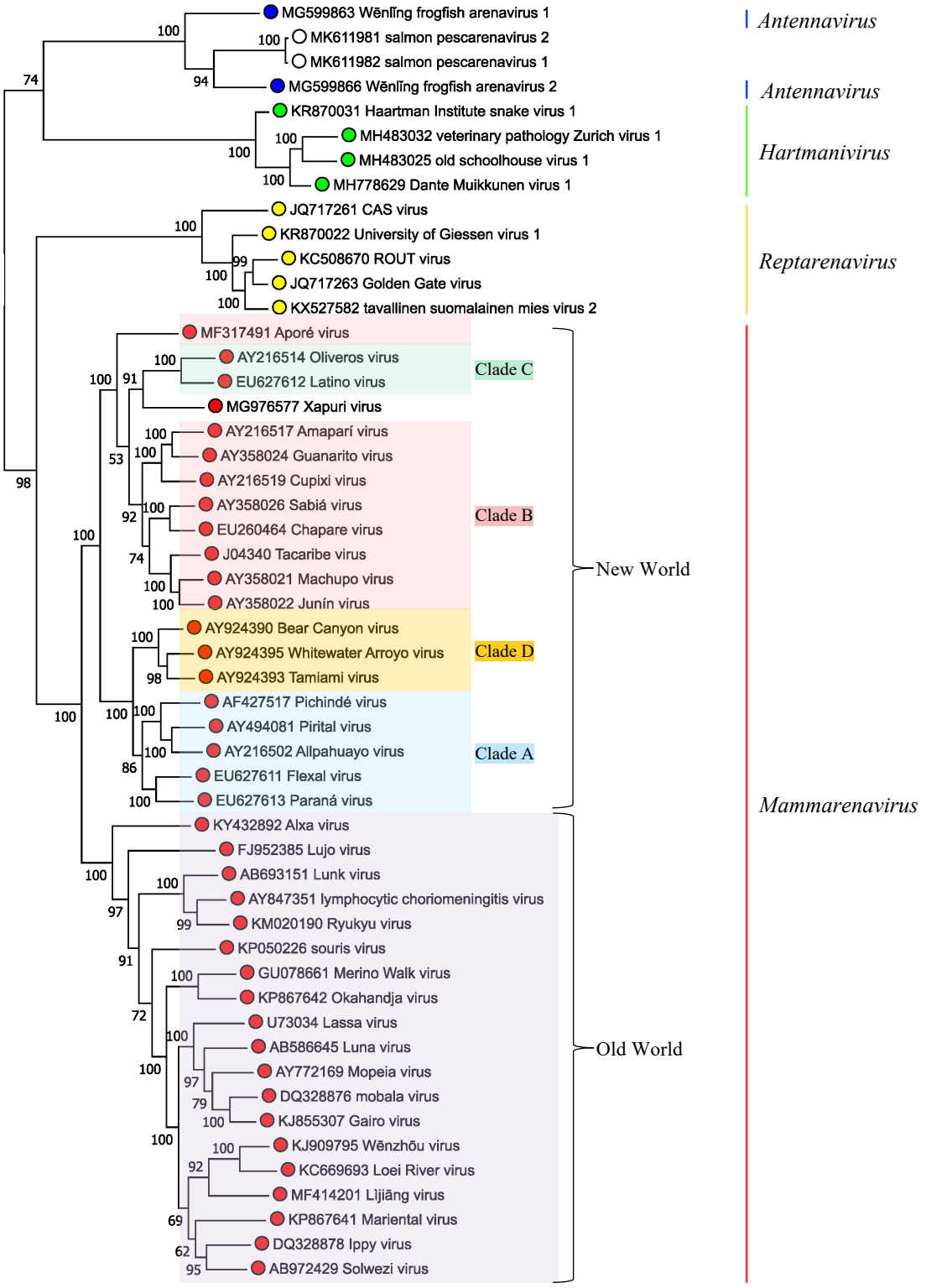

Figure 1.2: Phylogenetic Tree of the *Arenaviridae* Family 50 species from the *Arenaviridae* family were organised into a phylogenetic tree based on the L polymerase amino acid sequence. The species cluster into the four genera; *Antennavirus* (blue), *Hartmanivirus* (green), *Reptarenavirus* (yellow) and *Mammarenavirus* (red). There are also two unclassified virus species (blue rings). The tree was assembled by (Radoshitzky et al., 2019) and was mid-point rooted and visualised using FigTree (http://tree.bio.ed.ac.uk).

The *Mammarenavirus* genus comprises all the arenaviruses which have a mammalian host. Mammarenaviruses have a negative-sense RNA genome, which is bisegmented and encodes four proteins (L polymerase [LP], nucleocapsid protein [NP], the glycoprotein complex [GPC] and the Z matrix protein [ZP]) in an ambisense orientation, whereby LP and NP are transcribed from the negative-sense virion-associated RNA (vRNA) and GPC and ZP are transcribed from the positive-sense replicate of the vRNA (complement RNA; cRNA). The species in the *Mammarenavirus* genus are organised into Old World (Lassa-lymphocytic choriomeningitis serocomplex) and New World (Tacaribe serocomplex) groups. The New World group is further classified into four lineages; clades A, B, C and A/Recombinant (tentatively named D) (table 1.2). The *Mammarenavirus* genus has been traditionally organised into these groups since the late 1970s, based on serological analysis, geographical distribution and host association (Matthews, 1979). Subsequent phylogenetic analysis of the viral genes has supported this organisation (Radoshitzky et al., 2015). Viruses in clade D have been formed through recombination events between the arenaviruses. The S segments of clade D arenaviruses appear to have a chimeric origin, with an NP sequence most closely related to clade A arenaviruses and a GPC sequence most closely related to clade B arenaviruses (Archer and Rico-Hesse, 2002; Charrel et al., 2001, 2002; Fulhorst et al., 2002). Xapuri virus (XAPV; Brazil; 2015 (Fernandes et al., 2018)) was recently assigned to the New World group but phylogenetic analysis could not assign this virus to a clade. Phylogenetic analysis of the S segment, and the GPC sequence, revealed that it was most closely related to clade C viruses, whereas analysis of the L segment, and the NP, LP and ZP amino acid sequences, showed it was most closely related to viruses within clade B (Fernandes et al., 2018). Therefore, it was placed between clades B and C and it is thought that XAPV could be the first natural reassortant of the mammarenaviruses (Fernandes et al., 2018).

In 2015, the *Arenaviridae* family was extended by the creation of the *Reptarenavirus* genus, after the discovery of several novel arenaviruses in captive snakes exhibiting boid inclusion body disease (BIBD) (Stenglein et al., 2012; Bodewes et al., 2013; Hetzel et al., 2013). These reptarenaviruses had the distinctive arenavirus genome organisation, including the canonical ambisense orientation of the four mammarenavirus open reading frames, as well as the characteristic non-translated

gene regulatory elements. However, the reptarenaviruses were quite divergent from the mammarenaviruses in terms of sequence, with low overall homology between the amino acid sequences of NP (23-26 %) and LP (17-19 %) (Stenglein et al., 2012). In contrast, the reptarenaviruses were quite similar to each other, with NP and LP sequences exhibiting 55 % and 50 % identity, respectively (Stenglein et al., 2012) and thus supporting the establishment of an independent phylogeny, and new genus within the *Arenaviridae* family. The reptarenaviruses were even more divergent from the mammarenaviruses in the ZP sequence (16 %) ((Stenglein et al., 2012; Pontremoli et al., 2019)) and the reptarenavirus GPCs did not contain the structural features commonly associated with mammarenavirus GPCs. Interestingly though, the reptarenavirus GPCs shared a higher homology with the glycoproteins of filoviruses (e.g. Ebola virus) (Stenglein et al., 2012; Garry and Garry, 2019) suggesting a potential common ancestor virus of the *Arenaviridae* and *Filoviridae* families. Cryo-electron tomographic 3D reconstruction of the University of Helsinki virus (UHV) glycoproteins further supported this assertion, revealing structural homology between the reptarenavirus glycoprotein and Ebola virus glycoprotein, and striking differences between the UHV glycoprotein and the LASV glycoprotein (Hetzel et al., 2013; Li et al., 2016).

The *Hartmanivirus* genus was formed in 2018 (Maes et al., 2018) after pairwise sequence comparison (PASC) analysis on the BIBD-isolates suggested one of the novel reptarenaviruses, Haartman Institute snake virus (HISV), was sufficiently distant from the other reptarenaviruses to represent a new genus (Hepojoki et al., 2015, 2018). Next generation sequencing analysis and *de novo* sequence assembly revealed further information about the HISV1 isolate and identified three additional novel species (Hepojoki et al., 2018). Extensive sequencing revealed that hartmaniviruses possessed S and L segments, but that the L segment only encoded the LP, so these viruses did not appear to express a ZP (Hepojoki et al., 2018; Garry and Garry, 2019). Unlike members in the *Reptarenavirus* genus, the hartmanivirus glycoproteins share many of the proposed structural motifs present within the mammarenavirus glycoproteins (Hepojoki et al., 2018). There was also higher sequence homology between the hartmanivirus glycoprotein and the mammarenavirus glycoprotein (23 %), as opposed to 16 % when reptarenavirus Golden Gate virus (GGV) and LCMV were compared (Hepojoki et al., 2018; Garry

and Garry, 2019). Also, unlike reptarenaviruses, hartmaniviruses have not as yet been associated with any pathological effect in snakes (Hepojoki et al., 2018).

The *Antennavirus* genus is the most recently established genus of the *Arenaviridae* family (Abudurexiti et al., 2019) and their discovery resulted from a large metatranscriptomic study that identified hundreds of novel RNA viruses present in cold-blooded vertebrates (Shi et al., 2018), of which two were novel arenaviruses, infecting frogfish (*Antennarius striatus*) (Shi et al., 2018). Not only was this another expansion in the host range of the arenaviruses, but it represented the first arenaviruses with three RNA genomic segments instead of two. Antennaviruses have a negative-sense S segment, encoding the NP ORF; a negative-sense L segment, encoding the LP ORF; and an additional ambisense M segment, encoding the GPC ORF and a protein of unknown function (Shi et al., 2018; Garry and Garry, 2019). Similarly to members of the *Hartmanivirus* genus, antennaviruses do not encode a ZP. The antennaviruses were placed into the *Arenaviridae* family after sequence homology was found between the antennavirus NP and LP sequences and hartmanivirus NP and LP sequences (Shi et al., 2018; Pontremoli et al., 2019). Whilst the antennavirus GPC did not share sequence homology with arenavirus GPCs, it did share predicted structural motifs with mammarenaviruses and hartmaniviruses, but not reptarenaviruses (Garry and Garry, 2019).

1.1.4 Hosts and Transmission

Hosts of Arenaviruses

Each mammarenavirus is associated with a single or a small number of specific rodent reservoir hosts, except for TCRV. Generally, the reservoir hosts of any given virus are defined as animals or plants that permit persistence of an infectious agent in the environment, but do not typically experience disease upon infection (Salazar-Bravo et al., 2002). The rodent species with which each arenavirus is associated has been listed in table 1.2. The close association between rodent hosts and arenaviruses is thought to determine the geographic distribution of the arenaviruses. Nearly all the rodent host species of mammarenaviruses are classified within the *Muroidea* superfamily. The majority of Old World mammarenaviruses are associated with rodent species classified within Family: *Muridae*; Subfamily: *Murinae*, with the

exception of Alxa virus (associated with rodent species classified within the sister Superfamily: *Dipodoidea*; Family: *Dipodidae*; Subfamily: *Dipodinae*), Mariental and Okahandja viruses (associated with rodent species classified only within the *Muridae* family) and Wēnzhōu virus (associated with one rodent species that is classified within Family: *Soricidae*). New World mammarenaviruses are associated with rodent species classified within Family: *Cricetidae*; Subfamily: *Sigmodontinae*, with the exception of viruses in clade D, which are associated with rodent species classified within Family: *Cricetidae*; Subfamily: *Neotominae*. Some arenaviruses, such as MOPV and LASV, share rodent hosts. This can be beneficial to humans living in regions that are endemic for MOPV, because infection with MOPV can offer cross-protection for LASV, resulting in fewer cases of Lassa fever in that region (Zapata and Salvato, 2013).

TCRV is the only arenavirus which has never been associated with any rodent host. It was first isolated from fruit bats (*Artibeus* spp.) in Trinidad during a surveillance programme for rabies virus (Downs et al., 1963). It was also initially isolated from mosquitoes (Downs et al., 1963), although subsequent attempts to repeat this feat have proven unsuccessful (Sayler et al., 2014; Salazar-Bravo et al., 2002). Since its discovery, all attempts to identify a rodent host for TCRV have failed (Downs et al., 1963; Sayler et al., 2014). Bats were then proposed to be the natural reservoir of TCRV, but this has since been disputed (Cogswell-Hawkinson et al., 2012). There is serological evidence of TCRV infection in *Artibeus* bats, but there is no evidence it causes a persistent infection, suggesting bats are not the reservoir hosts (Malmlov et al., 2017). It has also been suggested that TCRV causes a fatal infection in bats (Cogswell-Hawkinson et al., 2012). It has subsequently been suggested that the reservoir host may be lone star ticks (*Amblyomma americanum*), giving the only known arthropod host of the arenaviruses (Sayler et al., 2014). Subsequent metatranscriptomic studies in arthropod hosts have not revealed any novel arenaviruses associated with arthropods (Shi et al., 2016). The natural hosts of reptilian arenaviruses have not been identified because they have only been detected in captive snakes and are associated with disease (Hetzel et al., 2013; Hepojoki et al., 2015, 2018; Stenglein et al., 2012).

Table 1.2: Organisation, Isolation, Distribution and Hosts of the *Mammarenavirus* Genus.

Virus	Isolated	Geographic Distribution	Host Species	GenBank ID
Old World				
Alxa virus	2014	China	*Dipus sagitta* (Northern three-toed jerboas)	KY432893.1
Lìjiāng virus	2015	China	*Apodemus chevrieri* (Chevrier's field mice)	MF414202.1
Gairo virus	2015	Tanzania	*Mastomys natalensis* (multimammate rat)	KJ855308.1
Ippy virus	1985	Central African Republic	*Arvicanthis* spp. (grass rat)	DQ328877.1
Lassa virus	1969	West Africa (Imported Cases in Europe, Japan, USA)	*Mastomys natalensis* (multimammate rat)	HQ688672.1
Loei River virus	2016	Thailand	*Bandicota indica* (Greater bandicoot rat), *Bandicota savilei* (Savile's bandicoot rat), *Niviventer fulvescens* (Chestnut white-bellied rat)	KC669698.1
Lujo virus	2008	Zambia, Republic of South Africa	Unknown	JX017360.1
Luna virus	2009	Zambia	*Mastomys natalensis* (multimammate rat)	AB586644.1
Lunk virus	2012	Zambia	*Mus minutoides* (African pygmy mouse)	AB693150.1
Lymphocytic choriomeningitis virus	1933	Americas, Europe, Asia	*Mus musculus* (house mouse)	AY847350.1
Mariental virus	2015	Namibia	*Micaelamys namaquensis* (Namaqua rock rat)	KM272987.1
Merino Walk virus	1985	Republic of South Africa	*Myotomys unisulcatus* (Karoo bush rat)	GU078660.1
Mobala virus	1983	Central African Republic	*Praomys* spp. (soft-furred mouse)	AY342390.1
Mopeia virus	1977	Mozambique, Zimbabwe	*Mastomys natalensis* (multimammate rat)	AY772170.1
Okahandja virus	2015	Namibia	*Micaelamys namaquensis* (Namaqua rock rat)	KM272988.1
Ryukyu virus	2017	China	*Mus caroli* (Ryukyu mouse)	KM020191.1
Solwezi virus	2016	Zambia	*Grammomys* sp. (thicket rat)	AB972428.1
Souris virus	2014	Cameroon	*Praomys* spp. (soft-furred mouse)	KP050227.1
Wēnzhōu virus	2015	China	*Rattus norvegicus* (brown rat), *Rattus losea* (Losea rat), *Rattus tanezumi* (oriental house rat), *Rattus rattus* (roof rat), *Suncus murinus* (Asian house shrew)	KJ909794.1
New World - Clade A				
Allpahuayo virus	2001	Peru	*Oecomys bicolor* (bicolored arboreal rice rat), *Oecomys paricola* (Brazilian arboreal rice rat)	AY012687.1
Flexal virus	1977	Brazil	*Oryzomys* spp. (rice rat)	AF512831.1

Continuation of Table 1.2

Virus	Isolated	Geographic Distribution	Host Species	GenBank ID
Paraná virus	1970	Paraguay	*Oryzomys buccinatus* (Paraguayan rice rat)	AF485261.1
Pichindé virus	1971	Colombia	*Nephelomys albigularis* (Tomes's rice rat)	K02734.1
Pirital virus	1997	Venezuela	*Sigmodon alstoni* (Alston's cotton rat)	AF485262.1
New World - Clade B				
Amaparí virus	1965	Brazil	*Oryzomys goeldi* (large-headed rice rat), *Neacomys guianae* (Guiana bristly mouse)	AF485256.1
Aporé virus	2008	Brazil	*Oligoryzomys mattogrossae* (pygmy rice rats)	MF317490.1
Chapare virus	2008	Bolivia	Unknown	EU260463.1
Cupixi virus	1965	Brazil	*Oryzomys capito* (large-headed rice rat)	AF512832.1
Guanarito virus	1989	Venezuela	*Zygodontomys brevicauda* (common cane mouse), *Sigmodon alstoni* (Alston's cotton rat)	AY129247.1
Junín virus	1958	Argentina	*Callomys musculinus* (Drylands vesper mouse)	AY358023.2
Machupo virus	1963	Bolivia	*Callomys callosus* (Large vesper mouse)	AY129248.1
Sabiá virus	1993	Brazil	Unknown	U41071.1
Tacaribe virus	1956	Trinidad, West Indies	Unknown	M20304.1
New World - No Clade				
Xapuri virus	2015	Brazil	*Neacomys musseri* (Musser's neacomys)	MG976578.1
New World - Clade C				
Latino virus	1973	Bolivia, Brazil	*Callomys callosus,* (Large vesper mouse) *Callomys callidus* (crafty vesper mouse)	AF512830.1
Oliveros virus	1996	Argentina	*Necromys obscuris* spp. (Dark bolo mouse)	U34248.1
New World - Clade D				
Bear Canyon virus	1998	USA	*Peromyscus californicus* (California mouse), *Neotoma macrotis* (Big-eared woodrat)	AY924391.1
Tamiami virus	1970	USA	*Sigmodon hispidus* (Hispid cotton rat)	AF485263.1
Whitewater Arroyo virus	1997	USA	*Neotoma* spp. (woodrat)	AF228063.1
Big Brushy Tank virus	2002	USA	*Neotoma albigula* (White-throated woodrat)	EF619035.1
Catarina virus	2007	USA	*Neotoma micropus* (Southern Plains woodrat)	DQ865245.1
Skinner Tank virus	2008	USA	*Neotoma mexicana* (Mexican woodrat)	EU123328.1
Tonto Creek virus	2001	USA	*Neotoma albigula* (White-throated woodrat)	EF619033.1

Arenavirus Infection in Rodents

Arenavirus infection in rodent host species typically manifests as persistent and sub-clinical, with few negative effects on the rodent. It has been suggested that infection can result in decreased size, reduced fertility and increased mortality, but this is dependent on host genetics and virus strain (Vitullo et al., 1987; Vitullo and Merani, 1988; Borremans et al., 2011; Zapata and Salvato, 2013). The majority of the time, arenavirus infection of the host species will present as asymptomatic, with high viral titres present in body fluids, including urine, faeces, blood and saliva (Zapata and Salvato, 2013; Salazar-Bravo et al., 2002). This mediates the horizontal transmission of arenaviruses throughout the rodent population, by close physical contact, inhalation of aerosolised body fluids and bites (Tagliapietra et al., 2009; Sarute and Ross, 2017; Milazzo et al., 2011). Arenaviruses can also be vertically transmitted, which has been proposed to be a factor for establishing chronic infections (Skinner and Knight, 1974; Tagliapietra et al., 2009; Milazzo et al., 2011). It is thought that because the rodent pups are born with the infection, an effective immune response is never mounted due to recognition of the viral antigens as self, leading to a chronic, life-long infection (King et al., 2018).

Arenaviruses are proposed to persist in chronically-infected rodents during periods of low rodent population density (Mariën et al., 2020a; Milazzo et al., 2011). In order to persist, the arenaviruses must not overrun the host because that could lead to immune detection and viral clearance. Therefore, LCMV, in particular, restricts its spread by cycling through periods of acute, productive infection and persistent, non-productive infection (King et al., 2018). Using a cell-culture model of persistent infection and fluorescent detection of single RNA molecules, it was found that the LCMV-infected cells cycle through periods of active viral replication and transcription and periods where viral RNA could no longer be detected (King et al., 2018). This cyclical loss and accumulation of viral RNA and viral antigens has also been shown *in vivo* (Francis and Southern, 1988). How arenaviruses are able to regulate this is unknown, but several models have been proposed involving defective interfering particles or replication-competent but transcription-incompetent genomes (King et al., 2018). Specific residues have been identified in different strains of LCMV, namely the Armstrong strain (LCMV-ARM) and its derivative Clone-13 (LCMV-Cl13), which have been attributed to the

establishment of either an acute (LCMV-ARM; F260 in GPC and K1079 in LP) or persistent (LCMV-Cl13; L260 in GPC and Q1079 in LP) infection (Grande-Pérez et al., 2016; Zapata and Salvato, 2013).

Arenavirus Transmission to Humans

Accidental exposure to humans and other mammals (including non-human primates) can occur through; disturbance, aerosolisation and subsequent inhalation of rodent excreta; ingestion of contaminated food or water; rodent bites; direct contamination of blood during handling of infected bush meat; or ingestion of infected bush meat (Ogbu et al., 2007; Sarute and Ross, 2017; Mariën et al., 2020b; Milazzo et al., 2011). Transmission of arenaviruses from rodents to humans typically happens when the rodents' natural habitats have been disturbed by changes in agricultural practices or extreme weather (Sarute and Ross, 2017; Charrel and de Lamballerie, 2010). The disturbance in habitat leads to the establishment of new territories, which could increase access to humans, their homes or their food stocks. During rainy seasons, there is also a sudden increase in the rodent population, which leads to territory expansion and increased contact with humans in addition to increased arenavirus transmission within the rodent population (Tagliapietra et al., 2009; Sarute and Ross, 2017). Furthermore, there is the potential for arenavirus infections in scientists that handle the infected rodents in either the field or in a laboratory setting, and for agricultural workers who can encounter infected rodents in the field (Ogbu et al., 2007; Charrel and de Lamballerie, 2010).

Arenaviruses can also be transmitted between humans. Nosocomial transmission is common with haemorrhagic fever-causing arenaviruses, posing a high risk to healthcare workers (Milazzo et al., 2011; Kernéis et al., 2009). This was demonstrated by the emergence of Lujo virus in 2008, which resulted in the death of four of the five infections, four of which were healthcare workers (Briese et al., 2009). Nosocomial transmission is common because of the high viral titre in bodily fluids and the lack of proper preventative measures, including personal protective equipment (PPE) and patient isolation (Ogbu et al., 2007; Sandige, 2018). Arenaviruses, specifically LASV and LCMV, can also be vertically transmitted between mother and fetus. LASV can result in a high mortality of both the mother and the fetus, whereby mortality is higher for women infected in a later trimester

(30 % as opposed to 7 % in the earlier trimester) and higher for fetuses infected in an earlier trimester (92 % as opposed to 75 % in the later trimester) (Ogbu et al., 2007; Price et al., 1988). There is also a 100 % fatality rate in neonates (Ogbu et al., 2007; Price et al., 1988). There is a high concentration of LASV in the fetal and placenta tissues and it is thought that this is the result of a lack of MHC presentation by these tissues, so the mother's immune system cannot attack these infected cells (Ogbu et al., 2007). LCMV infection in pregnant women can often be passed transplacentally to the fetus, causing fetal death and significant congenital deformities (Bonthius, 2012; Wright et al., 1997; Barton and Hyndman, 2000; Barton and Mets, 2001). It has even been shown that there can be sexual transmission of arenaviruses, including LASV and LCMV, due to the persistence of the virus in semen for many months after symptoms have disappeared (Raabe et al., 2017a; Ogbu et al., 2007; Trapecar et al., 2018). Finally, LCMV can also be transmitted between humans through organ transplantation; the recipient can become infected if the organ donor was asymptomatically infected with LCMV (Sarute and Ross, 2017; Fischer et al., 2006). The recipient receives immunosuppressive therapy in order to prevent transplant rejection, rendering the recipient vulnerable to a haemorrhagic fever-style LCMV infection (Peters, 2006; Fischer et al., 2006). Typically, in LCMV infections derived from organ transplantation, the fatality rate is very high, as is transplant rejection (Fischer et al., 2006).

1.1.5 Geographical Distribution

Arenaviruses are present in distinct geographical regions and rarely establish infections outside these regions. This is because the geographical distribution of the arenaviruses is limited to the range of the host rodent and unless a new rodent territory is established, then the arenavirus will not persist outside that range. Broadly speaking, Old World arenaviruses are located in Africa, while New World arenaviruses are found predominantly in South America, with the clade D arenaviruses being found in North America. LCMV has a worldwide distribution due to the worldwide distribution of its rodent host, *Mus musculus*. Some recently discovered Old World arenaviruses were identified in Asia, suggesting another location of arenavirus distribution. A map showing the geographic distribution of the arenaviruses has been shown in figure 1.3. The geographic distribution of

each mammarenavirus species has also been listed in table 1.2.

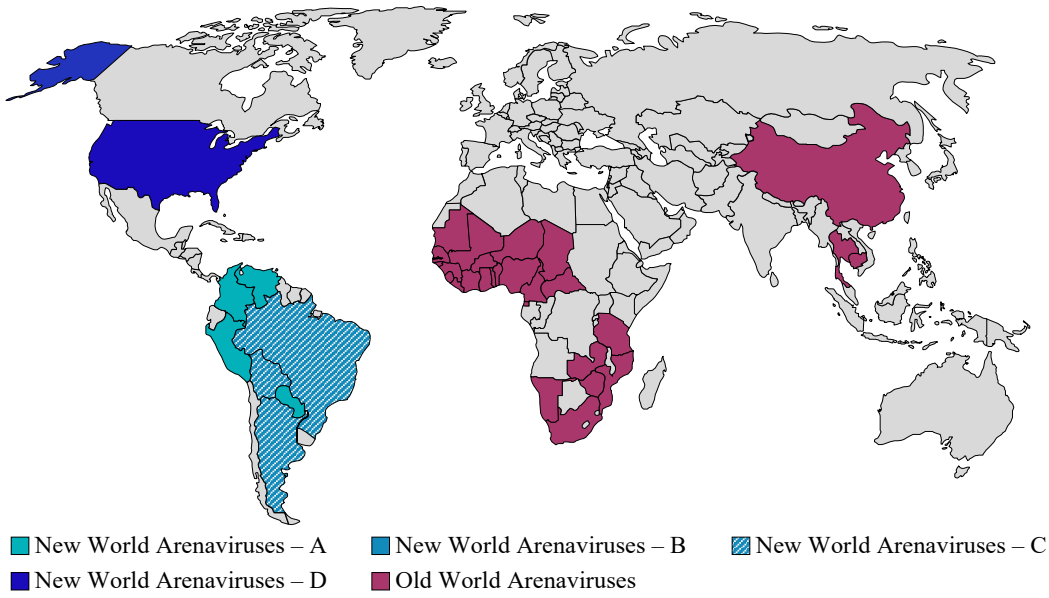

Figure 1.3: Geographic Distribution of the Mammarenaviruses by Country. Members of the Old World group of mammarenaviruses (pink) are predominantly found in African countries, with some species endemic in China. Members of the New World group of mammarenaviruses (blue) are predominantly found in South American countries, with some species endemic in the USA. This figure was created using information from (Radoshitzky et al., 2015; Fehling et al., 2012; Sarute and Ross, 2017; Li et al., 2015; Maes et al., 2018; Howley and Knipe, 2020).

Whilst arenavirus distribution rarely exceeds that of the rodent host, the distribution of arenaviruses does not necessarily cover the entirety of the rodent host distribution (Gryseels et al., 2017). For example, the rodent host *Mastomys natalensis* has a very broad distribution spanning sub-Saharan Africa, yet LASV infections have not been detected beyond the east of Nigeria (Gryseels et al., 2017). Furthermore, there are other arenaviruses which infect *Mastomys natalensis* but the regions occupied by these arenaviruses do not overlap (Gryseels et al., 2017). This is proposed to be due to the actual rodent host being a sub-taxon of the species level of rodent (Gryseels et al., 2017).

1.1.6 Pathogenesis and Disease

Humans generally acquire mammarenavirus infections through close contact with excreta from or directly with an infected rodent. Infections can also be transmitted directly between humans, either in nosocomial settings, during pregnancy or through organ donation. The severity of arenavirus infections in humans ranges

from asymptomatic infections to highly fatal haemorrhagic fever. The primary mammarenaviruses responsible for causing human disease include Old World mammarenaviruses LCMV and LASV and New World clade B mammarenaviruses JUNV, Machupo virus (MACV), Chapare virus (CHPV), Guanarito virus (GTOV) and Sabiá virus (SBAV).

LCMV and Meningitis

In immunocompetent adults, LCMV generally causes asymptomatic infections, or can result in mild "flu-like" symptoms (Lapošová et al., 2013). Occasionally, LCMV infection can result in aseptic meningitis and meningoencephalitis, with symptoms that include a fever, headache, stiff neck, nausea, confusion and motor-sensory abnormalities. However, LCMV rarely causes fatality in immunocompetent adults (Lapošová et al., 2013; Shao et al., 2015).

In immunocompromised individuals or developing fetuses, LCMV infection can result in serious disease, which carries high morbidity and high fatality rates (McLay et al., 2014). If an LCMV infection is acquired during pregnancy, it often severely affects the fetus, resulting in fetal death or severe, permanent visual and neurological defects (Shao et al., 2015; Labudova et al., 2009). Patients are also at risk of LCMV infection through organ donation, due to being temporarily immunosuppressed. LCMV infection in organ recipients can result in graft dysfunction, encephalopathy, multi-system organ failure and death (Goldsmith et al., 2013).

Old World Haemorrhagic Fevers

LASV is endemic in West Africa and causes approximately 300,000 infections annually, with a mortality rate of 1 % (Rojek et al., 2007). Roughly 80 % of LASV infections result in mild symptoms, including a slight fever, malaise and headache, and are undiagnosed. However, 20 % of LASV infections can progress to the development of Lassa fever, a highly fatal haemorrhagic fever, which is characterised by a high fever, "flu-like" symptoms, respiratory distress, oedema, shock, seizures, mucosal bleeding, multi-system organ failure, coma and death (Shao et al., 2015; Goncalves et al., 2013). The liver is commonly affected in LASV infection, resulting in hepatitis (Shao et al., 2015; McCormick et al., 1986a).

A percentage of LASV survivors also experience neurological symptoms after recovery, including tremors and encephalitis (Shao et al., 2015). On average, approximately 30 % of LASV survivors experience sudden, spontaneous deafness in one or both ears, which is thought to be the result of lesions in the inner ear that could occur during the course of the disease (Cummins, 1990; Mateer et al., 2018b; Okokhere et al., 2009). It remains to be determined whether the lesions occur as a result of direct viral damage or through immune cell-mediated damage (Cummins, 1990; Mateer et al., 2018b; Li et al., 2020). Ophthalmic manifestations have also been shown to occur during the course of Lassa fever, including conjunctivitis, conjunctival oedema, uveitis, and in poorer prognosis cases, subconjunctival haemorrhage (Li et al., 2020). Studies using guinea pigs as models for LASV infection revealed the presence of LASV RNA and antigens in the eye, and the initiation of an inflammatory response in the eye during acute disease (Gary et al., 2019). Ophthalmic disease has also presented in Lassa fever survivors, including cataract formation (18 %), retinal disease (13 %) and glaucoma (6 %), which can result in vision impairment and blindness (Li et al., 2020).

In 2008, there was the emergence of LUJV, another Old World mammarenavirus which caused haemorrhagic fever (Briese et al., 2009). Whilst there were only five cases of LUJV infection, it caused a severe haemorrhagic fever that resulted in death for 4 out of the 5 cases (Briese et al., 2009). The symptoms of Lujo haemorrhagic fever resembled those of Lassa fever, although bleeding was not prominent. Death from Lujo haemorrhagic fever was associated with rapid deterioration, neurological symptoms, respiratory distress and circulatory collapse (Shao et al., 2015; Sizikova et al., 2017).

New World Haemorrhagic Fevers

Five New World mammarenaviruses (JUNV, MACV, CHPV, GTOV and SBAV), all classified within clade B, cause haemorrhagic fever in humans (Martinez et al., 2013; Wolff et al., 2013a). JUNV is endemic in Argentina and infection can cause a mild illness, with "flu-like" symptoms and petechial haemorrhage, or a severe haemorrhagic fever, which results in severe shock, seizures, coma and death (Wolff et al., 2013b). Haemorrhagic fevers caused by MACV, CHPV, GTOV and SBAV have many different symptoms, including "flu-like" symptoms,

mucosal petechial haemorrhage, conjunctivitis, haematuria, respiratory distress, haemorrhaging and necrosis in the liver and gastrointestinal system, coma and shock (McLay et al., 2014). Unlike LASV, haemorrhagic fevers caused by the New World mammarenaviruses rarely include hepatitis as a symptom, but typically include neurological complications (Shao et al., 2015; McLay et al., 2014)

1.1.7 Therapeutic and Preventative Measures

There are a few measures available for the treatment or prevention of arenavirus infection, but they have limited efficacy and potential toxic side effects. These measures also require correct and rapid diagnosis early in infection, which may not be possible if the patient is unaware of infection until severe symptom development.

One of the most important strategies available to manage symptoms of haemorrhagic fever is supportive therapy (Howley and Knipe, 2020). This involves rest, sedation, hydration, pain relief and avoidance of intramuscular injections and blood-thinning drugs such as aspirin. Platelet transfusions and replacement of blood clotting factors can help relieve some symptoms of haemorrhagic fever (Howley and Knipe, 2020).

The early stages of arenavirus haemorrhagic fever correspond with low viraemia and therefore minimal spread. However, later stages present higher viraemia, posing a risk for nosocomial spread, especially to hospital staff treating patients with severe haemorrhagic fever (Carey et al., 1972). Exposure to the virus is most dangerous during parenteral (intramuscular, intravenous and sub-cutaneous) administration of treatment. Other than that, PPE can help protect against aerosols and bodily fluids. Another way to limit spread is to monitor for fever development in the patients' close contacts for 3 weeks. The patients' bodily fluids should also be evaluated for viral infectivity before release. Furthermore, advice can be given to the patient to use contraceptive methods to prevent spread through sexual transmission.

Potential Treatments

To date, there are no licensed treatments available for arenavirus infections. Therapies that are used include the nucleoside analog ribavirin and antibody therapy, but these are not licensed due to toxic side effects. The efficacy of these treatments also relies on being administered early in infection, requiring correct and

rapid diagnosis, which is difficult in areas that are endemic for other diseases that present with similar symptoms (such as malaria, influenza, dengue, yellow fever and Ebola virus disease) (Raabe and Koehler, 2017b).

Ribavirin is therapeutically effective against several arenaviruses in both cell culture and arenavirus haemorrhagic fever animal models, and it has lowered morbidity and mortality when given to humans with Lassa fever (Jahrling et al., 1980; Kenyon et al., 1986a; Kilgore et al., 1997; Sayler et al., 2014; Shtanko et al., 2010). However, ribavirin has optimal efficacy through intravenous delivery, which should typically be avoided for haemorrhagic fever patients. Furthermore, ribavirin poorly penetrates the cerebrospinal fluid (CSF), reducing its efficacy targeting the arenaviruses replicating in the central nervous system (CNS). Ribavirin also presents several serious side effects, including anaemia, liver damage and congenital disorders, exacerbating symptoms of arenavirus infection (McCormick et al., 1986b; Shao et al., 2019; Howley and Knipe, 2020). The mechanism of action of ribavirin is poorly understood, but it is thought to target multiple arenavirus lifecycle stages (Parker, 2005). Ribavirin remains the choice of therapeutic agent for the treatment of poor prognosis Lassa fever, and has also been shown to be effective in humans infected with JUNV, MACV and SBAV (Enria and Maiztegui, 1994; Barry et al., 1995; Kilgore et al., 1997). Prophylactic treatment with ribavirin is able to delay (when administered for 7-10 days) or even prevent (when administered for 14 days) the onset of acute disease in guinea pigs infected with PICV, LASV or JUNV, but its inability to penetrate the CSF meant JUNV was able to enter and replicate within the CNS and cause fatal encephalitis (Lucia et al., 1989; Shtanko et al., 2010; Kenyon et al., 1986a). Prophylactic therapy with ribavirin is successfully used to treat the close contacts of an infected patient, if they present with fever.

Several other anti-arenaviral compounds have been identified using *in vitro* high-throughput screening, but they have yet to be clinically trialled for their efficacy and safety *in vivo* (Mills et al., 1994). These compounds target multiple arenavirus lifecycle stages, including GPC fusion (ST-193; (Larson et al., 2008)) and RNA replication and transcription (targeting the RdRp; favipiravir; (Gowen et al., 2013; Furuta et al., 2017; Mendenhall et al., 2011; Safronetz et al., 2015)). Two types of drug can be identified in anti-arenaviral compound screens; direct acting antivirals (DAAs), which target the virus specifically, or host-targeting

antivirals (HTAs), which reduce availability or functionality of host machinery to the virus. The DAAs are typically well tolerated by the host, with few side-effects, but targeting the virus directly can trigger evolution and selection of resistant viral variants. Favipiravir (T-705; 6-fluoro-3-hydroxy-2-pyrazinecarboxamide) is a selective inhibitor of multiple viral polymerases (including arenaviruses), due to the high conservation of the viral polymerase active site (Furuta et al., 2017). The compound becomes phosphoribosylated in the cell, whereby it is recognised as a substrate by the viral polymerase and inhibits the RdRp activity. Favipiravir has shown *in vitro* inhibition of JUNV, GTOV, MACV, LASV, TCRV and PICV (Furuta et al., 2017; Mendenhall et al., 2011; Gowen et al., 2013; Safronetz et al., 2015). On the other hand, HTAs do not present such an evolutionary pressure on the virus and can potentially be effective for multiple arenaviruses, but they can have serious side effects on the host. PF429242 is a small molecule inhibitor of host SKI-1/S1P, which successfully prevented the arenavirus GPC processing and was able to inhibit LCMV and LASV infection *in vitro* (Kunz et al., 2002; Pasquato et al., 2012; Rodrigo et al., 2012; Rojek et al., 2008a; Urata and Yasuda, 2015).

An alternative treatment to antiviral compounds is to use convalescent plasma. This method has been successful in the treatment of JUNV infections, reducing the mortality rate from 15-30 % to 1-2 % when the treatment was administered within the first 8 days (Enria et al., 1984; Maiztegui et al., 1979). However, this treatment can result in a self-limited neurological syndrome that develops 3-6 weeks after treatment and includes symptoms of fever, headache, tremor and cranial nerve palsies (Howley and Knipe, 2020). Animal studies have also shown that antibody therapy could also be effective for the treatment of LCMV, LASV, MACV, GTOV (Baldridge and Buchmeier, 1992; Baldridge et al., 1997; Whitmer et al., 2018; Cross et al., 2016; Jahrling et al., 1984,b; Eddy et al., 1975; Kenyon et al., 1986b). However, antibody therapy requires a high concentration of virus-specific antibodies, which can be difficult to acquire (Maiztegui et al., 1979; Djomand et al., 2014). It also poses a problem in endemic regions where HIV-1 and malaria are also prevalent (Maiztegui et al., 1979; Djomand et al., 2014).

Arenavirus Vaccines

The only vaccine that has been successfully developed for the arenaviruses is Candid #1, which is extremely effective against JUNV. The Candid #1 strain was generated through serial passage of the JUNV XJ strain. After demonstrating the safety and efficacy in pre-clinical studies of guinea pigs and rhesus monkeys (McKee, Jr. et al., 1992), the vaccine was successfully trialled in agricultural workers in areas endemic for JUNV in Argentina (Maiztegui et al., 1998). Candid #1 has been licensed, but only for use in Argentina. There are some concerns about the limited understanding of the mechanisms behind attenuation of the Candid #1 strain and the potential development of virulent strains (Enria and Barrera Oro, 2002).

Due to the high morbidity, mortality and a large population at risk, LASV has been placed on the revised list of diseases considered to be a priority for vaccine development by the World Health Organisation (Bausch et al., 2004; Sewlall et al., 2014). However, the vaccine has to be inexpensive, highly effective, stable at multiple temperatures and user-friendly. Many LASV live-attenuated vaccines are in pre-clinical trials in non-human primates (Howley and Knipe, 2020). One vaccine, based on a measles virus vector, showed sufficient antibody-based protection in human clinical trials (Raju et al., 1990). The recombinant VSV (rVSV)-based LASV vaccine, where the G protein of VSV is replaced with the LASV GPC, has also shown promising development but there are some safety concerns (Geisbert et al., 2005; Safronetz et al., 2010; Huttner et al., 2017). Another live-attenuated LASV vaccine showing promise in pre-clinical development is ML29, which is a reassortant virus comprising the L segment from the non-pathogenic MOPV and the S segment from LASV (Carrion et al., 2007; Lukashevich et al., 2005).

1.2 The Structure of Arenavirus Virions

Arenavirus virions are generally spherical or pleomorphic, with sizes ranging between 40 nm to 300 nm in diameter (Murphy et al., 1969, 1970) although with a mean diameter of typically between 80 nm and 150 nm (Dalton et al., 1968; Mannweiler and Lehmann-Grube, 1973; Murphy and Whitfield, 1975; Neuman et al., 2005; Hetzel et al., 2013; Li et al., 2016). Mammarenaviruses are enveloped with a

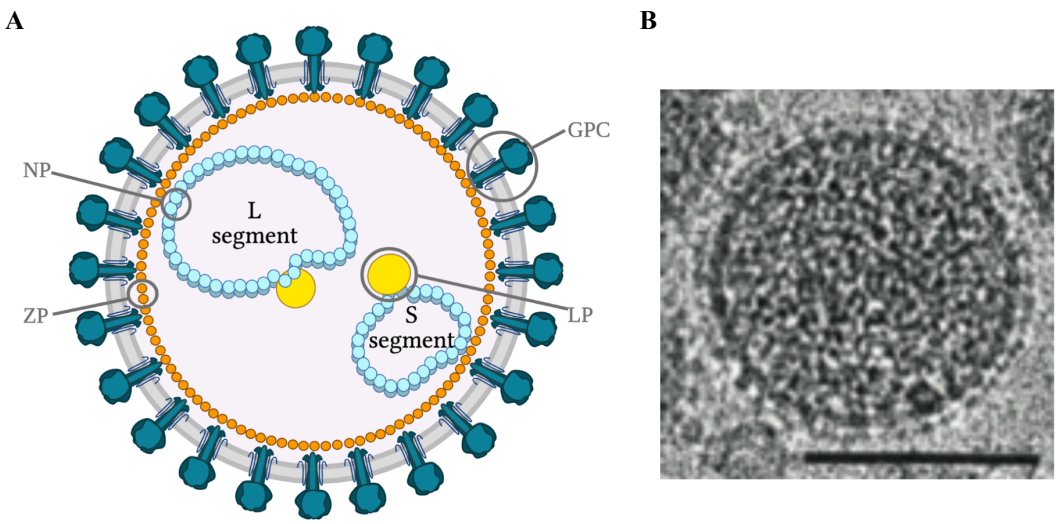

Figure 1.4: Schematic of the Mammarenavirus Virion.
(**A**)The genomic segments are tightly encapsidated by the nucleocapsid protein (NP; light blue) and coupled with the viral RNA-dependent RNA polymerase (LP; yellow) to form the ribonucleoprotein (RNP) complex. The Z matrix protein (ZP; orange) oligomerises to form a matrix layer on the inner side of the viral envelope. Glycoprotein spikes (GPC; teal) embed the viral envelope, present in a trimeric organisation. This figure was created using BioRender. (**B**) Cryo-electron microscopic image of purified arenavirus virions. The viral membrane can be seen, with surface projections corresponding to the GPC. The interior density is too disordered to identify RNP complexes. The scale bar indicates 100 nm. The images were obtained from (Salvato et al., 2011).

host cell-derived membrane, which is studded with randomly distributed surface projections that are spaced approximately 90 nm apart and are approximately 5-10 nm long (Murphy et al., 1970; Howard and Young, 1984; Li et al., 2016). Furthermore, there is an additional density beneath the membrane, proposed to be a layer formed of the ZP (Li et al., 2016; Hetzel et al., 2013). The viruses also appear to contain homogeneous, electron-dense granules, which are approximately 20-25 nm in diameter (Young and Howard, 1983). These granules were proposed to be ribosomes derived from the host cell, due to sharing similar density and sedimentation characteristics. Furthermore, 28S and 18S ribosomal RNAs were present within virus preparations (Murphy et al., 1970; Pedersen and Konigshofer, 1976). However, the inclusion of ribosomes within arenavirus virions has been subject to dispute, with the suggestion that the granule-containing viruses represent non-infectious viruses (Müller et al., 1983). It has also been proposed that the putative viral-associated ribosomes differ structurally and biochemically from host cell-associated ribosomes (Dalton et al., 1968; Mannweiler and Lehmann-Grube, 1973).

1.3 Introduction to the Viral Genome

All arenaviruses have a segmented, negative-sense RNA genome present in the virions (virus-associated RNA; vRNA). For the mammarenaviruses, reptarenaviruses and hartmaniviruses, the genome is divided into two segments, whereas the antennavirus genome is divided into three segments. In the mammarenaviruses and reptarenaviruses, the two segments are termed small (S; approximately 3.5 kb) and large (L; approximately 7.2 kb) and direct the expression of four viral proteins; the nucleocapsid protein (NP) and the glycoprotein complex (GPC) from the S segment and the L polymerase (LP) and the Z-matrix protein (ZP) from the L segment (figure 1.5A). The hartmanivirus genome is similar, except the L segment does not encode for the Z-matrix protein (figure 1.5A). The three antennavirus genome segments are termed small (S), medium (M) and large (L) and direct expression of the NP, GPC and LP, respectively (figure 1.5A). Additionally, the antennavirus M segment directs expression of a protein with an unknown function. With the exception of the hartmanivirus L segment and the antennavirus S and L segments, the arenavirus genomic segments utilise an ambisense coding strategy (figure 1.5B), which means that proteins are expressed from both the vRNA and the positive-sense replicate (complementary RNA; cRNA), strand. For the mammarenavirus and reptarenavirus S segment, the messenger RNA (mRNA) transcribed from the vRNA encodes NP, whereas the mRNA transcribed from the cRNA encodes GPC (figure 1.5). Similarly, for their L segment, the mRNA transcribed from the vRNA encodes LP, whereas the mRNA transcribed from the cRNA encodes ZP (figure 1.5). The antennavirus M segment expresses its GPC from the vRNA and the unknown protein from the cRNA.

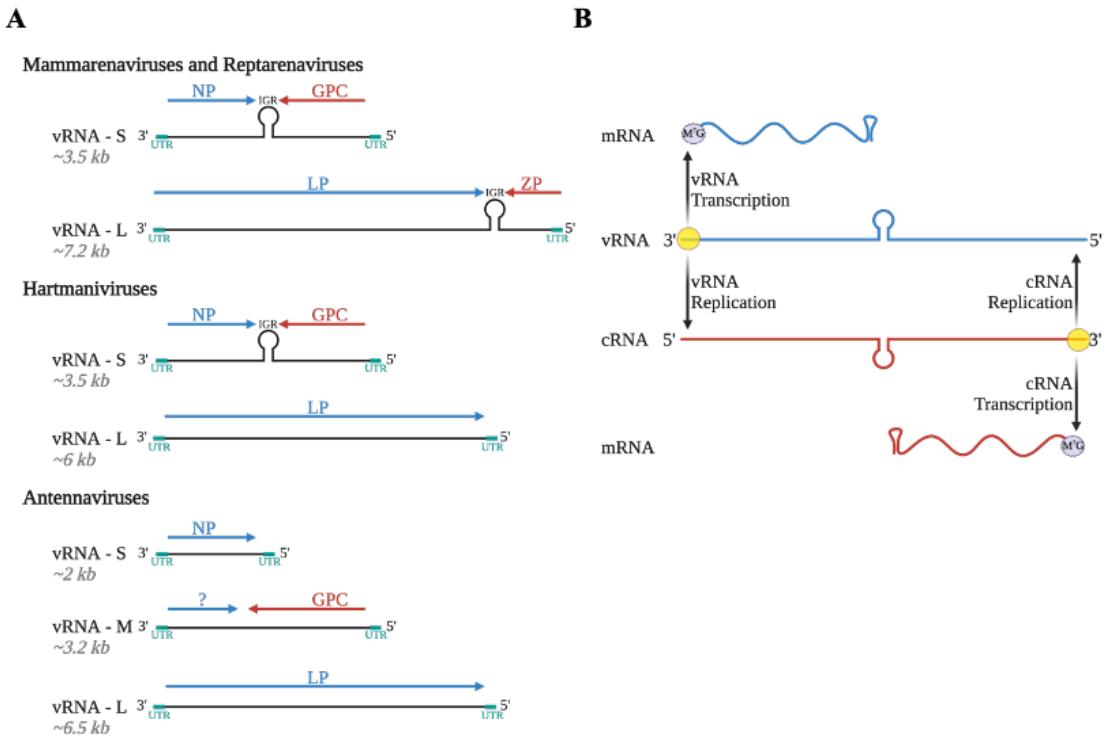

Figure 1.5: Schematic of the Arenavirus Genomes and the RNA Synthesis Strategy.
(**A**) The genomic segments (vRNA; S and L) of mammarenaviruses and reptarenaviruses direct the expression of four viral proteins; the nucleocapsid protein (NP) and the glycoprotein complex (GPC) from the S segment and the RNA-dependent RNA-polymerase (LP) and the Z-matrix protein (ZP) from the L segment. The vRNA is flanked by untranslated regions (UTR) and the viral genes are separated by the intergenic region (IGR), which is proposed to form a stem loop structure. The hartmanivirus genomic segments (vRNA; S and L) direct the expression of three viral proteins; NP and GPC from the S segment and LP from the L segment. The antennavirus genomic segments (vRNA; S, M and L) direct the expression of four viral proteins; NP from the S segment, GPC and an unknown protein from the M segment and LP from the L segment. The arenavirus genomic segments (mammarenavirus S and L, reptarenavirus S and L, hartmanivirus S and antennavirus M) utilise an ambisense coding strategy (**B**). The genes in blue (NP, LP, and the unknown) are transcribed into mRNA from the vRNA by the arenavirus LP. Transcription is terminated by the signals in IGR, which form a stable stem loop structure. The vRNA is replicated by the arenavirus LP to form a positive-sense intermediate (cRNA). The genes in red (GPC and ZP) are then transcribed into mRNA from the cRNA by the arenavirus LP. This figure was created using BioRender.

The open reading frames in the mammarenavirus and reptarenavirus segments are non-overlapping and they are separated by the intergenic region (IGR). The IGR is predicted to fold into a stable stem loop, the structure of which acts as a transcription termination signal for the LP. Transcription termination is thought to be mediated by a structural motif as opposed to sequence motifs due to termination occurring at multiple sequences present throughout the IGR stem (Meyer et al., 2002). Although all arenaviruses contain IGR sequences, there is no conservation of either sequence

or predicted structure, except between isolates of the same arenavirus. Some arenaviruses, such as TCRV and MOPV, even contain an IGR that is predicted to fold into two distinct stem loop structures (Meyer et al., 2002). The molecular switch for replication and transcription mediated by the LP is not known, although the transcription termination signal is ignored when the LP is replicating, allowing complete replication of the genome.

The 3' and 5' termini of the vRNA and cRNA contain untranslated regions (UTRs) that are present upstream and downstream of the viral protein open reading frames. Whilst the lengths, sequences and predicted structures of the UTRs do not appear conserved throughout the *Arenaviridae* family, the terminal 19 nucleotides are completely conserved and are complementary between the 3' and 5' UTRs. The complementarity of the terminal nucleotides is responsible for the formation of partially double-stranded RNA secondary structure, known as a panhandle, driven by non-covalent inter-terminal interactions, leading to pseudo-circularisation of the segment (figure 1.4A). These terminal nucleotides are also proposed to contain the vRNA (3') and cRNA (5' complement) promoters for LP and mutations within this region cannot be tolerated by the mini-genome assay (Perez and de la Torre, 2003a). For several arenaviruses, it has also been reported that there is an additional, non-templated G residue that is present at the 5' end of the vRNA (Garcin and Kolakofsky, 1990, 1992).

1.4 Introduction to the Viral Proteins

1.4.1 Nucleocapsid Protein

The nucleocapsid protein (NP) is responsible for encapsidating the RNA segments in a complex known as the ribonucleoprotein (RNP). The RNP is composed of multiple copies of the NP, lining up along the RNA segment, in association with the LP. The functions of the NP within the RNP are to form a scaffold that acts as the functional template for RNA synthesis by the LP and to assist ZP-mediated recruitment of the segments into newly formed viral particles (Iwasaki et al., 2015; Ortiz-Riano et al., 2011). Furthermore, the NP is proposed to have additional functions modulating the host cell response to infection, including counteracting the host interferon (IFN)

and apoptotic responses and recruiting cellular factors to promote the viral lifecycle (Martínez-Sobrido et al., 2006, 2009; Zhou et al., 2010; Pythoud et al., 2012; Baird et al., 2013; Wolff et al., 2013b; Reynard et al., 2014; Knopp et al., 2015; Loureiro et al., 2018; Shao et al., 2018).

Structure of Nucleocapsid Protein

The crystal structures of NPs from LASV, LCMV, JUNV, TCRV and MOPV have been solved by several groups (figure 1.6), either as full-length structures (Qi et al., 2010; Brunotte et al., 2011a; Hastie et al., 2011b) or as individual N-terminal and C-terminal domains (Hastie et al., 2011a,b; Zhang et al., 2013; Jiang et al., 2013; West et al., 2014; Yekwa et al., 2017). The N-terminal and C-terminal domains are connected by an unstructured, flexible linker, the site of which was initially suggested as the groove responsible for binding genomic RNA (Qi et al., 2010). However, when the structure of the N-terminal domain was solved in complex with single-stranded RNA, the genomic RNA binding site was proposed to be located in a deep cavity present in the N-terminal domain (Hastie et al., 2011b) (figure 1.6B). This N-terminal domain site was previously suggested to bind host 7-methylguanosine (M^7G) cap structures but mutations of the residues proposed to bind the cap structures resulted in an impairment of cRNA synthesis, rather than viral transcription (Qi et al., 2010; Brunotte et al., 2011a). Furthermore, attempts to co-crystallise LASV NP with the M^7G cap or isolate LASV NP with cap-conjugated beads failed (Hastie et al., 2011b).

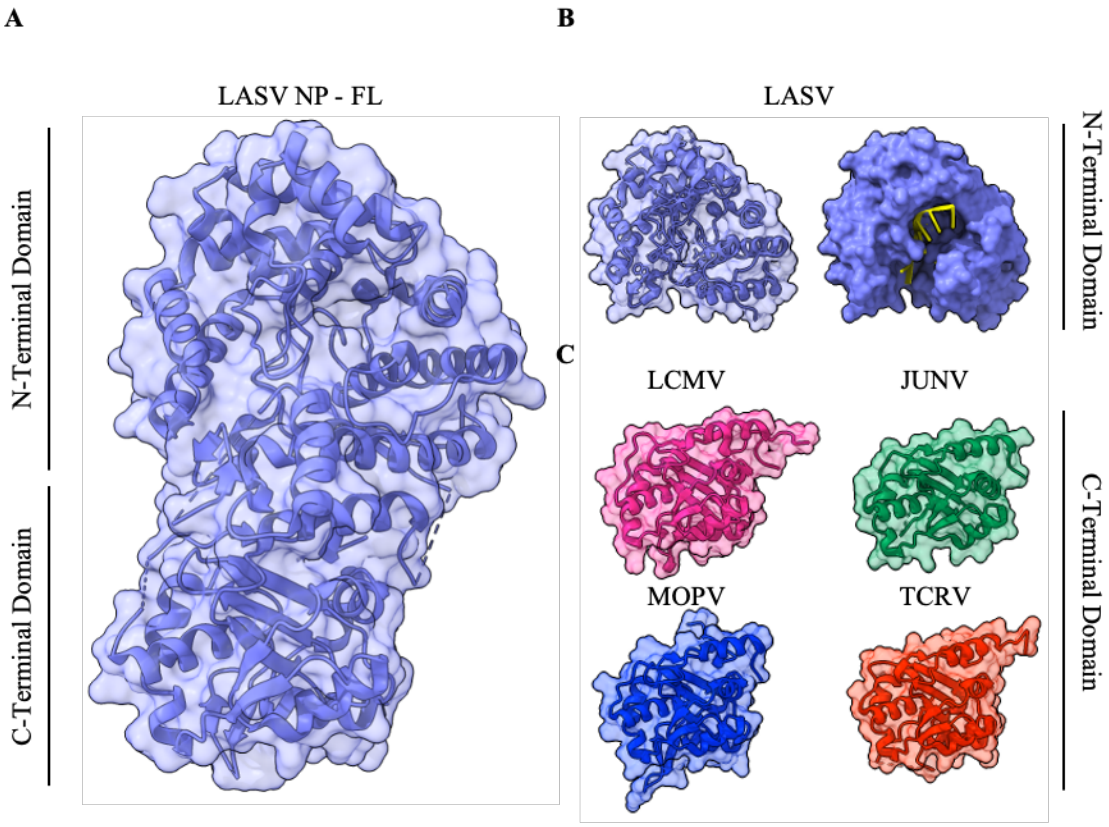

Figure 1.6: Structure of the Arenavirus Nucleocapsid Protein (**A**) The overall structure of the full-length Lassa virus nucleocapsid protein (LASV NP - FL; purple; PDB: 3MWP) shown as a cartoon with its partially transparent surface, reveals the N-terminal domain and C-terminal domain. (**B**) The N-terminal domain of the LASV NP (LASV; purple; PDB: 3T5N) has been shown as a cartoon, with partially transparent surface overlay, and as a solid surface, with RNA present in the deep, basic groove. (**C**) The C-terminal domains of the LCMV NP (LCMV; pink; PDB: 4O6H), the Junín virus NP (JUNV; green; PDB: 4K7E), the Mopeia virus NP (MOPV; blue; PDB: 5LRP) and the Tacaribe virus NP (TCRV; red; PDB: 4GVE) have been shown as cartoons, overlaid with a partially transparent surface. This figure was created using UCSF Chimera X.

The N-terminal domain is composed primarily of α-helices, which form "head" and "body" regions (Hastie et al., 2011b) (figure 1.6B). Between these regions is a deep cavity, which contains positively-charged residues that are thought to bind the negatively-charged sugar-phosphate backbone of single-stranded RNA (Hastie et al., 2011b). The comparison of full-length, RNA-free LASV NP and the RNA-bound, N-terminal domain of LASV NP revealed striking structural rearrangements that are suggested to represent a gating mechanism that regulates RNA binding (Hastie et al., 2011b). In the RNA-free structure, α-helices 5 and 6, and their connecting loop, block access to the RNA-binding crevice, which is stabilised by interactions with the C-terminal domain (Hastie et al., 2011b). In the RNA-bound structure, α-helix 5 is shortened to terminate before the RNA-binding crevice and α-helix 6 and the connecting loop are shifted away from the crevice (Hastie et al., 2011b).

This permits access to the crevice, where residues in the loop and the crevice can interact with the RNA (Hastie et al., 2011b).

The C-terminal domain is composed of a mixture of β-sheets and α-helices (Hastie et al., 2011a; Qi et al., 2010; Brunotte et al., 2011b) (figure 1.6C). The five-stranded β-sheet contains one anti-parallel strand and is surrounded by six α-helices, which are connected by flexible loops (Hastie et al., 2011a). A zinc atom is coordinated by residues present in the second β-strand, the sixth α-helix and the long, basic loop which connects the fifth and sixth α-helices (Hastie et al., 2011a). The structure of the C-terminal domain revealed a structural similarity with the characteristic fold of exonucleases within the DEDD superfamily (Qi et al., 2010; Hastie et al., 2011a). Exonucleases are enzymes that catalyse the cleavage of phosphodiester bonds between nucleotides at either the 3' or 5' end of the nucleotide chain. Members of the DEDD superfamily are characterised by Asp-Glu-Asp-Asp catalytic residues in the active site, in addition to a neighbouring histidine or tyrosine, which further sub-divides the superfamily (DEDDh and DEDDy) (Zuo and Deutscher, 2001). The substrate for the exonuclease activity of the arenavirus NPs was identified as double-stranded RNA (dsRNA), which is digested in a 3'-5' direction (Hastie et al., 2011a).

The higher-order structure of the NP within the RNP has not been fully understood. Trimerisation of the NP is thought to occur, but this has not been proposed to be involved with RNP formation because purified NP trimers are not associated with RNA (Pattis and May, 2020; Brunotte et al., 2011a; Hastie et al., 2011b; Lennartz et al., 2013; Qi et al., 2010). Currently, it is thought that NP forms trimers during viral transcription in order to prevent RNA binding and maintain a store of NP (Hastie et al., 2011b; Pattis and May, 2020). Upon RNA replication, an unknown signal disassembles the NP trimer, shifting the C-terminal domain away from the N-terminal domain and opening up the RNA-binding crevice to enable the NP to bind newly synthesised genomic RNA (Hastie et al., 2011b; Pattis and May, 2020). Structural analysis on the arenavirus RNPs has been limited, although low-resolution electron microscopic studies on the RNPs within PICV has revealed some structural understanding (Young and Howard, 1983) (figure 1.7). This study proposed that the RNPs were flexible filaments, composed of a linear array of multiple globular subunits, which were 4-5 nm in diameter (Young and

Howard, 1983) (figure 1.7). These subunits folded through many intermediate helical structures, ranging from flexible arrangements to increasingly structured arrangements, with an increasing number of NPs per turn. These filaments ranged between 12 and 15 nm in diameter and presented as a circular configuration (Young and Howard, 1983) (figure 1.7). Recently, studies have been performed on bacterially-expressed recombinant MOPV NP revealing RNP-like structures and a heptameric organisation of the NP, the diameter of which agrees with the previously seen RNPs (preliminary unpublished data) (Papageorgiou et al., 2020). However, there is still little structural data to offer insight into the organisation of the NPs in the RNP complex.

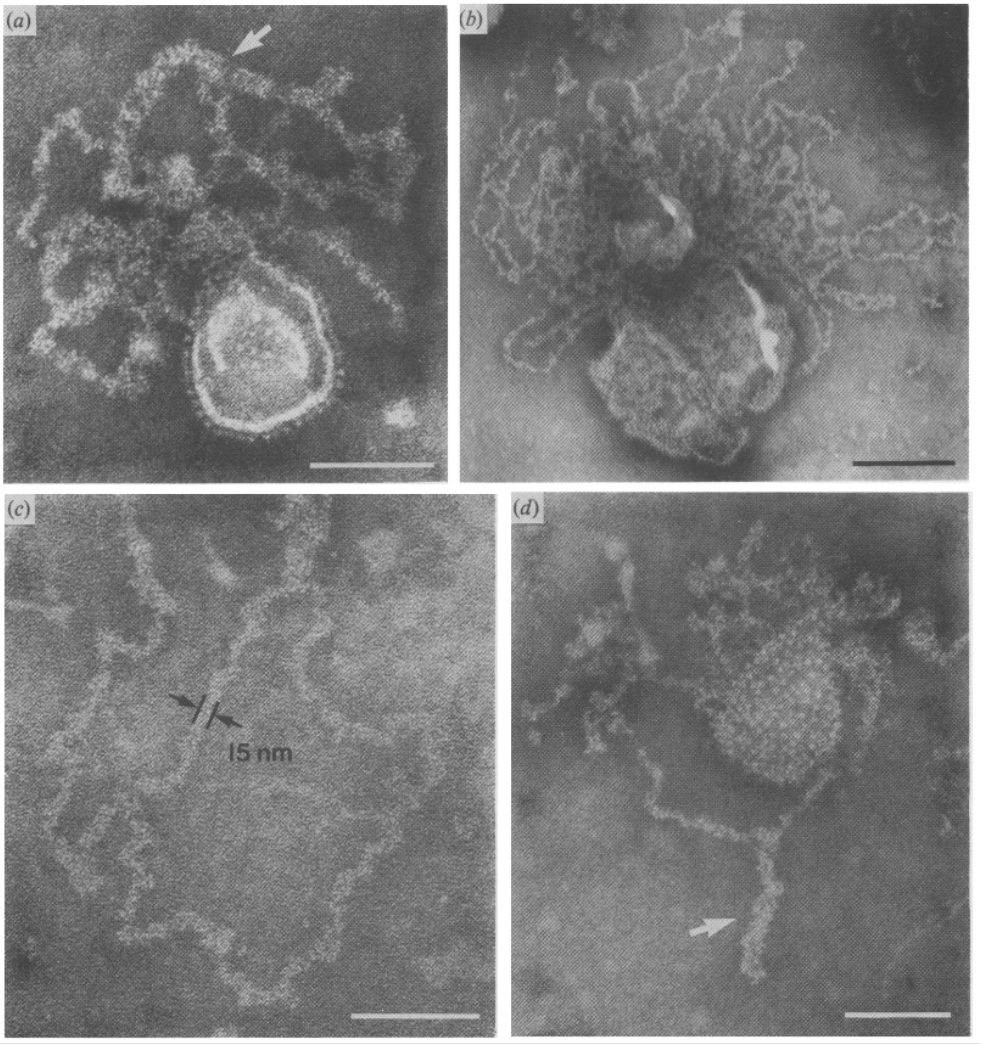

Figure 1.7: Electron Microscopy Reveals the Structural Organisation of the Ribonucleoprotein Complexes Virus particles were purified, lysed by osmotic shock and then negatively-stained with 2 % phosphotungstic acid, which released complexes that were 12-15 nm in diameter. Higher order structures, including twisting and super-coiling, were observed and had a diameter of 20 nm (arrows in (*a*) and (*d*)). Scale bars have been included and represent 100 nm in (*a*), (*c*) and (*d*) and 200 nm in (*b*). This figure was obtained from (Young and Howard, 1983).

Functions of Nucleocapsid Protein

In addition to encapsidating the genomic RNA, the NP has functions within the viral lifecycle and modulating the host cell environment, which have been described in more detail.

Formation of Replication-Transcription Complexes

One of the functions attributed to the NP is the formation of discrete sites of arenavirus RNA synthesis. These sites are called replication-transcription complexes (RTCs) and are thought to be the site of vRNA and cRNA replication and transcription (Baird et al., 2013). RTCs are associated with a cytosolic membrane, phosphatidylinositol-4-phosphate (PI4P) and several host proteins including translation initiation factors, ribosomal proteins and stress granule protein G3BP1 (Baird et al., 2013) (figure 1.8). The sites have not been associated with any membrane-bound organelles and appear to export any viral mRNAs for translation (Baird et al., 2013). The NP is thought to be the driving force for the formation of RTCs because immunofluorescence analysis of cells transfected with a NP-expressing plasmid reveal the characteristic discrete puncta seen in infected cells (Baird et al., 2013; Knopp et al., 2015) (figure 1.8 rN PI4P). It has been proposed that the establishment of these sites involves NP residue T206, which appears to be transiently phosphorylated. Mutating T206 to a residue that cannot be phosphorylated (T206A) changes NP distribution from discrete puncta to a disperse cytoplasmic diffusion and recombinant LCMV containing this mutation cannot be recovered from a reverse genetics system (Knopp et al., 2015). Mutating T206 to a phosphomimetic residue (T206E), thereby simulating constitutive phosphorylation, results in a phenotype reminiscent of WT NP and mutant NP T206A, showing both discrete puncta and a diffuse cytoplasmic distribution (Knopp et al., 2015). The NP is thought to drive the formation of RTCs either through aggregation or interaction with cellular proteins (Baird et al., 2013). Whilst this is not yet fully understood, the colocalisation of PI4P with NP at the RTCs could be the key to the formation of these sites. PI4P promotes membrane dynamics and the recruitment of cellular proteins involved with vesicular budding and has been implicated in membrane remodelling for other viruses (Baird et al., 2013). Further studies are required to understand NP interactions necessary for the formation of RTCs in addition to the

role of phosphorylation in these interactions.

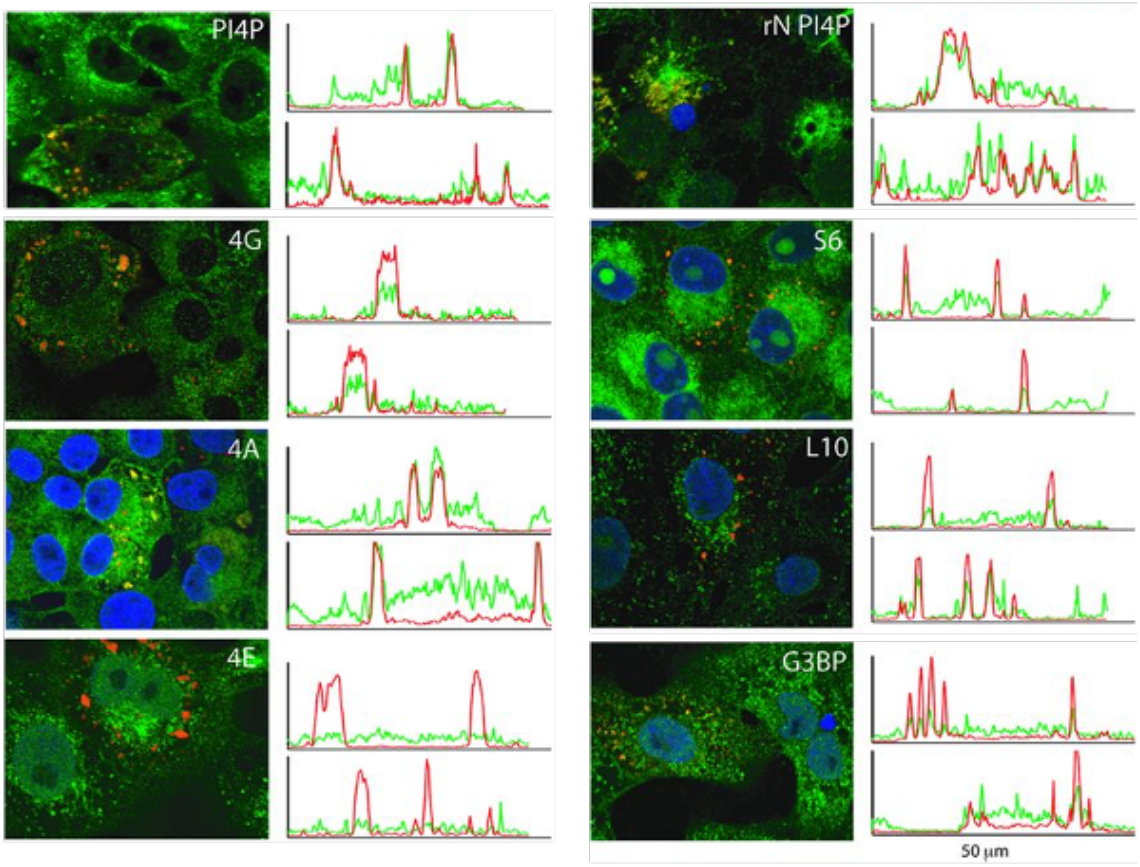

Figure 1.8: Co-localisation of Host Cell Components with Arenavirus NP in Replication-Transcription Complexes Vero cells were infected with Tacaribe virus (TCRV) and then fixed using 4 % paraformaldehyde, permeabilised using 0.1 % Triton-X-100 and stained with antibodies raised against the following proteins: phosphatidylinositol-4-phosphate (PI4P), small ribosomal subunit protein S6 (S6), large ribosomal protein L10a (L10), eIF4G (4G), eIF4A (4A) and eIF4E (4E) and Ras-GAP SH3 domain binding protein (G3BP) (all then stained with a secondary antibody conjugated to a 488 nm fluorophore; green). The TCRV NP was stained with an antibody conjugated to a 568 nm fluorophore (red). Co-localisation between the staining can be seen in each image in distinct puncta and the fluorescence intensities, which are spatially correlated. Co-localisation was also seen when recombinant NP was transfected into the cells (rN PI4P). This figure was obtained from (Baird et al., 2013).

Recruitment of Translation Initiation Factors

Within RTCs, the NP is proposed to have an additional function to interact with and recruit translation initiation factors, although this is variable between mammarenaviruses. Studies on Old World mammarenavirus LCMV shows that the NP colocalises with all three of the eIF4F components, but does not co-immunoprecipitate with any of them (Knopp et al., 2015). This suggests that the eIF4F complex is recruited to the RTCs in LCMV-infected cells, potentially through NP interactions, but the LCMV NP does not interact strongly with or replace any

of the eIF4F components (Knopp et al., 2015). For New World mammarenaviruses JUNV, TCRV and PICV, it has been proposed that the NP replaces the cap-binding protein of the eIF4F complex, eIF4E. Studies have shown that the NP from these viruses colocalises and co-immunoprecipitates with eIF4A and eIF4G in infected cells (Linero et al., 2013). These viruses can also not complete their lifecycle in cells that have expression of eIF4A or eIF4G knocked down by siRNA or pharmacological inhibition (Linero et al., 2013). However, there is no colocalisation or interaction between eIF4E and NP and the inhibition or siRNA knock-down of eIF4E does not affect infection by JUNV, TCRV or PICV. Furthermore, unlike LASV NP (Hastie et al., 2011a), the NPs from JUNV, TCRV and PICV were all retained by M^7G cap-conjugated beads (Linero et al., 2013). This suggests an alternative interaction between New World mammarenavirus NPs and the eIF4F complex and highlights the need for further investigation into the structure of New World mammarenavirus NPs, potentially in complex with M^7G caps. *Modulation of the Host Cell Immune Response*

Prior to the structure of the C-terminal domain being solved, an immunosuppressive function was attributed to the NP, specifically to residues within the C-terminal domain (Martínez-Sobrido et al., 2006, 2007, 2009). Viral replication can result in the generation of dsRNA, which is a well-known pathogen-associated molecular pattern (PAMP) (Hastie et al., 2011b). The detection of PAMPs in the host cytoplasm by pattern recognition receptors (PRRs), such as retinoic acid-inducible gene I (RIG-I) or melanoma differentiation-associated protein 5 (MDA5), can trigger the interferon (IFN) response (Papageorgiou et al., 2020) (figure 1.9). This leads to the expression of interferon-stimulated genes (ISGs) and the establishment of an anti-viral environment in the infected cell and neighbouring cells (Yekwa et al., 2019) (figure 1.9). It has been proposed that the arenavirus NP exonuclease functions to cleave any dsRNA intermediates resulting from viral replication, in order to prevent detection and initiation of the IFN response (Reynard et al., 2014; Shao et al., 2018; Zhou et al., 2010) (figure 1.9). Mutational analysis of residues involved in, and proximal to, the LASV exonuclease active site (D389, E391, D466, D533, H528, G392, and R492), in addition to residues which disturb the zinc coordination (E399, C506, H509, and C529), disrupted the exonuclease activity and the ability to suppress the IFN response (Hastie et al., 2011a). Furthermore, mutational

analysis of residues D382 and G385 in LCMV NP (corresponds to D389 and G392 in LASV NP) showed these residues, which were later attributed to exonuclease active site residues, were critical for anti-IFN activity (Martínez-Sobrido et al., 2009). Finally, attempts to rescue viruses (PICV, LASV or LCMV) with a mutant NP deficient of exonuclease activity either failed or significantly impaired viral replication (Martínez-Sobrido et al., 2009; Huang et al., 2015; Carnec et al., 2011).

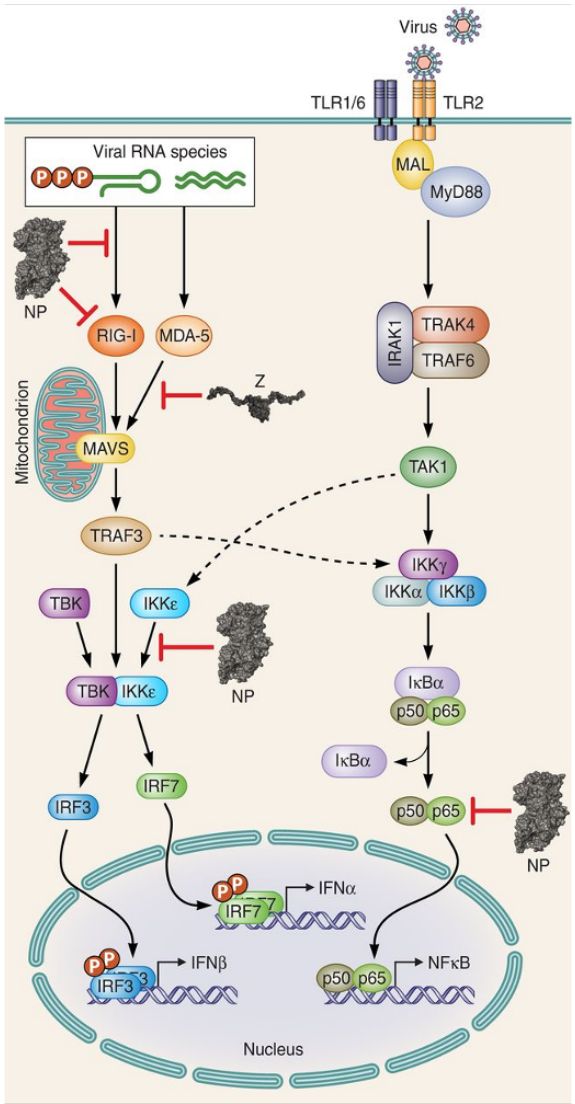

Figure 1.9: Inhibition of Steps in the Innate Immune Response by the Arenavirus Nucleocapsid Protein The diagram shows the signalling pathways for type I interferon (IFN) induction. Arenavirus non-poly-adenylated RNA and double-stranded RNA species are detected by RIG-I and MDA5. The arenavirus NP inhibits this detection and signalling by degrading the RNA species and possibly through binding to RIG-I directly. Arenavirus ZP also binds directly to RIG-I and MDA5 to prevent the activation of the mitochondrial antiviral signalling (MAVS) protein. The arenavirus NP also inhibits later stages of induction, through binding to IKK-epsilon and preventing activation of IFN-responsive factor 3 (IRF3) and through blocking activation of NF-κB, which is activated through detection of the arenavirus GPC by Toll-like receptors (TLRs). This figure was obtained from (Meyer and Ly, 2016).

Despite strict conservation of the exonuclease domain amongst arenaviruses, and many arenaviruses exhibiting anti-IFN activity, cells infected with non-pathogenic viruses TCRV and MOPV induce a strong IFN response (Martínez-Sobrido et al., 2007; Pannetier et al., 2004). This suggests a potential link between anti-IFN activity and viral pathogenesis, but also suggests that NP exonuclease activity may be conserved for an additional role in the viral lifecycle (Martínez-Sobrido et al., 2007; Yekwa et al., 2019). Recently, there has been a proposal that the arenavirus exonuclease activity may be necessary for genome editing (Yekwa et al., 2019). The *Coronaviridae* family is the only other viral family which has 3'-5' exonuclease activity in a viral protein (nsp14) (Minskaia et al., 2006; Bouvet et al., 2012). During the coronavirus lifecycle, nsp14 functions to remove mismatched bases from the RNA genome, maintaining genomic fidelity and stability (Bouvet et al., 2012; Eckerle et al., 2010; Denison et al., 2011; Ferron et al., 2018). Other studies have shown nsp14 has additional functions involved in immunosuppression (Becares et al., 2016). The exonuclease domains of the arenavirus NP and the coronavirus nsp14 are structurally similar, suggesting a potential additional role of genome editing for the arenavirus NP (Yekwa et al., 2019). The study proposed that the arenavirus NP exonuclease domain was able to cleave dsRNA which had a single mismatched nucleotide (3'), which could possibly represent the NP checking the quality of the UTRs forming the panhandle (Yekwa et al., 2019).

There are also other interactions between the arenavirus NP and various mediators of the host cellular immune response. When PRRs, such as RIG-I, MDA5 and dsRNA-detector protein kinase R (PKR), are activated by the presence of PAMPs, several pathways can be induced in order to mount an anti-viral IFN response. Activated RIG-I and MDA5 signal through IκB kinase (IKK) complexes to induce phosphorylation and nuclear translocation of interferon regulatory factor 3 (IRF3) and NF-κB (nuclear factor kappa-light-chain-enhancer of activated B cells) (figure 1.9). These activated transcription factors then induce expression of IFN-β, IFN-α and cytokines. Activated PKR can also phosphorylate and activate NF-κB to induce IFN expression, in addition to phosphorylation and inactivation of eIF2-α, preventing cap-dependent translation. Arenavirus NPs interact with many of these cellular proteins to interfere with the induction of the IFN pathway.

LCMV NP is able to block the nuclear translocation of both transcriptional

activators of IFN expression, IRF3 and NF-κB (Martínez-Sobrido et al., 2006) (figure 1.9). Which proteins are targeted specifically to prevent IRF3 activation has not been fully elucidated, although LCMV NP has been shown to interact specifically with the kinase domain in IKKϵ, which would block its auto-catalytic activity and subsequent IRF3 activation (Pythoud et al., 2012) (figure 1.9). It is further proposed that the LCMV NP sequesters IKKϵ from its cellular binding partner MAVS, due to a lack of colocalisation between IKKϵ and MAVS in presence of LCMV NP (Pythoud et al., 2012). LCMV NP has also been shown to interact with RIG-I and MDA-5, which could be another way by which the NP prevents induction of the IRF3 and NF-κB pathways (Zhou et al., 2010). However, IKKϵ, RIG-I and MDA-5 have not been identified in other studies exploring the NP interactome by mass spectrometry (King et al., 2017; Loureiro et al., 2018).

One of these studies revealed that both JUNV NP and LCMV NP interacted with activated PKR, but the phosphorylation and activation of eIF2-α was only prevented in JUNV infection (King et al., 2017). This suggested that JUNV NP was able to specifically block the downstream interactions of PKR activation (King et al., 2017). The other study showed LCMV NP, LASV NP and JUNV NP appeared to interact with DDX3 and require DDX3 for completion of the viral lifecycle (Loureiro et al., 2018). DDX3 is an RNA helicase that is involved with transcription, translation and nuclear export of RNA, stress granule assembly and activation of IFN-β expression (Loureiro et al., 2018). It is thought DDX3 could be recruited in early infection to assist viral RNA replication because mini-genome replication is reduced in cells depleted of DDX3 (Loureiro et al., 2018). However, it was also proposed to be required in LCMV-infected cells for an IFN-inhibitory effect later in infection (Loureiro et al., 2018).

The interactions between the arenavirus NP and host cellular proteins involved in innate immune pathways have not yet been fully understood, although it appears the NP may sequester, divert or prevent the activity of multiple proteins at multiple levels. The mechanisms by which the IFN response is suppressed, or potentially promoted, appear to be different for viruses within the Old World group as opposed to the New World group and could also be related to viral pathogenesis. Finally, these interactions could also differ based on which cell type is the primary target of arenavirus infection. Immune cells, including macrophages, dendritic cells

and natural killer cells, which are initially targeted in LASV infection, and IFN suppression in these cell types is tightly linked with subsequent disease prognosis (Pannetier et al., 2011; Huang et al., 2015). If an IFN response is established in early LASV infection, there is a much higher chance of survival. Alternatively, being able to oppose the IFN response may enable the virus to infect immune cells; non-pathogenic MOPV cannot negate the IFN response and also cannot establish productive infection in macrophages (Pannetier et al., 2004). This, however, differs to highly pathogenic New World arenaviruses (Huang et al., 2015). These differences may also be related to the ZP (Huang et al., 2015).

Modulation of Host Cell Apoptosis

Another proposed function of the NP involves the modulation of host cell apoptosis. Apoptosis is programmed cell death and can be induced through extrinsic (activation of tumour-necrosis factor [TNF] receptors) or intrinsic (cytochrome c release from the mitochondrial membrane) pathways (Wolff et al., 2016; Ashkenazi and Dixit, 1998; Granville and Gottlieb, 2002). The induction of these pathways results in the proteolytic activation of initiator caspases (2, 8, 9, 10 and 12) and effector caspases (3, 6, 7 and 14) (Wolff et al., 2013b; Nuñez et al., 1998). Caspases are cysteine-dependent aspartate-specific proteases; initiator caspases are responsible for cleaving and activating effector caspases, while effector caspases proteolytically degrade many cellular proteins to initiate cell death (Wolff et al., 2013b; Nuñez et al., 1998). Viral infection generates multiple stress signals in the cell, including production of reactive oxygen species, alterations of Ca^{2+} signalling and generation of PAMPs, all of which can induce apoptosis (Meyer and Groseth, 2018). Viruses have a complicated relationship with apoptosis; it can either be beneficial to the viral lifecycle, assisting with viral release, or it can be inhibitory to the viral lifecycle, sequestering necessary host cell factors and shortening the available time for completion of the lifecycle (Wolff et al., 2016).

Many studies have been performed to understand how arenaviruses are affected by, and interact with, components of the cellular apoptosis pathways (Meyer and Groseth, 2018). One particular study, trying to understand the multi-functionality of the JUNV NP within the host cell, found that the NP was cleaved in infected and transfected cells (Wolff et al., 2013b). This led to the identification of caspase cleavage motifs within the NP sequence and the proposal that the JUNV NP acted as

a decoy substrate for the caspases, diverting the caspases away from their targets so they fail to activate apoptosis (Wolff et al., 2013b). The NP cleavage products were also present within mature virions, so whether the NP caspase motifs were required to prevent apoptosis or to result in cleaved NP was not fully determined. Apoptosis induction was reduced in JUNV-infected cells, especially in comparison to the cells infected with non-pathogenic TCRV, which mounted an effective apoptosis response, potentially due to the NP lacking one of the caspase motifs and subsequently not being cleaved (Wolff et al., 2013b, 2016; Kolokoltsova et al., 2014). The activation of caspase 3 was also shown to be reduced in presence of JUNV NP but not affected by the presence of TCRV NP (Wolff et al., 2013b). Furthermore, TCRV replication and growth was not affected by a strong induction of apoptosis (Wolff et al., 2016). The differences in these two viruses in response to apoptosis induction may be related to pathogenesis, although further work is required to understand this. The presence of cleaved NP in mature virions of PICV and LASV also suggests other arenaviruses may utilise the conserved caspase motifs as a means for NP cleavage or for modulation of host cell apoptosis (Harnish et al., 1981; Clegg and Lloyd, 1983; Young et al., 1987). It has been observed that LCMV and LASV do not appear to induce apoptosis in cell culture, and the caspase motifs are conserved, strongly suggesting the NP could be involved with subverting the apoptotic response (Pythoud et al., 2012; Baize et al., 2004; Wolff et al., 2013b).

1.4.2 L Polymerase

The arenavirus L polymerase (LP), is a multi-domain protein that mediates transcription and replication of the genome. This is achieved through the LP's RNA-dependent RNA polymerase (RdRp) domain. However, the LP has additional functions because residues that are essential for correct LASV LP function have been identified both within and outside the RdRp domain (Lelke et al., 2010; Lehmann et al., 2014; Hass et al., 2008). Unlike the well-characterised influenza polymerase complex, sequence analysis of the LASV LP did not identify distinguishable RNA helicase or RNA capping functions (Vieth et al., 2004).

The structures of the LPs from LASV and Machupo virus (MACV) were recently solved to sub-4 Å resolution using cryo-electron microscopy and single-particle

reconstruction (Peng et al., 2020) (figure 1.10). The LASV and MACV LPs were structurally similar to each other, to bunyavirus La Crosse orthobunyavirus (LACV) and to the polymerase complexes of influenza virus (Peng et al., 2020). The LP is composed of a single polypeptide chain, which is organised into three structural domains; the N-terminal endonuclease-containing domain (PA-like region), the central RdRp-containing domain (RdRp region) and the C-terminal cap-binding domain (PB2-like region) (figure 1.10A and C). The N-terminal and C-terminal domains, after cleavage at specific positions, are able to functionally trans-complement each other (Brunotte et al., 2011b). These LASV and MACV LP structures supported previous EM examination of the MACV LP, which showed a core domain that was surrounded with appendages (Kranzusch and Whelan, 2012; Kranzusch et al., 2010).

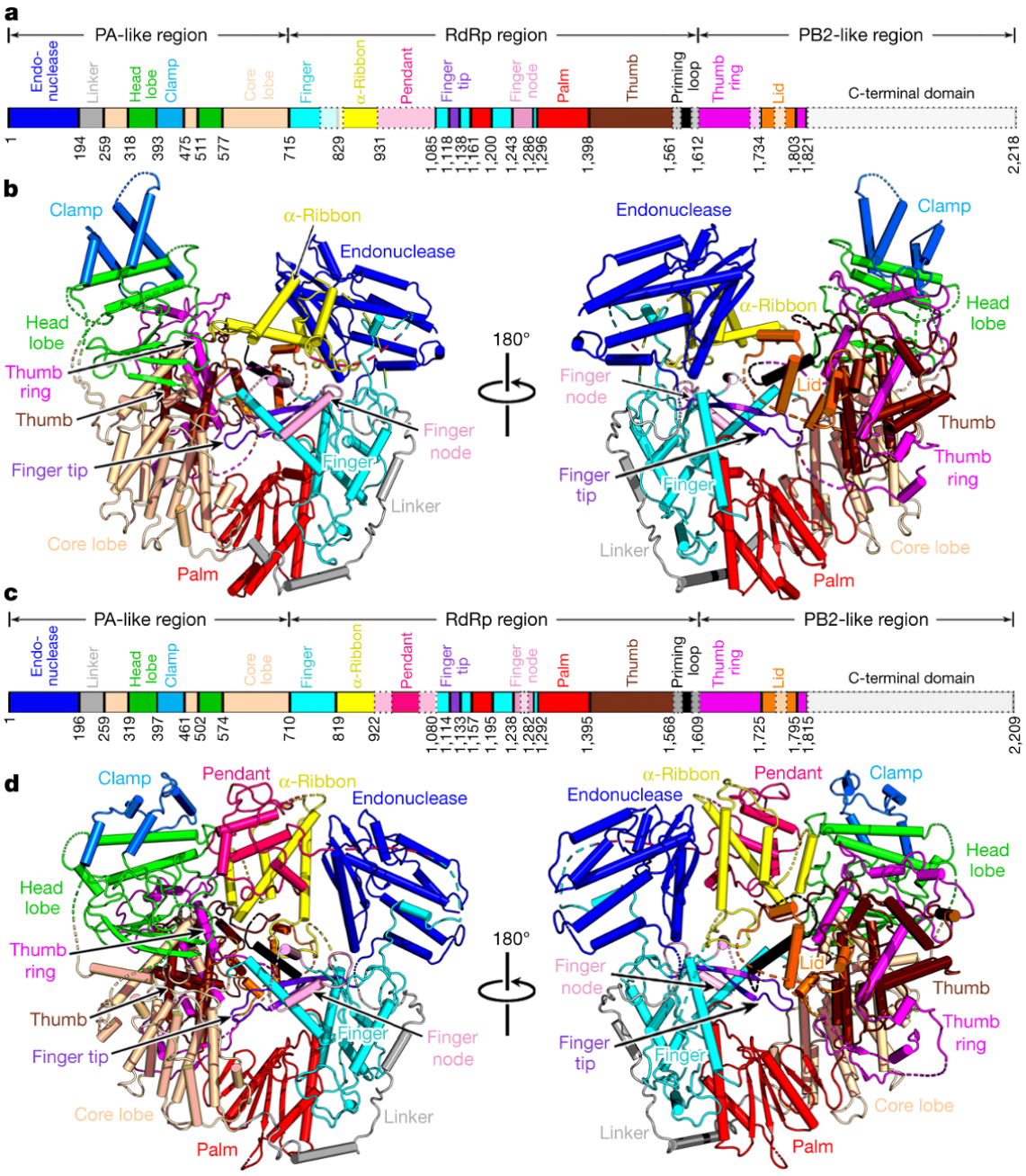

Figure 1.10: Structure of the LASV and MACV L Polymerases The three domains of the L polymerase (LP) has been schematically depicted for the LASV LP (**A**) and the MACV LP (**C**), showing the N-terminal PA-like region, the central RNA-dependent RNA-polymerase (RdRp) (PB1-like) region and the C-terminal PB2-like region. The regions that have not been structurally resolved yet are depicted as lighter colours with dashed outlines. The structures of the LASV (**B**) and MACV (**C**) LPs have been shown as a cartoon, with the different domains coloured the same as the schematic in (**A**) and (**C**). This figure was obtained from (Peng et al., 2020).

The N-terminal (PA-like) region contains the endonuclease region, which has been shown to share high structural homology between members of the *Arenaviridae* family (including California Academy of Sciences virus (CASV), a member of the *Reptarenavirus* genus), in addition to other bunyaviruses (from the *Peribunyaviridae*, *Hantaviridae* and *Phenuiviridae* families) and the orthomyxovirus influenza A virus (figure 1.11). The endonuclease region has a two-lobed structure; the first lobe comprises α-helices that form a helix bundle, whereas the second lobe is composed of a β-sheet and an α-helix (Olschewski et al., 2020). The second lobe also contains the PD(E/D)K endonuclease active site residues, which co-ordinate two divalent metal ions (Olschewski et al., 2020). Other viral polymerase endonucleases utilise an additional histidine residue in the first lobe to co-ordinate the first metal ion in the active site (figure 1.11C; His+). Arenavirus endonucleases do not contain this histidine residue, instead possessing a glutamate or aspartate residue that is involved with the co-ordination of the second metal ion (figure 1.11B; His-). Whilst the arenavirus endonuclease region had the structural conformation of the active site of enzymatically-active endonucleases from other viruses, the absence of the histidine residue (His-) reduces its *in vitro* endonuclease activity (Vogel et al., 2019; Olschewski et al., 2020). Biochemical analysis of the LASV LP N-terminal region showed it was unable to cleave RNA (Reguera et al., 2016; Vogel et al., 2019). The functional activity of the arenavirus endonuclease domain remains to be elucidated, but it has been proposed that there may be another component, as of yet unidentified, required to enable endonuclease activity (Vogel et al., 2019).

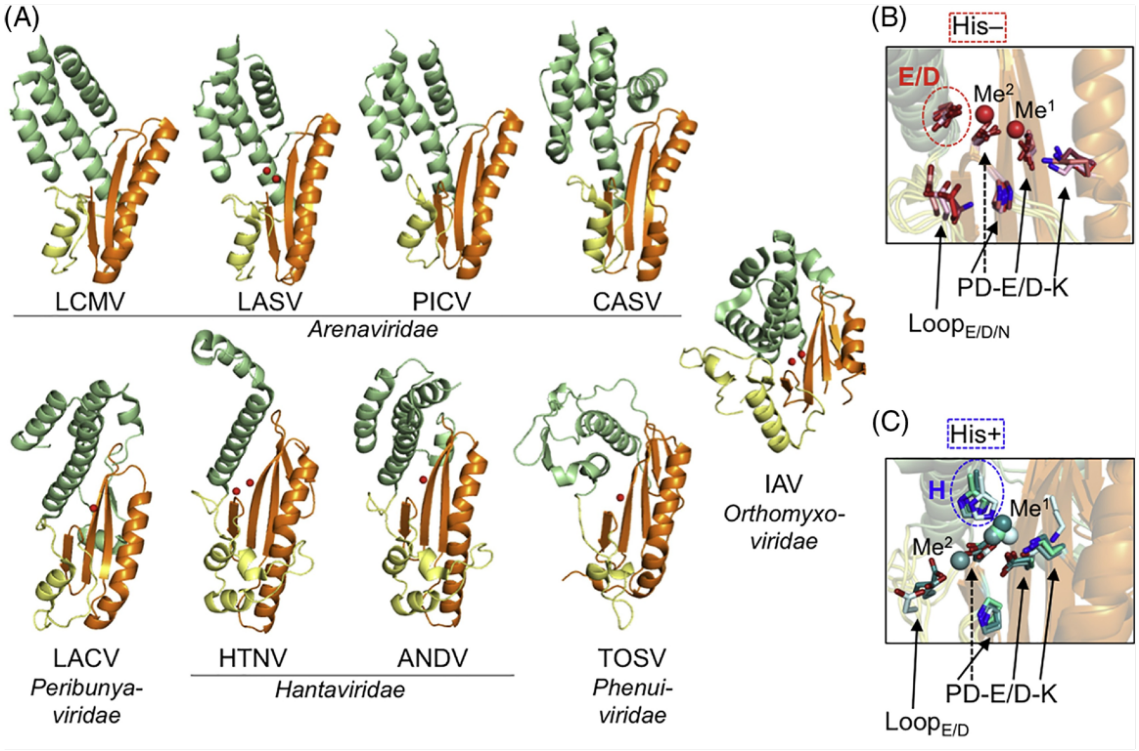

Figure 1.11: Structure of the Endonuclease Domains from Viral Polymerases (**A**) The structures of the endonuclease domains from multiple viral polymerases have been shown as cartoons for lymphocytic choriomeningitis virus (LCMV; PDB: 3JSB), Lassa virus (LASV; PDB: 5J1P), Pichindé virus (PICV; PDB: 4I1T), California Academy of Sciences virus (CASV; PDB: 5MV0), La Crosse virus (LACV; PDB: 2XI5), Hantaan virus (HTNV; PDB: 5IZE), Andes virus (ANDV; PDB: 5HSB), Toscana virus (TOSV; PDB: 6QVV) and influenza A virus (IAV; PDB: 2W69). Comparable structural elements have been coloured the same and divalent cations have been shown as red spheres. (**B** and **C**) The structures of the endonuclease active site have been overlaid for the His- endonucleases (LCMV, LASV, PICV, and CASV) and His+ endonucleases (LACV, HTNV, ANDV, and TOSV) and the active site residue side chains have been shown as sticks. The cations (Me1 and Me2) have been shown as spheres, and colour matched to either the His- or His+ model. This figure was obtained from (Olschewski et al., 2020).

The C-terminal PB2-like region only had 30 % of its structure solved in the monomeric structures of LASV LP and MACV LP, suggesting inherent flexibility. The region of the C-terminal domain that remains unresolved in these structures is proposed to contain the putative cap-binding domain (Lehmann et al., 2014; Rosenthal et al., 2017; Peng et al., 2020). Mutational analysis of the LASV LP found that mutation of conserved residues within the C-terminus affected transcription but not replication, suggesting the C-terminus has a role in cap-snatching (Lelke et al., 2010; Olschewski et al., 2020). Structural determination of the LP C-terminal region of CASV (Rosenthal et al., 2017) also showed structural similarity with the influenza virus PB2 cap-binding domain (Olschewski et al., 2020) (figure 1.12).

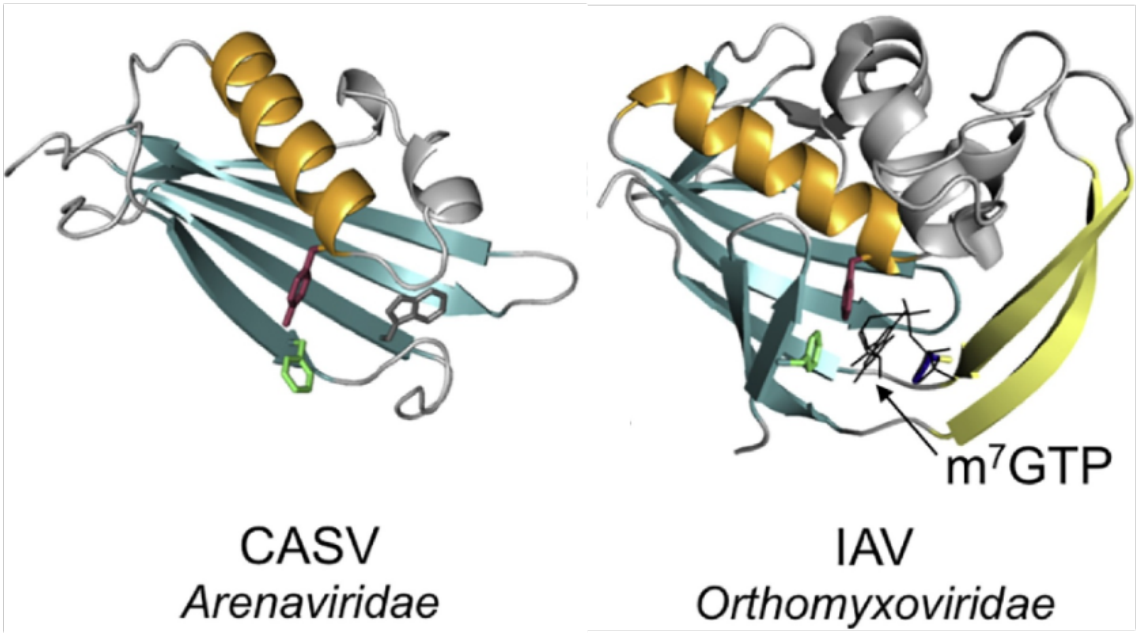

Figure 1.12: Structural Comparison of the Cap-Binding Domains from a Reptarenavirus and Influenza A Virus The crystal structure of the C-terminal domain of the L polymerase (LP) of California Academy of Sciences virus (CASV; PDB 5MUZ) has been shown with the structure of the cap-binding domain within PB2 from influenza A virus PB2 (IAV; PDB 2VQZ). Both structures have been depicted as cartoon, with comparable structures coloured the same, and the proposed cap-binding residues have been shown as sticks. The (m^7G) cap structure has been shown with IAV PB2 and has been depicted as black lines. This figure was obtained from (Olschewski et al., 2020).

The central RdRp region of the arenavirus LP contains the typical motifs that are conserved amongst most viral polymerases (Peng et al., 2020; Poch et al., 1989). One specific motif (the finger-tip) has been unresolved in the other viral polymerases, until the LP is solved in complex with 5'vRNA sequences, in which case the finger-tip is stabilised and the structure can be resolved. However, in the LASV and MACV LPs, the finger-tip motif is highly ordered and the structure could be resolved. It is thought that the finger-tip motif is stabilised through interactions with the core lobe in the PA-like region (Peng et al., 2020). The arenavirus RdRp active site therefore appears "switched on" and does not require 5' vRNA activation like the other viral polymerases (Peng et al., 2020). This supports other biochemical analyses where LASV and MACV demonstrated both replicase and transcriptase activities in the presence of 3' vRNA, but only replicase activities in presence of 5' vRNA (Kranzusch et al., 2010; Pyle and Whelan, 2019; Peng et al., 2020). This is unlike other viral polymerases, which experience improved replication and transcription in presence of 5' vRNA (Peng et al., 2020). This may be a unique feature to the arenaviruses, due to the presence of the core lobe stabilising residues, which are conserved between

the arenaviruses but not in other viral families (Peng et al., 2020).

The MACV LP was also solved in complex with the 3' vRNA and the ZP (Peng et al., 2021) (figure 1.13). This revealed that the 3' vRNA bound in a highly positively charged groove found between the head lobe of the PA-like region and the thumb of the RdRp, which was comparable to the binding of 3' vRNA by the LACV LP and the influenza polymerase (Peng et al., 2021). Furthermore, this structure gives insight to understanding the mechanism behind the ZP's regulation of LP activity. Previously, residues in the RdRp region (H1189 and D1329) of the TCRV LP were shown to be essential for ZP-LP interaction (Wilda et al., 2008). Here, the residues were mapped to the entrance site of the RNA, suggesting that the ZP could limit replication and transcription through occluding this entrance (Peng et al., 2020, 2021).

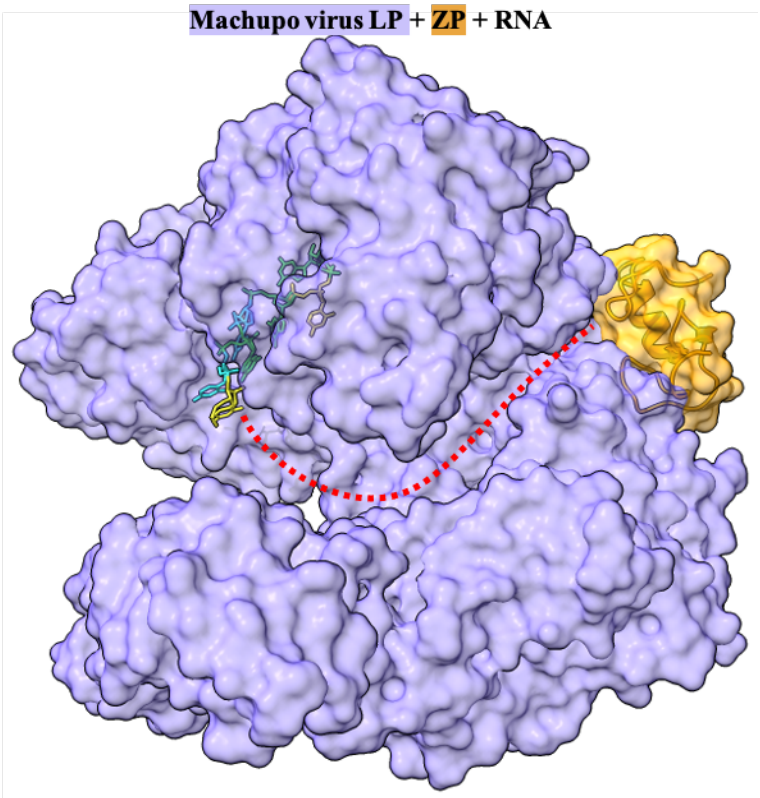

Figure 1.13: Structure of the MACV LP in Complex with 3' vRNA and ZP The Machupo virus (MACV) LP has been shown in complex with 3' vRNA and the MACV ZP (PDB: 7ELC; (Peng et al., 2021)). The MACV LP (purple) has been shown as its transparent surface, the 3' vRNA has been shown as sticks, coloured to corresponding nucleotides, and the MACV ZP (orange) has been shown as a cartoon, overlaid with its transparent surface. The 3' vRNA is bound in a deep groove found in between the PA-like region and the RdRp region. The groove (indicated by a dashed red line), which forms the entrance site of nucleotide chains, appears to be blocked by the ZP. This figure was created using UCSF Chimera X.

1.4.3 Glycoprotein Complex

The glycoprotein complex (GPC) is present on the viral surface and has a trimeric organisation (Schlie et al., 2010a). GPC is translated as a single polypeptide and is later proteolytically processed into the mature tripartite GPC, comprising GP1 (approx. 44 kilodalton (kDa)), GP2 (approx. 35 kDa) and the stable signal peptide (SSP; approx. 5 kDa) (figure 1.14; inset) (Burri et al., 2012a; Hastie and Saphire, 2018).

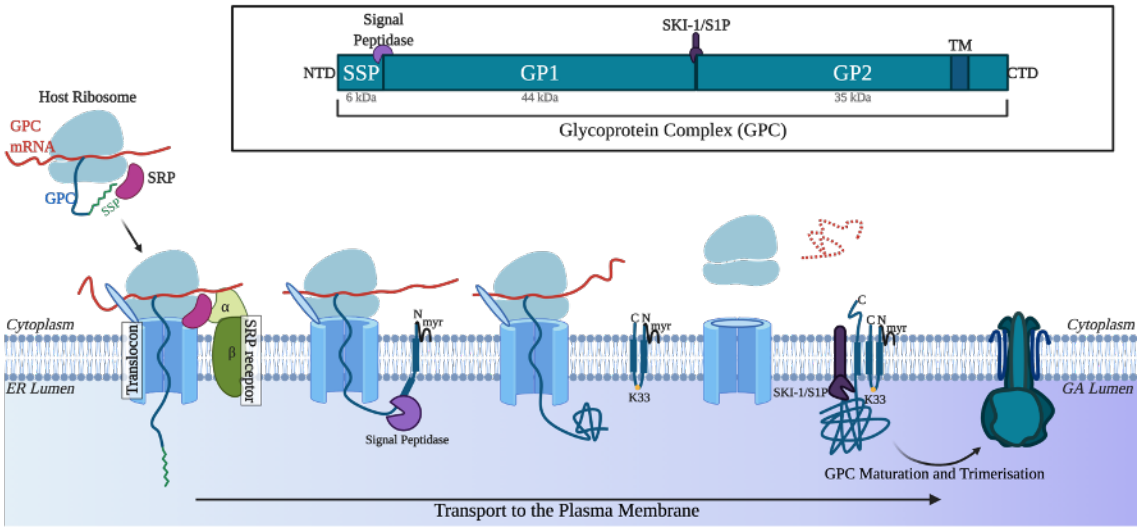

Figure 1.14: Post-Processing of the Arenavirus Glycoprotein Complex (Inset)The glycoprotein complex (GPC) is composed of the stable signal peptide (SSP), GP1 and GP2. The transmembrane domain of GP2 has been indicated (TM), as have the cleavage sites of signal peptidase and SKI-1/S1P. Translation of the GPC mRNA is halted when the SSP is recognised by the signal recognition particle (SRP). The SRP binds to the SRP receptor in the endoplasmic reticulum (ER) membrane and translation resumes through a translocon into the ER lumen. Signal peptidase cleaves the SSP from the rest of the GPC and the SSP becomes embedded in the membrane through two transmembrane domains and the addition of an N-terminal myristic acid (myr). Translation of the GPC mRNA continues and the GP2 TM domain embeds the GPC in the membrane, in association with the SSP. The GPC is later proteolytically processed by SKI-1/S1P. The mature tripartite complex (SSP, GP1 and GP2) then trimerises to form the trimeric GPC spike. This figure was created using BioRender and information from the following citations (Burri et al., 2012b; Pasquato et al., 2018).

Translation of the GPC mRNA is redirected to the endoplasmic reticulum (ER) when the ribosome reaches the SSP (Nunberg and York, 2012) (figure 1.14). Signal peptidase cleaves the SSP from the GPC, but the SSP unusually remains associated with the GPC (Nunberg and York, 2012; York et al., 2004). The SSP is different to most conventional signal peptides; it is significantly longer (58 amino acids as opposed to 18-30 amino acids) and has two hydrophobic regions, instead of one

(von Heijne, 1985; Froeschke et al., 2003; Eichler et al., 2003; York et al., 2004). The arenavirus SSP also has a conserved myristoylation motif ($GX_3(S/T)$ where X is any amino acid), which directs the covalent attachment of a myristoyl group to the second glycine residue of the SSP, anchoring it to the membrane (York et al., 2004; York and Nunberg, 2016). The hydrophobic regions, which are separated by a single positively-charged lysine residue (K33), are thought to cross the membrane in an anti-parallel fashion (Froeschke et al., 2003; Agnihothram et al., 2007). The K33 residue is proposed to interact with the GP2 ectodomain in the ER lumen and is important for pH-mediated GP2 fusion; it is thought that K33 has roles in stabilising the metastable glycoprotein prior to membrane fusion (Nunberg and York, 2012; York and Nunberg, 2006, 2009). The C-terminal tail of the SSP of JUNV (residue C57) interacts with residues in the GP2 cytoplasmic tail (H447, H449, C455, H485, H459, C467, and C469) to form a zinc-binding domain (Agnihothram et al., 2007; York and Nunberg, 2007; Briknarová et al., 2011). The arenavirus SSP is also thought to mask the GPC's ER retention motif, permitting progression to the Golgi, for subsequent processing and trafficking to the plasma membrane (Agnihothram et al., 2006).

The immature GPC is translated as a transmembrane protein, embedded in the ER membrane (figure 1.14). Post-translationally, the GPC is subject to extensive N-glycosylation (Burri et al., 2012a). Whilst specific N-glycosylation sites are not necessarily conserved between arenaviruses, particularly on GP1, a high proportion of the sites are actively used by the arenavirus GPCs (LASV GPC uses all the predicted N-glycosylation sites and LCMV GPC requires eight out of nine sites) (Eichler et al., 2006; Bonhomme et al., 2011). Some of the N-glycosylation sites are necessary for the correct proteolytic processing of the GPC, whereby mutation of these sites results in the trafficking of uncleaved GPC to the plasma membrane (Eichler et al., 2006). However, it has not been fully elucidated on whether these mutations affect the tertiary/quaternary structure, which prevents enzyme cleavage, or whether the N glycosylation sites are required for enzyme activity (Burri et al., 2012a). Furthermore, it is thought that glycosylation plays a role in masking the glycoprotein from the host humoral immune response, forming a glycan shield that prevents access of the antibodies to the viral glycoprotein (Hastie and Saphire, 2018; Sommerstein et al., 2015; Igonet et al., 2011). The arenavirus GPC is proteolytically

processed by the proprotein convertase, subtilisin kexin isozyme-1/site-1 protease (SKI-1/S1P) (figure 1.14) (Lenz et al., 2001; Beyer et al., 2003). Cleavage by SKI-1/S1P occurs at the conserved consensus motif (RXΦX, where X is any amino acid except cysteine and Φ is any hydrophobic residue) in the GPC and results in the formation of the GP1 and GP2 subunits, which remain non-covalently associated (Burri et al., 2012b,a). The cleavage motif appears to play a role in which intracellular compartment the arenavirus glycoprotein is cleaved, whereby the LASV "RRLL" motif directs cleavage in the ER/*cis* Golgi and the LCMV "RRLA" motif directs cleavage in the late Golgi (figure 1.14) (Lenz et al., 2001; Burri et al., 2012b; Wright, 1990).

The structures of the pre-fusion GPCs of the LCMV, LASV and UHV have been solved by either x-ray crystallography (LCMV and LASV) (figure 1.16) or tomographic reconstruction (LASV and UHV) (figure 1.15) (Hastie et al., 2016a, 2017; Li et al., 2016; Hetzel et al., 2013). The tomographic reconstruction of the LASV glycoproteins on chemically fixed virions revealed "spikes" on the viral membrane, which had a trimeric organisation and were approximately 10 nm in width and 9 nm in height (figure 1.15) (Li et al., 2016). There were also "legs" connecting the spikes to the membrane, which were spaced 4 nm apart and were thought to correspond to the GP2 domain (figure 1.15) (Li et al., 2016). Furthermore, there was electron density corresponding to the GP2 intra-viral tails (figure 1.15) (Li et al., 2016). In comparison to the tomographic reconstruction of the LASV GPC, the "spike" structures present on the UHV membrane were similar in size (11 nm in width and 10 nm in height) and were also trimeric (Hetzel et al., 2013). However, comparison of the glycoprotein of UHV with that of LASV and EBOV showed that the UHV GPC had a much higher structural homology with EBOV GPs than with LASV, suggesting an evolutionary history involving filoviruses (Li et al., 2016; Gallaher et al., 2001).

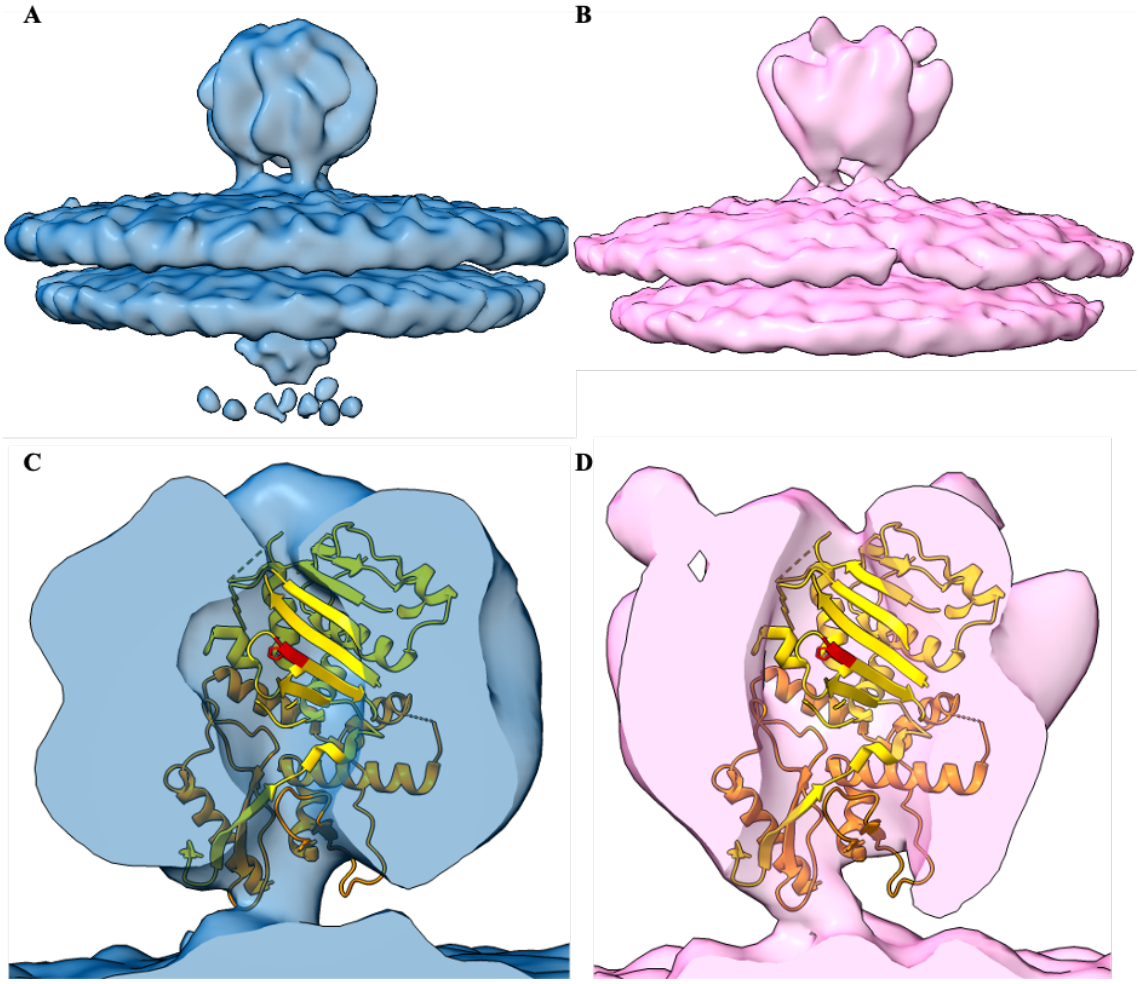

Figure 1.15: Comparison of the LASV GPC at pH 7 and pH 5 The tomographic reconstructions of the LASV GPC (from fixed virions; EMD: 3290) at pH 7 (**A**) and LASV GPC (from virus-like particles; EMD: 3293) at pH 5, with lysosomal associated membrane protein (LAMP1) (**B**). The crystal structure of the Lassa virus GPC (LASV; PDB: 5VK2; yellow) has been shown as a cartoon and was docked into the tomographic reconstruction of the LASV GPC at pH 7 (**C**) and the LASV GPC at pH 5 (**D**). The histidine triad, which is proposed to be responsible for binding secondary receptor, has been shown as sticks and coloured red. This figure was created using UCSF Chimera X.

In order to solve the structure of the pre-fusion GPCs of LCMV and LASV by x-ray crystallography, mutations had to be introduced to stabilise the interactions between the GP1 and GP2 domains. The crystal structure of the LASV GPC aligned well with both the crystal structure of the LCMV GPC and the tomographic reconstruction of LASV (figures 1.15 and 1.16A and B)) (Hastie et al., 2017; Hastie and Saphire, 2018). While the tomographic reconstruction of the LASV GPC provided information on how native GPCs presented on the virion surface, albeit in a chemically fixed conformation, the crystal structures provided further information on the interactions between the GP1 and GP2 domains as well as positioning of residues required for receptor binding and regions exposed to antibody recognition (figure 1.16) (Hastie et al., 2016a, 2017).

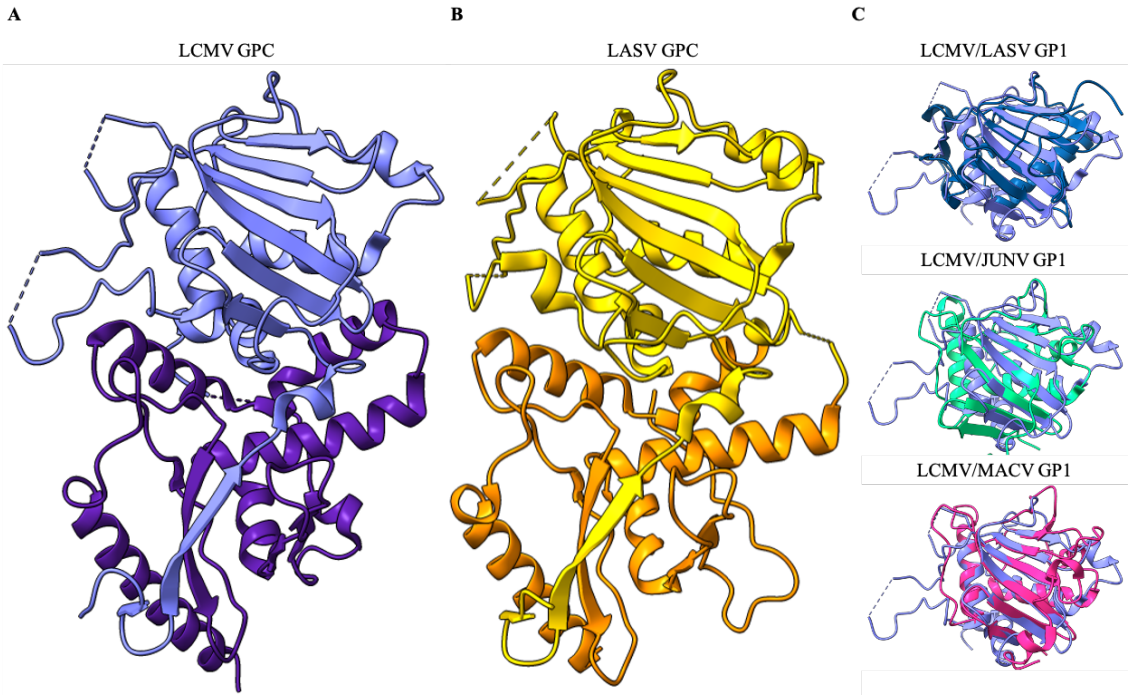

Figure 1.16: Structure of the Arenavirus Glycoprotein Complex The overall structures of the full-length LCMV (**A**; PDB: 5INE; purple) and Lassa virus (**B**; LASV; PDB: 5VK2; yellow) have been shown as a cartoon with the GP1 domains shown as light purple (LCMV) and yellow (LASV) and the GP2 domains shown as dark purple (LCMV) and orange (LASV). (**C**) The LCMV GP1 domain (PDB: 5INE; light purple) overlaid with the GP1 domains (solved without the GP2 domain) of LASV (PDB: 4ZJF; blue) and New World mammarenaviruses Junín virus (JUNV; PDB: 5EN2; green) and Machupo virus (MACV; PDB: 2WFO; pink), showing a high structural homology. This figure was created using UCSF Chimera X.

The GP1 (amino acids 59-265) domain mediates attachment to the host cell receptor. The domain can be divided into three structural features; the N-terminal β-strand, the upper "β-sheet" face and the lower "helix-loop" face (figure 1.16C) (Hastie et al.,

2016a). The upper "β-sheet" face is composed of a six-stranded, anti-parallel β-sheet and is highly glycosylated, contributing to the glycan shield (Hastie et al., 2016a). The lower "helix-loop" face has five α-helices and three extended loops (Hastie et al., 2016a). The N-terminal β-strand extends from GP1 to interact with GP2 and form a three-stranded, anti-parallel β-sheet (Hastie et al., 2016a).

Structures of the GP1 domain of many arenaviruses has been solved, either independently (Bowden et al., 2009; Cohen-Dvashi et al., 2015, 2018; Israeli et al., 2017; Shimon et al., 2017; Pryce et al., 2018) or in complex with their receptor (Abraham et al., 2010), antibody fragments (Mahmutovic et al., 2015; Zeltina et al., 2017; Clark et al., 2018) or GP2 (Hastie et al., 2016a, 2017). There is a high structural homology shared by these GP1 domains, all of which contain the characteristic α/β fold (figure 1.16C). Differences can be attributed to the inherent flexibility in the loops (Hastie et al., 2016a; Pryce et al., 2018). The biggest differences were seen comparing LCMV GP1 (in complex with GP2) and LASV GP1 (independent of GP2). Here, the N- and C termini, which were orientated towards GP2 in LCMV, were orientated in the opposite direction in LASV (Hastie et al., 2016a). Furthermore, two α-helices (α-1 and α-2) present in the LCMV GP1 formed a single α-helix in LASV, which was perpendicular to the rest of the GP1 structure (Hastie et al., 2016a). The third α-helix of the helix-loop face was also positioned 45° away from the position of α-3 in LCMV (Hastie et al., 2016a). These striking differences cannot be attributed to the absence of GP2, because of similarities between LCMV GP1 (-GP2) and LCMV GP1 (+GP2), nor can it be attributed to pH differences because of the similarities seen between MACV GP1 (at pH 5.5) and JUNV GP1 (at pH 8), despite these GP1 domains sharing a lower sequence homology (20 %) than LCMV and LASV GP1 domains share (63 %) (Hastie et al., 2016a). The GP1 domain of WWAV was solved in both pH 7 and pH 5.5 and there were no conformational changes (Pryce et al., 2018).

The host cell receptor of Old World arenaviruses is α-dystroglycan (α-DG), although additional secondary receptors have been identified; LASV requires lysosomal associated membrane protein (LAMP1) (Jae et al., 2014) and LUJV requires neutrophilin-2 (Raaben et al., 2017). Five residues (136, 153, 155, 190 and 260), all present within the GP1 subunit, have now been identified as critical for binding to α-DG, although their exact functions have yet to be clarified (Hastie et al., 2016a).

Residues Ser153 and Leu260 are present in the lower helix-loop face of GP1 (Hastie et al., 2016a) and confer high affinity binding to α-DG and the establishment of viral persistence (Smelt et al., 2001; Teng et al., 1996; Sevilla et al., 2000). Binding to α-DG cannot be mediated by GP1 alone, suggesting there are some factors mediated by the complete GPC necessary for the conformation or orientation of GP1 (Hastie et al., 2016a). This additional interaction between the LASV GPC and LAMP1 necessitates a histidine triad (H92, H93 and H230) present in the LASV GP1 domain (Cohen-Dvashi et al., 2015). The histidine triad is present within the β-sheet face and appears in the centre of the GPC spike in the tomographic reconstruction, when it is overlaid with the LASV GPC crystal structure (figure 1.15). The structure of the LASV GPC, at pH 5, and in complex with LAMP1, has also been shown (figure 1.15B). Although the histidine triad is conserved between LASV and LCMV (Armstrong strain), LAMP1 has not been shown as a requirement for LCMV infection (Jae et al., 2014). However, recombinant viruses bearing mutations in the histidine triad residues fail to rescue, suggesting a potential role of stability for the histidine triad, or additional, as of yet unidentified, receptor for LCMV (Hastie et al., 2016a).

The GP2 (266-498 aa) domain directs membrane fusion between the viral and the host cell membranes in order to release the RNPs into the cytoplasm. The structure of the GP2 domain has been solved (figure 1.17), by x-ray crystallography, in both pre-fusion (Hastie et al., 2016a, 2017) and post-fusion forms (Igonet et al., 2011; Zhang et al., 2019; Shulman et al., 2019; Parsy et al., 2013; Koellhoffer et al., 2014). The structure of GP2 can be divided into three regions; an N-terminal α-helix, a C-terminal α-helix and a "T loop" region which connects the two α-helices (Igonet et al., 2011; Parsy et al., 2013).

GP2 is considered a class I viral fusion protein (Eschli et al., 2006), although it has features of all three classes of fusion protein. It is considered a class I fusion protein because it requires proteolytic processing in order to release the fusion peptide and it has α-helices which form the class I characteristic six-helix bundle post fusion, although the orientation of these α-helices in arenavirus GPC is contrary to that of the other class I fusion GPCs. The LASV GP2 subunit is thought to have both an N-terminal fusion peptide (termed F1; commonly seen in class I viral fusion proteins) and an internal fusion loop (termed F2; seen in Ebola virus GP, and all

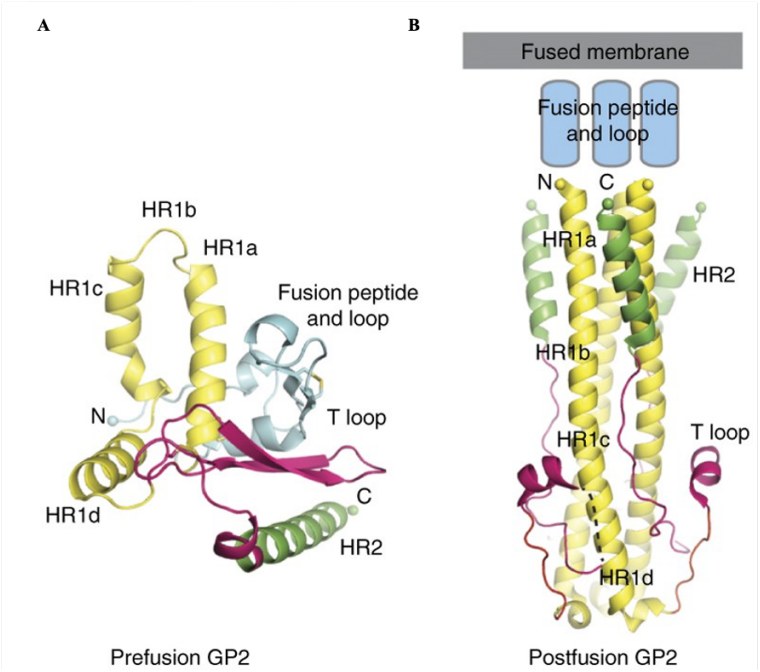

Figure 1.17: Comparison of Pre- and Post-Fusion Forms of LCMV GP2 The pre-fusion form of LCMV GP1 shows heptad repeat (HR) 1 is present as four segments (HR1a-d; yellow), which are connected to the α-helical HR2 by the T-loop, present as two anti-parallel β-strands (pink). The post-fusion form of GP2 (which has been shown as trimeric, forming the characteristic six-helix bundle of class I viral fusion proteins) reveals that HR1a-d form a single α-helix, which is connected to the α-helical HR2 by the T-loop, which is now present as an α-helix. This figure was obtained from (Hastie et al., 2016a).

class II and III viral fusion proteins) (Klewitz et al., 2007; Hastie et al., 2016a). F1 and F2 are highly conserved across the arenavirus family (Hastie et al., 2016a). In the LCMV GP2 structure, the F1 N-terminal peptide is partly helical and is present at the GP1-GP2 interface, while the F2 fusion loop is a connecting loop of two anti-parallel β-strands (Hastie et al., 2016a). The arenavirus GP2 also contains two heptad repeats (HR). There are huge conformational changes in these regions when the pre- and post-fusion forms of GP2 are compared (figure 1.17). Post-fusion, the HRs form the individual N- and C-terminal helices, connected by the "T loop", which also has an α-helical structure. The two HRs come together, with the other two protomers, to form the anti-parallel six-helix bundle commonly seen in class I viral fusion proteins (Hastie et al., 2016a). In the pre-fusion GP2 structure, HR1 is present as four segments (HR1a-d), which form helices except for HR1b, which is present as an extended loop. The "T loop" is present as two anti-parallel β-strands in the pre-fusion form (Hastie et al., 2016a). There are also glycosylation sites on the T loop, suggesting the glycan shield extends beyond GP1 (Hastie et al., 2016a).

1.4.4 Z Matrix Protein

The Z matrix protein (ZP) is the smallest of the arenavirus proteins, comprising between 90 and 99 amino acids with an approximate molecular weight of 11 kDa. Despite its small size, the true multi-functionality of the arenavirus proteins is reflected with the ZP. A critical role of the ZP is to act as the viral matrix protein, forming a matrix layer on the inner side of the viral envelope and linking the glycoprotein spikes with the packaged RNP complexes. The ZP is also responsible for the recruitment and packaging of all the viral components into newly formed viruses. Furthermore, ZP recruits host cell machinery to promote viral budding from the host plasma membrane. The ZP also has multiple interactions with other host cell proteins, including eIF4E and promyelocytic leukaemia protein (PML), as well as playing a role in IFN antagonism.

Structure of the Z Matrix Protein

The structure of the ZP has been determined by nuclear magnetic resonance (NMR) and x-ray crystallography (figure 1.18) (Volpon et al., 2010; Hastie et al., 2016b). The ZP has three domains: the N-terminal domain, the central domain and the C-terminal domain. The N- and C-terminal domains are both highly flexible (figure 1.18C) (Hastie et al., 2016b). The second glycine residue of the ZP, present in the N-terminal domain, is myristoylated, which permits membrane anchorage and potentially initiates oligomerisation (Strecker et al., 2006; Capul et al., 2007; Loureiro et al., 2011). The N-terminal domain also contains conserved basic residues, thought to further assist membrane association through interaction with the acidic phospholipids (Fehling et al., 2012). The N-terminal myristoylation is conserved between Old World and New World mammarenaviruses and it is critical for the ZP-GP(SSP) interaction (Capul et al., 2007). Mutation of this residue to alanine or treatment of WT ZP with myristic acid analogues has been shown to alter the intracellular distribution of ZP and affect the structure of ZP (Strecker et al., 2006), as well as reducing interaction with the GP, although whether this reduction is due to altered localisation or altered structure is not yet known (Fehling et al., 2012).

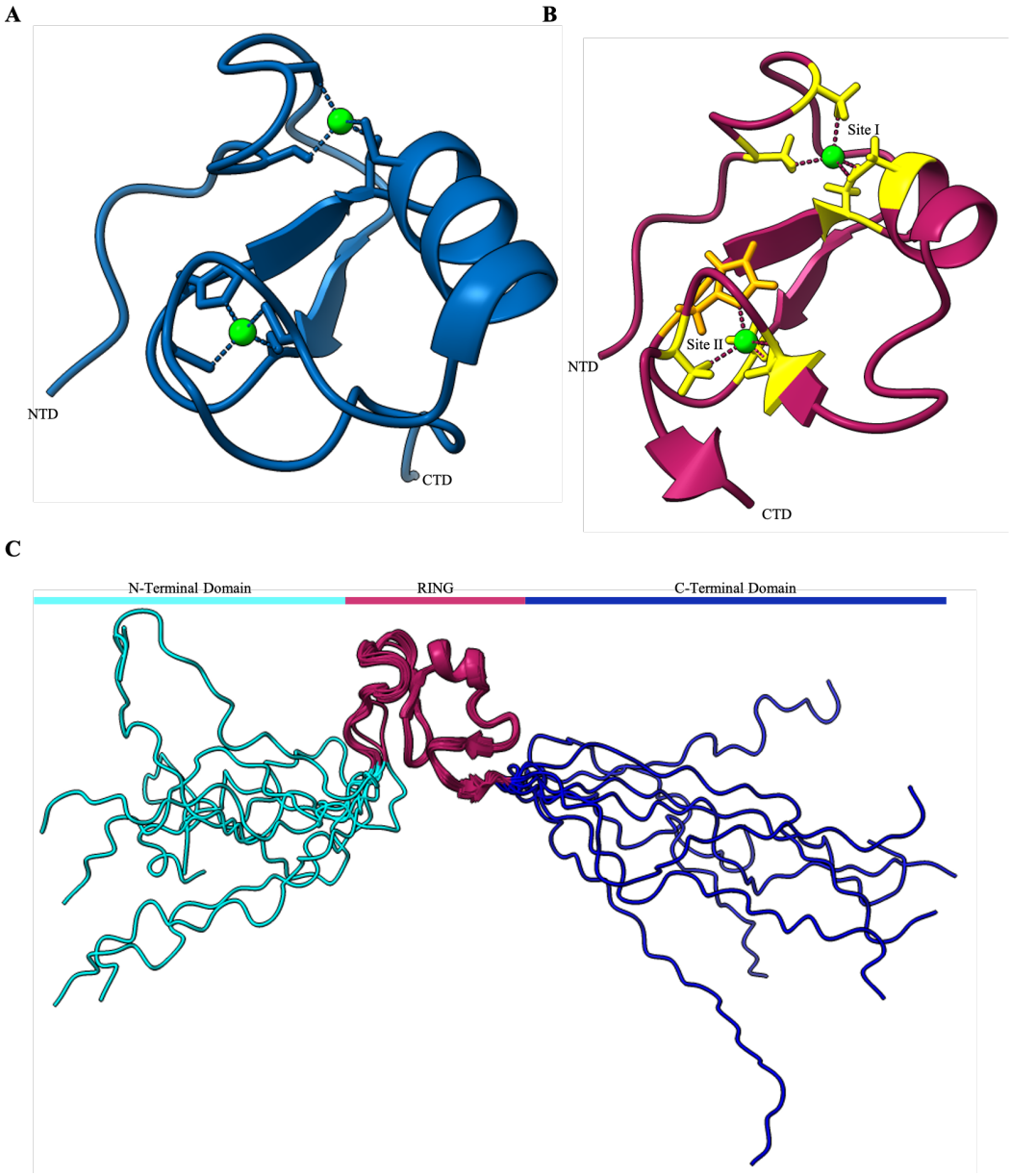

Figure 1.18: Structure of the Arenavirus Z Matrix Protein The crystal structure of the RING domain of the LASV Z matrix protein (ZP) has been shown as a cartoon (**A**; PDB: 5I72; blue). The NMR reconstruction of the RING domain of LASV ZP has also been shown as a cartoon (**B**; PDB: 2M1S; pink). The two zinc ions which are coordinated by the RING domain have been shown as green spheres and the residues which coordinate them (C31, C34, C50 and C53 form one coordination site and C44, H47, C64 and C67 form the other site; cysteine residues has been shown in yellow whereas histidine residues have been shown in orange) have been shown as sticks. (**C**) shows the schematic organisation of the ZP and all the 10 structures solved by NMR, showing the flexibility of the N- and C-terminal domains. This figure was created using UCSF Chimera X.

Within the central domain of ZP is a 60-amino acid RING domain, which contains the characteristic features typically seen with RING domain including a conserved $Cys_3HisCys_4$ motif that co-ordinates two zinc cations at two co-ordination sites, referred to as site I and site II (figure 1.18A and B). The RING domain comprises a single α-helix, two anti-parallel β-strands and two loops, with the zinc-coordination sites present on the α-helix (Hastie et al., 2016b). The RING domain, especially site I, is important for the self-assembly of ZP because expression of the RING domain alone is sufficient to drive the formation of spherical cytoplasmic structures (Kentsis et al., 2001, 2002a,b). X-ray crystallographic analysis of ZP showed a dodecameric organisation within crystals and it has been proposed that this is also the organisation within virions (Hastie et al., 2016b). The RING domain is also similar to the globular type of zinc-binding domains, which are known to interact with proteins, as opposed to a zinc-finger domain which interacts with nucleic acids (Fehling et al., 2012).

The C-terminal domain contains many late-domain motifs that are conserved amongst the Old World and New World arenaviruses. Late-domain motifs are tetra-peptide motifs (either "P[T/S]AP", "PPxY", or "YxxL" where x is any amino acid), which mediate interactions between the viral protein and proteins of the endosomal sorting complexes required for transport (ESCRT) (Fehling et al., 2012). The Old World arenaviruses typically contain "PPxY" motifs and occasionally a "P[T/S]AP" motif. The New World arenaviruses do not contain "PPxY" motifs, but they do generally contain the "P[T/S]AP" motif, except for New World clade A arenaviruses, which have overlapping "PSAP" and "APPY" ("PPPY"-like) motifs that are similar to the overlapping late domains of VP40 from Ebola virus (Fehling et al., 2012). It is thought that the "PPxY" motif mediates binding with Nedd4-like ubiquitin ligases, although direct interactions have yet to be shown. The "P[T/S]AP" motif binds tumour susceptibility gene 101 (Tsg101), which in turn recruits ESCRT1 (Martin-Serrano et al., 2001). Many of the arenaviruses, both Old World and New World, also contain a "YxxL" motif located in the RING domain, which is able to bind Alix/AIP1 to form multi-vesicular bodies and interact with Tsg101 to recruit ESCRT1 (Strack et al., 2003). There are a couple of exceptions to this; LUJV contains another "YxxL" motif in the C-terminal domain instead of a "PPPY" motif and TCRV contains an "ASAP" motif instead of the "P[T/S]AP" motif. The "ASAP"

and "YxxL" motifs in TCRV were not required for ZP-mediated budding, indicating a different mechanism for budding (Urata et al., 2009). TCRV ZP-mediated budding was also weak and not enhanced by replacement of the "ASAP" motif with a "P[T/S]AP" motif, but it was enhanced by presence of the TCRV NP, which also contains a "YxxL" motif and mutation of the NP "YxxL" motif blocks ZP-mediated virus-like particle (VLP) release (Groseth et al., 2010).

Functions of the Z Matrix Protein

The ZP has several functions in the arenavirus life cycle including regulating synthesis of viral RNA, recruitment of viral components for assembly and cellular components to direct budding and interaction with host cell proteins to promote viral translation and inhibit host cell apoptosis.

The ZP is thought to be responsible for halting viral replication and transcription to begin the formation of the viral assembly complexes and initiate viral budding from the host cell membrane. In a dose-dependent manner, ZP has an inhibitory effect on replication and transcription in mini-genome assays (López et al., 2001; Cornu and de la Torre, 2001). It has been observed that the ZP (of TCRV) can directly interact with the LP (Jaòcamo et al., 2003). There are two putative Z-binding sites on the LP, one at the N-terminus of the LP and one within the RNA polymerase domain (Wilda et al., 2008). The residues identified as important for the ability of ZP to inhibit viral RNA synthesis are thought to be the residues required for LP binding. The RING domain is essential for inhibition of RNA synthesis, in addition to residues that coordinate the zinc cations and a conserved tryptophan residue within the RING domain (Loureiro et al., 2011; Capul et al., 2011; Cornu and de la Torre, 2002). The direct interaction between the LP and ZP inhibits the catalytic activity of the L polymerase (Kranzusch and Whelan, 2011) but does not affect its ability to bind viral RNA, which would be important for packaging of the viral genome and recruitment of LP into newly synthesised virions (Fehling et al., 2012). Furthermore, ZP interaction with the NP is thought to further inhibit LP RNA synthesis activities (Fehling et al., 2012).

The ZP is also responsible for the recruitment of each viral component to the site of assembly. The LP is recruited through direct binding as discussed above. The RING

domain of the ZP is also important for interaction with the NP because mutation of the RING domain abolishes the incorporation of NP into ZP-induced VLPs (Casabona et al., 2009). Furthermore, for MOPV, it is thought that the ZP-NP interaction is mediated by both proteins interacting with Alix/AIP1 (Shtanko et al., 2011). The ZP-NP interaction has been proposed to play a predominant role in recruiting the genomic RNP complexes into newly synthesised virions (Fehling et al., 2012). Finally, the interaction between ZP and the GPC is thought to be mediated through the myristoylation of residues within the N terminal domain of the ZP and the SSP of the GPC. The interaction of the ZP with all the viral proteins is a principal role, due to a lack of direct interaction between NP and the GP. ZP therefore acts as a bridge between the NP and GP, whereby cells only expressing GPC and NP show no colocalisation between the two and no incorporation of NP in GP-directed VLPs, but expression of ZP shows colocalisation of GPC and NP and the NP is incorporated into VLPs (Schlie et al., 2010b).

The ZP also recruits the ESCRT complex components to the viral assembly site, in order to catalyse the budding of the newly synthesised viruses from the host cell membrane (Fehling et al., 2012). There are four ESCRT protein complexes (ESCRT-0, ESCRT-I, ESCRT-II, ESCRT-III) that associate with additional factors including the ATPase Vps4 and adaptor protein Alix/AIP1 (ALG-2-interacting protein 1). The ESCRT complexes typically initiate recruitment of ubiquitinated cargoes to endosomes (ESCRT-0) and direct membrane budding (ESCRT-I and -II) and membrane scission (ESCRT-III) to release vesicles into multi-vesicular bodies (Wollert et al., 2009). Vps4 assists this process by disassembling ESCRT-III from the membrane after scission (Fehling et al., 2012). Interaction between the ZP "P[T/S]AP" motif and ESCRT-I complex member Tsg101 enables recruitment of the ESCRT complexes to the viral assembly site (Martin-Serrano et al., 2001). The ZP "YxxL" motif also recruits ESCRT complexes through interactions with Alix/AIP1, which binds Tsg101 (of ESCRT-I) and components of ESCRT-III (Strack et al., 2003). Finally, the ZP "PPxY" motifs recruit ESCRT complexes through interactions with Nedd4(Neuronal precursor cell-expressed developmentally down-regulated 4)-like E3 ubiquitin ligases, which are involved with the ubiquitination enzyme cascade of proteins (Fehling et al., 2012). The ESCRT complexes often recruit proteins through ubiquitination, offering a suggestion for why the ZP would interact

with Nedd4-like E3 ubiquitin ligases. It has been observed that the LASV ZP can directly bind Nedd4 and Nedd4-like ubiquitin ligases, an interaction that requires the "PPxY" motif, but the role of these proteins and of ubiquitination in virus budding has not been fully elucidated (Fehling et al., 2012).

The ZP has also been shown to interact with multiple host cellular proteins, including PML, ribosomal P proteins, eukaryotic translation initiation factor 4E (eIF4E) and the proline-rich homeodomain protein (PRH) (Fehling et al., 2012). PML has roles in apoptosis and the immune response. It has been shown that during LCMV infection, and when the ZP (of LASV and LCMV) is solely expressed, PML is relocalised from the nucleus to the cytoplasm where it forms large bodies that colocalise with ZP (Borden et al., 1998a). This interaction has been suggested to help arenaviruses evade host cell apoptosis or the innate immune responses (Fehling et al., 2012). Ribosomal P proteins (P0, P1, P2) are components of the large subunit of the ribosome. In infected cells, LCMV ZP has been shown to colocalise with P0, P1 and P2 in the nucleus but it does not result in their redistribution, rather the down-regulation of P1 and P2 expression, which is thought to affect ribosome function (Borden et al., 1998b). However, the expression of P0 is not down-regulated by Z, which instead binds directly to P0 and potentially incorporates P0, and possibly ribosomes, into new virions (Borden et al., 1998b). It is thought that ZP may recruit P0 for processing activities, such as excision repair and endonuclease activity, that may be required for viral genomic replication (Fehling et al., 2012). eIF4E assists host ribosomal binding of mRNA M^7G caps to initiate cap-dependent translation. Direct binding between the ZP (LCMV and LASV) and eIF4E has been shown and this interaction results in conformational changes within the eIF4E cap-binding site, which therefore limits eIF4E-dependent protein synthesis (Volpon et al., 2010). This could result in a reduction of translation of regulators of the immune response or potentially promote translation of viral mRNAs, with the suggestion that the NP replaces the eIF4E cap-binding function. PRH is a transcription factor necessary for early development of the brain, thyroid and liver, as well as regeneration of the liver cells following damage or disease. The expression of PRH was found to be significantly reduced in hepatic cell lines following infection with the highly pathogenic LCMV-WE strain but not after infection with the LCMV-ARM strain, which is considered to have reduced pathogenicity (Djavani

et al., 2005). Proliferation of hepatocytes is also induced in rhesus macaques infected with LCMV-WE but not when infected with LCMV-ARM (Lukashevich et al., 2004). It is proposed that the down-regulation of PRH reduces the anti-proliferative effects of PRH, which promotes cell division, therefore supporting viral infection, but results in higher pathogenicity because the liver cells cannot be regenerated. It has been shown that the RING domain of the LCMV ZP can directly interact with PRH (Djavani et al., 2005; Topcu et al., 1999) leading to the suggestion that ZP mediates the down-regulation of PRH but this has not been fully elucidated and other viral proteins may play a role.

Finally, it has also been shown that the ZP, of New World arenaviruses TCRV, GTOV, JUNV, MACV and SBAV, assists the NP in antagonism of the IFN response. This occurs through an interaction between the ZP and RIG-I (Fan et al., 2010). This interaction is thought to disrupt the interaction between RIG-I and MAVS, which is essential in the signalling cascade that leads to the production of IFN-β (Fan et al., 2010). The LASV and LCMV ZPs are not thought to antagonise the IFN response because their ZPs do not interact with RIG-I.

1.5 Introduction to the Arenavirus Lifecycle

The mammarenaviruses follow a similar lifecycle (figure 1.19). Initially, the mammarenavirus GPC binds a cellular receptor on the plasma membrane and the virus enter the cell through receptor-mediated endocytosis. Following acidification of the endosome, the GPC mediates viral and host membrane fusion for release of the RNPs into the host cytoplasm. The vRNA is then transcribed and replicated (to form the cRNA, which is also transcribed and replicated), in the host cytoplasm, by the LP. The mRNAs of the viral proteins are translated by host ribosomes in the cytoplasm, except for the GPC, which is translated into the endoplasmic reticulum (ER) and matures through the Golgi apparatus (GA) towards the plasma membrane (figure 1.14). All the viral proteins assemble at the host plasma membrane and host complexes are recruited to drive budding from the membrane and formation of a new virion.

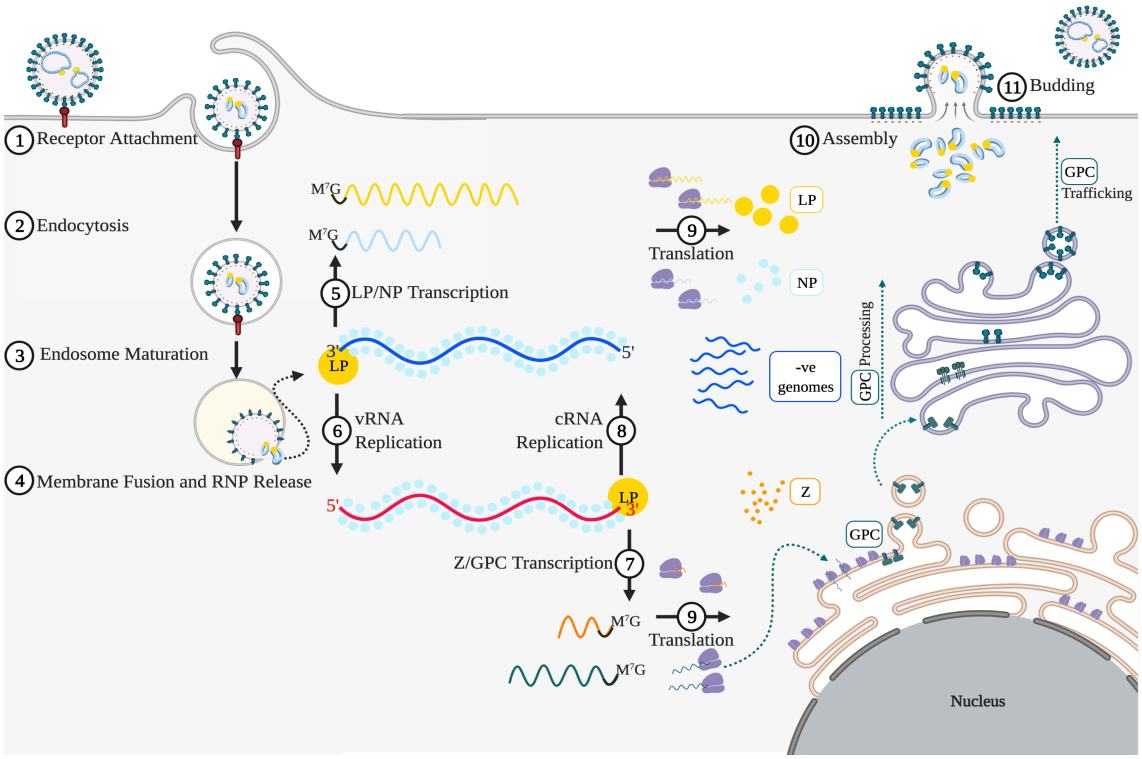

Figure 1.19: Schematic of the Mammarenavirus Lifecycle.
The mammarenavirus attaches to its host cell receptor (1) and is internalised through an endocytic pathway (2). The internalised endosome becomes increasingly acidic (3), inducing host and viral membranes to fuse and release the ribonucleoproteins (RNPs) (4). The viral polymerase (LP) then transcribes (5) the nucleocapsid protein (NP) and L polymerase (LP) genes and replicates (6) the vRNA to form the cRNA (6). The cRNA is then bound by the LP, to transcribe (7) the glycoprotein (GPC) and Z matrix protein (ZP) genes and replicate the cRNA to produce more vRNA copies (8). The viral mRNAs are translated (9) and the NP, LP and genome segments assemble to form ribonucleoprotein complexes. The GPC is processed in the rough endoplasmic reticulum and Golgi apparatus. The Z matrix protein (ZP) recruits the RNPs and GPCs to the plasma membrane for assembly (10) and budding (11). This figure was created using BioRender.

1.5.1 Entry

Arenaviruses enter host cells through receptor-mediated endocytosis, but Old World and New World (clade B specifically) mammarenaviruses adopt different entry mechanisms, and utilise different receptors. The entry pathway and receptor of New World clade A mammarenaviruses have not yet been identified, whilst it has been shown that New World clade C mammarenaviruses (Oliveros virus and Latino virus) utilise the same receptor and entry pathway as Old World mammarenaviruses (Rojek et al., 2007, 2008b; Nunberg and York, 2012).

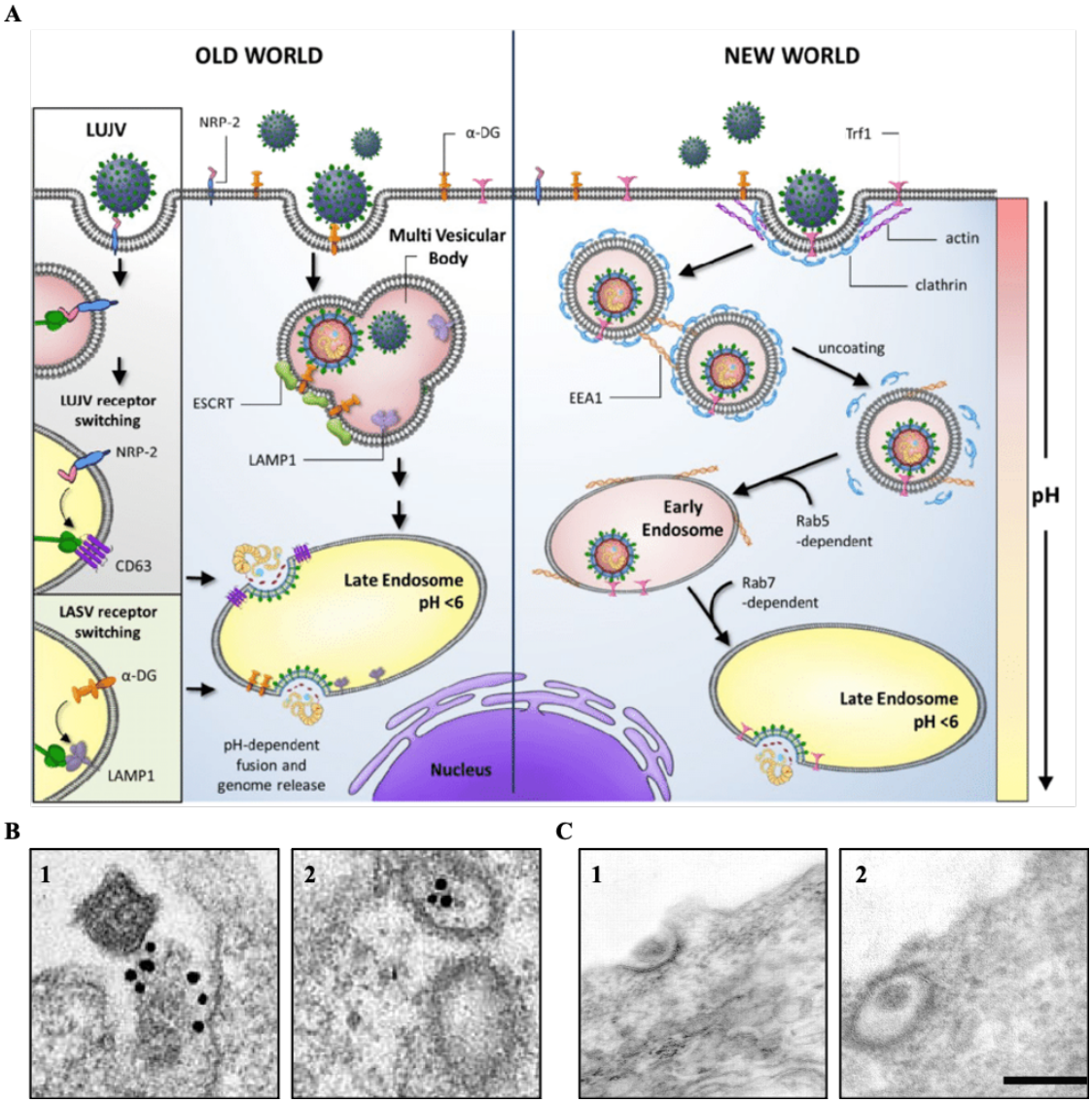

Figure 1.20: The Different Entry Pathways of Different Mammarenaviruses. (**A**) shows a schematic of the different entry pathways of mammarenaviruses. Old World mammarenaviruses (and New World clade C) typically enter cells after binding to host cell membrane protein α-dystroglycan (α-DG), except for Lujo virus (LUJV), which binds neuropilin 2 (NRP-2). Old World mammarenaviruses are then internalised into the host cell in an endocytic mechanism that involves the formation of multi-vesicular bodies, which mature into late endosomes, in a Rab5- and Rab7-independent manner. The decrease in pH induces structural changes in the GPC that mediates membrane fusion and release of the ribonucleoprotein complexes (RNPs). For LUJV and Lassa virus (LASV), the reduction in pH induces a receptor switch (to tetraspanin CD63 for LUJV and lysosome associated membrane protein 1 [LAMP1] for LASV), which is necessary to mediate membrane fusion and RNP release. New World (clade B) mammarenaviruses bind transferrin receptor 1 (TfR1) and enter the host cell through clathrin-mediated endocytosis. The virions are initially delivered to early endosomes and then to late endosomes, in a Rab5 and Rab7-dependent manner. The pH decrease induces GPC structural changes, which direct host and viral membrane fusion and RNP release. This figure was obtained from (Stott et al., 2020). (**B** and **C**) show electron microscopy evidence of LCMV (**B**) and JUNV (**C**) entering cells. LCMV (labelled with 10 nm gold particles) was found associated with smooth (**B**1) and clathrin-coated (**B**2) structures (Quirin et al., 2008). JUNV was shown to internalise through clathrin-coated structures (**C** 1 and 2) (Martinez et al., 2007).

Cellular Entry of Old World Mammarenaviruses

The cellular receptor for many Old World (including LCMV and LASV) and New World clade C mammarenaviruses has been identified as α-dystroglycan (α-DG), which is a widely-expressed cell surface protein that is highly conserved and found on many cell types (Cao, 1998; Kunz et al., 2002). α-DG forms part of the dystroglycan complex that connects the extracellular matrix (ECM) to the cytoskeleton (Rojek et al., 2007). α-DG is extensively post-translationally modified and O-glycosylation of α-DG was found to be critical for arenavirus entry (Kunz, 2009; Rojek et al., 2007) (figure 1.20A). Specifically, successful arenavirus infection was dependent on the addition of the negatively-charged matriglycan sugar to α-DG, which is mediated through like-acetylglucosaminyltransferase (LARGE)-directed glycosylation (York and Nunberg, 2009; Rojek et al., 2010; Kunz, 2009; Rojek et al., 2007). Furthermore, during arenavirus infection, the GPC disrupts the LARGE-mediated modification of α-DG, which reduces the presence of functional α-DG at the cell surface (Kunz, 2009). There is an extremely high binding affinity between the GPC and α-DG (Cao, 1998; Smelt et al., 2001; Sevilla et al., 2000; Kunz et al., 2001, 2005) and therefore it is thought that the down-regulation of the expression of functional α-DG at the cell surface assists viral exit and prevents re-infection of the same cell (Kunz, 2009).

Interestingly, a second essential entry receptor, lysosomal associated membrane protein (LAMP1), has been identified for LASV infection (Jae et al., 2014; Cohen-Dvashi et al., 2015). LAMP1 is found intracellularly in late endosomes and lysosomes. It is thought that through dissociating from α-DG and interacting with LAMP1, the LASV GPC can mediate membrane fusion and RNP escape into the cytoplasm in less acidic endosomes (Hulseberg et al., 2018) (figure 1.20A). Through switching receptors to LAMP1, LASV therefore avoids trafficking to increasingly acidic endosomes, which may be inactivate virions before fusion (Torriani et al., 2017; Hulseberg et al., 2018). LCMV has not been shown to require LAMP1 for infection, suggesting differences in cellular receptors and entry pathways even between the Old World mammarenaviruses (Jae et al., 2014). Furthermore, there have been several other entry factors that have been identified for LASV, including receptor tyrosine kinases Axl and Tyro3/Dtk, and C-type lectins Dendritic Cell-Specific Intercellular adhesion molecule-3-Grabbing Non-integrin (DC-SIGN) and LSECtin (Goncalves et al., 2013). These entry factors have been proposed to function as alternative

receptors for LASV cellular entry in the absence of functional α-DG (Fedeli et al., 2017; Herrador et al., 2019; Goncalves et al., 2013).

LUJV does not utilise the same entry receptors as LCMV, LASV and other Old World mammarenaviruses, or the New World mammarenaviruses. Instead, the LUJV GPC binds neuropilin 2 (NRP2) and has the tetraspanin CD63 as a secondary entry receptor, performing a similar receptor switch as LASV in the late endosome (Raaben et al., 2017) (figure 1.20A).

α-DG-mediated internalisation of Old World mammarenaviruses, specifically LCMV and LASV, is thought to involve macropinocytosis (Iwasaki et al., 2014; Oppliger et al., 2016) (figure 1.20A). These viruses are able to enter cells in a way that is dependent on sodium-hydrogen exchangers (critical in macropinocytosis) and actin remodelling, but independent of clathrin, dynamin-2, Arf6, calveolae, lipid rafts, Rab5 and Rab7 (Iwasaki et al., 2014; Oppliger et al., 2016; Shao et al., 2015). The viruses are internalised initially into a multivesicular endosome, and the receptor (and attached virion) is then delivered to the late endosome, which involves ESCRT complexes (Pasqual et al., 2011; Fedeli et al., 2018). It is unknown whether the virus GPCs hijack a natural trafficking, degradation or recycling pathway of α-DG or whether the interaction between the virus GPCs and α-DG induces a novel endocytic route (Boulant et al., 2015). Interestingly, electron microscopy of LCMV entry showed LCMV particles were internalised into smooth vesicles, but a small number of virions were found internalised into clathrin-coated vesicles, suggesting there could potentially be a different entry pathway or use of alternative entry receptors (Quirin et al., 2008) (figure 1.20B).

Cellular Entry of New World Mammarenaviruses

The cellular receptor of New World clade B mammarenaviruses was identified as the transferrin receptor-1 (TfR1) (Radoshitzky et al., 2007, 2008). Pathogenic New World clade B mammarenaviruses (such as JUNV and MACV) are able to bind human TfR1, whereas TCRV, AMPV and CPXV, are apathogenic to humans because the GPC is unable to bind human TfR1 (Shao et al., 2015). However, these viruses are able to bind rodent orthologs of the transferrin receptor, permitting entry into their hosts' cells (Shao et al., 2015). Furthermore, some of these viruses are

able to bind multiple TfR1 orthologs, including JUNV, which can bind the feline TfR1 ortholog (Martinez et al., 2013). This poses a threat because apathogenic viruses could be selected, or mutate, to successfully bind human TfR1, potentially enabling human infection (Fedeli et al., 2018; Abraham et al., 2009). Other cellular factors have also been identified as necessary for JUNV entry, including C-type lectins DC-SIGN and L-SIGN (Martinez et al., 2013).

The New World clade B mammarenaviruses enter cells through clathrin-mediated endocytosis into early endosomes, following the normal internalisation and recycling pathway of TfR1 (Radoshitzky et al., 2007) (figure 1.20A). However, the optimal pH for JUNV GPC membrane fusion is less than 5.5, meaning fusion cannot occur in the early endosomes, where the pH is approximately 6. JUNV GPC is proposed to prevent TfR1 recycling and instead redirect it to the late endosomes (in a Rab7-dependent manner), where the virus can direct membrane fusion at the lower pH (McLay et al., 2014). Electron microscopy has confirmed the entry pathway through clathrin-mediated endocytosis through observation of JUNV associated with clathrin-coated vesicles (Martinez et al., 2007) (figure 1.20B).

1.5.2 Replication and Gene Transcription

After fusion of the viral and late endosome membranes, the S and L vRNAs, which are present as the RNP complexes, are released into the host cytoplasm (figure 1.19 4). The input vRNA is then transcribed and replicated by the virion-associated LP (Wallat et al., 2014) (figure 1.19 5-6). The RNA synthetic activities of the LP is dependent on several structures and sequences present in the arenavirus vRNA, including the IGR, promoter sequences in the 3' and 5' UTRs, the double-stranded pan-handle structure formed by the 3' and 5' UTRs and a non-templated G residue present at the 5' end of the vRNA. Mini-genome assays have shown that NP and LP are the minimal viral trans-acting factors that are required for the transcription and replication of the arenavirus genome (of LCMV, LASV, JUNV, TCRV and PICV) (Hass et al., 2004; Albariño et al., 2009; López et al., 2001; Lan et al., 2009). Oligomerisation of the LCMV LP has also been shown to be important for its activity (Salvato, 1993). The arenavirus ZP has an dose-dependent inhibitory effect on transcription and replication of the arenavirus genomes (specifically LCMV,

LASV and TCRV) (Cornu and de la Torre, 2001, 2002; Cornu et al., 2004; Hass et al., 2004; López et al., 2001).

Initially, the NP and LP genes are transcribed from the vRNA. Sequencing of the NP and LP mRNAs showed the presence of non-viral sequences at the 5' end of the mRNA (Raju et al., 1990; Meyer and Southern, 1993; Polyak et al., 1995). This suggested that the LP utilises its endonuclease activity to cleave a short 5'-M^{7}G-capped primer from host cellular mRNAs (Lelke et al., 2010; Howley and Knipe, 2020). This is a mechanism shared by other viruses, including bunyaviruses and orthomyxoviruses (Olschewski et al., 2020). However, the *in vitro* endonuclease activity of LASV and LCMV LP is much lower than the other viral endonucleases (Reguera et al., 2016). Mini-genome assays have shown residues in the endonuclease region are essential for *in vivo* viral transcription but not for replication (Reguera et al., 2016). This 5'-M^{7}G-capped primer is able to prime viral mRNA synthesis. The IGR functions as a bona fide transcription termination signal for LP (Pinschewer et al., 2005). The LP transcribes capped viral mRNAs, which are non-polyadenylated (Meyer et al., 2002). The cap assists the ribosome in recognising, and therefore translating, the viral mRNAs. It was proposed that the LASV NP replaces the cap-binding activity of eIF4E in the translation-initiation complex (Qi et al., 2010), although Hastie et al. showed that mutations in the proposed cap-binding site did not reduce levels of viral mRNA and the LASV NP was unable to pull down the cap-structure (Hastie et al., 2011b). The NPs from Junín, Tacaribe, and Pichindé mammarenaviruses have also not been shown to have a direct interaction with the cap-structure (Olschewski et al., 2020).

Following the increase in NP and LP expression, the LP switches from its transcriptase activity to its replicase activity. Arenavirus promoter sequences are present in the 3' UTRs of the vRNA and the cRNA. The 3' and 5' UTRs are complementary, which is necessary for the formation of the panhandle structure. The sequence and the structure of the UTR promoters has been shown to be important for promoter activity in LCMV, LASV and MACV (Hass et al., 2006; Perez and de la Torre, 2003a). There is a non-templated G residue at the 5' ends of the vRNAs and cRNAs, which is the result of a prime-and-realign mechanism that is used to initiate LP replication (Garcin and Kolakofsky, 1990, 1992; Radoshitzky et al., 2011; Vogel et al., 2019). The arenavirus LP (and other viral polymerases) initiate de novo

RNA synthesis with GTP and therefore initiation of RNA replication has to start at an internal templated C residue (Howley and Knipe, 2020). Once the initial phosphodiester bond has been formed, LP and this uncapped primer slips back on the vRNA template and realigns with position 1 at the 3' end of the vRNA, and continues RNA replication, incorporating the non-templated G residue at the 5' end of the newly synthesised RNA (Howley and Knipe, 2020). In order to keep the length of the genomic vRNA constant, the LP terminates replication by removal of the last base at the 3' end of the newly synthesised RNA.

In the replicase mode, the LP synthesises RNA molecules that are different to the mRNAs synthesised in the transcriptase mode. During replication, the LP reads through the IGR termination signals to produce a complete complementary copy of the vRNA, called the complementary RNA (cRNA). This cRNA is full-length, uncapped and encapsidated by the NP, unlike mRNAs. This intermediate cRNA, which is positive-sense, then acts as a template for the synthesis of mRNAs of the GPC and ZP and negative-sense vRNA copies (figure 1.19 7-8). Initially, the low expression levels of the ZP promotes LP transcription and replication (Kranzusch and Whelan, 2011, 2012). Increasing ZP expression levels then have a dose-dependent inhibitory effect on LP transcription and replication (Perez et al., 2003b; Stinebaugh et al., 1966). The ZP has been proposed to directly interact with the LP in order to lock it in a catalytically-inactive state (Kranzusch and Whelan, 2011, 2012). This is thought to promote progression onto the assembly and budding stages of the viral lifecycle.

1.5.3 Assembly and Exit

The assembly and exit of the newly-synthesised arenavirus virions requires the ZP and the GPC (figure 1.19 10-11). The GPC is translated into the endoplasmic reticulum (ER) and proteolytically processed in the ER/Golgi apparatus (GA) lumen by signal peptidase and SKI-1/SIP1, into the trimeric, tripartite SSP/GP1/GP2 complex, which is directed to the plasma membrane (figure 1.14) (Lenz et al., 2000, 2001; Pinschewer et al., 2003). The ZP is also targeted to the plasma membrane, through myristoylation of its second glycine residue, which is thought to initiate ZP oligomerisation (Perez et al., 2004; Strecker et al., 2003).

The ZP recruits all of the viral proteins to the assembly site through interactions with the LP (Kranzusch and Whelan, 2011), the NP (Shimojima et al., 2012) and the GPC (Capul et al., 2007; Urata et al., 2006). The ZPs (of LASV and LCMV) have been shown to drive virion budding from the plasma membrane, through recruitment of cellular ESCRT complexes using its late-budding motifs ("PTAP" and/or "PPPY") (Perez et al., 2003b; Stinebaugh et al., 1966; Freed, 2002). Arenavirus virions also package the cellular cargo receptor endoplasmic reticulum (ER)-Golgi intermediate compartment 53-kDa protein (ERGIC-53), which interacts with the GPC and localises to the assembly site. This has been shown to be required for infectivity of the progeny virions (Klaus et al., 2013).

Whilst the predominant method of arenavirus budding occurs through the action of ZP-mediated recruitment of host cellular ESCRT complexes, some arenaviruses lack the necessary late motifs (TCRV) or ZP entirely. It has been shown that the late motifs of TCRV ZP are not required for ZP-mediated budding and their replacement with other arenavirus ZP motifs did not enhance budding, suggesting alternative methods (Urata et al., 2009). Whilst budding mediated by the TCRV ZP was weak, budding was enhanced by the presence of the TCRV NP. The TCRV NP contains a "YxxL" late motif and mutation of this motif blocks VLP release (Groseth et al., 2010). This suggests that the budding activity of the ZP can be replaced by motifs that can be present in the NP. Similarly, reptarenaviruses lack late domain motifs in the ZP, but budding is thought to be achieved through a conserved "PPPY" late motif in the NP and other late domain-like motifs present in the NP C-terminal domain (Stenglein et al., 2012). Furthermore, viruses in the *Hantaviridae* family of the *Bunyavirales* order do not encode a ZP-like protein and instead utilise late-domain motifs located within the Gn cytoplasmic tail to direct budding (Strandin et al., 2013). The lack of ZP in hartmaniviruses and antennaviruses suggests alternative budding methods are employed for their exit. Furthermore, the presence of a conserved "P[Y/F]PHYP" stretch in the hartmanivirus GP2 cytoplasmic tail has indicated that hartmanivirus budding is mediated through binding between GP2 and apoptosis-linked gene 2 (ALG-2), which then bridges Alix and the ESCRT-I complex (Hepojoki et al., 2018). The budding activities of the antennaviruses has not yet been well described.

1.6 Project Aims

The work presented in this thesis aimed to develop molecular tools in order to further the understanding of arenavirus infection, arenavirus RNP complexes and arenavirus GPC entry spikes. This thesis focused on two biosafety level 2 classified arenaviruses; LCMV as a representative of the Old World mammarenaviruses and PICV as a representative of the New World mammarenaviruses. Study of these viruses can be extrapolated to biosafety level 4 classified arenaviruses, which are responsible for severe human morbidity and mortality. Three main objectives were established for this project:

1. *Generation of LCMV NP antisera for its use as an arenavirus detection tool.* LCMV NP was purified for the generation of a polyclonal antibody, which was subsequently used to investigate intracellular localisation of the NP during arenaviral infection and to develop a focus-forming assay for the titration of LCMV, using fluorescence microscopy.

2. *Development of a reverse genetics system designed to recover infectious LCMV.* This system was used to generate high titre stocks of LCMV for subsequent structural examination. This system was also engineered to investigate the incorporation of eGFP into the S segment and the fusion of the 6xHis tag to the C-terminus of the NP, permitting the development of high-throughput screening methods and structural examination of the arenavirus RNP, using fluorescence and electron microscopy.

3. *Structural examination of the PICV and LCMV GPCs by cryo-electron tomography.* Sub-tomogram averaging was subsequently performed to permit structural investigation into the differences between glycoprotein complex (GPC) spikes of New World (PICV) and Old World (LCMV) arenaviruses.

In summary, the aim of this project was to generate an LCMV NP antibody, which enabled the optimisation of the LCMV reverse genetics system. The LCMV NP antibody can be used for easy identification of successful infection and further investigation into the cellular localisation of the NP during the viral lifecycle. The LCMV reverse genetics system permits mutational analysis of the viral proteins, as

well as the incorporation of fluorescent tags or purification tags for high throughput screening assays or structural investigation into arenavirus RNPs. Both the tools developed here permitted the generation of high titre LCMV stocks for the structural examination of the GPC spike and comparison to the PICV GPC spike. The study of the GPC spikes from both Old World and New World mammarenaviruses can potentially provide explanations for differences in arenavirus entry and highlight structural targets for the development of small molecule inhibitors.

Chapter 2

Materials and Methods

2.1 Materials

2.1.1 Vectors

The LCMV NP open reading frame (ORF) was supplied in pMK-RQ and it was sub-cloned into the pET28a(+)-His-SUMO expression vector for bacterial expression and protein purification.

The LCMV (strain: Armstrong; clone 13 derivative) S and L segment sequences (GenBank accession numbers: DQ361065 and DQ361066 for S and L respectively) were synthesised by GENEWIZ in the pUC57 vector. The NP and LP support plasmids were made by sub-cloning the NP and LP ORFs from pUC57-S and pUC57-L into a pUC57 vector.

2.1.2 Bacterial Cell Strains

The *Escherichia coli* (*E. coli*) DH5-α strain was used for plasmid amplification, unless otherwise specified. For bacterial expression of LCMV NP, a range of *E. coli* expression strains were used, as described in table 2.1. All *E. coli* strains were produced in house by Susan Matthews.

Name	**Manufacturer**	**Genotype**
BL21-**Gold**(DE3)pLysS	Agilent Technologies	*E. coli* B F- *ompT hsd*S(r_B-m_B-) *dcm*$^+$ Tet^R *gal* λ(DE3) *end*A Hte [pLysS Cam^R]
BL21-**Star**(DE3)pLysS	Invitrogen	*E. coli* F- *ompT hsd*SB(r_B-m_B-) *gal dcmrne*131 λ(DE3) [pLysS Cam^R]
BL21-**Rosetta**(DE3)pLysS	Millipore	*E. coli* F- *ompT hsd*SB(r_B-m_B-) Tet^R *gal dcm* λ(DE3) [pLysSRARE Cam^R]
BL21-**Rosetta 2**(DE3)pLysS	Millipore	*E. coli* F- *ompT hsd*SB(r_B-m_B-) Tet^R *gal dcm* λ(DE3) [pLysSRARE2 Cam^R]
BL21-**CodonPlus**(DE3)-RIPL	Agilent Technologies	*E. coli* B F- *ompT hsd*S(r_B-m_B-) *dcm* Tet^R *gal* λ(DE3) *end*A Hte [argU proL Cam^R] [argU ileY leuW Strep/$Spec^R$]
Lemo21(DE3)	New England Biolabs	*fhuA2* [*lon*] *ompT gal* λ(DE3) [*dcm*] Δ*hsdS*/pLemo(Cam^R)

Table 2.1: Table of Bacterial Expression Strains

2.1.3 Mammalian Cell Lines

The cell lines used in this work include Baby Hamster Kidney 21 (BHK) cells, BSR-T7 cells, SH-SY5Y cells, A549 cells, Vero cells, VeroE6 cells and SW13 cells. BHK-21 cells were isolated from kidney tissue of Syrian golden hamsters (*Mesocricetus auratus*) (Stoker and Macpherson, 1964). BSR-T7 cells were derived from the BHK-21 cell line and have been stably transformed to constitutively express T7 RNA polymerase (T7P; (Buchholz et al., 1999)). BSR-T7 cells were also additionally supplemented with G418 (1 mg/mL) every other passage to maintain the T7P plasmid. SH-SY5Y cells were sub-cloned from an original cell line called SK-N-SH, which was derived from the bone marrow of a four-year-old female with neuroblastoma (Biedler and Schachner, 1978). A549 cells are derived from human adenocarcinomic alveolar basal epithelial cells, which were cultured from a tumour from a 58-year-old male (Giard et al., 1973). Vero cells originated from epithelial cells isolated from the kidney tissue of the African Green Monkey (*Cercopithecus aethiops*). Vero-E6 cells were kindly provided by Professor Roger Hewson (Public Health England, UK) and originate from the Vero76 clone, which itself is a clone of the original Vero cell line (Ammerman et al., 2008). SW13 cells have been derived from human adrenocortical carcinoma (Leibovitz et al., 1973).

2.1.4 Virus Strains

Clone-13 (LCMV-Cl13), which derived from the parent Armstrong strain of LCMV (LCMV-ARM), was isolated from the spleen tissue of a mouse that was persistently infected with LCMV-ARM from birth (Ahmed et al., 1984) and was the strain chosen in the design of the LCMV rescue system described here. There are 15 nucleotide differences between the genomes of the LCMV-ARM and LCMV-Cl13 strains (6 in the S segment and 9 in the L segment) but only 2 of these result in coding changes. Typically, the LCMV-ARM strain is associated with acute infections and strong immune responses whereas the LCMV-Cl13 strain is associated with persistent infections and immunosuppression (Zapata and Salvato, 2013). This difference in persistence between LCMV-ARM and LCMV-Cl13 has been attributed to the two coding changes; F260L in the GPC and K1079Q in the LP (Grande-Pérez et al., 2016; Zapata and Salvato, 2013).

The P18 strain of Cali mammarenavirus (previously known as Pichindé virus; PICV) was used in these experiments, kindly provided by Professor Roger Hewson (Public Health England, UK).

2.1.5 Antibodies

The antibodies used for western blotting analysis (WB), immunofluorescence analysis (IF) and focus forming assays (FFA) have been detailed in table 2.2.

Antibody	**Species**	**Dilution (v/v)**	**Label**	**Company**
Anti-LCMV NP	Sheep	WB (1:1000) IF (1:500) FFA (1:1000)	N/A	Antibody Applications
Anti-HAZV NP	Sheep	WB (1:3000) IF (1:500)	N/A	Alta Bioscience
Anti-GAPDH	Mouse	WB (1:7500)	N/A	Cell Signalling Technologies
Anti-β-Actin	Rabbit	WB (1:5000)	N/A	abcam
Anti-6xHis Tag	Mouse	WB (1:1000)	N/A	ThermoFisher Scientific
Anti-GFP (B-2)	Mouse	WB (1:1000) IF (1:250)	N/A	Santa Cruz Biotechnology
Anti-Goat IgG	Donkey	WB (1:10000)	IRDye 800CW	LI-COR Biosciences
Anti-Mouse IgG	Donkey	WB (1:10000)	IRDye 680RD	LI-COR Biosciences
Anti-Rabbit IgG	Donkey	WB (1:10000)	IRDye 800CW	LI-COR Biosciences
Anti-Sheep IgG	Donkey	IF (1:1000)	Alexa Fluor 594	Cell Signalling Technologies
Anti-Mouse IgG	Chicken	IF (1:1000)	Alexa Fluor 488	Cell Signalling Technologies
Anti-Sheep IgG	Donkey	FFA (1:500)	Horseradish Peroxidase	Sigma-Aldrich

Table 2.2: Table of Antibodies

2.2 Molecular Biology

2.2.1 Polymerase Chain Reaction (PCR)

PCR was used for the amplification of the ORFs and to introduce flanking restriction enzyme sites to permit ligation with a complementary vector. The LCMV NP ORF, from plasmid pMK-RQ and the pUC57-S plasmid, the LCMV L polymerase ORF, the eGFP-P2A ORF and the pUC57 plasmid were all amplified by PCR. The oligonucleotide primers that were used in the reaction have been described in table 2.3.

Primer Name	**Primer Sequence (5' - 3')**
LCMV NP Forward	ACCAAGGATCCATGTCCTTGTCTAAGGAAGTTAAGAGCTTCCAATGG
LCMV NP Reverse	TATAATCTCGAGTCAGGGAGGCCCAGAGG
NP ORF Forward	CAGAAGCTAGCAAGATCCTAGGCATTTGATTG
NP ORF Reverse	GAAGTCTCGAGTAGTCTTAGAGTGTCACAACATTTG
LP ORF Forward	CAGAAGCTAGCAACTAGGCTTTTTGATGCGC
LP ORF Reverse	GAAGTCTCGAGTACATCAGTCGATGTCCTCGG
pUC57 Promoter	AGGTGCGCTAGCACCTATAGTGAGTCGTATTAGAATTCACTGGCCG
pUC57 Terminator	ATTCCTCGAGAACTAGCATAACCCCTTGGGGCCTCTA
S-Segment Forward	CATACATAGCTTGTAGAACATCGATTG
S-Segment Reverse	GGAAAAGACGCTGAAGAACAGCGCCTC
eGFP Forward	CTCACCATGGATGGTGAGCAAG
eGFP Reverse	GATCGCGGCCGCGGTCCAGG
Insert eGFP Forward	CGGCCGCATGTCCTTGTCTAAG
Insert eGFP Reverse	CCCATGGCTTGTTGCTCAATGG
*Xho*I Forward	CAGGGAAGCCTCGAGGGAGTATGAAG
*Xho*I Reverse	GTCATTTCAACATCGATAAGCTTAATG

Table 2.3: Table of Oligonucleotide Primers

PCR was performed in a volume of 50 µL and contained; 50 ng template DNA, 10 mM dNTPs, 10 µM forward primer, 10 µM reverse primer, 1X Q5 Reaction Buffer and 1 U Q5 High Fidelity DNA Polymerase (Q5 High Fidelity Kit; New England Biolabs). PCR cycling was performed in a thermocycler (ProFlex^{TM}) using the following conditions; 98 ℃ for 30 seconds, then 25 cycles of; 98 ℃ for 10 seconds, an annealing temperature for 30 seconds, then 72 ℃ for 30 seconds/kb, followed by a final extension step at 72 ℃ for 2 minutes. The optimal annealing temperature for the primers was determined by using a temperature gradient, ranging from 50 ℃ to 70 ℃.

Insertions, substitutions and deletions were also carried out using PCR and the primers were designed according to the manufacturer's instructions (Q5 Site-Directed Mutagenesis Kit, New England Biolabs). Here, PCR was performed in a total volume of 25 µL, using a mastermix which contains the Q5 Reaction Buffer, the Q5 Hot Start High-Fidelity DNA Polymerase, 10 mM dNTPs and 2 mM (final concentration) Mg^{2+} to which the following was added; 10 µM forward primer, 10 µM reverse primer and 25 ng template DNA. The PCR cycling conditions were the same as above. Following PCR amplification, 1 µL of the PCR mix was treated with kinase, *Dpn*I and ligase, for 5 minutes, to re-circularise the mutated vector, which was then transformed into *E. coli* DH5-α.

2.2.2 Restriction Digest

Restriction digests were performed either to generate sticky ends for ligating PCR products into new vectors or as a diagnostic digest. 1 µg of the DNA sample was mixed with 1 U of each restriction enzyme and the appropriate enzyme buffers. This reaction was incubated for a minimum of 1 hour at 37 ℃. The enzymes were then either heat-inactivated (according to the manufacturer's instructions) or removed using the Monarch DNA Gel Extraction Kit or the Monarch PCR and DNA Cleanup Kit.

2.2.3 Agarose Gel Electrophoresis

In order to examine diagnostic restriction digests or to purify DNA samples through gel extraction, DNA samples were separated by agarose gel electrophoresis. The DNA samples were mixed with 1X gel loading dye (New England Biolabs) and were loaded on to a 1 % agarose gel (made in 1X TAE buffer [40 mM Tris-acetate, 1 mM EDTA; TAE] and stained with SYBR^{TM} Safe DNA Stain [Thermo Fisher Scientific, diluted 10,000-fold]). Hyperladder I (Bioline) was loaded alongside the DNA samples as a molecular marker. The agarose gel was run at 100 V for 1 hour in 1X TAE buffer. DNA was visualised using blue light trans-illumination.

2.2.4 Ligation

When the amplified PCR product needed to be ligated with a vector, the amplified cDNA was first treated with 10 U of *Dpn*I enzyme, incubated in CutSmart buffer for 1 hour at 37 ℃. *Dpn*I cleaved any methylated template DNA which was present in the reaction, in order to prevent the original template DNA being transformed into bacteria instead of the ligated product.

After the restriction enzyme digest, *Dpn*I treatment and DNA clean up, the vector and the PCR insert were mixed at a 1:5 ratio. On ice, T4 DNA ligase buffer (New England Biolabs) and 20 U T4 DNA ligase (New England Biolabs) were added and gently mixed. The reaction was incubated at room temperature for 10 minutes then heat-inactivated at 65 ℃.

2.2.5 Transformation

E. coli DH5-α were used for the amplification of plasmid DNA. 50 µL of bacterial cells was mixed with 50 ng DNA and incubated on ice for 30 minutes. The cells were heat-shocked at 42 ℃ for 45 seconds, before incubating on ice for a further 5 minutes. 950 µL (LB) media was added to the cells, which were incubated for 1 hour at 37 ℃, with shaking. 100 µL of this was plated on to an LB agar plate containing the appropriate antibiotic (100 µg/mL ampicillin or 50 µg/mL kanamycin) and was incubated at 37℃ overnight.

2.2.6 DNA Amplification

A single bacterial colony was used to inoculate 50 mL (small-scale), 100 mL (large-scale; high copy number plasmid) or 200 mL (large-scale; low copy number plasmid) LB media, which had appropriate antibiotic selection. This was incubated overnight at 37 ℃, with shaking. The bacterial cells were pelleted by centrifugation at 4000 *x g* at 4 ℃ for 30 minutes. Plasmid DNA was extracted using QIAprep Spin Miniprep Kit (QIAGEN) or QIAGEN Plasmid Midi or Maxi Kits (QIAGEN), following the manufacturer's instructions. DNA concentration and purity was determined by spectrophotometry using a NanoDrop 1000 (Thermo Scientific) and was confirmed as correct through Sanger sequencing, performed by GENEWIZ.

2.3 Protein Expression and Purification

2.3.1 IPTG Induction

The pET28a(+)-His-SUMO-LCMV NP expression vector was transformed into BL21-DE3 *E. coli* variants (table 2.1), using the method described in section 2.2.5. Single colonies were used to inoculate 10 mL LB media, with selection antibiotic kanamycin added, and this was incubated overnight at 37 ℃, with shaking. The overnight culture was then used to inoculate 1 L 2YT media (0.5 % NaCl, 1.6 % tryptone, 1 % yeast extract), which was incubated at 37 ℃ with shaking at 180 RPM until the optical density, measured at a wavelength of 600 nm (OD_{600}) reached 0.6-0.8. A sample of the uninduced sample was taken and then 500 mM isopropyl β-D-1-thiogalactopyranoside (IPTG) was added to the media to induce T7P expression of LCMV NP. The induced culture was incubated at 37 ℃, with shaking. After incubation for 24 hours, the culture was harvested and centrifuged at 4000 *x g* for 30 minutes at 4 ℃. The pellet was resuspended in lysis buffer (500 mM NaCl, 20 mM Tris-HCl [pH 6.8], 20 mM $MgCl_2$, 20 mM imidazole, 1 % Triton-X-100, 0.5 % NP40, 0.5 % Tween-20, 10 % glycerol, 0.1 mM phenylmethylsulfonyl fluoride (PMSF), 0.1 mM Tris(2-carboxyethyl)phosphine hydrochloride (TCEP-HCl), 0.1 % [w/v] lysozyme from chicken egg white (Sigma-Aldrich), 1 U/mL DNase, 1 U/mL RNase) and incubated on ice for 30 minutes. The resuspension was then sonicated using a Soniprep 150 to complete cell lysis. Sonication was performed on ice using 10 microns amplitude for 10 seconds, with 50 seconds in between cycles, for a total of 30 cycles. A whole cell lysate sample was taken and the remainder was centrifuged at 40,000 *x g* for 30 minutes. The supernatant was taken into a new tube and contained the soluble fraction of the bacterial cells. The pellet was resuspended in resuspension buffer (400 mM NaCl, 20 mM Tris-HCl [pH 6.8]) and contained the insoluble portion of the bacterial cells. All samples were then prepared for SDS-PAGE analysis, which has been described in section 2.4.1.

Lemo21(DE3) cells (New England Biolabs) were also transformed with the pET28a(+)-His-SUMO-LCMV NP expression vector, in an attempt to improve solubility. Single colonies were picked to inoculate 10 mL LB media, with selection antibiotics kanamycin and chloramphenicol added, and this was incubated overnight

at 37 ℃, with shaking. 1 mL of the overnight culture was then used to inoculate 100 mL 2YT media, which was incubated at 37 ℃ with shaking at 180 RPM, until OD_{600} reached 0.6-0.8. At this point, an uninduced sample was taken and the culture was divided into 10 mL, where 500 mM IPTG and L-rhamnose (Sigma Aldrich), concentration ranging from 0 µM - 2000 µM, were added. The samples were incubated at 37 ℃, with shaking, for 24 hours and the soluble and insoluble fractions were harvested in the same manner as above.

2.3.2 Autoinduction

The pET28a(+)-His-SUMO-LCMV NP expression vector was transformed into Rosetta strain and expression was induced by autoinduction, the method of which was previously described by (Studier, 2005). Briefly, 10 mL of an overnight culture was added to 1 L autoinduction media (42 mM Na_2HPO_4, 22 mM KH_2PO_4, 2 % tryptone, 0.5 % NaCl and 0.5 % yeast extract) supplemented with 0.22 µm filter-sterilised 60 % glycerol (final concentration; 0.6 %), 10 % glucose (final concentration; 0.05 %), 8 % lactose (final concentration; 0.2 %) and kanamycin and was incubated for 60 hours at 18 ℃ with shaking at 150 RPM. Samples were harvested as described in section 2.3.1.

2.3.3 Immobilised Metal Affinity Chromatography

Before applying the soluble fraction to the nickel (Ni^{2+}) resin, it was filtered through a 0.45 µM filter and the resin was equilibrated with binding buffer (500 mM NaCl, 20 mM Tris-HCl; pH 7 and 20 mM imidazole). It was then applied to 5 mL HisTrap™ High Performance (GE Healthcare) Ni^{2+} resin column at 4 ℃ and the flowthrough was collected. The Ni^{2+} resin was washed with increasing concentrations of imidazole (ranging from 20 mM to 100 mM), in 500 mM NaCl and 20 mM Tris-HCl; pH 7 buffer, before elution at 500 mM imidazole. The Ni^{2+} resin was then washed in 1 M imidazole (500 mM NaCl and 20 mM Tris-HCl; pH 7) to remove any bound proteins, before final water washes and storage in 20 % ethanol. The imidazole concentration was reduced by overnight dialysis in 500 mM NaCl and 20 mM Tris-HCl; pH 7, and the 6xHis-SUMO tag was removed using 1 U/mL ULP1.

For further purification, the dialysed/cleaved elution was once again applied to a

clean 5 mL HisTrap^{TM} High Performance (GE Healthcare) column and the flow through was collected, which contained untagged LCMV NP. The Ni^{2+} resin was then washed with a 20 mM imidazole (500 mM NaCl and 20 mM Tris-HCl; pH 7) buffer and in 1 M imidazole (500 mM NaCl and 20 mM Tris-HCl; pH 7) to remove other bound proteins. Samples were collected throughout and were prepared for SDS-PAGE analysis, as described in section 2.4.1.

2.3.4 Ion-Exchange Chromatography

Ion-exchange chromatography (IEC) was performed on SP sepharose resin (GE Healthcare), which was loaded into a glass column and washed with 5 M NaOH and ddH_2O. The resin was equilibrated by 3 cycles of alternate washes (5 column volumes) of low salt buffer (50 mM NaCl, 20 mM Tris; pH 7) and high salt buffer (1 M NaCl, 20 mM Tris; pH 7), before a final wash with 10 column volumes low salt buffer. The flowthrough collected from the HisTrap HP column, containing LCMV NP, was diluted, in low salt buffer, to reduce the NaCl concentration from 500 mM to 50 mM. The diluted LCMV NP was then passed over the SP sepharose resin by gravity flow. The resin was subsequently washed with increasing concentrations of salt (50 mM-1 M) and constant 20 mM Tris, at pH 7. Samples were collected throughout and were prepared for SDS-PAGE analysis, as described in section 2.4.1.

The IEC fractions containing the highest concentration of LCMV NP were pooled and concentrated to 0.5 mg/mL, using a 10 kDa molecular weight cut-off concentrator (Amicon). This was then analysed by SDS-PAGE (described in 2.4.1) and Coomassie staining (described in section 2.4.2). Purity (>85 %) was confirmed by densitometry using ImageJ software.

2.3.5 Size-Exclusion Chromatography

Size-exclusion chromatography (SEC) was performed on a HiLoad 26/600 Superdex prep grade column (GE Healthcare), which had previously been equilibrated with filtered and degassed equilibration buffer (500 mM NaCl and 20 mM Tris-HCl; pH 7). The flowthrough collected from the HisTrap HP column, containing LCMV NP, was concentrated to 5 mL using a 10 kDa molecular weight cut-off concentrator (Amicon). This was injected onto the column using an ÄKTA prime and a flow rate

of 0.5 mL/min. After the void volume (120 mL), 3 mL fractions were collected and the absorbance at 280 nM (mAU) was measured. Fractions containing the highest concentration of LCMV NP were pooled, concentrated to 1 mg/mL and analysed by SDS-PAGE analysis (as described in 2.4.1).

2.3.6 Generation of the LCMV NP antisera

α-LCMV NP antibody was generated by immunising a sheep with 4x 200 mg inoculations of purified LCMV NP (Antibody Applications). Serum was collected pre-inoculation and post-1, -2, -3 inoculations and verified as reactive to the original sample through enzyme-linked immunosorbent assays (ELISA) analysis. α-LCMV NP serum was clarified by centrifugation at 4000 x g for 20 minutes at 4 ℃ to remove debris, aliquoted to avoid repeated freeze-thaw cycles and stored at -20 ℃. Subsequent western blotting and immunofluorescence assays were performed using clarified serum collected from the post-3 inoculation.

2.4 Protein Analysis Techniques

2.4.1 SDS Polyacrylamide Gel Electrophoresis

Proteins were resolved by sodium dodecyl-sulphate polyacrylamide gel electrophoresis (SDS-PAGE). Samples were prepared with 4X lithium dodecyl sulphate (LDS; made in house) and 10X dithiothreitol (DTT) (both final concentration at 1X) and denatured by heating at 95 ℃ for 5 minutes. The samples were loaded onto 12 % SDS PAGE resolving gels, which were overlaid with 5 % stacking gels. The gels were run at 180 V for 1 hour, or until the loading dye front has run off the gel, in 1X SDS-PAGE running buffer (25 mM Tris, 192 mM glycine, 0.1 % [w/v] SDS).

2.4.2 Coomassie Staining and Silver Staining

The proteins resolved by the SDS-PAGE gels were fixed using a fixative solution (40 % [v/v] ethanol, 10 % [v/v] acetic acid). This was incubated at room temperature

for 1 hour and the gel was then washed using water and stained using the Colloidal Coomassie G-250 stain (2 % [v/v] phosphoric acid, 10 % [w/v] ammonium sulphate, 0.1 % [w/v] Coomassie Brilliant Blue G-250 dye). The gel was stained overnight at room temperature. Resolution was improved by destaining the gel overnight in 1 % acetic acid.

To improve sensitivity of the protein staining, silver staining was performed instead using the ProteoSilver^{TM} Kit (Sigma-Aldrich). The gel was stained following the manufacturer's protocol.

2.4.3 Western Blotting

In order to detect specific proteins using antibodies, proteins resolved by SDS-PAGE were transferred to a polyvinylidene fluoride (PVDF) membrane. The membrane was first activated in 100 % methanol and then washed in TOWBIN (22 mM Tris, 192 mM glycine, 20 % methanol). The SDS-PAGE gel was also washed in TOWBIN and the filter papers were soaked in TOWBIN before assembly. The transfer was performed at 15 V for 1 hour, using the Trans-Blot semi-dry cell (Bio-Rad). After transfer, the membrane was briefly rinsed in 1X PBS-T (1X PBS supplemented with 0.1 % tween-20) before being incubated in Odyssey blocking buffer (PBS) (Licor; diluted 1 : 1 with 1X PBS), for 1 hour rocking. Subsequently, the blocking buffer was removed and the membrane was stained with the primary antibodies (made in 1:4 [blocking buffer:PBS-T]; for antibody concentrations, see table 2.2) for 1 hour rocking. The membrane was washed three times (5 minutes each) in 1X PBS-T, and then rocked for 1 hour with secondary antibody (made in 1:4 [blocking buffer:PBS-T]; for antibody concentrations, see table 2.2). The secondary antibody is reactive to the species of the primary antibody and is conjugated to fluorescent dyes, either IRDye 680RD or IRDye 800CW. The membrane was washed three times (5 minutes each) in 1X PBS-T before a final wash in 1X PBS (5 minutes) and then a rinse in UltraPure Distilled Water (Thermo Fisher Scientific). The membrane was dried and visualised on the Licor Odyssey Sa Infrared imaging system.

2.5 Cell Culture

2.5.1 Continuous Cell Culture

All cell lines were incubated in a humidified environment, at 37 ℃ with 5 % CO_2. The cell lines were maintained in high-glucose Dulbecco's modified Eagle medium (DMEM; Sigma-Aldrich), supplemented with 10 % heat-inactivated foetal bovine serum (FBS), 100 µg of streptomycin/mL and 100 U of penicillin/mL (complete media). The absence of mycoplasma contamination was confirmed using MycoAlert^{TM} (Lonza).

Cells were routinely passaged when confluence was reached. Media was washed from the cells using 1X PBS. The cells were detached from the flask by adding 1X Trypsin-EDTA solution (Sigma-Aldrich) and incubating at 37 ℃ for 3-5 minutes.

2.5.2 Freezing and Thawing Cells

All cell lines were stored in liquid nitrogen. In order to freeze cells, the cells were washed with 1X PBS and trypsinised as in section 2.5.1. The cell suspension was then centrifuged at 500 x g for 5 minutes. The cell pellet was resuspended in a solution containing 40 % FBS, 10 % dimethyl sulfoxide (DMSO) and 50 % DMEM. The resuspension was then aliquoted into cryo-vials and frozen at a controlled rate (approximately -1 ℃/min) using a Corning CoolCell alcohol-free freezing container. The frozen cells were then transferred to liquid nitrogen.

Frozen cells would be thawed rapidly at 37 ℃. The defrosted cell suspension would then be centrifuged at 500 x g for 5 minutes. The pellet would be resuspended in complete media and transferred to a T-25 flask and incubated overnight. When confluency was reached, the cells would be transferred to a T-75 flask and then eventually to a T-175 flask.

2.5.3 Mammalian Cell Lysis

Cell lysates were collected by removing the complete media, washing the cells once in 1X PBS and then adding 1X radioimmunoprecipitation assay (RIPA) buffer (50 mM

Tris-HCl pH 7.5, 150 mM NaCl, 1 % (v/v) NP40 alternative, 0.5 % (w/v) sodium deoxycholate and 0.1 % sodium dodecyl sulphate (SDS; w/v)), supplemented with 1X cOmplete^{TM}, Mini, EDTA-free Protease I inhibitor cocktail (Sigma-Aldrich). This was incubated on ice for 20 minutes before collecting and transferring the cell lysate to a 1.5 mL eppendorf. The lysate was centrifuged at 13,000 *x g* for 10 minutes and the supernatant was stored at -20 ℃.

2.6 Virological Techniques for LCMV

2.6.1 LCMV Infection and Propagation

In order to infect cells with LCMV, the cells were seeded the previous day to a density which would provide 60-70 % confluency. The cells were washed with 1X PBS and after PBS removal, LCMV clarified supernatant was added in serum-free DMEM (SFM) at a specified multiplicity of infection (MOI). The cells were incubated at 37 ℃, with regular manual rocking, for one hour, to allow LCMV to adsorb to the cells. The LCMV clarified supernatant was then removed and replaced with DMEM containing 2 % FBS and incubated for the necessary time before harvesting the supernatant or the cell lysate. Mock infections were carried out in the same manner, but using SFM only instead of LCMV clarified supernatant.

In order to propagate LCMV, T175 flasks were seeded with 5 x 10^6 BHK-21 cells. The following day, the cells were washed with 1X PBS and infected with LCMV at an MOI of 0.001. After 1 hour incubation, the media was replaced with 15 mL DMEM containing 2 % FBS and incubated for 72 hours. At this point, the supernatant was collected and clarified by centrifugation at 4000 *x g* for 15 minutes at 4 ℃. The clarified supernatant was aliquoted into cryo-vials and stored at -80 ℃.

2.6.2 LCMV Purification for Electron Microscopy

12x vented T175 cm^2 flasks were seeded with 5x10^6 BHK-21 cells at least 24 hours before infection. When the BHK-21 cells were approximately 80-90 % confluent, the cells were washed twice with 1x PBS and then LCMV, at a MOI of 0.001, was allowed to adsorb for 1 hour in serum free media at 37 ℃. LCMV was removed after

the adsorption time and replaced with 15 mL complete media. The infection was allowed to proceed for approximately 65 hours and was regularly rocked to move the media around. The supernatant was collected and centrifuged for 30 minutes at 4000 *x g* at 4 ℃. The supernatant was then filtered through a 0.45 µm filter and centrifuged again for 30 minutes at 4000 *x g* at 4 ℃. The supernatant was then transferred to ultra-centrifuge tubes and 8 mL 20 % sucrose (supplemented with 1X cOmplete^{TM}, Mini, EDTA-free Protease I inhibitor cocktail (Sigma-Aldrich)) was underlayed. The tubes were balanced and then centrifuged for 3 hours at 90,000 *x g* at 4 ℃. The sucrose cushion and supernatant were removed after centrifugation and the pellet was air-dried for 5 minutes, upside down on tissue. 15 µL resuspension buffer (0.1X PBS + 0.1 mM $MgCl_2$ + 0.1 mM $CaCl_2$ + 1X cOmplete^{TM}, Mini, EDTA-free Protease I inhibitor cocktail (Sigma-Aldrich)) was added to the virus pellet and the ultra-centrifuge tubes were covered with two layers of parafilm, before incubating on a rocker overnight at 4 ℃. The resuspended pellet was collected the following morning and aliquots were flash-frozen using liquid nitrogen and then stored at -80 ℃. Samples were taken for western blotting analysis (section 2.4.3), plaque assay (section 2.6.4) and negative-stain EM (section 2.10.1). For preparation of cryo-EM grids (section 2.10.2), aliquots were removed from -80 ℃ storage and defrosted on ice.

2.6.3 Titre Determination by Crystal Violet Plaque Assay

Crystal violet plaque assays were attempted to determine the titre of the LCMV stocks. The crystal violet plaque assay protocol was adapted from (Ziegler et al., 2016). VeroE6 cells were seeded in six-well plates at 1 x 10^5 and the following day were infected with serially diluted LCMV (10-fold). LCMV was allowed to adsorb to the cells for 90 minutes at 37 ℃ and then the cells were overlaid with 1.4 % agarose, mixed at a 1 : 1 ratio with complete media (final agarose concentration was 0.7 %). The cells were incubated for 4 days, at which point they were fixed with 2.5 % formaldehyde diluted in 3X PBS. The agarose was removed and the cells were stained with 0.1 % crystal violet in 2.1 % ethanol.

2.6.4 Titre Determination by Focus Forming Assay

The titre of LCMV stocks was successfully determined using focus forming assays. Six-well plates were seeded with 5 x 10^5 BHK-21 cells and incubated overnight. The following day, the cells were infected with serial dilutions of LCMV (10-fold) and incubated for 1 hour, allowing LCMV to adsorb to the cells. The dilutions were removed from the cells, which were then overlaid with methylcellulose (1.6 % mixed 1 : 1 with complete media; final concentration of methylcellulose 0.8 %) and incubated for 3 days. After incubation, the overlay was removed and the cells were washed with 1X PBS. 4 % formaldehyde (made in 1X PBS) was added and the cells were fixed for 15 minutes. The 4 % formaldehyde was removed and the cells were washed twice with 1X PBS. The cells were then permeabilised by adding 0.5 % Triton-X-100 (made in 1X PBS) and incubating for 15 minutes at room temperature, with rocking. The cells were then washed twice with 1X PBS and blocked using 0.5 % FBS (made in 1X PBS) which was incubated for 1 hour at room temperature, with rocking. The blocking buffer was removed and the cells were washed twice with 1X PBS. The cells were then stained with anti-LCMV NP (for dilution, see table 2.2), made in 0.5 % FBS containing 0.1 % tween-20. After 2 hours incubation, the antibody solution was removed and the cells were washed three times in 1X PBS. The cells were then stained for 1 hour at room temperature with an anti-sheep secondary antibody (for dilution, see table 2.2), which was either conjugated to a fluorophore (568 nm) or to horseradish peroxidase (HRP).

For the fluorophore-conjugated secondary antibody staining, the cells were washed five times with 1X PBS and left in the final wash. The entire well was then imaged at 4X magnification using the EVOS FL 2 automated microscope. Foci were counted as individual regions of more than one cell that were fluorescing brighter than the background.

For the HRP-conjugated secondary antibody staining, the cells were washed five times with 1X PBS. 4-Chloro-1-naphthol (4C1N; Sigma) was made previously, by dissolving 1 tablet in 10 mL 100 % methanol, which was then stored at -20 ℃. On the day, 4C1N was diluted 1 : 10 in 1X PBS and 30 µL hydrogen peroxide was added to 10 mL. 200-500 µL was then added to the cells, which were incubated for 15 minutes or until purple foci had appeared. The wells were imaged and the foci

were counted. Titre was calculated using the following equation:

$$Virus\ titre\ (ffu/mL) = \frac{average\ number\ of\ foci}{dilution\ factor\ *\ volume\ (mL)}$$

2.7 Virological Techniques for PICV

2.7.1 PICV Infection and Propagation

In order to infect cells with PICV, the cells were seeded the previous day to a density which would provide 60-70 % confluency. The cells were washed with 1X PBS and after PBS removal, PICV clarified supernatant was added in serum-free DMEM (SFM) at a specified multiplicity of infection (MOI). The cells were incubated at 37 ℃, with regular manual rocking, for one hour, to allow PICV to adsorb to the cells. The PICV clarified supernatant was then removed and replaced with DMEM containing 2 % FBS incubated for the necessary time before harvesting the supernatant or the cell lysate. Mock infections were carried out in the same manner, but using SFM only instead of PICV clarified supernatant.

In order to propagate PICV, T175 flasks were seeded with 5 x 10^6 BHK-21 cells. The following day, the cells were washed with 1X PBS and infected with PICV at an MOI of 0.001. After 1 hour incubation, the media was replaced with 15 mL DMEM containing 2 % FBS and incubated for 72 hours. At this point, the supernatant was collected and clarified by centrifugation at 4000 *x g* for 15 minutes at 4 ℃. The clarified supernatant was aliquoted into cryo-vials and stored at -80 ℃.

2.7.2 PICV Purification for Electron Microscopy

12x vented T175 cm^2 flasks were seeded with 1x10^7 BHK-21 cells at least 24 hours before infection. When the BHK-21 cells were approximately 80-90 % confluent, the cells were washed twice with 1x PBS and then PICV, at a MOI of 0.001, was allowed to adsorb for 1 hour in serum free media (rocking at 37 ℃). PICV was removed after the adsorption time and replaced with 15 mL DMEM containing 2 % FBS and 0.01 % DEAE. The infection was allowed to proceed for 72 hours and was regularly rocked to move the media around. The supernatant was collected and

centrifuged for 30 minutes at 4000 *x g* at 4 ℃. The supernatant was then filtered through a 0.45 µm filter and centrifuged again for 30 minutes at 4000 *x g* at 4 ℃. The supernatant was then transferred to ultra-centrifuge tubes and 8 mL 30 % sucrose (supplemented with 1X cOmplete™, Mini, EDTA-free Protease I inhibitor cocktail (Sigma-Aldrich)) was underlayed. The tubes were balanced and then centrifuged for 3 hours at 150,000 *x g* and at 4 ℃. The sucrose cushion and supernatant were removed after centrifugation and the pellet was air-dried for 5 minutes, upside down on tissue. 15 µL resuspension buffer (0.2X PBS + 0.1 mM $MgCl_2$ + 0.1 mM $CaCl_2$1X cOmplete™, Mini, EDTA-free Protease I inhibitor cocktail (Sigma-Aldrich)) was added to the virus pellet and the ultra-centrifuge tubes were covered with two layers of parafilm, before incubating on a rocker overnight at 4 ℃. The resuspended pellet was collected the following morning and samples were taken for western blotting analysis (section 2.4.3), plaque assay (section 2.7.3) and negative-stain EM (section 2.10.1). The remainder of the resuspended pellet was immediately taken to make cryo-EM grids (section 2.10.2).

2.7.3 Titre Determination by Crystal Violet Plaque Assay

In order to titre PICV stocks, vero cells were seeded in 12-well plates at 2 x 10^5 and the following day were infected with serially diluted PICV (10-fold). PICV was allowed to adsorb to the cells for 1 hour at 37 ℃ and then the cells were overlaid with 2.4 % agarose, mixed at a 1 : 1 ratio with complete media (final agarose concentration was 1.2 %). The cells were then incubated for 6 days, at which point they were fixed with 4 % formaldehyde, which was added directly to the overlay. The overlay was removed, the cells were washed twice with 1X PBS and then stained with 2.5 % crystal violet in 20 % ethanol. The stain was incubated for 15 minutes, after which it was removed and the cells were washed with water, dried and imaged. The plaques were counted and titre was calculated using the following equation:

$$Virus\ titre\ (pfu/mL) = \frac{average\ number\ of\ plaques}{dilution\ factor\ *\ volume\ (mL)}$$

2.8 Reverse Genetics

2.8.1 Design of Plasmids

Plasmids pUC57-S and pUC57-L were synthesised by GENEWIZ, as described in section 2.1.1. The plasmids were designed according to previous papers (Sánchez and de la Torre, 2006; Flatz et al., 2006). The segments were flanked by the T7 RNA polymerase (T7P) promoter sequence at the 5' end of the segment and the T7P terminator sequence at the 3' end. This permitted permits the intracellular synthesis of cRNA species from the plasmids by T7P. The T7P promoter was truncated, leaving a single G residue at the 3' end of the promoter sequence, which permits the generation of S and L RNA species (vRNA and cRNA) containing the characteristic non-templated G residue at the 5' end. Immediately upstream of the T7P terminator is the hepatitis delta virus (HDV) ribozyme sequence. This sequence self-cleaves to generate the hairpin sequence found at 3'-termini of arenavirus RNA species. An extra C residue was added to the 3' end of the ribozyme sequence to improve self-processing (Perrotta and Been, 1991; Sánchez and de la Torre, 2006).

Plasmids pUC57-NP and pUC57-LP were synthesised using PCR to sub-clone the NP ORF and the LP ORF into the pUC57 vector using complementary flanking restriction sites. The primers used in the PCR have been described in table 2.3 (NP ORF Forward; NP ORF Reverse; LP ORF Forward; LP ORF Reverse; pUC57 Promoter; pUC57 Terminator). These fragments were then digested with the restriction enzymes (section 2.2.2) and ligated (section 2.2.4) with one another (NP ORF with the pUC57 vector and LP ORF with the pUC57 vector). The ligation mix was transformed into DH5-α bacterial cells (section 2.2.5) and successful ligation colonies were picked for plasmid amplification (section 2.2.6).

2.8.2 Transfection

BSR-T7 cells were seeded in 6-well plates (CytoOne) at a seeding density of $2x10^5$ cells/well. The following day, 1.6 µg of pUC57-S, 1.6 µg of pUC57-NP, 2.8 µg pUC57-L, 2 µg of pUC57-LP and 0.6 µg of a pUC57-T7 was added to 200 µL OptiMEM media, followed by 2.5 µl/µg TransIT-LT1 transfection reagent (Mirus)

and this was incubated for 30 minutes at room temperature. This was then diluted in 800 µl OptiMEM and added to cells. At 19 hour post transfection (hpt), the media was removed and replaced with 1 mL of DMEM supplemented with 2 % FBS. At 120 hpt, the supernatant was removed and clarified by centrifugation at 4000 x g for 5 min. The clarified supernatant was used to infect BHK-21 cells, seeded the previous day at $2x10^5$ cells/well in 6-well plates (CytoOne). All infections were carried out as described in section 2.6.1.

2.8.3 Incorporation of a Silent Mutation

In order to confirm that LCMV was being recovered from the transfection of the rLCMV-WT rescue system plasmids, a single nucleotide mutation was introduced into plasmid pUC57-S using PCR. The primers used in the PCR have been described in table 2.3 (*Xho*I Forward; *Xho*I Reverse). This mutation created a new *Xho*I restriction site in the S segment, allowing the identification of the mutated S segment in rLCMV-XhoI. The transfection was carried out as described in section 2.8.2, replacing pUC57-S with pUC57-S-XhoI. The supernatant was harvested from the BHK-21 cells at 96 hpi and was used to infect a fresh set of BHK-21 cells, which had been seeded the previous day. The supernatant from this infection was then harvested at 96 hpi and RNA was extracted from the supernatant using the QIAamp Viral RNA Mini Kit (QIAGEN), following the manufacturer's protocol. The extracted RNA was then converted to DNA and amplified by PCR, using the OneTaq One-Step reverse-transcription PCR (RT-PCR) Kit (New England Biolabs), following the manufacturer's protocol. S segment-specific primers were used and have been described in table 2.3 (S-Segment Forward; S-Segment Reverse). The amplified DNA was then digested with *Xho*I (NEB), as described in section 2.2.2 before being analysed by agarose gel electrophoresis (section 2.2.3).

2.8.4 Incorporation of Enhanced Green Fluorescent Protein

In order to generate rLCMV-eGFP, an eGFP-P2A ORF (GenBank accession number: QFU20120.1) was ordered from GENEWIZ and sub-cloned from the plasmid, using primers "eGFP Forward" and "eGFP Reverse" to introduce flanking

restriction sites. These restriction sites were also introduced into the plasmid pUC57-S (rLCMV-WT), using primers "Insert eGFP Forward" and "Insert eGFP Reverse". The restriction sites were inserted in between the start codon of the NP ORF and the 3' end of the untranslated region (UTR) of the S segment. The primers used in both reactions have been described in table 2.3. The eGFP ORF was separated from the NP ORF by the porcine teschovirus 1 (PTV-1) 2A self-cleaving peptide sequence (ATNFSLLKQAGDVEENPGP) (GenBank accession number: MH358390). Transfection of the rLCMV rescue system plasmids was carried out as described in section 2.8.2, replacing plasmid pUC57-S with plasmid pUC57-S-eGFP. eGFP fluorescence in both transfected and infected cells was examined by the EVOS FL 2 automated microscope (Thermo Scientific Invitrogen).

2.9 Confocal Microscopy Techniques

2.9.1 Fixing and Staining Cells

Glass coverslips were washed in 100 % ethanol and allowed to dry. The coverslips were then placed into a 6-well plate (CytoOne) and washed once with 1X PBS prior to cell seeding. The cells were left to adhere to the coverslips for a minimum of 18 hours before infection. Infection was allowed to proceed for 24 hours before the cells were washed once in 1X PBS and then fixed using 4 % formaldehyde for a minimum of 15 minutes at room temperature (all subsequent steps were performed at room temperature). The 4 % formaldehyde was then removed and the fixed cells were washed three times in 1X PBS. The 1X PBS was removed and the cells were permeabilised by adding 0.5 % Triton-X-100 (made in 1X PBS) and incubating for 10 minutes, rocking. The permeabilisation buffer was then removed and the cells were washed three times in 1X PBS before blocking using 2 % FBS (made in 1X PBS) for 15 minutes, with rocking. The blocking buffer was removed and the cells were then stained with primary antibodies (made in 2 % FBS; for concentrations, see table 2.2) for 2 hours, with rocking. The cells were then washed three times with 1X PBS before staining with secondary antibodies, conjugated to Alexa Fluor fluorophores (made in 2 % FBS; for more detail, see table 2.2), for 1 hour rocking in the dark. The cells were then washed five times in 1X PBS, before a final wash in

ddH_2O. The coverslips were then dabbed onto tissue to remove excess fluid before being mounted onto microscope slides using ProLong Gold Antifade Mountant with DAPI (ThermoFisher Scientific). The coverslips were then sealed with nail varnish and mounting media was allowed to cure overnight in the dark.

2.9.2 Confocal Microscopes

Images were acquired using either the Zeiss LSM700 Inverted Microscope or the Zeiss upright LSM880 Microscope. All the images required multicolour imaging and in order to do this, individual fluorescent signals were acquired sequentially. Image contrast and fluorescent signal were adjusted using Fiji software.

2.10 Electron Microscopy Techniques

2.10.1 Negative Stain Electron Microscopy

Purification of LCMV (section 2.6.2) and PICV (section 2.7.2) was deemed suitable for cryo-EM after examination using negative-stain EM. Immediately prior to sample application, carbon-coated electron microscopy grids were rendered hydrophilic by glow discharge for 45 s using a PELCO easyGlow glow discharge system. 3 µL of the sample, which was diluted 1:10, was then put onto the charged grids and incubated at room temperature for 1 minute. Excess sample was then blotted and the grids were washed three times in water droplets, and excess wash was blotted away each time. The grids were then stained with 1 % uranyl acetate, which was immediately blotted away and then reapplied, which was incubated for 1 minute. The stain was blotted and the grids were allowed to air-dry before visualisation, using either the JEOL 1400 transmission electron microscope or the FEI Tecnai T12 transmission electron microscope (at a defocus of -1 µm - 5 µm).

2.10.2 Cryo-Electron Microscopy Grid Preparation

Purified virus samples were mixed 1:1 with 10 nm colloidal gold, which would act as fiducial markers during the tomogram alignment (PICV; Protein A -

10 nm Gold labelled, Aurion or LCMV; Protein A, Colloidal gold (10 nm), Boster Immunoleader). The samples (3 µL) were then immediately applied to glow-discharged (45 seconds) carbon-coated grids (PICV; QR 2/2, 400-mesh or LCMV; QR 2/2, 200-mesh), which were kept at a pre-set temperature and high humidity and then blotted (3.5 seconds) and rapidly plunged into liquid ethane using the Leica EM GP automated grid plunge freezer (all procedures performed here were with the help of either Dr Juan Fontana or Dr Daniel Maskell). Frozen grids were then transferred to a pre-cooled grid container in liquid nitrogen and stored in liquid nitrogen until imaging.

2.10.3 Cryo-Electron Microscopy and Tomography

Vitrified PICV EM grids were initially clipped, loaded and screened by the FEI Titan Krios I (performed by facility managers Dr Rebecca Thompson and Dr Emma Hesketh, Astbury Biostructure Laboratory Electron Microscopy Facility). Screening was performed to assess the quality of the fiducial concentration and spread, virus concentration and spread, ice formation or other contamination. Dr Juan Fontana and Dr Emma Hesketh helped collect the images (pixel size = 4.7 Å).

With the help of Dr Juan Fontana and the Astbury Biostructure Facility staff, cryo-ET on vitrified PICV grids was set up for an automated data collection on the FEI Titan Krios II, using Tomography 4 software (FEI). Single axis tilt-series data was collected at grid angles from -50° to +50°, with 2° increments. Projections were collected at 53,000x magnification, with a -1 µm defocus and using the Volta phase plate. The pixel size was 2.72 Å resulting in an electron dose of 1.8 e^- per image. The microscope alignments were performed by the Astbury Biostructure Facility staff. With the help of Dr Juan Fontana and Dr Emma Hesketh, grid locations of interest were specified manually and then autofocus and automated data collected was performed by Tomography 4.

Vitrified LCMV EM grids were initially clipped, loaded and screened by the FEI Titan Krios I (performed by facility manager Dr Daniel Maskell, Astbury Biostructure Laboratory Electron Microscopy Facility). Screening was performed by Dr Daniel Maskell to assess the quality of the fiducial concentration and spread, virus concentration and spread, ice formation or other contamination.

Dr Daniel Maskell also set up the automated data collection on the vitrified LCMV EM grids, using the FEI Titan Krios II and Tomography 4 software (FEI). Single axis tilt-series data was collected at grid angles from -60° to +60°, with 2° increments. Projections were collected at 53,000x magnification, with a -1 µ defocus and using the Volta phase plate. The pixel size was 2.72 Å resulting in an electron dose of 1.8 e^- per image. The microscope alignments were performed by the Astbury Biostructure Facility staff.

2.10.4 Tomogram Reconstruction

Following the data collection, the tilt-series were imported into IMOD for tomogram reconstruction using Etomo. All the PICV tilt-series were manually reconstructed whereas the LCMV tilt-series were reconstructed using batch tomogram reconstruction, in order to perform this as high-throughput.

The images firstly went through a pre-processing step to remove any outlying pixels or artefacts and then each 2D projection of the tilt-series was roughly aligned. Gold particles were then selected as fiducial markers to track through the tilt-series, detect particle movement between the projections and refine the alignment. This was then used by IMOD to reconstruct the 3D tomogram volume (Cope et al., 2011). The images were then binned by a factor of 2, resulting in a final pixel size of 5.44 Å. The images were then filtered using Gaussian Blur 3D in ImageJ. The tomogram reconstructions were performed by A Shaw, with help from Dr Juan Fontana.

2.10.5 Sub-Tomogram Averaging

In an attempt to resolve the structure of the GPC from PICV and LCMV, STA was performed using the Particle Estimation for Electron Tomography (PEET) software (IMOD). PEET permits alignment, averaging and iterative refinement of 3D particles (Cope et al., 2011). The settings for PEET and the angles for the iterations were decided according to previous work (Cope et al., 2011; Li et al., 2016; Punch et al., 2018). All STA was performed by A Shaw, with assistance from Dr Juan Fontana.

Model Generation

In order to inform PEET of the positioning and size of the GPC spikes, with respect to the viral membrane, a model was generated using 3dmod (IMOD). Briefly, an object was created to define the centre of the virus and was increased in size until it matched the viral membrane, and assuming the virus is near-spherical, the object matched the viral membrane throughout the 3D volume. Then another object was added to define the position where the GPC spikes meet the viral membrane. Models were manually generated for all tomograms and spikeInit (PEET programme, IMOD) was then utilised to create an initial orientation list (the initial motive list), which makes the assumption that the spikes sit perpendicular to the viral membrane.

Automated particle selection and refinement

The models and initial motive lists generated in section 2.10.5 provided information for the STA by PEET. The spikes, as specified by the model, were then averaged and roughly aligned. PEET was allowed to identify the optimal alignment of the spikes by altering of the lateral spike location on the membrane (theta (forward/back tilting) and psi (left/right tilting)) and the twist orientation of the particles around the Y-axis (phi). The averages generated in this first run were then C120-symmetrised to remove any specific features and used as the reference particle for automatic particle alignment in the next run.

In order to improve the resolution of the GPC spike structures, further iterative refinement steps were performed in PEET. For all the steps, the average from the previous step was used as the reference for the following step in order to improve and refine the alignment of the particles. Some of the PEET runs had a wide search range and therefore a parameter was set to remove duplicate particles because when the search range is wide, it can exceed the spacing between individual spikes. This means some spikes can be erroneously averaged multiple times, which could lead to an overestimation of resolution. PEET will identify these cases of duplication and remove the particles from further averaging. The tolerance was set at 10 pixels apart (or 5.44 nm) in 360°, which means any particles that are closer than this will be considered duplicates. In the PEET runs, missing-wedge compensation was enabled

to account for the data that was not collected (i.e. tilt angles greater than +50/+60° and smaller than -50/-60°). In the initial runs, a broad search range was applied in every direction to account for differences in predicted spike location. This was also accounted for in the initial sub-tomogram volume, which was set to 40 voxels (~22 nm), with a large spherical mask of 30 pixels (~16 nm) until the initial average, and size of the GPC spike, was determined.

In the next stage, a smaller spherical mask, which was centred on the glycoprotein base, was used in order to identify evidence of three-fold (C3) symmetry. The averages were then iteratively refined, beginning with a large search range (+/- 180°) and reducing at each iteration in order to improve the alignment. The iterations aimed to improve three angles of the GPC spike; phi (twisting around the Y-axis), theta (forward/back tilting) and psi (left/right tilting).

The previous stage identified C3 symmetry (Li et al., 2016) and therefore the C3 symmetry was applied to those averages to provide the reference for this stage. The average here was further refined with smaller searches in the spike orientation and location, and an increase in the high and low frequency cut-offs, in order to only focus on the high resolution information, which would improve the final resolution.

In order to calculate the final resolution, calcFSC (PEET) was used, using Fourier shell correlation (FSC), which was cut-off at a threshold of 0.5. UCSF Chimera (RBVI) was then used to created isosurface rendered 3D reconstructions of the averaged density maps (Goddard et al., 2007), which could be overlaid with each other, overlaid with the LASV density map (Li et al., 2016) or have rigid-body-fitting of crystal structures (Hastie et al., 2016a) into the electron density. Electron density map can be obtained from the Electron Microscopy Data Bank (EMDB) under accession numbers: EMD-3290 for the LASV GPC spike (Li et al., 2016).

2.10.6 Electron Microscopes

The JEOL 1400 and FEI Tecnai T12 transmission electron microscopes (LaB6 electron source and 120 kV operating voltage) were used for negative-stain EM. Tilt-series were collected on the FEI Titan Krios II electron microscope (X-FEG electron source and 300 kV operating voltage).

Chapter 3

Production of LCMV NP Antisera as an Arenavirus Detection Tool

3.1 Chapter Introduction

Currently, whilst there are many commercially available arenavirus NP antibodies, their reliability to function in biological assays is questionable. Furthermore, LCMV infection in cellular culture has also been reported to be non-cytolytic (Abdel-Hakeem, 2019), making it difficult to detect and quantify infectivity of LCMV through conventional crystal violet-based plaque assays, which rely on cytopathic effect. Without these tools, the study of arenavirus biology is very difficult, therefore the solution was to make a highly-specific antibody against LCMV NP, which can be used to develop assays for LCMV titration.

Expression of recombinant proteins, followed by effective purification techniques, allows the isolation of large quantities of high-quality proteins for their study in basic research, therapeutics and biotechnology. Highly pure protein preparations are often required to investigate the protein's structure and function using structural and biochemical approaches, but also to serve as starting material for production of highly specific recognition molecules such as antibodies. The various expression and purification methodologies are selected based upon the characteristics of the protein of interest and the final purpose of its production.

A variety of recombinant protein expression systems exist, utilising prokaryotic cells, eukaryotic cells or even cell-free systems. This chapter describes the large-scale production of the LCMV nucleocapsid protein (NP) using a bacterial expression system and its subsequent purification, resulting in a purity of >85 %. This LCMV NP preparation was then used as an antigen to generate polyclonal antibodies.

LCMV NP was chosen as the priming antigen for antibodies because of its abundance in virally-infected cells, offering an easily identifiable indicator of successful infection. This chapter also describes the validation of the resulting LCMV NP antisera, using techniques including western blotting and immunofluorescence, and its subsequent application in a focus forming assay to determine the titre of LCMV stocks.

3.1.1 Introduction of Recombinant Protein Expression

In order to express recombinant protein, it is first necessary to determine which expression system to use. There are multiple expression systems available, some of which use bacterial, yeast, insect or mammalian cells, and each of these present several advantages and disadvantages (summarised in table 3.1). Which expression system is chosen depends on the required yield and purity for the downstream applications, in addition to the protein characteristics including molecular mass, solubility and post-translational modifications such as glycosylation, phosphorylation or disulphide bond formation.

Table 3.1: Advantages, Disadvantages and Applications of Various Protein Expression Systems.

Protein Expression System	Advantages	Disadvantages	Applications
Bacterial Cell Expression	Rapid growth and expression	Lack of eukaryotic post-translational modifications	Structural analysis
	Relatively inexpensive and simple	Alternative codon usage to eukaryotes	Functional assays
	Very high product yield	Protein insolubility and proteolytic degradation	Analysis of protein interactions
	Easy to culture and to large-scale	Complicated purification	Expression of bacterial proteins,
	Extensive knowledge of physiology and genetics	Endotoxins present, affecting downstream applications	cytokines, enzymes and antigens
Yeast Cell Expression	Rapid growth and expression	Some proteolytic degradation	Structural analysis
	Relatively inexpensive and simple	Potential for hypermannosylation of protein	Functional assays
	High product yield and simple purification	No chaperonins, so proper folding may not occur	Analysis of protein interactions
	Easy to culture and to large-scale	Lacks more complex post-translational modifications	Expression of cytokines, enzymes
	Simple post-translation modifications and processing		and antigens
Insect Cell Expression	High product yield and easy to large-scale	Slow growth	Structural analysis
	Flexibility of gene size (up to 15kb)	Expensive production costs	Functional assays
	Improved protein solubility and folding	Time-consuming and laborious protocol	Virus Production
	Post-translational modifications similar to mammalian	Proteins can be improperly folded at later stages	Expression of cytosolic proteins,
	Able to secrete proteins (with secretion sequences)	Secretion can be inefficient	enzymes, transmembrane proteins
			and toxic proteins
Mammalian Cell Expression	Excellent protein folding	Very slow growth	Structural analysis
	Native post-translational modifications	Expensive production costs	Functional assays
	Very safe with few immunogenicity concerns	Time-consuming and laborious	Analysis of protein interactions
		Difficult to large-scale	Virus Production
		Complex purification procedures due to endogenous proteases	Expression of antibodies and
			antibody fragments

3.1.2 Overview of Bacterial Expression of Recombinant Proteins

Expression of recombinant proteins using the prokaryote *Escherichia coli* (*E. coli*) has many advantages (Rosano and Ceccarelli, 2014; Demain and Vaishnav, 2009). The bacterial protein expression system has been extremely well-characterised genetically and large yields of recombinant protein can be rapidly generated, in a relatively easy and inexpensive manner (Kaur et al., 2018). The system is also easily scaled-up to significantly increase the yield of recombinant protein, without increasing expense or time. However, bacterial expression systems are unable to perform eukaryotic post-translational modifications, including disulphide bond formation, phosphorylation and glycosylation. This can cause the degradation of the recombinant protein by host proteases or an accumulation of the recombinant protein in inclusion bodies, rendering the protein insoluble (Kaur et al., 2018; Rosano and Ceccarelli, 2014). Bacterial expression systems also utilise an alternative codon strategy, occasionally requiring recombinant proteins to be codon-optimised for expression (Rosano and Ceccarelli, 2014). Despite these disadvantages, the bacterial expression system was chosen for experiments in this chapter due to its simplicity, affordability, the large yield of recombinant protein that can be attained and relative ease of subsequent purification.

Introduction to Bacterial Expression Vectors

To produce the recombinant protein in a bacterial expression system, the gene of interest needs to be cloned into an appropriate expression vector. There are many bacterial expression vectors are available for protein expression in *E. coli* cells, combining different replication origins (and thus copy numbers per cell), promoters, antibiotic selection markers, multiple cloning sites, and the provision to add fusion proteins or tags to the protein of interest. The pET bacterial expression vectors are commonly used due to their high efficiency for protein production, with expressed recombinant protein representing up to 50 % of the total bacterial cell protein content (Rosano and Ceccarelli, 2014). Following transformation of the recombinant protein into the bacterial cells, further optimisation of protein expression induction, scaling up and purification is required.

Experiments described in this chapter utilised the pET28a(+)-His SUMO vector, which puts the recombinant protein under control of a bacteriophage T7 RNA polymerase (T7P) promoter and a *lac* operator (Studier, 2005). This vector also adds a six histidine (6xHis) residue tag and a small ubiquitin-related modifier (SUMO) tag to the N-terminus of the recombinant protein. The 6xHis tag is added to aid downstream purification, whereas the SUMO tag improves expression and solubility of the protein. The efficient and specific removal of the 6xHis-SUMO tag is then mediated by Ubiquitin-like-specific protease 1 (ULP1), which cleaves based on the tertiary structure of the SUMO tag, reducing the chance of erroneous cleavage at alternative sites (Marblestone et al., 2006; Malakhov et al., 2004).

Introduction to Bacterial Expression of Recombinant Protein

Some methods of induction of recombinant protein expression, such as autoinduction, are reliant on the process of bacterial carbohydrate metabolism. *E. coli* are able to switch metabolic processes dependent on the presence of glucose and lactose (Jacob and Monod, 1961) and this can be exploited for recombinant protein expression. In this chapter, BL21(DE3) *E. coli* strains were used for recombinant protein expression. These strains have been genetically altered to encode extra elements, such as the T7 bacteriophage RNA polymerase (T7P), which is present in the chromosome under control of a *lac*UV5 promoter, and T7 lysozyme, which is present in the pLys plasmid that has been stably transformed into these strains (the genetic composition has been summarised in table 2.1) (Studier and Moffatt, 1986; Kaur et al., 2018).

There are several major regulatory elements to be aware of in this process. Firstly, there is the T7P, which binds to a T7 promoter region to transcribe the gene encoding the target protein. Next, there is the *lac* repressor, which is encoded by the *lac*I gene and binds at *lac* operator sequences but the binding overlaps onto polymerase promoter regions, preventing RNA polymerase and T7P transcription (Wagner et al., 2008; Studier, 2005; Dubendorf and Studier, 1991). There is also the T7 lysozyme, which binds to the T7P, repressing its activity (Studier, 1991). Finally, there is the *E. coli* RNA polymerase (RNAP), which binds its promoter region to transcribe multiple genes including the T7P, T7 lysozyme, the *lac* gene and the *lac* operon genes.

The *lac* operon is a series of genes that are required to transport and metabolise lactose. The *lac* operon under the control of the *lac* operator, a RNAP promoter and a catabolite activator protein (CAP) site (Studier, 1991; Fox and Blommel, 2009). There are three genes in the *lac* operon; *lacZ* encodes β-galactosidase, the enzyme that metabolises lactose; *lacY* encodes lactose permease, the membrane protein that imports lactose; and *lacA* encodes galactosidase acetyltransferase, which is proposed to reduce the toxicity of remaining metabolites (Studier, 2005; Marbach and Bettenbrock, 2012). The *lac* operon is only expressed in presence of lactose (or presence of an inducer such as isopropyl β-D-1-thiogalactopyranoside (IPTG)) and an absolute absence of glucose.

In the presence of glucose, expression of the *lac* operon genes and target protein is repressed. The *lac* repressor is bound at the *lac* operator sites, preventing RNA polymerase binding to its promoter and transcription of the *lac* operon genes (from the RNAP promoter), of T7P (from the *lac*UV5 promoter) and of the target protein (from the T7P promoter) (Dubendorf and Studier, 1991). Basal expression of T7P is also repressed by T7 lysozyme (Dubendorf and Studier, 1991). Furthermore, the presence of glucose means there is no signal to up-regulate cyclic adenosine monophosphate (cAMP) (Kimata et al., 1997). This is important because cAMP assists the catabolite activator protein (CAP) binding at the CAP site, which is located upstream of the RNA polymerase promoter of the *lac* operon genes (Griffiths et al., 2000). Binding of cAMP/CAP at the CAP site assists RNA polymerase binding to its promoter, meaning without cAMP, neither CAP not RNAP can bind to their respective sequences (Griffiths et al., 2000). Finally, the uptake of lactose by lactose permease is prevented by glucose through catabolite repression (Studier, 2005).

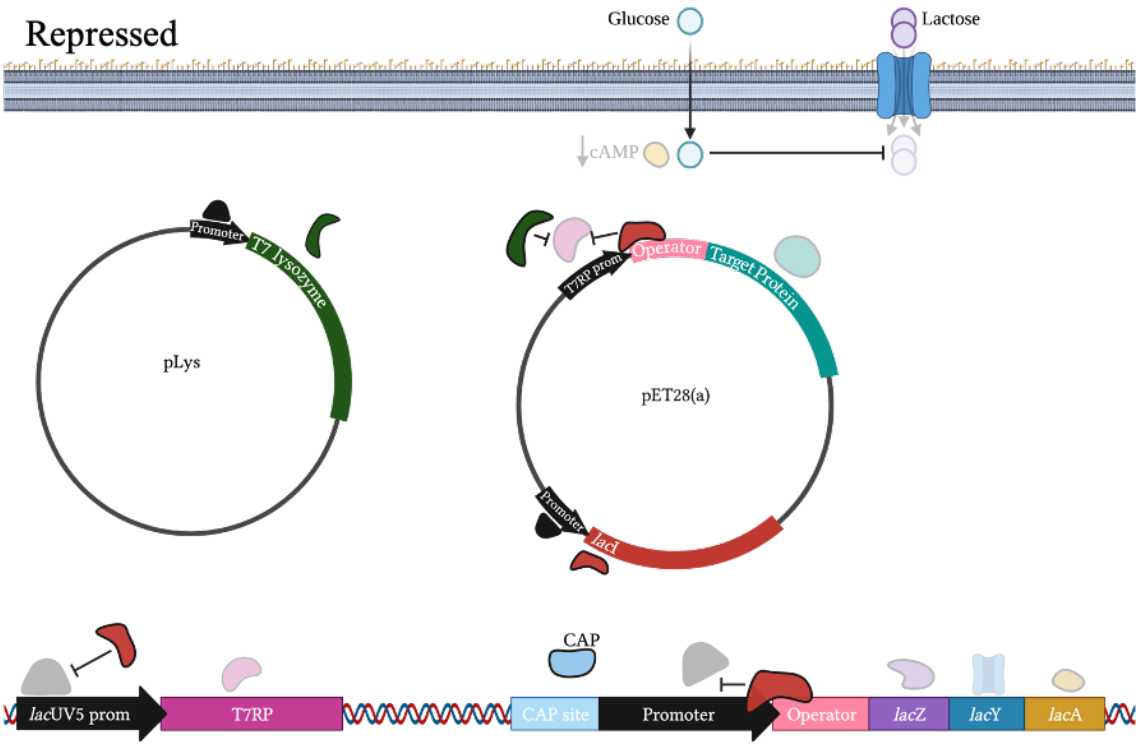

Figure 3.1: Repression of Recombinant Protein Expression.
Schematic representation of the process by which expression is repressed in bacteria that have a source of glucose and an absence of lactose. The expression of T7 lysozyme and the *lac*I repressor is constitutive. T7 lysozyme binds to the T7 RNA polymerase (T7P) to prevent it from binding its promoter. The *lac*I repressor is able to bind at the *lac* operator, preventing RNA polymerase and T7P transcription of the *lac* operon genes and the target protein. The presence of glucose means there is no need for the up-regulation of cAMP, which therefore does not assist CAP binding the CAP site and helping the polymerase bind the promoter site of the *lac* operon. This figure was created using BioRender.

When the glucose source is depleted, there is a metabolic switch to initiate lactose uptake and metabolism, which generates allolactose as a by-product. Allolactose, or lactose analogue IPTG, bind to the *lac* repressor and alter its structure, preventing it binding to the *lac* operator and the *lac*UV5 promoter sequences (Daber et al., 2007). This induces expression of the *lac* operon genes and the T7P (Studier, 2005). Expression of the T7P, and the absence of the *lac* repressor at the *lac* operator site, permits expression of the target protein (Studier, 2005). Furthermore, the depletion of glucose signals to the cell to up-regulate cAMP, which binds to CAP (Griffiths et al., 2000). CAP-cAMP can then bind to the CAP-site, which promotes RNA polymerase binding at the promoter site and enables transcription of the *lac* operon genes (Griffiths et al., 2000).

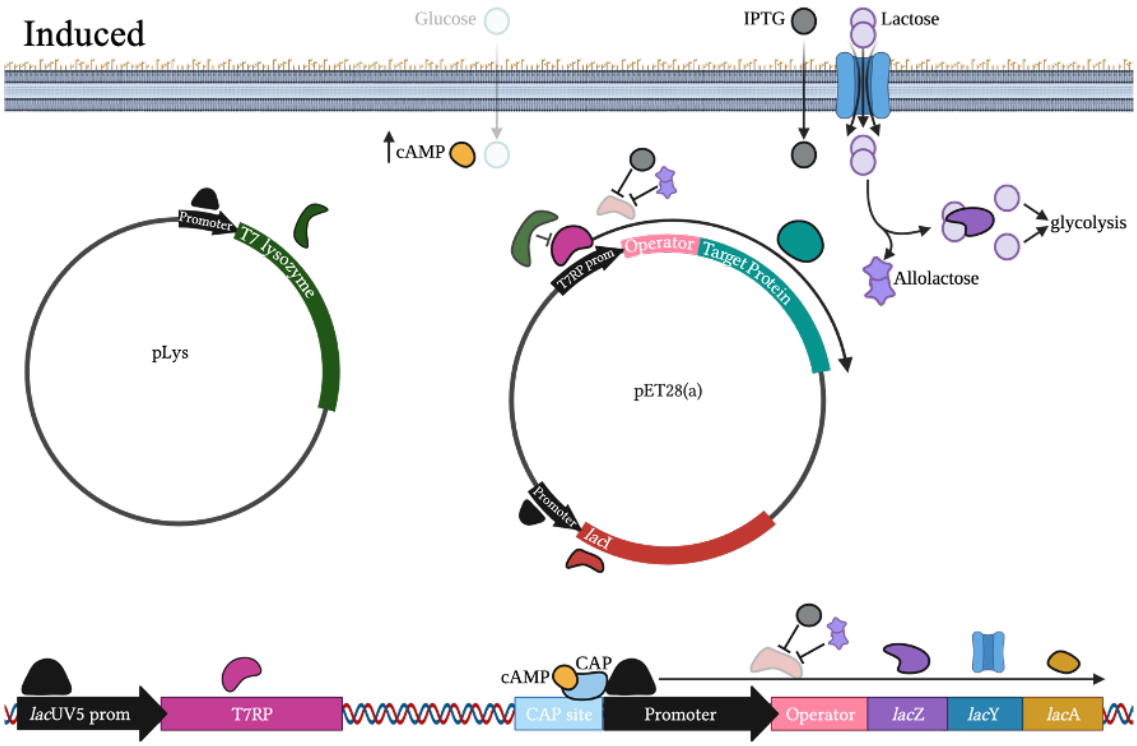

Figure 3.2: Induction of Recombinant Protein Expression by IPTG or Lactose. Schematic representation of the metabolic switch and induction of expression in bacteria when lactose is present or isopropyl β-D-1-thiogalactopyranoside (IPTG) is added. The depletion of glucose up-regulates cAMP, which binds to CAP and assists it binding to the CAP site. The presence of CAP at the CAP site permits binding of the RNA polymerase at the *lac* operon promoter site. The presence of IPTG and allolactose (generated as a byproduct of lactose) prevents *lac*I repressor from binding the *lac* operon sequences, permitting the RNA polymerase transcribing the genes expressing the *lac* operon genes and the target protein. This enable a positive feedback loop to further increase expression. This figure was created using BioRender.

Occasionally, the sudden and abundant expression of the recombinant protein overwhelms the *E. coli* translational machinery, leading to the formation of incorrectly folded insoluble aggregates called inclusion bodies (Burgess, 2009). One way to combat insolubility is fusing the SUMO tag to the recombinant protein because SUMO can exert a chaperoning effect by acting as a nucleation site for the correct folding of recombinant protein (Costa et al., 2014; Marblestone et al., 2006; Malakhov et al., 2004; Gaberc-Porekar and Menart, 2001). Solubility can also be improved by reducing expression of the target protein to relieve the stress on the translational machinery, reducing incorrect folding and subsequent aggregation (Burgess, 2009; Kaur et al., 2018). One such technique to improve target protein solubility is to induce recombinant protein expression using autoinduction, which gradually expresses the protein as opposed to IPTG-induction, and therefore there

is less stress on the bacterial translational machinery. Another technique is to use Lemo-21(DE3) cells, which are an *E. coli* strain that have been stably transformed with a plasmid that expresses T7 lysozyme under control of the rhaBAD promoter, allowing tunable T7 lysozyme expression using L-rhamnose (Wagner et al., 2008; Schlegel et al., 2012). Expression of the target protein is induced using IPTG but the expression of T7 lysozyme can be increased by increasing the concentration of L-rhamnose. T7 lysozyme reduces the expression of the T7P, which reduces target protein expression and can improve target protein solubility (Studier, 1991; Wagner et al., 2008).

3.1.3 Introduction to Chromatographic Methods of the Purification of Recombinant Proteins

Introduction to Protein Purification

The aim of the protein purification process is to remove unwanted material, concentrate the protein and transfer the protein to a stable environment, such as an appropriate buffer. Chromatographic techniques are one of the most effective and widely used protein purification methods. These techniques involve the retention of molecules from their solvent (mobile phase) after their physical interaction with a specific material (stationary phase). The most common experimental configuration consists of a stationary phase packed into a column through which a mobile phase, containing the target protein, is pumped. The degree of interaction between the target protein (and other proteins in the mobile phase) and the stationary phase determines how fast they are carried by the mobile phase. Different properties of the target protein, such as size, charge, isoelectric point, hydrophobicity and bio-molecular interactions, influence its interaction with the stationary phase, which is exploited to purify it from the contaminating proteins. There are several types of chromatography, which have different compositions, matrices and exploit different properties of the protein. Often, multiple chromatographic techniques will be used in combination, with metal affinity-based methods followed by either ion-exchange or size-exclusion techniques, as was applied in this chapter.

Immobilised Metal-Affinity Chromatography

Protein purification through affinity-based chromatography involves the reversible interaction between the target protein and a ligand that is attached to a matrix, followed by elution of the target protein from the matrix, without affecting any of the protein's properties. The interaction can be mediated through electrostatic interactions, hydrophobic interactions, van der Waals forces or hydrogen bonding. Immobilised metal-affinity chromatography (IMAC) is one of the most commonly used chromatographic techniques for recombinant protein purification. IMAC involves the addition of an affinity tag to the target protein, which interacts with a metal ion ligand immobilised on the matrix (Bornhorst and Falke, 2000). In most cases, an affinity tag comprising a minimum of six histidine residues (6xHis) is added to the recombinant protein. The 6xHis tag interacts strongly with the transition metal ions (most commonly Ni^{2+} but also Co^{2+}, Cu^{2+} or Zn^{2+}) that are immobilised on a matrix (composed of nitrilotriacetic acid (NTA) for Ni^{2+} ions), which is attached to the sepharose support resin (Gaberc-Porekar and Menart, 2001). Histidine residues interact with the metal ions through their imidazole side chain, which contains nitrogen atoms that are free to interact with the two unoccupied co-ordination sites on the ions (Bornhorst and Falke, 2000). The number of histidine residues present in the tag produces a stronger interaction of the target protein than contaminating proteins, which either do not interact or the interaction can be disrupted using a weak imidazole-containing buffer. The interactions between the 6xHis tag of the recombinant protein and the metal ions can then be disrupted through the addition of a buffer with a higher imidazole concentration, which can out-compete to interact with the two unoccupied co-ordination sites on the ions (Bornhorst and Falke, 2000; Gaberc-Porekar and Menart, 2001). This results in the elution of the target protein.

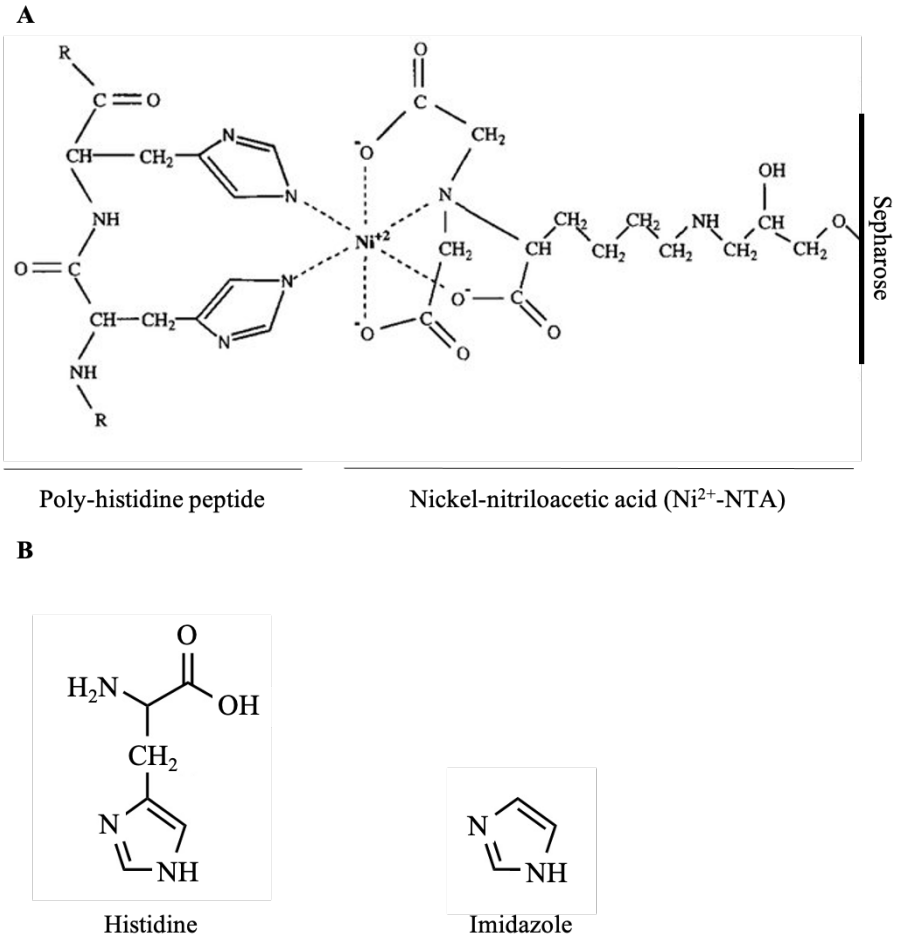

Figure 3.3: Chemical Composition of Ni^{2+}-NTA Chromatography.
(A) Schematic representation of the Ni^{2+} ions, which are attached to the sepharose resin through nitriloacetic acid. Two free coordination sites from the Ni^{2+} ions can be seen and interact with the nitrogen from the side-chain of the poly-histidine tag on the target protein. (B) Chemical structures of histidine and imidazole. The similarities between imidazole and the histidine side-chain allow imidazole to compete with the target protein for binding to Ni^{2+}-NTA. Adapted from (Bornhorst and Falke, 2000)

Ion-Exchange Chromatography

Ion-exchange chromatography (IEC) exploits ionic interactions to separate proteins based on their net surface charge. The basis of separation occurs through competition of differently charged proteins for interaction with the oppositely charged ion-exchange matrix. Proteins are ampholytes, which means they have a complex mixture of positively-charged residues (such as histidine, lysine and arginine) and negatively-charged residues (such as glutamate and aspartate) (Hedhammar et al., 2006). The sum of the ionisable amino acid residues gives the overall charge of the protein, but this is also subject to the buffer pH of the protein (Hedhammar et al., 2006). The isoelectric point (pI) of a protein is the

pH at which the protein has no net overall charge (Dunn and Pennington, 2003). Altering the buffer pH to a pH below the pI of the target protein creates a net positive charge, allowing interaction with a negatively-charged cationic exchange chromatographic matrix (Hedhammar et al., 2006). Altering the buffer pH to a pH above the pI of the target protein creates a net negative charge, allowing interaction with a positively-charged anionic exchange chromatographic matrix (Costa et al., 2014; Hedhammar et al., 2006). In order to achieve strong interaction between the target protein and the oppositely-charged matrix, ion-exchange chromatography is typically performed in buffers at least one pH unit above or below the target protein's pI. The target protein is separated from proteins with the same charge as the matrix, or with a neutral charge, because those proteins pass straight through the column whereas the target protein interacts with the matrix (Hedhammar et al., 2006). The affinity of this interaction is then reduced either by altering the pH or the ionic strength of the buffer. Altering the pH can lead to precipitation of the target protein on the column, due to a decrease of solubility at pH closer to the pI (Hedhammar et al., 2006). Therefore, increasing the ionic strength of the buffer, through increasing the concentration of a non-buffering salt (i.e., NaCl) is a more commonly used strategy. The ions compete with the bound proteins for binding to the charged resin, and weaker interactions are disrupted at lower NaCl concentrations and stronger interactions are disrupted at higher concentrations (Costa et al., 2014; Regnier, 1982; Hedhammar et al., 2006).

IEC offers the advantage of performing chromatography under mild conditions, therefore not disrupting the native conformation of the target protein. IEC is also easy to perform and control, and the resins can be reused many times. However, IEC does not offer the selectivity that other chromatographic methods can offer (Hedhammar et al., 2006).

Size-Exclusion Chromatography

Another protein purification method is size-exclusion chromatography (SEC), which is a technique that separates molecules based on the molecular size and shape after their interaction with a porous matrix. Materials used for the matrices include natural polymers (i.e., agarose or dextran) and synthetic polymers (i.e., polyacrylamide). These are inherently porous, but they can also be cross-linked,

which can result in different pore sizes (Hedhammar et al., 2006). Molecules that are bigger than the pores will not be able to enter and therefore pass straight through the matrix, being the first to be eluted. Molecules that are smaller than the pores can enter and are therefore retained for a longer period than larger molecules. Molecules that are smaller than the smallest engineered pore are retained the longest and this provides the basis by which the molecules are separated by size (Barth et al., 1994; Hedhammar et al., 2006). Molecular shape also has an effect on whether the molecules are excluded from the pores, whereby globular molecules, such as proteins, access the pores more easily than linear molecules, such as nucleic acids or polysaccharides, which occupy a larger hydrodynamic volume (Hedhammar et al., 2006).

For the SEC experiments in this chapter, Superdex was used, which is composed of dextran covalently bonded to highly cross-linked agarose. As an indication of protein presence, elution from the column is monitored through the measurement of absorbance at 280 nm with an ultraviolet (UV) light. This result is then mapped onto a chromatogram, whereby the absorbance at 280 nm (protein concentration) is plotted against elution volume (mL).

In addition to separation of proteins by size, SEC can also be used to determine protein characteristics, such as oligomeric state or interactions with other molecules. SEC can also be used for buffer exchange where proteins of interest are separated from the buffer components e.g., salts.

3.1.4 Chapter Aims

The aims of this chapter were to express recombinant LCMV NP with a 6xHis-SUMO affinity tag from a bacterial expression system and to then purify LCMV NP using a variety of chromatographic techniques. Purified LCMV NP was then to be used as the priming antigen to generate polyclonal antibodies. The LCMV NP antisera would permit analysis of LCMV infection through western blotting analysis and immunofluorescence analysis. Furthermore, the LCMV NP antisera would allow the development of a focus forming assay to assist the determination of LCMV stock titres.

3.2 Results

3.2.1 Construction of the pET-28a(+)-His-SUMO-LCMV NP Vector

The native LCMV NP sequence (accession number: P09992) was successfully isolated from a synthetic mammalian expression vector (pMK-RQ) using PCR, which also permitted introduction of *Bam*HI and *Xho*I restriction sites. The PCR fragment and pET28a(+)-His-SUMO expression vector were digested with *Bam*HI and *Xho*I and ligated together to form the pET28a(+)-His-SUMO-LCMV NP construct (figure 3.4A). This enabled the expression of LCMV NP, in frame with the 6xHis-SUMO tag at the N-terminus of the NP, as shown in (figure 3.4B). The amino acid sequence of 6xHis-SUMO-LCMV NP was predicted to have a molecular weight of ~75.3 kDa and a theoretical pI of 8.04, using the ExPASy ProtParam tool (Gasteiger et al., 2005). These parameters were also calculated for the LCMV NP amino acid sequence (without the 6xHis-SUMO tag); the molecular weight was ~62.2 kDa and the theoretical pI was 8.80.

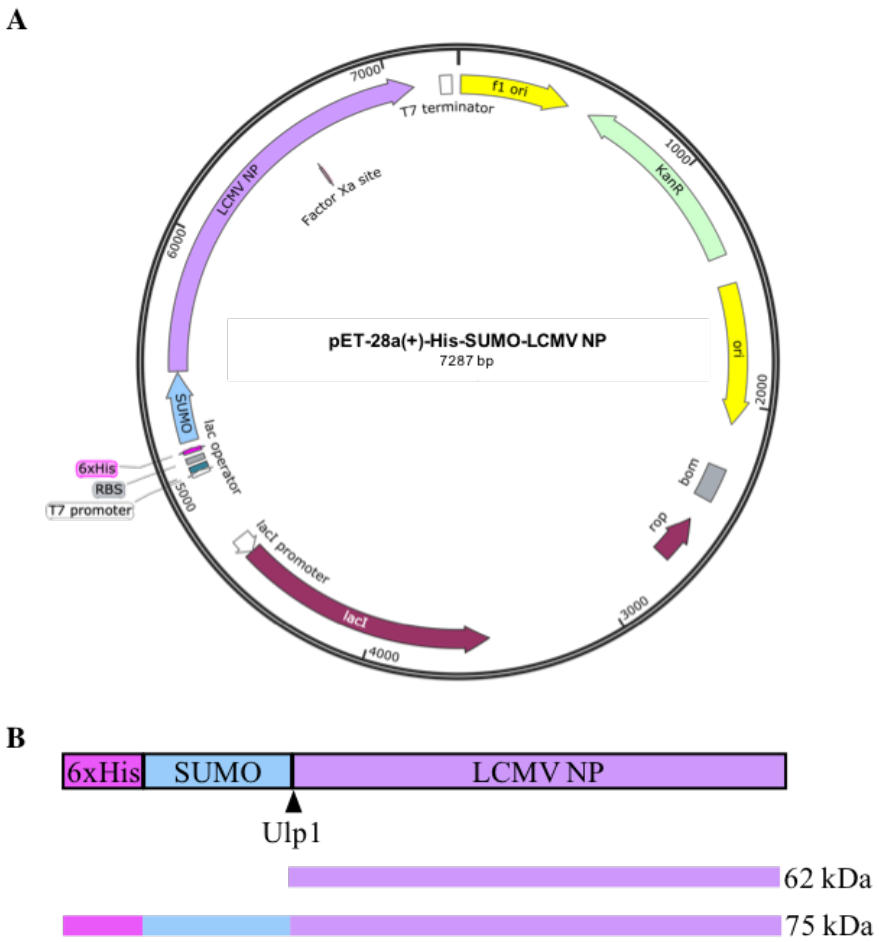

Figure 3.4: Vector Map of pET-28a(+)-His-SUMO-LCMV NP.
Schematic representation of the LCMV NP open reading frame in the pET28a(+)-His-SUMO expression vector (**A**), which produces LCMV NP fused to the 6xHis-SUMO tag (**B**). The 6xHis-SUMO tag is removed at the site indicated by the arrow, after cleavage using Ubiquitin-like-specific protease-1 (ULP1). The molecular weights of 6xHis-SUMO-LCMV NP and untagged LCMV NP have been shown and were predicted using the ExPASy ProtParam tool. The plasmid map was created using SnapGene software.

3.2.2 Optimisation of Recombinant LCMV NP Expression

Expression Trials Using IPTG-Induction

Expression of pET28a(+)-His-SUMO-LCMV NP was trialled in a range of BL21(DE3) *E. coli* strains; Gold, Star, Rosetta, Rosetta 2 and CodonPlus. These bacterial strains all carry the T7 RNA polymerase (T7RP) gene to allow T7RP-directed expression of recombinant proteins. Furthermore, these strains are deficient in the Lon protease (naturally deficient) and the OmpT protease (engineered to be deficient), which reduces degradation of the recombinant protein. The Gold and CodonPlus strains do not express endonuclease A, limiting plasmid

DNA degradation. The Star strain also has a mutation in the RNaseE gene, which limits mRNA degradation. Finally, the Rosetta, Rosetta 2 and CodonPlus strains are also engineered to express tRNA genes for codons that are rarely used in *E. coli*, which assists expression of eukaryotic recombinant proteins. The CodonPlus strain is engineered to express five additional tRNA genes, which supply codons for arginine, isoleucine, leucine and proline. The Rosetta and Rosetta 2 strains are engineered to express six and seven, respectively, additional tRNA genes, which supply codons for arginine, isoleucine, leucine, proline and glycine.

Initially, pET28a(+)-His-SUMO-LCMV NP was transformed into the Gold, Star, Rosetta, Rosetta 2 and CodonPlus *E. coli* strains. Expression of the tagged protein was induced using 100 µM IPTG, and the cells were incubated at 37 ℃ for 24 hours, after which the cells were harvested. The cells were lysed (whole cell lysate) and then separated into soluble and insoluble fractions. The whole cell lysates, soluble and insoluble fractions were examined using SDS-PAGE analysis, followed by Coomassie staining, in order to determine which strain yielded the highest expression of soluble protein (figure 3.5). The CodonPlus strain appeared to result in strongest expression, having the most abundant band of the correct predicted molecular weight. However, the majority of the protein was in the insoluble fraction.

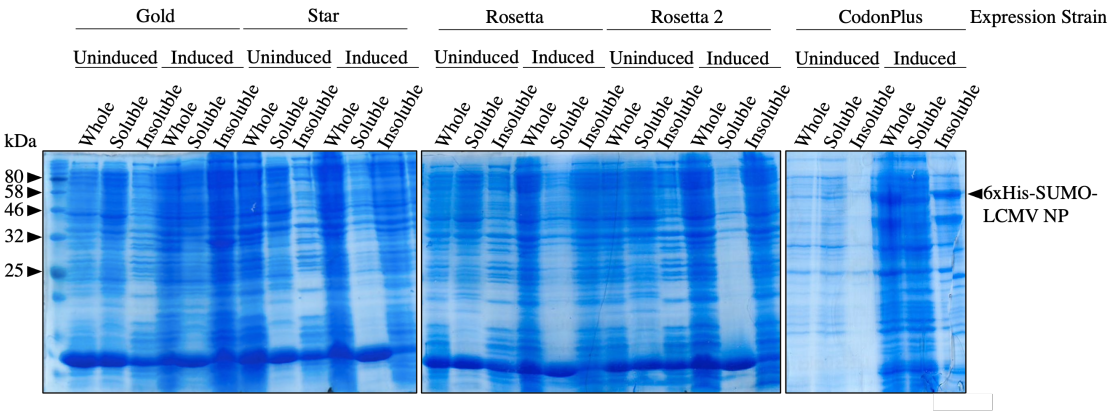

Figure 3.5: Initial Expression Trials of 6xHis-SUMO-LCMV NP by IPTG Induction.
SDS-PAGE analysis, followed by Coomassie staining, of the initial expression trials of 6xHis-SUMO-LCMV NP (predicted molecular weight: ~75 kDa) in a variety of BL21(DE3) *E. coli* strains; Gold, Star, Rosetta, Rosetta 2 and CodonPlus. Expression was induced using 100 µM IPTG and the cultures were incubated at 18 ℃ for 24 hours before harvest. The cultures were pelleted and resuspended in lysis buffer after which the lysates were subjected to three freeze-thaw rounds. Soluble and insoluble fractions were collected by centrifugation. The band thought to be 6xHis-SUMO-LCMV NP has been indicated by an arrowhead.

In an attempt to improve solubility of the recombinant protein, expression by another *E. coli* strain was trialled. Lemo-21(DE3) cells have been proposed to improve solubility of the target protein by reducing its expression through increasing concentration of L-rhamnose. This allows more time for the correct folding of the target protein, preventing its accumulation within inclusion bodies. After Lemo-21(DE3) cells were transformed with pET28a(+)-His-SUMO-LCMV NP, cultures were induced using 100 µM IPTG and increasing concentrations of L-rhamnose were added. The cells were then incubated (at 37 ℃ for 24 hours) at which point the cells were harvested, lysed and the soluble and insoluble fractions were collected. SDS-PAGE examination, followed by Coomassie staining, of the insoluble fractions revealed that increasing the concentration of L-rhamnose reduced the expression of 6xHis-SUMO-LCMV NP, as expected. This was shown by a reduction of the band size between 0 µM and 100 µM L-rhamnose, followed by the disappearance of the band in higher L-rhamnose concentrations. The solubility of 6xHis-SUMO-LCMV NP was not improved because there were still no appropriately sized bands in the soluble fractions (figure 3.6).

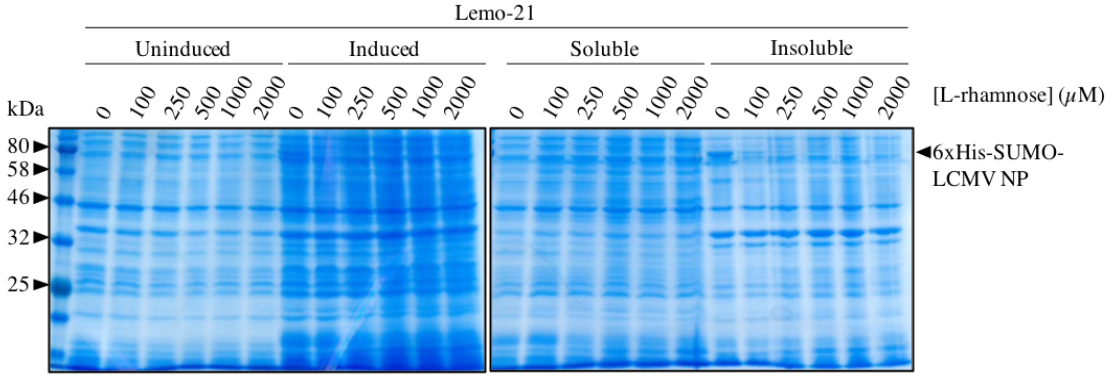

Figure 3.6: Expression of 6xHis-SUMO-LCMV NP in Lemo-21(DE3) *E. coli*. SDS-PAGE analysis, followed by Coomassie staining, of the expression of 6xHis-SUMO-LCMV NP (predicted molecular weight: ~75 kDa) in the Lemo-21(DE3) *E. coli* strain. Expression was induced using 100 µM IPTG but it is limited in the presence of increasing concentrations (ranging between 0 µM and 2000 µM) of L-rhamnose, in an attempt to reduce insolubility. Samples of Lemo-21 cells which had not been induced with IPTG (uninduced) were also examined. The total cell lysate of the induced cells were examined (induced) in addition to the soluble and insoluble fractions.

Autoinduction was then attempted as an alternative to IPTG-induction. This approach was proposed to result in a more gradual induction of expression, which can improve protein solubility. Therefore, pET28a(+)-His-SUMO-LCMV NP was transformed into the CodonPlus strain and a starter culture was then used to

inoculate autoinduction media (a mixture of glucose, lactose and glycerol), which was incubated at either 37 ℃ or 18 ℃ (figure 3.7) for a total of 54 hours. Samples were collected at 0, 3, 5, 8, 24, 32 and 54 hours post inoculation of the autoinduction media. The samples were lysed and the soluble and insoluble fractions were analysed by SDS-PAGE analysis, followed by Coomassie staining. This revealed that whilst a large proportion of the expressed 6xHis-SUMO-LCMV NP remained insoluble, an intensely stained band representing 6xHis-SUMO-LCMV NP was evident in the soluble fraction. Expression of soluble 6xHis-SUMO-LCMV NP was thus achieved using an autoinduction protocol, with harvesting at 54 h after incubation at 18 ℃ (figure 3.7: red box).

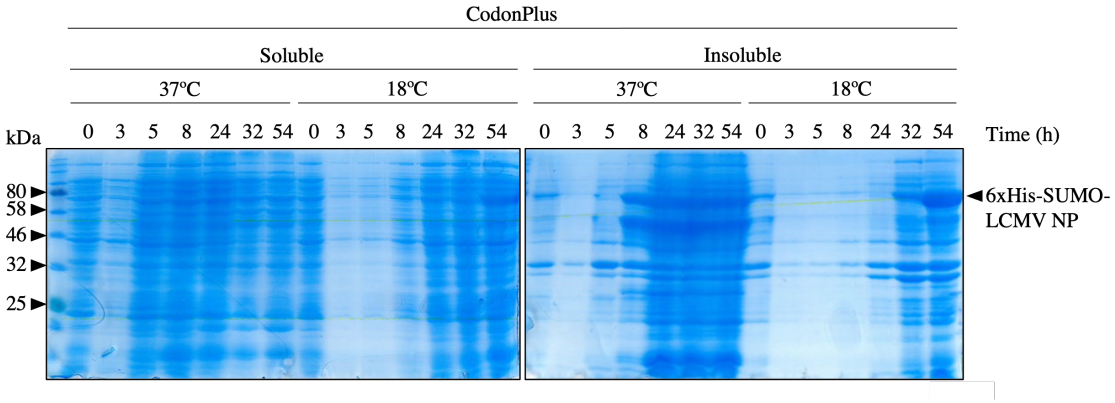

Figure 3.7: Expression of 6xHis-SUMO-LCMV NP by Autoinduction. SDS-PAGE analysis, followed by Coomassie staining, of the expression of 6xHis-SUMO-LCMV NP (predicted molecular weight: ~75 kDa) in the CodonPlus strain of *E. coli*. Cultures were used to inoculate autoinduction media, which was incubated at either 37 ℃ or 18 ℃ for 54 hours (h), with samples collected at 0 h, 3 h, 5 h, 8 h, 24 h, 32 h and 54 h. Soluble and insoluble fractions were examined to determine whether the solubility of 6xHis-SUMO-LCMV NP had been improved. A band corresponding to the molecular weight of 6xHis-SUMO-LCMV NP in the soluble fraction has been indicated using a red box.

3.2.3 Purification of Recombinant LCMV NP

Purification by Immobilised Metal-Affinity Chromatography

Following its expression, initial purification of soluble 6xHis-SUMO-LCMV NP was attempted using immobilised metal-affinity chromatography (IMAC). However, there was too little of the resulting purified 6xHis-SUMO-LCMV NP for any downstream applications (data not shown). Therefore, in an attempt to increase the abundance of purified 6xHis-SUMO-LCMV NP, batch purification trials with the *E.*

coli strains Gold, Star, Rosetta, Rosetta 2 and CodonPlus were attempted. Initially, all the strains were transformed with pET28a(+)-His-SUMO-LCMV NP and starter cultures were used to inoculate autoinduction media, which was incubated at 18 ℃ for 54 hours. The soluble fractions were collected from each culture and passed over Ni^{2+} resin. The resin was subsequently washed with increasing concentrations of imidazole, before the target protein was eluted at 300 mM imidazole (figure 3.8). Again, there was little resulting purified 6xHis-SUMO-LCMV NP. However, this suggested that the Rosetta strain was expressing the most soluble 6xHis-SUMO-LCMV NP and therefore this was chosen for large-scale purification.

It also became evident, through SDS-PAGE analysis and Coomassie staining of the purification steps of 6xHis-SUMO-LCMV NP, that there appeared to be two major purification products of approximately 80 kDa (thought to be 6xHis-SUMO-LCMV NP) and 58 kDa. These bands could not be separated by IEC or SEC (data not shown). Mass spectrometry analysis (data not shown) revealed that both bands had sequences that corresponded to LCMV NP and the 6xHis-SUMO tag, suggesting that the 6xHis-SUMO-LCMV NP was potentially being degraded. This degradation was later successfully abrogated by adding serine protease inhibitor, phenylmethylsulfonyl fluoride (PMSF).

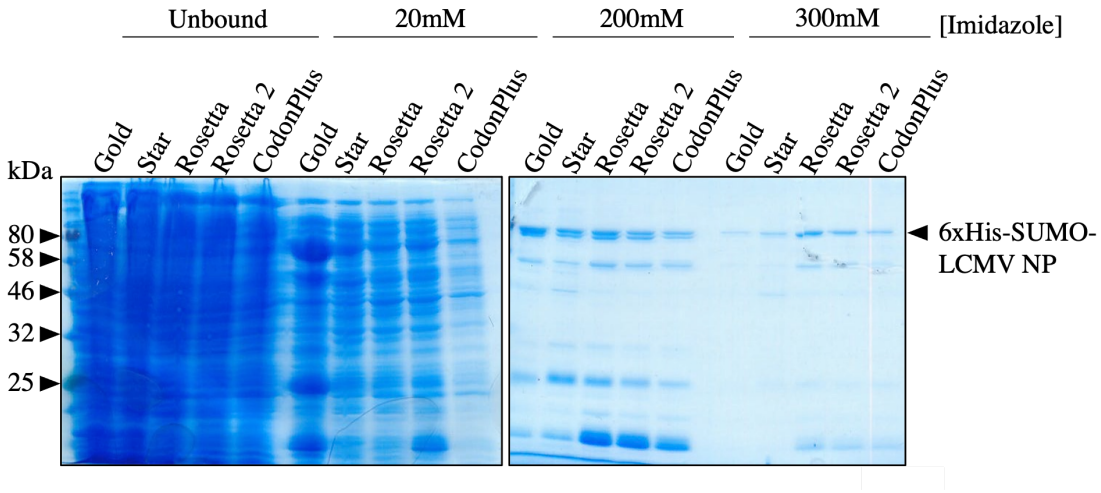

Figure 3.8: Initial Purification Trials of 6xHis-SUMO-LCMV NP
SDS-PAGE analysis, followed by Coomassie staining, of batch immobilised metal-affinity chromatography (IMAC) purification of 6xHis-SUMO-LCMV NP (predicted molecular weight: ~75 kDa), which was expressed by autoinduction in a variety of BL21(DE3) *E. coli* strains; Gold, Star, Rosetta, Rosetta 2 and CodonPlus. Soluble fractions were collected and passed over Ni^{2+} resin, which was washed with solutions containing increasing concentrations of imidazole. 6xHis-SUMO-LCMV NP was eluted at 300 mM imidazole.

Further Purification by Size-Exclusion Chromatography

The large-scale IMAC purification of 6xHis-SUMO-LCMV NP was performed and sufficient amounts of 6xHis-SUMO-LCMV NP were eluted, using 500 mM imidazole, from the IMAC column. The elutions collected were then examined by SDS-PAGE analysis (figure 3.9A). To further purify from contaminants, SEC was performed. The elution was passed over Superdex^{TM} 200 column and the absorbance at 280 nm was measured to determine which fractions contained protein after elution from the Superdex^{TM} matrix (figure 3.9B). These fractions were then analysed by SDS-PAGE and Coomassie staining (figure 3.9C), which revealed that there was there was still contamination of the target protein, despite removal of some lower molecular weight contaminants. This suggested that 6xHis-SUMO-LCMV NP was either strongly interacting with a bacterial protein, or it was being degraded. Due to the presence of contaminants in the 6xHis-SUMO-LCMV NP sample after SEC, other purification methods were investigated.

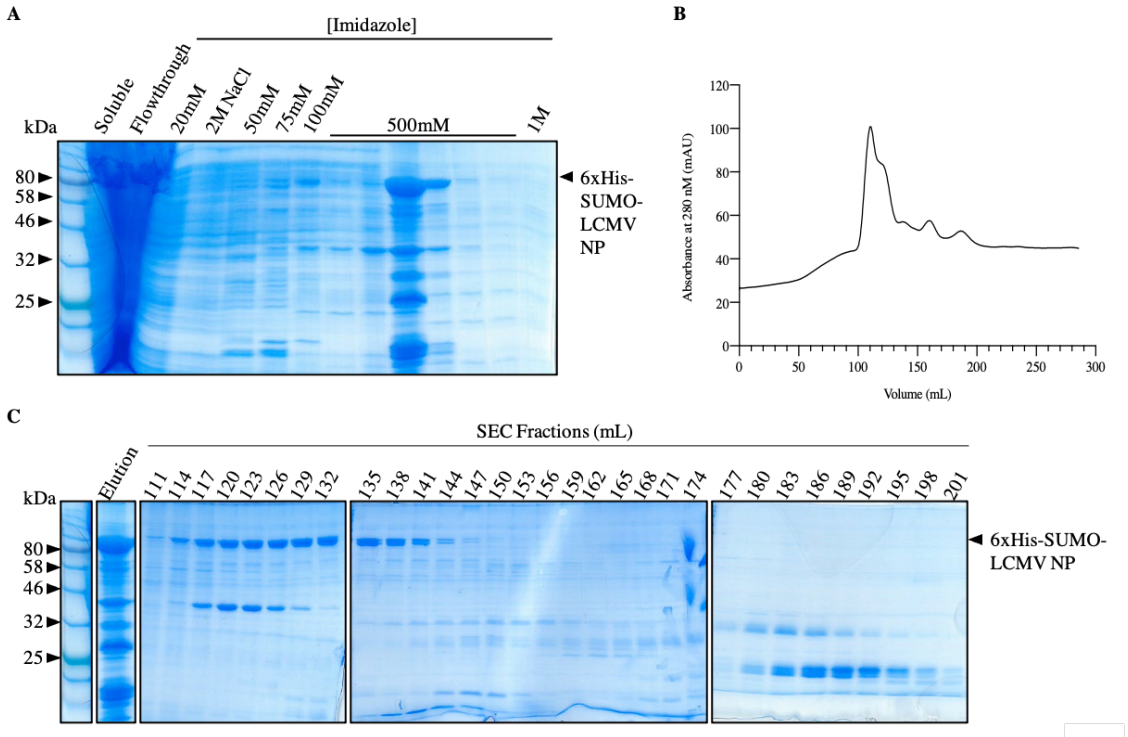

Figure 3.9: Purification of 6xHis-SUMO-LCMV NP by Size-Exclusion Chromatography
6xHis-SUMO-LCMV NP (predicted molecular weight: ~75 kDa) expression was induced by autoinduction in the Rosetta strain of *E. coli*. 6xHis-SUMO-LCMV NP was collected in a series of fractions, after it was eluted from Ni^{2+} resin using 500 mM imidazole (**A**). The elution was then resolved through size-exclusion chromatography. 3 mL fractions were collected and analysed by absorbance readings at 280 nm (**B**) and SDS-PAGE analysis, followed by Coomassie staining (**C**).

Further Purification by Immobilised Metal-Affinity Chromatography

It was then thought the purity of the 6xHis-SUMO-LCMV NP eluted from the first IMAC purification step could be improved by removing the 6xHis-SUMO tag and performing a second round of IMAC purification. Simultaneously, the 6xHis-SUMO tag was removed by ULP1 cleavage and dialysis was performed to reduce the imidazole concentration. This resulted in a mixed population of the 6xHis-SUMO tag, ULP1, uncleaved 6xHis-SUMO-LCMV NP and the desired untagged LCMV NP, which was collected in the flowthrough from the second IMAC purification (figure 3.10A).

Further Purification by Ion-Exchange Chromatography

In order to further purify and concentrate LCMV NP, the flowthrough collected from the second IMAC purification was then subjected to IEC. Fractions at each salt concentration were collected and analysed by SDS-PAGE (figure 3.10B). The fractions containing the highest concentrations of LCMV NP were pooled and then concentrated to 1 mg/mL using a centrifugal concentrator with a 10 kDa molecular weight cut off. Following densitometry calculated using ImageJ software, the purity was estimated to be approximately >85 %. On this basis, the purified LCMV NP was judged to be suitable to be used as the priming antigen for antibody production.

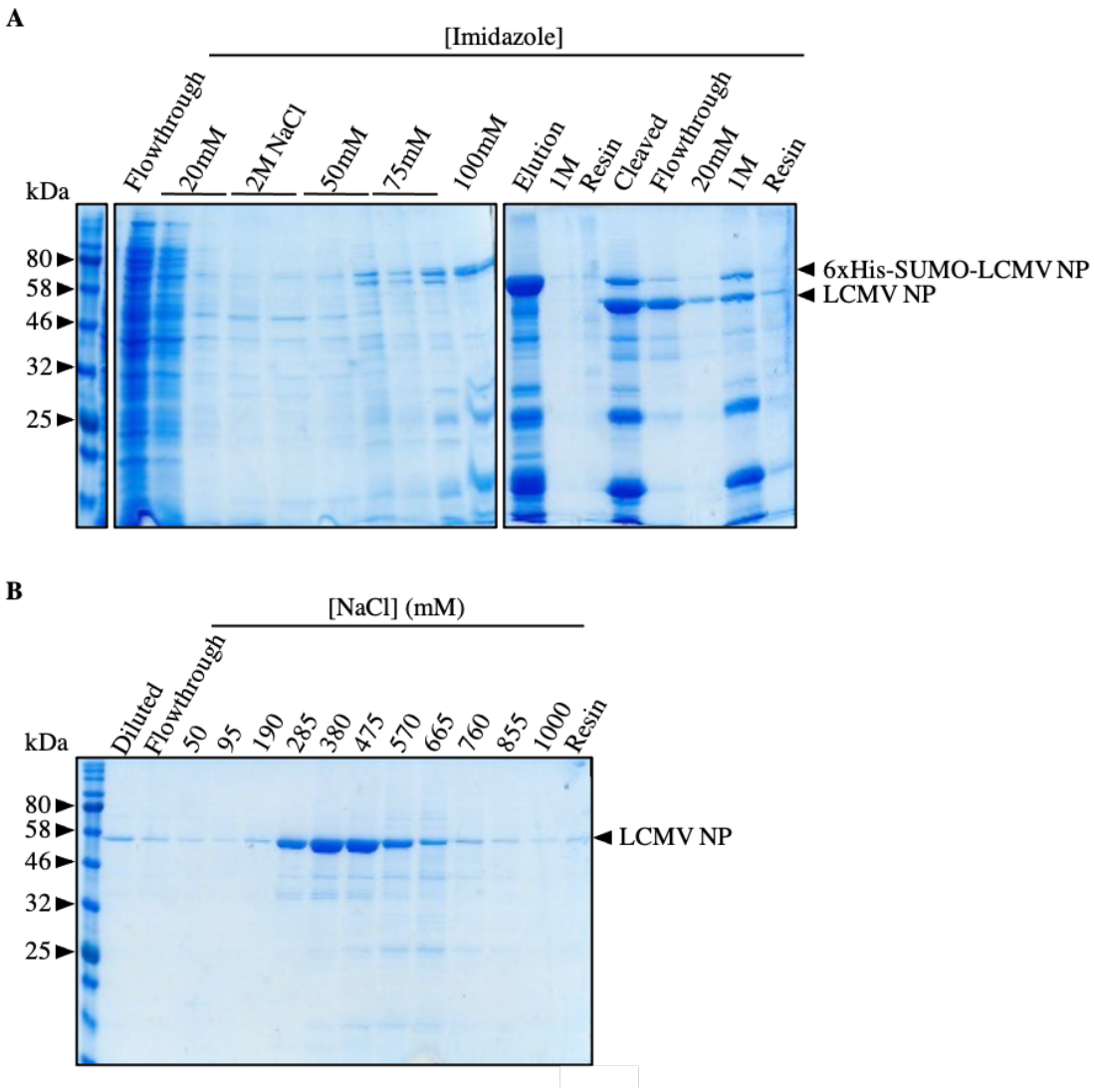

Figure 3.10: Purification of 6xHis-SUMO-LCMV NP
6xHis-SUMO-LCMV NP (predicted molecular weight: ~75 kDa) was passed over Ni^{2+} resin, attaching by its 6xHis-SUMO tag. Contaminating proteins were washed from the resin using increasing concentrations of imidazole and 6xHis-SUMO-LCMV NP was eluted using 500 mM imidazole. The washes and elution were collected to be examined by SDS-PAGE analysis, followed by Coomassie staining (**A**). The 6xHis-SUMO tag was then cleaved from 6xHis-SUMO-LCMV NP, the imidazole concentration was reduced by dialysis and LCMV NP (predicted molecular weight: ~62 kDa) was reapplied to Ni^{2+} resin, in order to further purify LCMV NP. LCMV NP was collected in the flowthrough and the contaminating proteins collected in subsequent imidazole washes, all of which were examined by SDS-PAGE analysis and Coomassie staining. The flowthrough from the second Ni^{2+} column was then further purified through ion-exchange chromatography and LCMV NP was eluted between 285 mM NaCl and 665 mM NaCl. Each fraction to examine by SDS-PAGE analysis and Coomassie staining (**B**).

3.2.4 Generation of LCMV NP Antisera

Immunisation of a sheep using 0.9 mg purified LCMV NP was performed by Antibody Applications Limited. Serum was collected pre-inoculation (day 0), post-1

inoculation (collected on day 21), post-2 inoculations (collected on 49) and post-3 inoculations (collected on day 77). The final harvest, collected on day 77 after the third inoculation, was used in the following western blotting and immunofluorescence assays.

Enzyme-linked immunosorbent assays (ELISA) performed by Antibody Applications Limited (data not shown) showed that the LCMV NP antisera was reactive to the LCMV NP antigen. However, it was necessary to determine the ability of the antisera to detect LCMV NP in complex cellular protein mixtures.

3.2.5 Validation of LCMV NP Antisera

Western Blotting Analysis

Initially, western blotting analysis was performed on ten-fold dilutions of the LCMV NP antigen sample using the antisera at dilutions between 1:1000 to 1:5000. This revealed that the LCMV NP antisera, at 1:5000, was capable of detecting 4.67 ng of LCMV NP from the original purified sample on a western blot (figure 3.11A). The LCMV NP antisera also reacted with several other bands at different molecular weights, which could have resulted from LCMV NP degradation.

Western blotting analysis was then performed on lysates harvested from BHK-21 and SHSY5Y cells, which had been infected with LCMV, at an MOI of 0.1, and incubated at 37 ℃ for 48 hours (figure 3.11B). Western blot analysis was also performed on lysates from vero and A549 cells, which had been infected with PICV, at an MOI of 1, and incubated at 37 ℃ for 24 hours (figure 3.11(C)). These western blots were stained with the LCMV NP antisera at a 1:1000 dilution and the GAPDH antibody (1:10000) as a loading control. A band was clearly visible in LCMV- and PICV-infected cell lysates, which was not present in mock-infected cell lysates, strongly suggesting the band corresponds to the NP. The cross-reactivity between the LCMV NP antisera and the PICV NP band also suggests that the LCMV NP antisera could be broadly reactive with NPs from viruses from across the *Mammarenavirus* genus.

It was also investigated whether the LCMV NP antisera would be cross-reactive to distantly related bunyavirus Hazara virus (HAZV). Western blot analysis was performed on lysates from SW13 and BSR-T7 cells, which had been infected with

HAZV, at an MOI of 0.1, and incubated at 37 ℃ for 48 hours. The western blot was probed with LCMV NP antisera (1:1000) and GAPDH antibody (1:10000) as a loading control (figure 3.11(D; α-LCMV NP)). There were no appropriately sized bands that could correspond to the HAZV NP when probed with the LCMV NP antisera, so the same western blot was then probed with HAZV NP antisera to confirm there was a successful HAZV infection (figure 3.11(D; α-HAZV NP)). There was a strong band corresponding to the HAZV NP after probing with the HAZV NP antisera, which suggests the LCMV NP antisera was not cross-reactive with HAZV. This was expected due to HAZV being classified within the *Nairoviridae* family and possessing an NP that shows little similarity in terms of primary amino acid sequence.

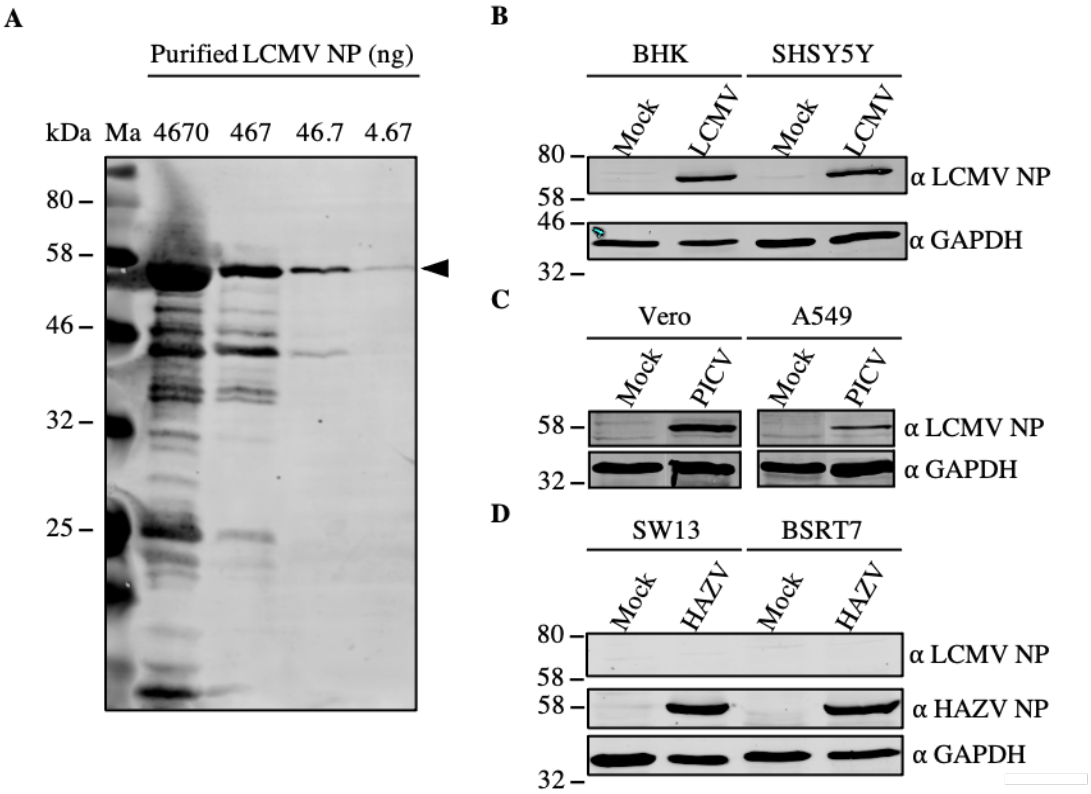

Figure 3.11: Validation of LCMV NP Antisera by Western Blotting
Western blotting analysis revealed that LCMV NP antisera (1:5000) was able to detect 4.67 nanograms of LCMV NP (**A**) from a purified sample. The antisera (1:1000) was also reactive with LCMV NP from LCMV-infected (**B**) BHK-21 and SHSY5Y cell lysates and with PICV NP from PICV-infected (**C**) vero and A549 cell lysates. The LCMV NP antisera (1:1000) was not cross-reactive with the distantly related HAZV NP from HAZV-infected SW13 and BSR-T7 cell lysates (**D**; α-LCMV NP) but the same samples showed successful HAZV infection after probing with HAZV NP antisera (1:3000) (**D**; α-HAZV NP). The position of relevant size marker bands have been indicated and the un-cropped western blots of **B**, **C** and **D** have been shown in chapter 7, in figures 7.1, 7.2 and 7.3 respectively.

Immunofluorescence Analysis

In addition to western blot analysis, the LCMV NP antisera was used to detect the subcellular localisation of the LCMV NP by immunofluorescence (IF) analysis. BHK-21 and SHSY5Y cells, which had been infected with LCMV at an MOI of 0.1 and incubated for 24 hours at 37 ℃, were fixed, permeabilised, stained with the LCMV NP antisera (1:500 dilution) and then stained with an anti-sheep secondary antibody conjugated to an Alexa-fluor 594 nm fluorophore, followed by mounting using ProLong Gold Anti-fade Mountant containing DAPI. IF analysis was also used to determine the distribution of the PICV NP in vero and A549 cells, which had been infected with PICV at an MOI of 0.1 and incubated for 24 hours at 37 ℃ and then stained in the same manner as above. IF analysis with the LCMV NP antisera was also performed on mock-infected BHK-21 and A549 cells, to determine whether there was any cross-reactivity with cellular proteins. The IF analysis revealed a cytoplasmic distribution of the LCMV NP in both infected BHK-21 and SHSY5Y cells, and it appeared that the staining was either throughout the entire cytoplasm, or present in distinct puncta of varying sizes, ranging from approximately 0.1 µm to 2.5 µm, some of which appeared to have a perinuclear localisation (figure 3.12). Several cells also showed both diffuse cytoplasmic distribution and perinuclear puncta distribution of the LCMV NP, suggesting different localisation of the LCMV NP throughout the viral lifecycle. The IF analysis also revealed a cytoplasmic distribution of the PICV NP in infected A549 and vero cells, but as opposed to LCMV, the PICV NP distribution showed primarily the formation of discrete puncta of varying sizes, ranging from approximately 0.2 µm to 4.5 µm (figure 3.12). At the 24 hour timepoint, it appeared there was little diffuse cytoplasmic distribution of the PICV NP in either A549 or vero cells, although there were many puncta were present throughout the cytoplasm, with some puncta having a perinuclear localisation. The mock-infected cells that were stained with LCMV NP antisera and analysed by IF showed no evidence of cross-reactivity between the antisera and the cellular proteins from either BHK-21 or A549 cells (figure 3.12).

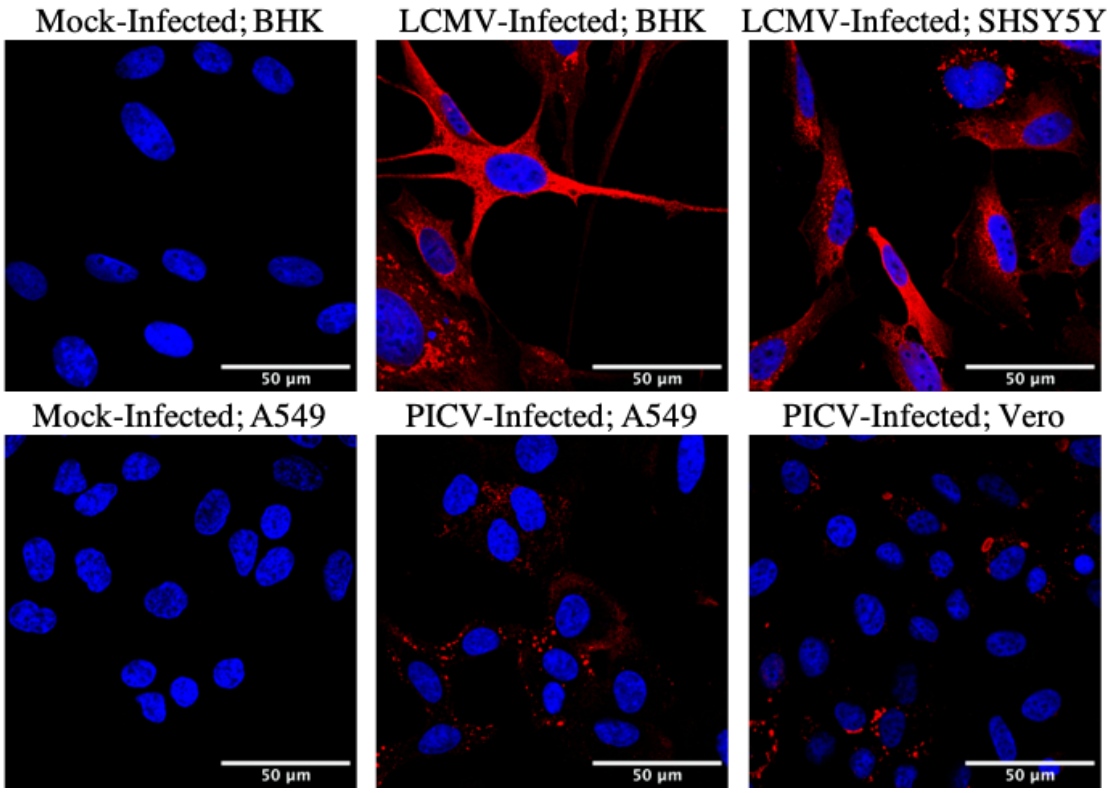

Figure 3.12: Validation of LCMV NP Antisera by Immunofluorescence
Immunofluorescence analysis confirmed that LCMV NP antisera (1:500) was able to detect LCMV NP in infected BHK-21 and SHSY5Y cells and not in mock-infected BHK-21 cells (top panels). The LCMV NP antisera (1:500) was also cross-reactive with PICV NP in infected A549 and vero cells and not in mock-infected A549 cells (bottom panels).

3.2.6 Development of the LCMV Focus Forming Assay

The LCMV NP antisera was also used to develop an assay to determine the titre of LCMV stocks. Previously, crystal violet staining had been performed on BHK-21 cells which had been infected with serially diluted LCMV (figure 3.13A). However, due to a lack of cytopathic effect (CPE) on these cells, no discernible plaques were evident, making LCMV stock titration problematical. One option that has proven successful for other similarly non-cytolytic viruses is the use of focus forming assays, in which viral antigens produced during infection of cells are detected and stained, thus revealing infected cell foci. Here, BHK-21 cells were infected with serially diluted LCMV, overlaid with methylcellulose, a semi-solid medium, and incubated for three days at 37 ℃. The BHK-21 cells were then fixed, permeabilised, blocked and stained with the LCMV NP antisera (diluted 1:1000). At this point, two types of focus forming assay were developed, one which used a colorimetric method (horseradish peroxidase [HRP]) to visualise foci and one which used fluorescence

(EVOS). After LCMV NP antibody staining, the HRP focus forming assay was washed with PBS and then stained with a HRP-conjugated anti-sheep secondary antibody (1:500). Then, 4-chloro-1-naphthol (4C1N) was added to the cells, which is converted into a purple precipitate in presence of HRP. This results in the formation of purple foci that are visible by eye (figure 3.13B). Alternatively, for the EVOS focus forming assay, the LCMV NP antibody staining was followed with staining with an Alexa-fluor 594 nm fluorophore-conjugated anti-sheep secondary antibody (1:1000). The entire well was then imaged at 4X magnification using the EVOS FL 2 automated microscope (figure 3.13(C)). In both types of focus forming assay, the LCMV NP antisera was reactive with the infected cells and showed foci of infection, with each arisen from a single infected cell, which can therefore provide a titre in focus forming units (ffu). BHK-21 cells were also mock-infected in all these assays (figure 3.13; Mock), incubated and stained in the same manner as the infected. There were no discernible foci in the mock-infected BHK-21 cells, confirming the foci had arisen from LCMV-infected cells. For titre determination in the future chapters, the EVOS focus forming assay was used, due to the ease of visualising the foci.

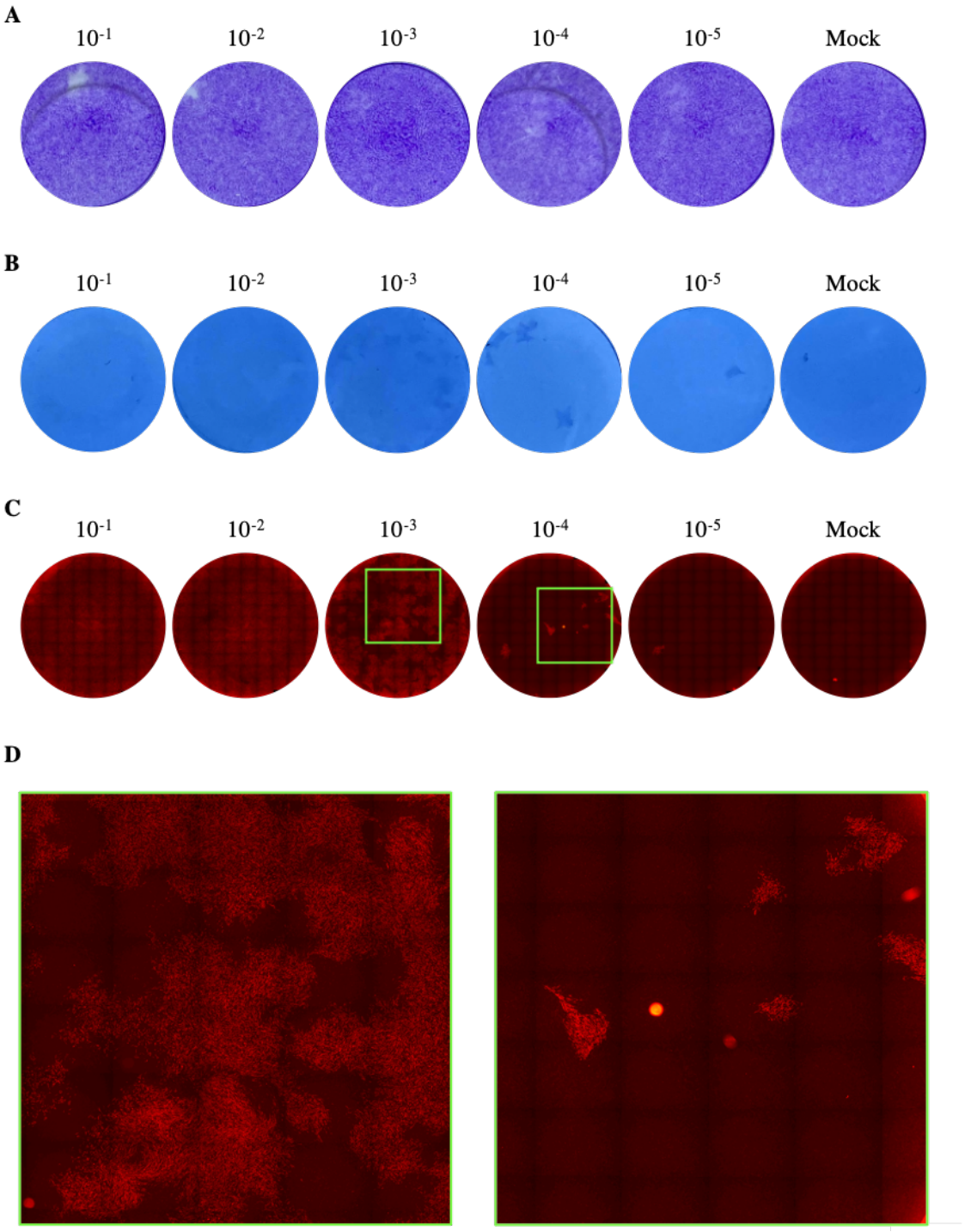

Figure 3.13: Development of Focus Forming Assay to Determine LCMV Titre The LCMV NP antisera was used to develop a focus forming assay in order to be able to determine the titre of LCMV stocks. Previously crystal violet staining techniques of LCMV-infected BHK-21 plaque assays were unsuccessful (**A**). BHK-21 cells were infected with serial dilutions of LCMV and stained with LCMV NP antisera (1:1000). Some LCMV-infected BHK-21 plaque assays were stained with anti-sheep secondary antibodies, which were conjugated to horseradish-peroxidase (1:500), and then stained with 4-chloro-1-naphthol to visualise a colour change at the infected foci (**B**). The other LCMV-infected BHK-21 plaque assays were then stained with anti-sheep secondary antibodies, which were conjugated to 594 nm fluorophores (1:1000), and fluorescent foci were imaged on the EVOS FL 2 automated microscope (**C**). Magnified images from the 10^{-3} and 10^{-4} dilutions have been shown in (**D**). All images in (**B**), (**C**) and (**D**) had their brightness and contrast adjusted using the same values, in ImageJ and PowerPoint.

3.3 Chapter Summary and Discussion

This chapter describes the generation of LCMV NP antisera, which was successfully used to analyse the subcellular distribution of LCMV NP during infection using immunofluorescence and to identify infected cells as a means of determining the titre of LCMV stocks. Here, the expression and the purification of the recombinant LCMV NP from *E. coli* was optimised to produce sufficient recombinant LCMV NP as an antigen for the generation of a polyclonal antibody. The antibody was reactive with the LCMV NP from infected BHK-21 and SHSY5Y cells and did not react with the unpurified lysates from mock-infected cells. The LCMV NP antisera was also cross-reactive with PICV, a mammarenavirus classified within the New World clade of the *Mammarenavirus* genus, but it was not cross-reactive with viruses in the *Nairoviridae* family.

Immunofluorescence experiments performed in this chapter utilising the LCMV NP antibody successfully identified a cytoplasmic localisation of the LCMV NP in BHK-21 and SHSY5Y cell lines and of the PICV NP in A549 and Vero cell lines. These experiments showed both a diffuse cytoplasmic distribution and puncta-formation of the NP during the LCMV infection cycle, but it appeared the NP predominantly adopted a puncta formation in PICV infected cells. This was in accordance with previous research that found a cytoplasmic distribution and puncta formation in LCMV NP-transfected and LCMV-infected cells and were able to attribute the puncta formation to a single phosphorylated residue (T206) (Baird et al., 2013; Knopp et al., 2015). The research here shows that the PICV NP also appears to form puncta in infected cells, suggesting that this is a feature also attributed to New World clade A arenavirus members. PICV NP also shares the T206 residue identified in LCMV NP as the phosphorylated residue responsible for puncta formation, which could suggest the same method of puncta regulation.

The LCMV NP antibody generated here could also be used to develop inexpensive and robust diagnostic tools, such as colorimetric immunoassays (including enzyme-linked immunosorbent assays and lateral flow assays). This could allow easy and rapid identification of LCMV-infected individuals, which may help prevent morbidity associated with organ transplantation-transmitted LCMV infections. The reactivity with PICV also suggests a cross-reactivity with multiple

mammarenaviruses and such a diagnostic tool could be extrapolated to easily identify and diagnose cases of Lassa fever and New World haemorrhagic fevers, permitting earlier therapeutic intervention and improving disease outcome. The simplicity of these assays and the requirement of basic equipment would also permit their use in lower economy countries.

Further work could involve improving the yield of soluble recombinant LCMV NP. The yield of LCMV NP could be improved by expression from a different vector, such as the pET46-ek/LIC vector or the pMAL-c2X-derived pLou3 vector, both of which were successfully used to express full-length LASV NP in a bacterial expression system and resulted in a high yield, which was suitable for crystallisation (Hastie et al., 2011a; Qi et al., 2010). The LCMV NP yield could also be improved by incorporating a bacterial signal peptide to translocate the protein to the periplasm of *E. coli* for expression. The oxidising environment of the periplasm would allow disulphide bond formation, which could provide a more native conformation, improving solubility (Malik, 2016). In the trials attempted in this chapter, the recombinant LCMV NP appeared to have the highest yield of soluble protein in the Rosetta and CodonPlus strains, both of which have been supplied with rare codons (Kaur et al., 2018). This suggests the need for either codon-optimisation of the LCMV NP sequence or its expression in another system. Full-length LASV NP was also successfully expressed using a baculovirus/insect expression system, suggesting insect expression or eukaryotic expression systems would produce a higher yield of soluble LCMV NP (Brunotte et al., 2011b). Alternatively, expression of individual N-terminal and C-terminal domains may be more successful, as shown previously (Hastie et al., 2011a,b; Zhang et al., 2013; Jiang et al., 2013; West et al., 2014; Yekwa et al., 2017).

Increasing the yield of soluble recombinant LCMV NP significantly could allow the determination of its full-length structure, either through x-ray crystallography or electron microscopy techniques. This project demonstrated that bacterial expression of LCMV NP resulted in low yield of full-length soluble LCMV NP, either due to degradation or loss through insolubility. With the availability of the full-length LASV NP structure and the C-terminal domain of LCMV NP, an alternative method to predict the structure of the full-length LCMV NP could be to employ the use of artificial intelligence software, such as AlphaFold or RosettaFold. Understanding

the structure of the NP is important to determine the interactions between NP and RNA and the mechanisms behind NP multimerisation for RNP formation, both of which can be targeted for disruption in the development of antivirals.

Chapter 4

Development of a Reverse Genetics System to Recover Infectious LCMV

4.1 Chapter Introduction

Reverse genetics systems allow the manipulation of viral genomes and the subsequent investigation into the effects particular mutations have on the viral lifecycle. The transfection of plasmids, which express the viral vRNA or cRNA and support proteins, into cells allows the establishment of a viral replication-transcription cycle and the formation of infectious virus particles. Introduction of mutations into the viral genome and proteins permits further understanding of the virus lethality, pathogenesis and identification of individual residues that can be responsible for viral protein cellular localisation or protein-protein interactions.

This chapter describes the creation of a reverse genetics system designed to generate recombinant infectious lymphocytic choriomeningitis virus (rLCMV) entirely from complementary DNA (cDNA) sources within mammalian cells. This system was constructed in order to provide a platform for the generation of genetically-altered LCMV variants, as well as providing a source of infectious wild type (WT) LCMV with a consistent genotype that exhibited stable growth properties and high viral titres.

4.1.1 Introduction to Forward and Reverse Genetics

Forward and reverse genetics are terms used to describe the workflow of genetic analysis that aim to link genotype with phenotype, thus assigning functions to genetic elements. Forward genetics described experiments in which an initially observed phenotype is assigned to a subsequently identified genetic lesion. On the contrary, reverse genetics describes an experimental workflow in which genetic elements are first altered, after which an associated phenotype, and thus gene function, is described. In the context of viruses, a reverse genetics system is one that allows site directed manipulation of any part of the viral genome that can subsequently be used to assign gene function. Some such systems allow the recovery of autonomously replicating viruses that are indistinguishable from natural isolates, whereas other systems generate truncated viral genomes known as "replicons" or "mini-genomes", which require the co-expression of viral proteins to support gene expression activities, and these "support" proteins are most often expressed from transfected plasmids. Such mini-genome systems carry a major drawback in that they do not represent authentic self-replicating entities, but they do offer an important advantage in that they can often allow the study of mutations that would be lethal in the context of infectious virus.

Virus reverse genetics provides the opportunity to study *cis*-acting sequences involved in the control and regulation of gene expression, such as promoters, secondary structure elements, transcription start and stop sites, and genome packaging signals. Reverse genetics also allows interrogation of roles of *trans*-acting factors such as entire proteins, their motifs, and single amino acid residues. The introduction of specific mutations into the viral genome, via reverse genetics, provides tools to help understand host-virus interactions and mechanisms of viral virulence. Determining the genetic regulation over viral virulence also assists with the development of safer attenuated recombinant arenavirus vaccines (Martínez-Sobrido and de la Torre, 2016).

The use of reverse genetics systems also permits the manipulation of viral genomes for studies not directly associated with gene function. A common example of this is the generation of genetically altered viruses in which fluorescent proteins or epitope tags have been fused to viral proteins, which, for example, can facilitate the analysis

of viral replication kinetics, identify subcellular localisation of viral proteins or assist purification of viral complexes from cells.

4.1.2 Development of Viral Reverse Genetics Systems

The first virus to be rescued entirely from transfected DNA sequences was in 1976 and involved the rescue of infectious recombinant SV40 that contained phage λ sequences (Goff and Berg, 1976). Then, the first RNA virus to be rescued from transfected DNA sequences, in 1978, was bacteriophage Qβ (Taniguchi et al., 1978), followed shortly in 1981 by the rescue of poliovirus from transfected cells (Racaniello and Baltimore, 1981). The positive-sense RNA genomes of bacteriophage Qβ and poliovirus are also in the messenger RNA sense, so their transcription from DNA plasmids results in the presence of the correct sense genome that can express the viral proteins and establish an infection. The development of reverse genetics systems for negative sense RNA viruses proved more difficult because negative-sense RNA genomes are not expressed in the messenger RNA sense, meaning viral proteins will not be transcribed and translated to kick-start infection (Pekosz et al., 1999). Furthermore, negative-sense vRNAs and the positive-sense cRNAs both require encapsidation for recognition by the negative-sense viral polymerase and subsequent replication and transcription (Pekosz et al., 1999). Therefore, in order to generate infectious negative-sense RNA viruses, trans-complementation of all viral proteins involved in viral transcription and replication is required, often by supplying corresponding support plasmids (Pekosz et al., 1999).

In 1989, a "mini-genome" reverse genetics system was developed for influenza A virus, a segmented negative-sense RNA virus, but it required infection with "helper" influenza virus (Luytjes et al., 1989). Subsequently, in 1994, rabies virus, a non-segmented negative-sense RNA virus, was successfully rescued from transfected cDNAs, without the need of infection with "helper" virus (Schnell et al., 1994). Following this, several other reverse genetics systems were developed for non-segmented negative-sense RNA viruses including vesicular stomatitis virus (VSV) (Whelan et al., 1995; Lawson et al., 1995), measles virus (Radecke et al., 1995), Sendai virus (Garcin et al., 1995) and respiratory syncytial virus (Collins et al., 1995). Then, in 1996, a reverse genetics system was developed to rescue

Bunyamwera virus (BUNV), a segmented negative-sense RNA virus, which did not require infection with "helper" virus (Bridgen and Elliott, 1996). This was achieved through the transfection of cells with plasmids expressing the full-length cDNA copy of each of the three BUNV genomic segments, which were flanked with a bacteriophage T7 promoter and the hepatitis delta virus ribozyme sequence. This enabled the expression of cRNA segments, which were transcription- and replication-competent and could therefore establish an infection. This system has since been applied to many other viruses, permitting in-depth analysis of how the viral genomic elements are responsible for virulence and pathogenesis.

4.1.3 Arenavirus Mini-Genome Systems

The first mini-genome systems for the arenaviruses were developed in the early 2000s, for LCMV (Lee et al., 2000), TCRV (López et al., 2001) and LASV (Hass et al., 2004), followed shortly by mini-genome systems for JUNV (Albariño et al., 2009) and PICV (Lan et al., 2009). The process involves the transfection of the necessary viral proteins and a short model genome, which expresses a reporter gene such as chloramphenicol acetyltransferase (CAT). This therefore allows the study of the transcription and replication stages of the viral lifecycle, but not the study of entry, packaging or budding because the structural proteins that are required for formation of infectious particles and subsequent entry (i.e., GPC and ZP) have been replaced with the reporter gene. Mini-genome systems have been instrumental for determining the multiple roles of the viral proteins and the genomic regulatory elements. Their use has led to the recognition that the LP oligomerises, which is necessary for its replicative and transcriptive activities (Sánchez and de la Torre, 2005; Brunotte et al., 2011b). Furthermore, it was through using mini-genome systems that endonuclease activity of the LP was found to be necessary for viral transcription (Morin et al., 2010). Mini-genome systems were also used for understanding the minimum residues in the 3' and 5' UTRs required to act as the LCMV LP promoter and the importance of these residues in the formation of the genomic panhandle (Perez and de la Torre, 2003a). Additionally, mutations introduced using mini-genome systems identified the IGR as a transcription termination signal (Pinschewer et al., 2005).

4.1.4 Arenavirus Reverse Genetics Systems for Recovery of Infectious Virus

The first reverse genetics system for the recovery of infectious arenaviruses was designed to rescue pseudotyped LCMV, which expressed VSV glycoproteins (rLCMV/VSVG) (Pinschewer et al., 2003). Here, the LCMV GPC ORF was replaced with the VSV G in the cDNA copy of the S segment (Pinschewer et al., 2003). This was then transfected into cells, which were subsequently infected with WT LCMV. Following this, a selective pressure was applied by passaging the viruses through SKI-I/S1P-deficient cells and therefore selecting for rLCMV/VSVG (Pinschewer et al., 2003). Whilst this method successfully generated infectious recombinant LCMV, the genome of which could be mutated and analysed, it was laborious and time-consuming. In 2006, this problem was solved through the simultaneous development of two reverse genetics systems designed to rescue infectious LCMV (Sánchez and de la Torre, 2006; Flatz et al., 2006). Another reverse genetics system, designed to rescue docile and aggressive strains of LCMV, was then developed in 2008 (Chen et al., 2008). It was quickly followed by reverse genetics systems for PICV (Lan et al., 2009), JUNV (Albariño et al., 2009; Emonet et al., 2011), LASV (Albarino et al., 2011), LUJV (Bergeron et al., 2012) and MACV (Patterson et al., 2014). Recently, a reverse genetics system has been designed to rescue TCRV (Ye et al., 2020).

Reverse genetics systems involve the transfection of plasmids expressing the positive sense copy of the vRNA (cRNA) and the minimal trans-acting viral factors, which, in the case of arenaviruses, is NP and L. This results in the synthesis of recombinant infectious viruses. For PICV and JUNV, the cRNA segments are sufficient to generate recombinant viruses, suggesting the cRNA may be able to function as mRNA (Lan et al., 2009; Albariño et al., 2009). The development of reverse genetics systems for the arenaviruses has allowed further study of LASV entry, the cellular S1P/SKI-1 processing sites of the arenavirus GPC and the role of the NP in subversion of the IFN-I induction pathway (Rojek et al., 2008b; Albariño et al., 2009; Martínez-Sobrido et al., 2009). Furthermore, reverse genetics has allowed identification of viral genetic determinants of virulence, by creating avirulent and virulent forms of PICV (Lan et al., 2009; Liang et al., 2009) and docile and aggressive

forms of LCMV (Chen et al., 2008). Finally, arenaviruses expressing reporter genes have also been created, simplifying the screening platform for identifying necessary host genes or successful antivirals (Emonet et al., 2009; Ngo et al., 2015; Caì et al., 2018). Initially, in order to include a reporter gene in recombinant infectious viruses, the reverse genetics system was used designed to rescue trisegmented arenaviruses (Emonet et al., 2009). Here, the NP and GPC ORFs were physically separated onto two S segments, offering a selective pressure on the virus to retain both S segments, and providing two possible sites for the reporter gene (Emonet et al., 2009). Subsequently, reverse genetics systems have been developed where the reporter gene is upstream of the NP gene, but separated by a self-cleaving peptide (Ngo et al., 2015; Caì et al., 2018).

4.1.5 Introduction to T7P-driven Reverse Genetics Systems

In 2006, when the LCMV reverse genetics systems were developed simultaneously, one system employed a T7P-driven expression (Sánchez and de la Torre, 2006) while the other system utilised RNA polymerase I/II-driven expression (pol-I/II) (Flatz et al., 2006). Both systems were successful and were found to have similar efficiencies (Sánchez and de la Torre, 2006). T7P-driven reverse genetic systems have since been developed for many other mammarenaviruses, including LASV (Cai et al., 2020), PICV (Lan et al., 2009), TCRV (Casabona et al., 2009; López et al., 2001), LUJV (Bergeron et al., 2012) and JUNV (Albariño et al., 2009). The T7P-driven system was chosen for experiments performed in this chapter because the expression of the pol I/II system in the nucleus raises the potential risk of splicing of the primary viral RNA transcripts, which would severely limit the rescue of infectious virus (Flatz et al., 2006). Moreover, the T7P-driven system can be functional in multiple cell lines because the cells can be stably transfected with a plasmid expressing the T7P whereas pol I/II-driven systems are reliant on the plasmids containing the promoter sequence that corresponds to the species-specific polymerase and therefore can only be performed in cell lines of that species (Flatz et al., 2006). Performing the reverse genetics system in different cell lines can be useful when introducing mutations would make the virus sensitive to host cell factors that are present in the current cell line;

the system can therefore be transferred to a cell line deficient in these factors. Here, we use the BSR-T7 cell line, which has been stably transformed with a plasmid expressing T7P. BSR-T7 cells are derived from BHK-21 cells and both are deficient in retinoic acid-inducible gene I (RIG-I) (Habjan et al., 2008). The initial T7P transcript of the cRNA is not capped with M^7G, exposing the 5' triphosphate group and strongly activating the RIG-I-mediated type I IFN response (Hornung et al., 2006; Kim et al., 2004; Pichlmair et al., 2006; Plumet et al., 2007). This response is circumvented by using the RIG-I-deficient BSR-T7 cell line (Habjan et al., 2008).

4.1.6 Chapter Aims

In this chapter, the aim was to design a reverse genetics system that generated recombinant infectious LCMV from cDNA. Following this, subsequent aims were to optimise this system in order to generate a high titre of recombinant LCMV. Previous studies discovered that our current WT LCMV stock had issues with repeated stock passaging and limiting titres, therefore generation of the recombinant LCMV from this system provided a way to circumvent these issues. Another aim of this chapter was to utilise the reverse genetics system to produce genetically-altered LCMV variants that expressed fluorescent (eGFP) or purification (6xHis) tags, in order to permit the development of anti-arenaviral-drug screening platforms and the purification of RNPs from virally-infected cells.

4.2 Results

4.2.1 Design of the Reverse Genetics Plasmids

Based on studies by (Sánchez and de la Torre, 2006) and (Flatz et al., 2006), a reverse genetics system designed to rescue recombinant wildtype LCMV (rLCMV-WT) was developed. Plasmids pUC57-S and pUC57-L were designed to express the cRNA species of the S and L segments of the clone 13 strain of LCMV, respectively (GenBank accession numbers: S; DQ361065.2 and L; DQ361066.1). In pUC57-S and pUC57-L, the S and L segments were flanked at their 5' ends by a T7RP promoter sequence (T7P) and at their 3' ends with the hepatitis delta virus ribozyme (HDV

Rz) and T7RP terminator sequences (T7T) (figure 4.1).

Typically, the T7P sequence end in three terminal G residues, which improves T7RP activity for increased synthesis of primary RNA transcripts. The T7P sequences in pUC57-S and pUC57-L lack two of the three G residues because the addition of two non-viral G residues to the 5' end of the cRNA reduces its recognition by the viral LP (Perez and de la Torre, 2003a). Perez and de la Torre (2003) showed that whilst a T7P containing a single terminal G residue did reduce the levels of T7RP transcripts, it improved the subsequent amplification by the LCMV LP (Perez and de la Torre, 2003a). The single terminal G residue improves amplification by the LCMV LP because it acts as the non-templated G residue characteristically found at the 5' end of arenavirus cRNAs (Garcin and Kolakofsky, 1990, 1992).

The T7RP has low termination efficiency at the T7T sequence and can result in runoff transcription (Mairhofer et al., 2015; Pattnaik et al., 1992). This can result in the appearance of additional sequences on the 3' end of the primary transcript, which can negatively affect the formation of authentic arenavirus ends and the structure of the panhandle. In order to promote the formation of authentic arenavirus ends, a self-cleaving ribozyme, such as the HDV Rz, is added (Pattnaik et al., 1992). The HDV Rz (complementary sense) was incorporated downstream of the 3' UTR but upstream of the T7T in both pUC57-S and pUC57-L. The HDV Rz is not influenced by upstream sequences, except for the residue that is immediately 5' adjacent to the cleavage site, where C is the preferential residue and G is the least preferential residue (Perrotta and Been, 1991; Perez and de la Torre, 2003a). The arenavirus genome terminates with an essential G residue, which cannot be mutated because it results in a complete lack of RNA synthesis (Perez and de la Torre, 2003a). However, the presence of this G residue next to the cleavage site resulted in less than 1 % of MG transcripts being cleaved (Perez and de la Torre, 2003a). In order to promote ribozyme autolytic activity without affecting RNA synthesis, an additional C residue was introduced between the 3' end of the segment and the 5' start of the ribozyme, enabling site-specific cleavage and improving the processivity of the ribozyme (Ke et al., 2004; Perez and de la Torre, 2003a; Sánchez and de la Torre, 2006). This allowed a high rate of RNA synthesis with correctly formed arenavirus ends.

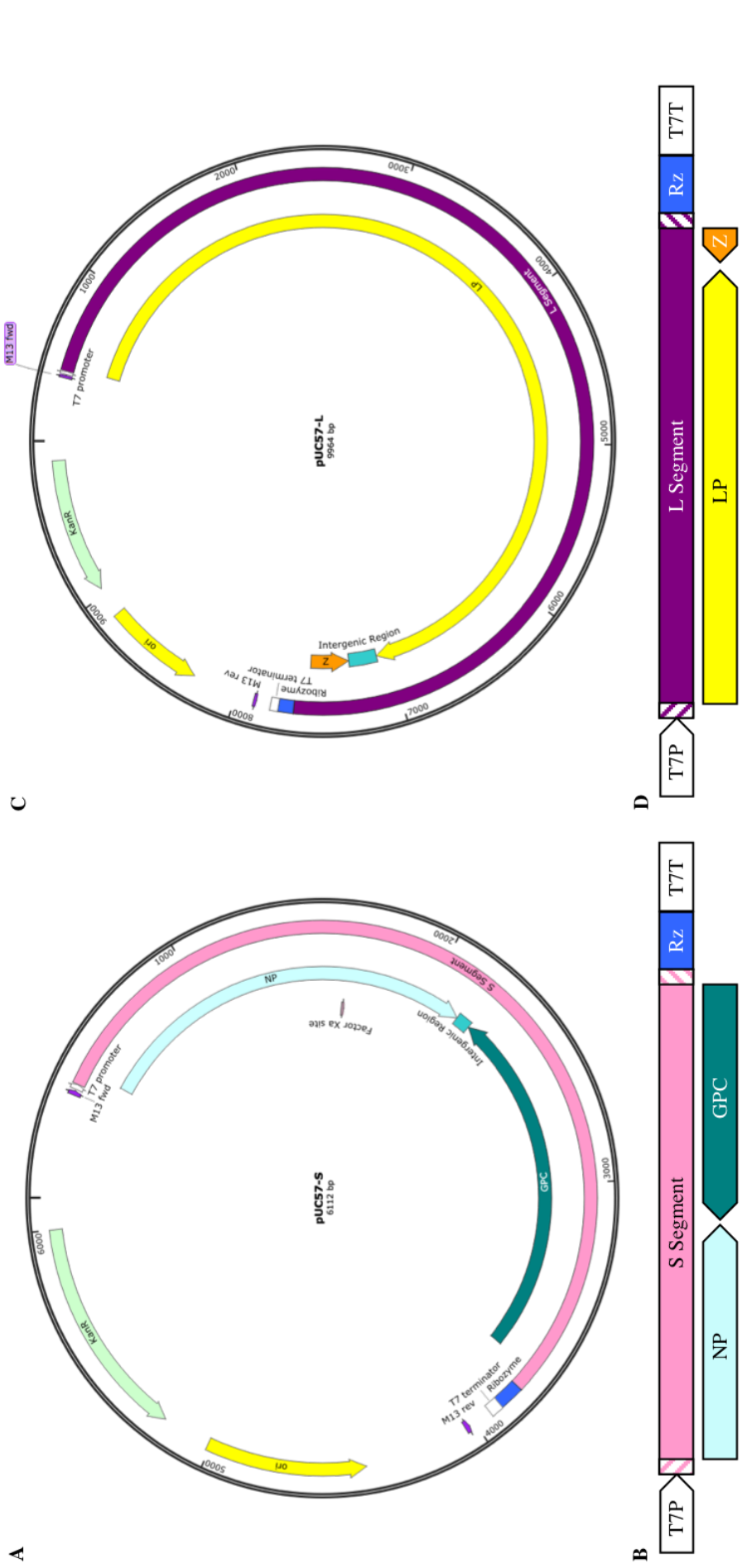

Figure 4.1: Vector Maps of pUC57-S and pUC57-L Vector maps of pUC57-S (**A**) and pUC57-L (**C**), showing the LCMV S segment (pink) and the LCMV L segment (purple) in the pUC57 vectors. The open reading frames have also been depicted separately to show the direction of translation and are labelled as follows; the nucleocapsid protein (NP; light blue), the glycoprotein complex (GPC; teal), the L polymerase (LP; yellow), the Z matrix protein (Z; orange) and the untranslated regions of the S and L segments (pink or purple diagonal) (**B** and **D**). The position of the cRNA segments in respect to the T7RP promoter (T7P; white), hepatitis delta virus ribozyme (Rz; blue) and the T7RP terminator (T7T; white) has also been shown (**B** and **D**). The vector maps were created using SnapGene software.

We also constructed support plasmids to provide an initial source of LCMV NP and LP. cDNAs representing these ORFs were successfully isolated from pUC57-S and pUC57-L, using specific primers designed to amplify the NP and LP ORFs without the segment-specific untranslated regions. The primers also introduced flanking complementary restriction sites, *Nhe*I and *Xho*I, which were used to ligate the NP and LP ORFs into the pUC57 vector, forming constructs pUC57-NP and pUC57-LP (figure 4.2).

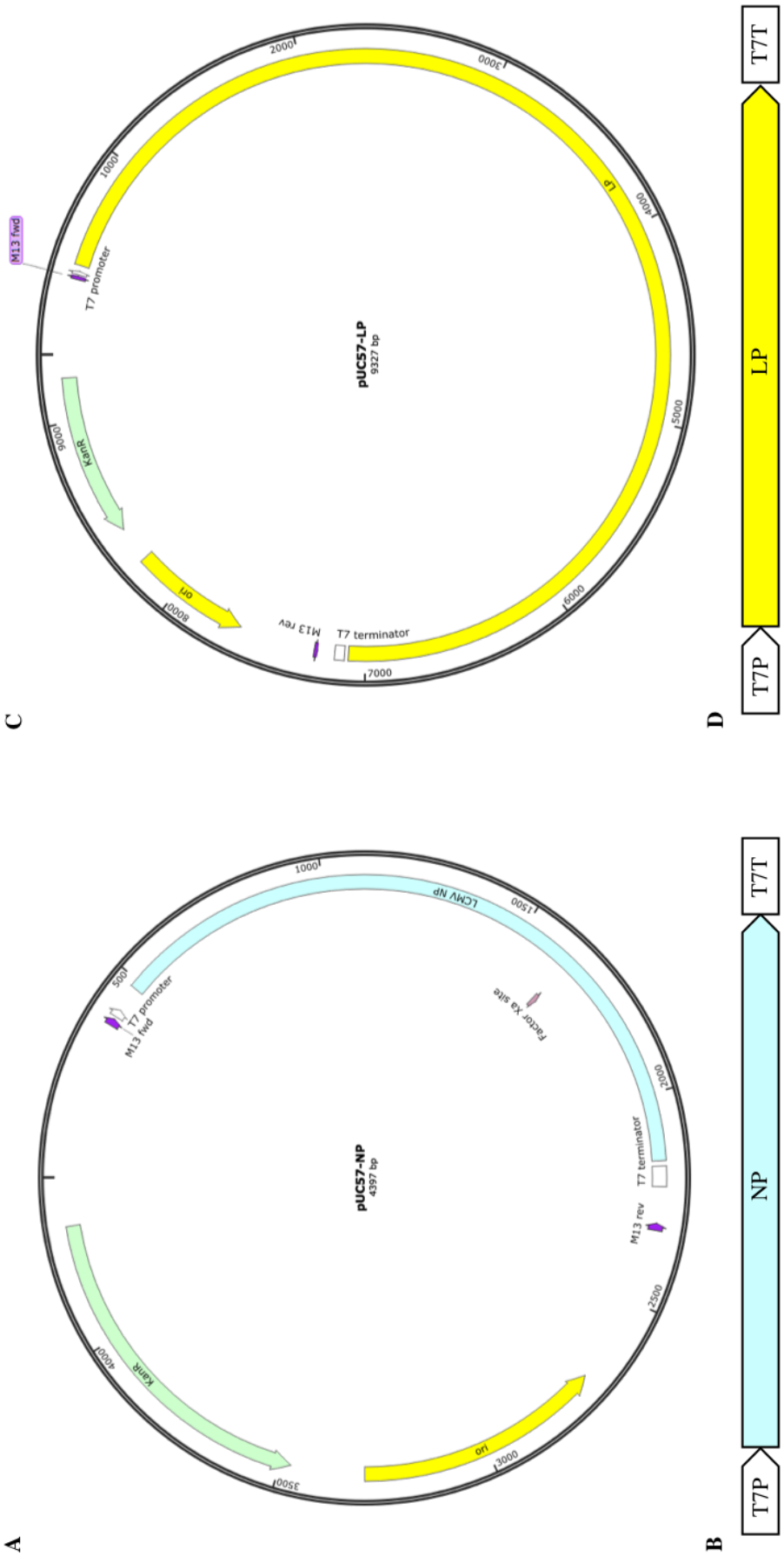

Figure 4.2: Vector Maps of pUC57-NP and pUC57-LP
Vector maps of pUC57-NP (**A**) and pUC57-LP (**C**), showing the LCMV NP ORF (light blue) and the LCMV LP ORF (yellow) in the pUC57 vectors. The open reading frames have also been depicted separately to show the direction of translation and are labelled as follows; the nucleocapsid protein (NP; light blue) and the L polymerase (LP; yellow) (**B** and **D**). The position of the open reading frames in respect to the T7RP promoter (T7P; white) and the T7RP terminator (T7T; white) has also been shown (**B** and **D**). The vector maps were created using SnapGene software.

4.2.2 Generation of Recombinant Wildtype LCMV

To generate recombinant wildtype LCMV (rLCMV-WT), pUC57-S, pUC57-L, pUC57-NP and pUC57-LP (figures 4.1 and 4.2) were transfected into BSR-T7 cells, in addition to a T7RP-expressing plasmid (pUC57-T7), following the process depicted in figure 4.3. pUC57-T7 was added to ensure uniform expression of the T7RP in the BSR-T7 cells. Mock and control transfections in which either no plasmids were provided (mock) or the plasmids pUC57-L and pUC57-LP were omitted (-L) and for which rescue of rLCMV was not possible were performed alongside.

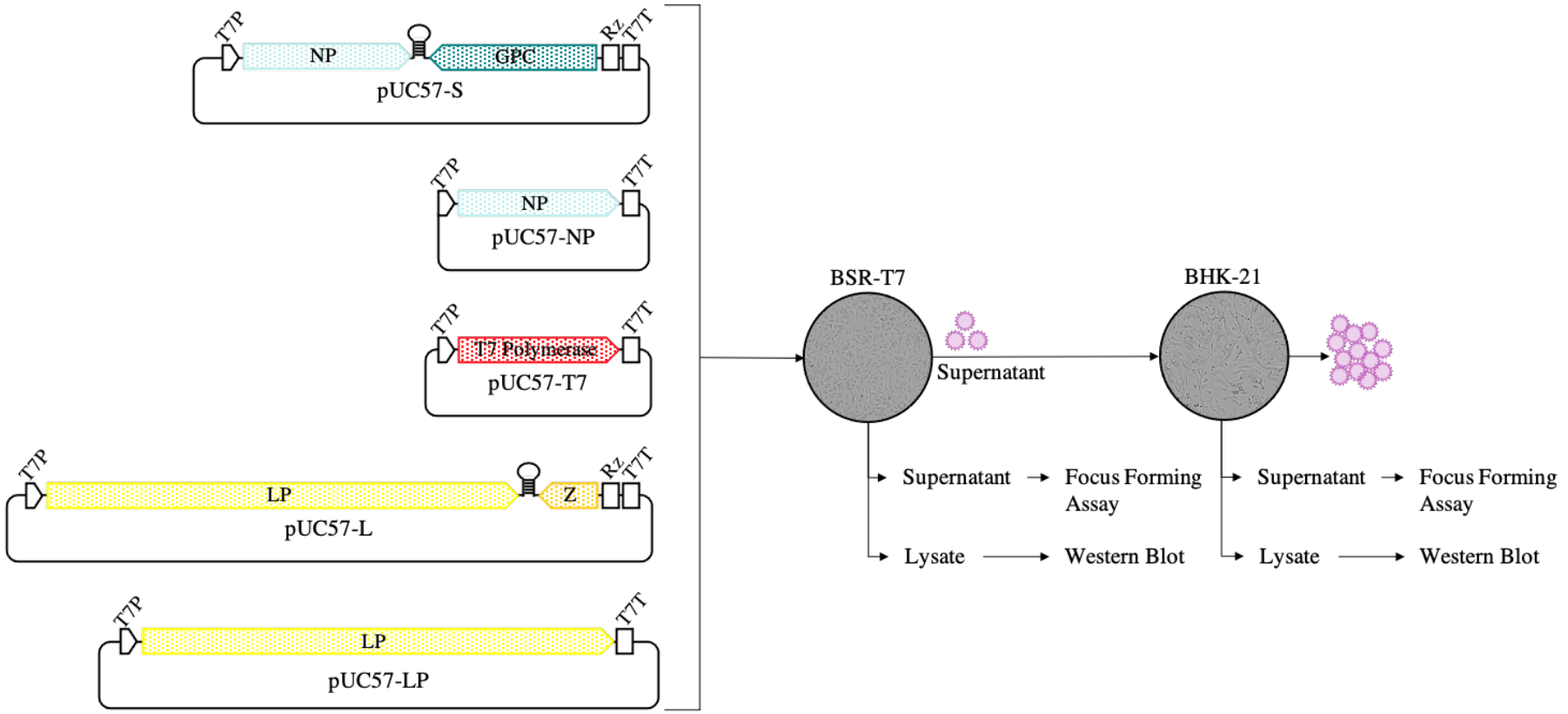

Figure 4.3: Schematic of the rLCMV-WT Rescue System
This figure describes the plasmids required for the the rLCMV-WT rescue system. It depicts the the open reading frames (and their direction of translation) of nucleocapsid protein (NP; light blue), the glycoprotein complex (GPC; teal), the L polymerase (LP; yellow), the Z matrix protein (Z; orange) and T7 RNA polymerase (T7 Polymerase; red) and their position in respect to the T7 RNA polymerase promoter (T7P; white), the hepatitis delta virus ribozyme (Rz; white) and the T7 RNA polymerase terminator (T7T; white). These plasmids were transfected into BSR-T7 cells and incubated for 120 hours. The supernatant, containing rLCMV-WT viral particles, was then harvested, titred using the focus forming assay and used to infect freshly seeded BHK-21 cells. 96 hours post infection, the supernatant from the infected BHK-21 cells was collected and the titre of this supernatant was also determined using the focus forming assay. The lysates of the transfected BSR-T7 cells and the infected BHK-21 cells were also collected for western blot analysis.

In order to monitor the success of the rescue procedure, lysates from transfected BSR-T7 cells were harvested at every 24 hours up until 144 hours post transfection (hpt) and were analysed by western blot analysis using LCMV NP antisera (figure 4.4A). Expression of LCMV NP served as a marker for virus amplification and thus successful virus rescue. A band representing LCMV NP was first visible in the 48 hpt lysate. The LCMV NP band became increasingly more intense in the lysates of the later (72-144 hpt). The most intense NP signal was detected in the 144 hpt harvested sample. There were no appropriately sized bands corresponding to LCMV NP in the mock lysates, confirming that the band was not the result of cross-reactivity with a host cellular protein. This western blot analysis suggests that transfection of the reverse genetics plasmids results in LCMV NP expression, but the subsequent increase indicates that infectious rLCMV virus was rescued and was amplified within the BSR-T7 cell culture.

To confirm successful rescue of infectious rLCMV-WT, an additional experiment was performed, in which supernatants from BSR-T7 cells (transfected with the reverse genetics plasmids) were collected in triplicate. Supernatant samples were collected every 24 hours up until 144 hpt. The viral titre of the harvested supernatants was then determined by focus forming assay and the average titre was plotted onto a graph (figure 4.4B). This revealed that the first detectable titre was in the 48 hpt supernatant, coinciding with the LCMV NP band first being visible in the 48 hpt cell lysate. The titres then steadily increase until the 144 hpt timepoint, which contained the highest viral titre, with an average of $8.2 \text{x} 10^6$ ffu/mL.

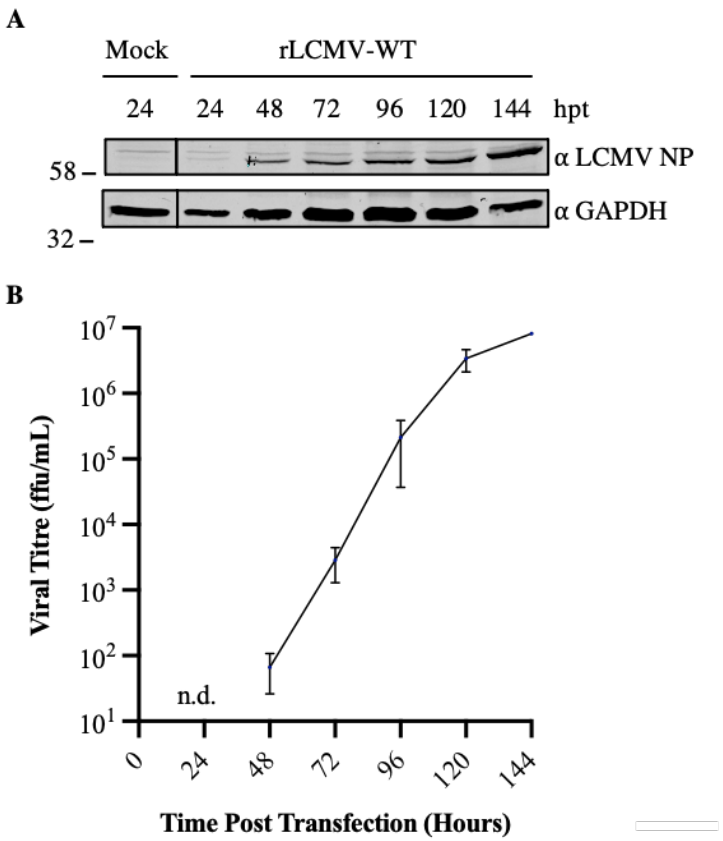

Figure 4.4: Generation of Recombinant LCMV from Transfection
BSR-T7 cells were transfected with pUC57-L, pUC57-LP, pUC57-NP, pUC57-T7 and pUC57-S. The cells were incubated for 144 hours with cell lysates and supernatant being collected every 24 hours. The lysates were subject to western blot analysis, which was stained for LCMV NP and GAPDH as a control (**A**). The supernatants were serially diluted and used to infect BHK-21 cells, before staining for LCMV NP and determining the titre by focus forming assay (**B**). The position of relevant size marker bands have been indicated and the un-cropped western blot has been shown in chapter 7, in figure 7.4A.

4.2.3 Amplification of Recombinant Wildtype LCMV

In order to amplify the rescued rLCMV-WT, supernatant was collected from the initially transfected BSR-T7 cells and was used to infect BHK-21 cells. Supernatants from four initial rescue transfections were harvested at 120 hpt, pooled and used to infect BHK-21 cells after which cell lysates were collected every 24 hours until 96 hpi. Western blot analysis using LCMV NP antisera showed the LCMV NP band was visible in all the timepoints examined and was not present in the mock cell lysate (figure 4.5A). The most abundant LCMV NP band was in the lysate harvested at 96 hpi. Furthermore, the corresponding supernatants were also collected every 24 hours up until 96 hpi. Here, the highest viral titre, which was determined by the focus forming assay performed in triplicate, was seen at 48 hpi and was approximately

$3x10^6$ ffu/mL (figure 4.5B). The subsequent timepoints (72 and 96 hpi) showed a slight decrease in rLCMV-WT titre, whereas the NP band in the western blot analysis actually slightly increases in size between 72 and 96 hpi.

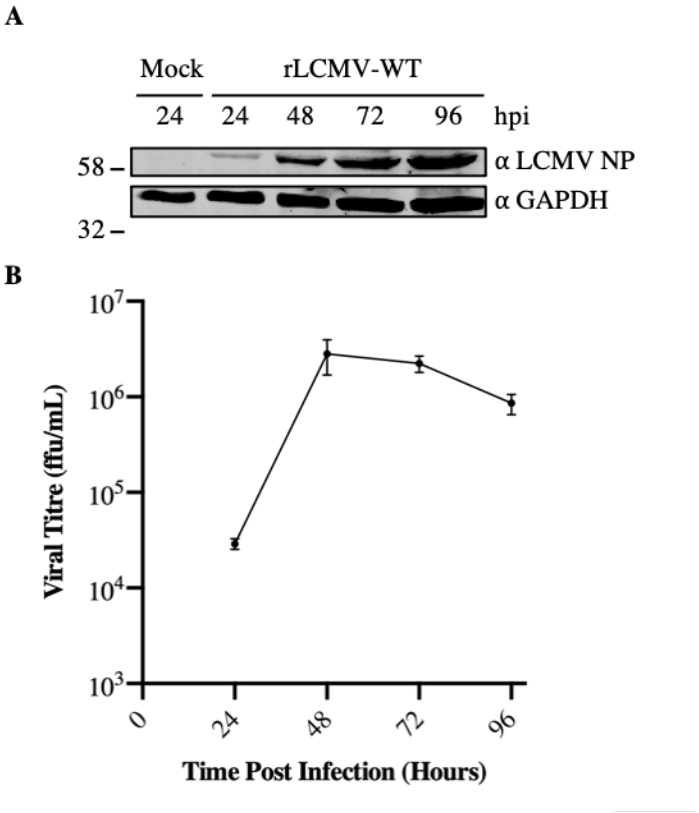

Figure 4.5: Generation of Infectious Recombinant LCMV
The timepoint which produced the highest titre from transfected cells in figure 4.4 was used to infect BHK-21 cells, after which the supernatant and cell lysates were collected every 24 hours for 96 hours. The lysates were subject to western blot analysis and were stained for LCMV NP and GAPDH as a control (**A**). The supernatants were serially diluted and used to infect BHK-21 cells, before staining the cells for LCMV NP and using a focus forming assay to determine the titre (**B**). The position of relevant size marker bands have been indicated and the un-cropped western blot has been shown in chapter 7, in figure 7.4B.

Upon comparison of the harvested lysates and supernatants from the transfected BSR-T7 cells (figure 4.4) and the infected BHK-21 cells (figure 4.5), it appeared that the NP band was larger in the infected BHK-21 cells, suggesting a greater number of viruses was generated by infection of BHK-21 cells. However, the viral titre was lower than the highest seen following transfection. Reasons for this are unknown, but one possibility was an accumulation of defective interfering particles as early as the first passage of virus.

4.2.4 Validation of the Rescue System

In order to confirm the reverse genetics system was the source of LCMV-WT, rather than a non-recombinant contaminant, site-directed mutagenesis was used to introduce a silent, non-coding T1292 to C1292 change, which incorporated a *Xho*I restriction site within pUC57-S, creating plasmid pUC57-S-XhoI (figure 4.6A). This nucleotide change was chosen so as not to disturb any existing or potential RNA regulatory signals (UTRs or IGR) or the NP amino acid sequence (figure 4.6B), with the resulting *Xho*I site in pUC57-S allowing easy confirmation of successful mutagenesis.

Additionally, in order to further prove that the LCMV NP band in the western blot analysis of infected BHK-21 cell lysates had resulted from rLCMV-WT created from transfection of the reverse genetics plasmids, control transfections were also performed alongside, with either no plasmids (mock) or pUC57-S, pUC57-NP and pUC57-T7 only (WT (-L)). The lack of LP (pUC57-L and pUC57-LP) present in the cells would mean that the cRNA cannot be replicated and the virus lifecycle cannot be established. Cell lysates were collected from transfected BSR-T7 cells at 120 hpt and the supernatant was used to infect BHK-21 cells, which were incubated for 96 hours before the cell lysate was collected. The LCMV NP band was present, albeit at lower levels, in the transfected BSR-T7 cells at 120 hpt, resulting from transient plasmid-driven NP expression, and the band was not present in the mock-transfected cells (figure 4.6C). The LCMV NP band appeared stronger in the BSR-T7 cells that had been transfected with all the reverse genetics plasmids (WT), suggesting that there was additional NP expression resulting from rLCMV-WT-specific gene expression. A band corresponding to the LCMV NP was not seen in the cell lysate of the BHK-21 cells infected with the "mock" or the "WT (-L)" supernatant, but was present in the lysates of BHK-21 cells infected with "WT" supernatant. This suggests the NP band in the infected cells arises from rLCMV-WT that has been generated from the "WT" transfection (figure 4.6C).

BSR-T7 cells were also transfected with pUC57-L, pUC57-NP, pUC57-LP, pUC57-T7P and pUC57-S-XhoI, which replaced pUC57-S. At 120 hpt, the BSR-T7 cell lysates were collected and the supernatant was used to infect fresh BHK-21 cells. At 96 hpi, the BHK-21 cell lysates were also collected. The cell lysates were

examined by SDS-PAGE and western blotting analysis, and staining with LCMV NP antisera showed that there was a similarly sized LCMV NP band, suggesting there was little detriment to rLCMV-XhoI infectivity and replication (figure 4.6C).

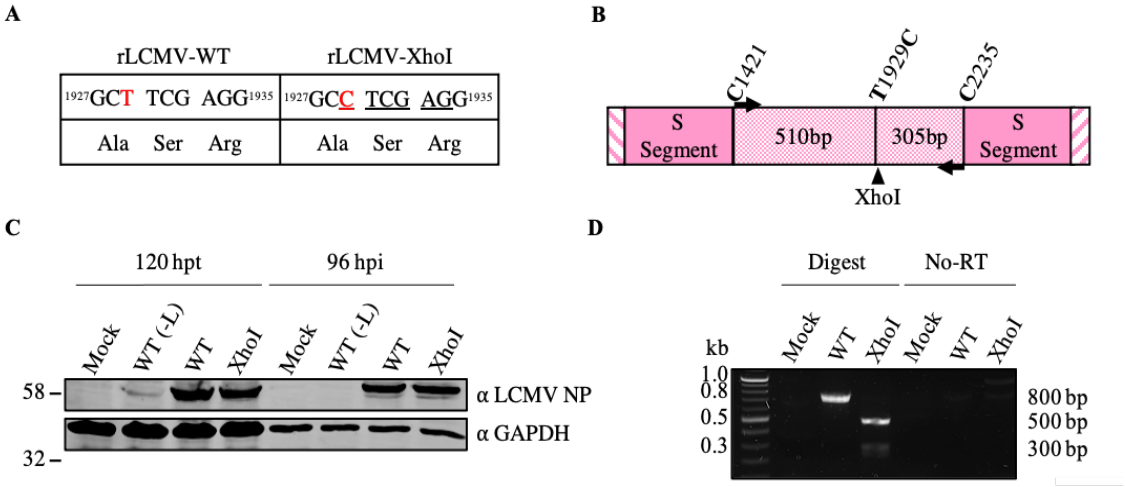

Figure 4.6: Validation of the Generation of Recombinant LCMV expressing a Silent Mutation
A silent mutation was introduced to show that the recombinant virus derived from the transfected plasmids. T1929 (red) was mutated to C (red) introducing a *Xho*I restriction site (underlined) without affecting the amino acid sequence (**A**). Primers were designed to bind 510 bp upstream (C1421) from the mutation and 305 bp downstream (C2235) of the mutation (**B**). BSR-T7 cells were transfected with pUC57-L, pUC57-LP, pUC57-NP, pUC57-T7 and either pUC57-S (WT) or pUC57-S-XhoI (*Xho*I). The cells were incubated for 120 hours and then the supernatant was used to infect fresh BHK-21 cells. The lysate was collected from both the transfected cells and the infected cells at 120 hours and 96 hours respectively and was examined by western blot analysis, staining with anti-LCMV NP and anti-GAPDH as a control (**C**). The position of relevant size marker bands have been indicated and the un-cropped western blot has been shown in chapter 7, in figure 7.5. The supernatant from the infected BHK-21 cells was used to infect fresh BHK-21 cells and at 96 hpi, the supernatant was collected and RNA was extracted. The RNA extracted from the virus was reverse transcribed into complementary DNA and digested with *Xho*I before agarose gel electrophoresis analysis (**D**). A control experiment was set up which did not have the reverse transcription step, demonstrating the bands had not come from any contaminating DNA plasmids carried over from the transfected cells. The *Xho*I restriction site is not present in the rLCMV-WT harvested RNA but is present in the rLCMV-XhoI harvested RNA, which results in the ~800 bp band being cleaved into ~500 bp and ~300 bp bands.

Furthermore, the supernatants from the infected BHK-21 cells were collected and used to infect a second set of BHK-21 cells to remove the possibility of supernatant contamination with the original plasmid from the transfection. At 96 hpi, the supernatant was collected for extraction of the viral RNA, which was used to generate cDNA using reverse transcriptase. This cDNA was then used as template for PCR amplification of an 800 base pair (bp) fragment using S segment-specific primers, which included the introduced *Xho*I restriction site (as depicted in figure

4.6B). The RT-PCR amplified cDNA fragments from both the rLCMV-WT and rLCMV-XhoI infections were then digested with restriction enzyme *Xho*I and analysed by agarose gel electrophoresis. This revealed a strong band of the correct size (~800 bp) in the rLCMV-WT infection and two bands (~500 bp and ~300 bp) in the rLCMV-XhoI infection (figure 4.6D). This confirms that the virus infecting the BHK-21 cells has been generated from the plasmids transfected into the BSR-T7 cells. Alongside these experiments, a control experiment (no-RT) was also performed to ensure the source of the cDNA used in the PCR amplification and digestion had arisen from the viral RNA. Here, the RNA extracted from the supernatant was not treated with reverse transcriptase. Following PCR, no cDNA amplification was detected in the no-RT control (figure 4.6D), confirming the source of the amplified cDNA was from viral RNA, and not contaminating plasmid carried over from previous transfections. Mock-transfected/infected samples were also included to show there was no contamination of the media (figure 4.6D).

4.2.5 Design of an LCMV Reverse Genetics System Expressing eGFP

Reverse genetics systems allow the modification of viral genomes to express fluorescent reporter proteins, such as enhanced green fluorescent protein (eGFP). This provides useful viral tools for investigating the LCMV lifecycle, replication kinetics and for screening anti-viral candidates. Here, we used the rLCMV reverse genetics system to rescue an rLCMV variant (rLCMV-eGFP) in which eGFP ORF was incorporated into the S segment, and expressed as a separate and non-fused protein. The eGFP ORF was introduced into the LCMV S segment, upstream of the LCMV NP ORF, generating the plasmid pUC57-S-eGFP (figure 4.7A). The eGFP and LCMV NP ORFs were separated by the porcine teschovirus 1 2A self-cleaving peptide linker sequence (P2A), which induces ribosome skipping on the S segment mRNA, forming two independent mRNAs (figure 4.7B) (Donnelly et al., 2001; Funston et al., 2008; Kim et al., 2011). Incorporating the eGFP sequence into the S segment ensures its retention through passaging and separating the two ORFs with the P2A sequence prevents the alteration of NP function by fusion of eGFP to its N-terminal domain.

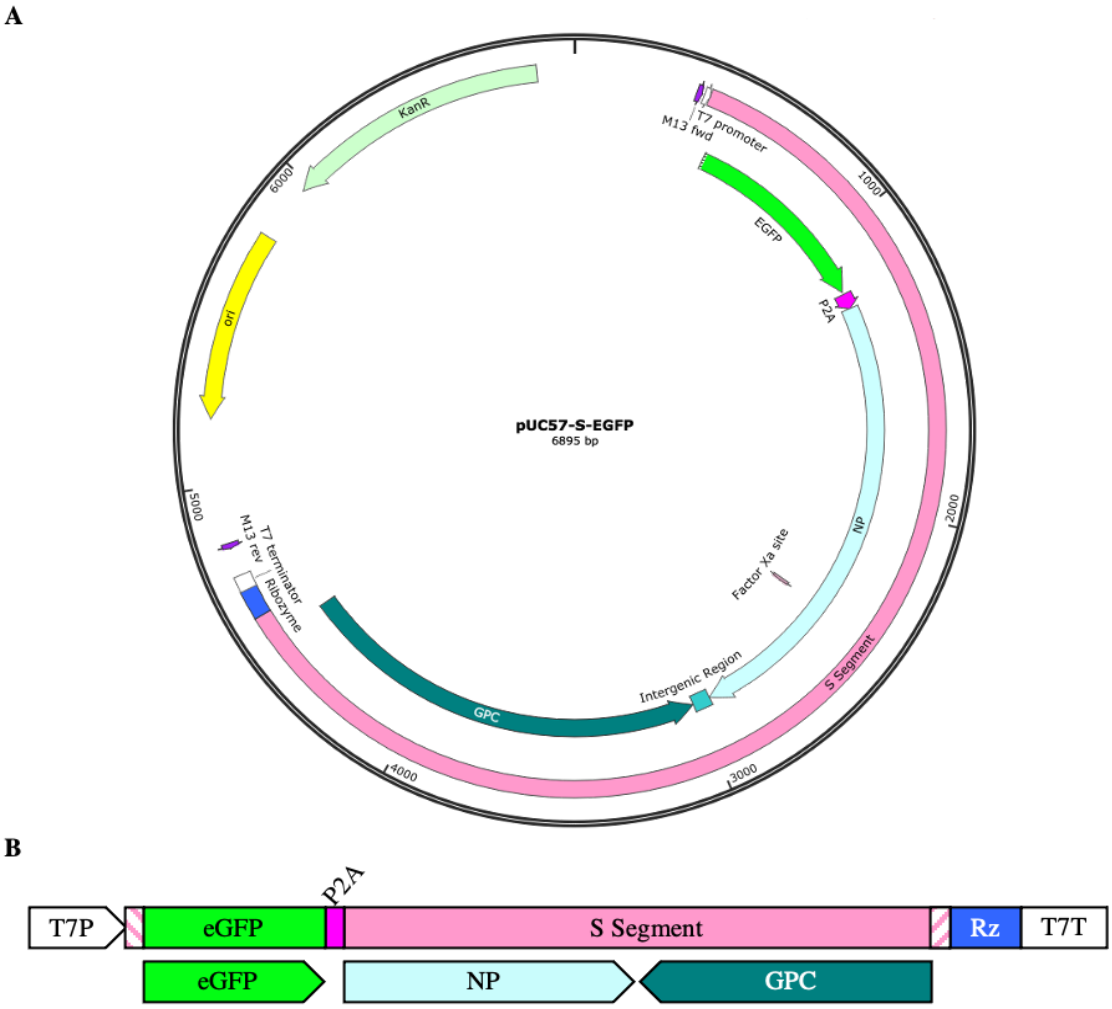

Figure 4.7: Vector Map of pUC57-S-eGFP
Schematic representation of the LCMV S Segment expressing eGFP in the pUC57 vector (**A**). The open reading frames have also been depicted separately to show the direction of translation (**B**). The enhanced green fluorescent protein open reading frame (eGFP; green) was put downstream of the T7RP promoter (T7P; white) and the S segment untranslated region (pink diagonal). The eGFP ORF was in frame with the nucleocapsid protein ORF (NP; light blue) but was separated by the porcine teschovirus 1 2A self-cleaving peptide sequence (P2A; pink). The vector map was created using SnapGene software.

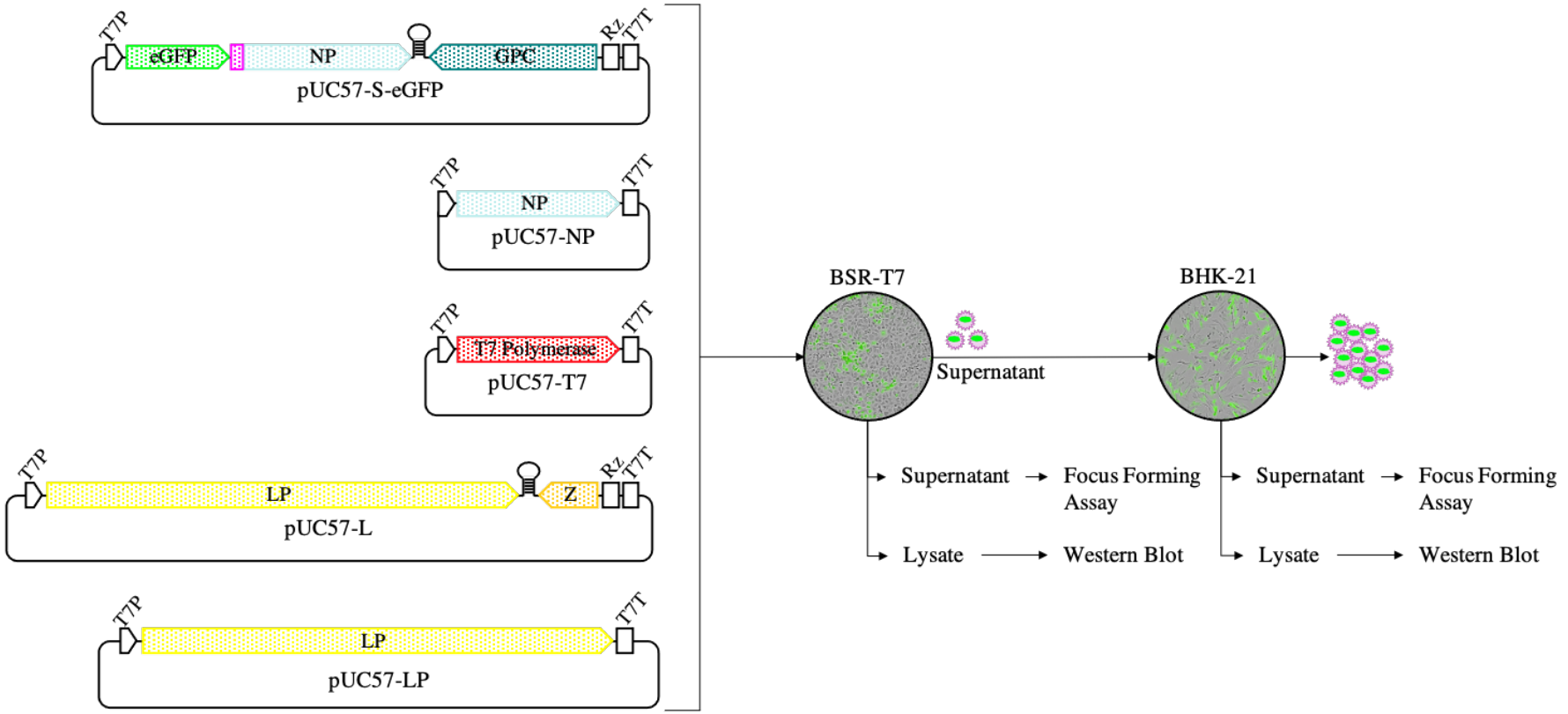

Figure 4.8: Schematic of the rLCMV-eGFP Rescue System
This describes the plasmids used in the rLCMV-eGFP rescue system. It shows the organisation of the T7 RNA polymerase promoter (T7P; white), the open reading frames (and their direction of translation) of the enhanced green fluorescent protein (eGFP; green), the nucleocapsid protein (NP; light blue), the glycoprotein complex (GPC; teal), the L polymerase (LP; yellow), the Z matrix protein (Z; orange) and T7 RNA polymerase (T7P; red), the hepatitis delta virus ribozyme (Rz; white) and the T7 RNA polymerase terminator (T7T; white). It also shows how the open reading frame of eGFP is separated from the NP open reading frame by the porcine teschovirus 1 2A self-cleaving peptide sequence (P2A; pink). These plasmids were transfected into BSR-T7 cells and incubated for 120 hours when the supernatant, containing rLCMV-eGFP viral particles, is used to infect BHK-21 cells. The supernatant was collected from the BHK-21 cells at 96 hours post infection to determine the titre. The lysates of the BSR-T7 and the BHK-21 cells were also collected for western blot analysis.

4.2.6 Generation of Recombinant LCMV Expressing eGFP

The protocol for the rescue of recombinant LCMV expressing eGFP (rLCMV-eGFP) was the same as for rLCMV-WT (figure 4.8), except pUC57-S was replaced with pUC57-S-eGFP (figure 4.7A). The ability of the resulting rescued virus to express eGFP allowed easy monitoring of transfection and infection success by visualising eGFP expression as a representative of LCMV gene expression. BSR-T7 cells were either mock-transfected (mock), transfected with pUC57-NP, pUC57-T7 and pUC57-S-eGFP only (eGFP (-L)) or transfected with pUC57-L, pUC57-LP, pUC57-NP, pUC57-T7 and pUC57-S-eGFP (eGFP). Every 24 hpt, supernatant samples (in triplicate) were collected from the transfected BSR-T7 cells. These samples were titred using the focus forming assay and the average titres were plotted on a graph (figure 4.9A). Similarly to the results obtained with rLCMV-WT, the first detectable titre of rLCMV-eGFP was in the 48 hpt supernatant. The rLCMV-eGFP titres steadily increase until 120 hpt, which contained the highest viral titre, with an average of $2.2\text{x}10^5$ ffu/mL. At 120 hpt, the BSR-T7 cells were also imaged using the EVOS FL 2 microscope (figure 4.9 (C)) and the lysates were subsequently collected for SDS-PAGE and western blot analysis (figure 4.9B). The transfected BSR-T7 cells were imaged using phase-contrast to show that the cells were equally confluent. The transfected BSR-T7 cells were also imaged using green fluorescence, which revealed that there was no fluorescence in the "mock"-transfected cells, but there was fluorescence in the "eGFP (-L)" and "eGFP"-transfected cells, although there were more fluorescent cells in the "eGFP"-transfected cells, suggesting that the additional fluorescence was the result of rLCMV-eGFP replication and infection. This was corroborated by the western blot analysis, where the bands, corresponding to the LCMV NP and eGFP, were smaller in the "eGFP (-L)" lysate than the "eGFP" lysate. "WT (-L)" and "WT" lysates, where the transfection was performed the same but with pUC57-S instead of pUC57-S-eGFP, were also included to show that the eGFP band was only present in the transfections performed with pUC57-S-eGFP.

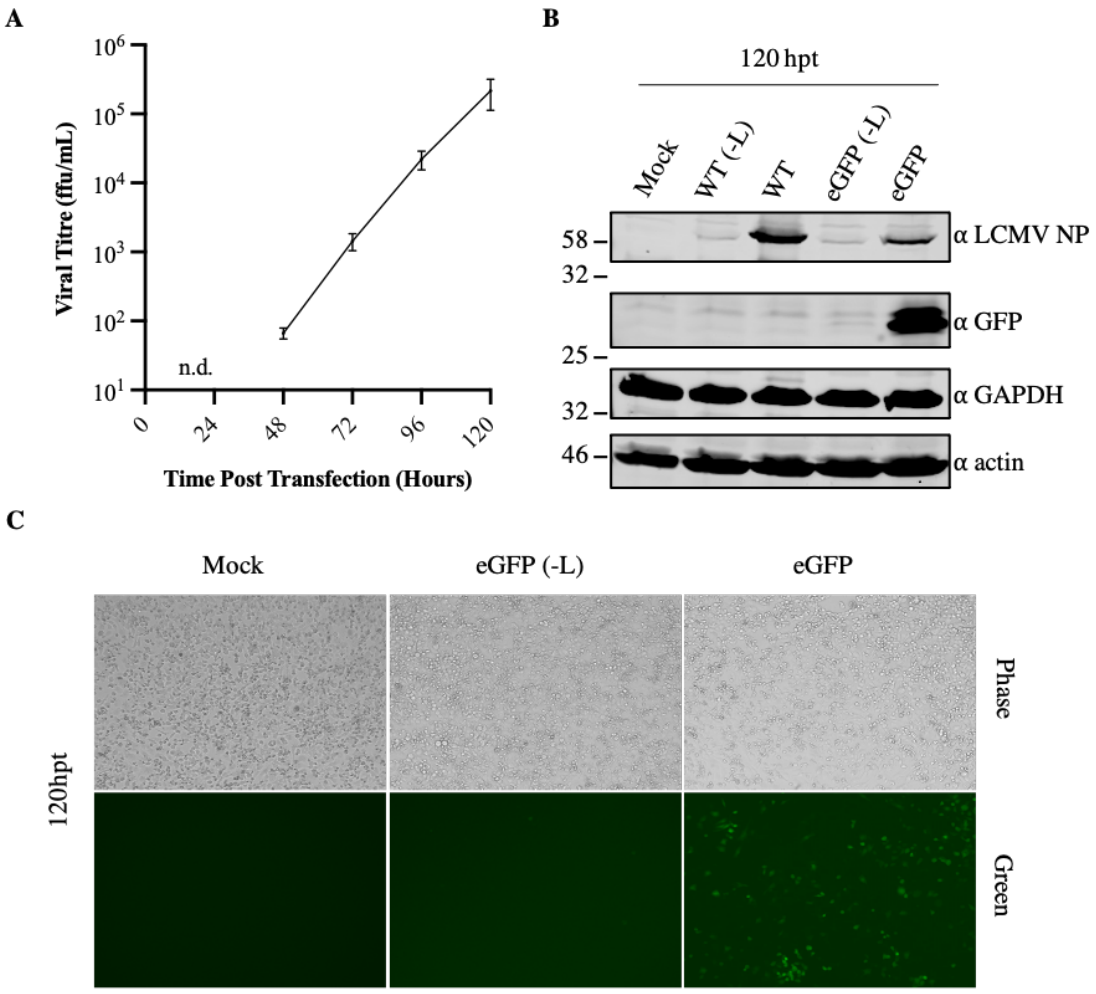

Figure 4.9: Generation of Recombinant LCMV expressing eGFP from Transfection
BSR-T7 cells were either mock-transfected, transfected with pUC57-NP, pUC57-T7 and pUC57-S-eGFP only (eGFP(-L)) or transfected with the pUC57-L, pUC57-LP, pUC57-NP, pUC57-T7 and pUC57-S-eGFP (eGFP). Control transfections were also performed substituting pUC57-S-eGFP for wildtype pUC57-S (WT(-L) and WT). The cells were incubated for a total of 120 hours and supernatant was collected every 24 hours and stored at -80 ℃. The titres of the supernatants collected every 24 hours were determined through the focus forming assay, which was performed in triplicate (**A**). Lysates were also collected at this 120 hpt for SDS-PAGE and western blot analysis, whereby the western blots were stained with antibodies against LCMV NP (α-LCMV NP) or GFP (α-GFP) and loading controls GAPDH (α-GAPDH) or actin (α-actin) (**B**). The position of relevant size marker bands have been indicated and the un-cropped western blots have been shown in chapter 7, in figure 7.6. At 120 hours post transfection (hpt), phase-contrast and green fluorescent images of the mock, eGFP (-L) and eGFP-transfected BSR-T7 cells were also collected on the EVOS FL 2 automated microscope (**C**).

4.2.7 Amplification of Recombinant LCMV Expressing eGFP

Following the "mock", "eGFP (-L)" and "eGFP" transfections, the BSR-T7 cells were incubated for 120 hpt before the supernatant was harvested and used to infect

BHK-21 cells. Every 24 hours until 96 hpi, supernatant samples (in triplicate) were collected from the infected BHK-21 cells. These samples were titred using the focus forming assay and the average titres were plotted on a graph (figure 4.10A). Comparably to the results obtained with rLCMV-WT, the highest viral titre was seen at 48 hpi (approximately $6x10^5$ ffu/mL) and subsequently there was a decrease in rLCMV-eGFP titre. At 96 hpi, the BHK-21 cells were also imaged using the EVOS FL 2 microscope (figure 4.10 (C)) and the lysates were subsequently collected for SDS-PAGE and western blot analysis (figure 4.10B). The infected BHK-21 cells were imaged using phase-contrast to show that the cells were equally confluent. The infected BHK-21 cells were also imaged using green fluorescence, which revealed that there was no fluorescence in the "mock"-infected cells or the "eGFP (-L)"-infected cells, but there was fluorescence in the "eGFP"-infected cells, suggesting that the fluorescence at this point was only the result of rLCMV-eGFP infection. This was supported by the western blot analysis, where the bands, corresponding to the LCMV NP and eGFP, were only present in the "eGFP" lysate. "WT (-L)" and "WT"-infected lysates were also included to show that the eGFP band was only present in the infections performed with rLCMV-eGFP.

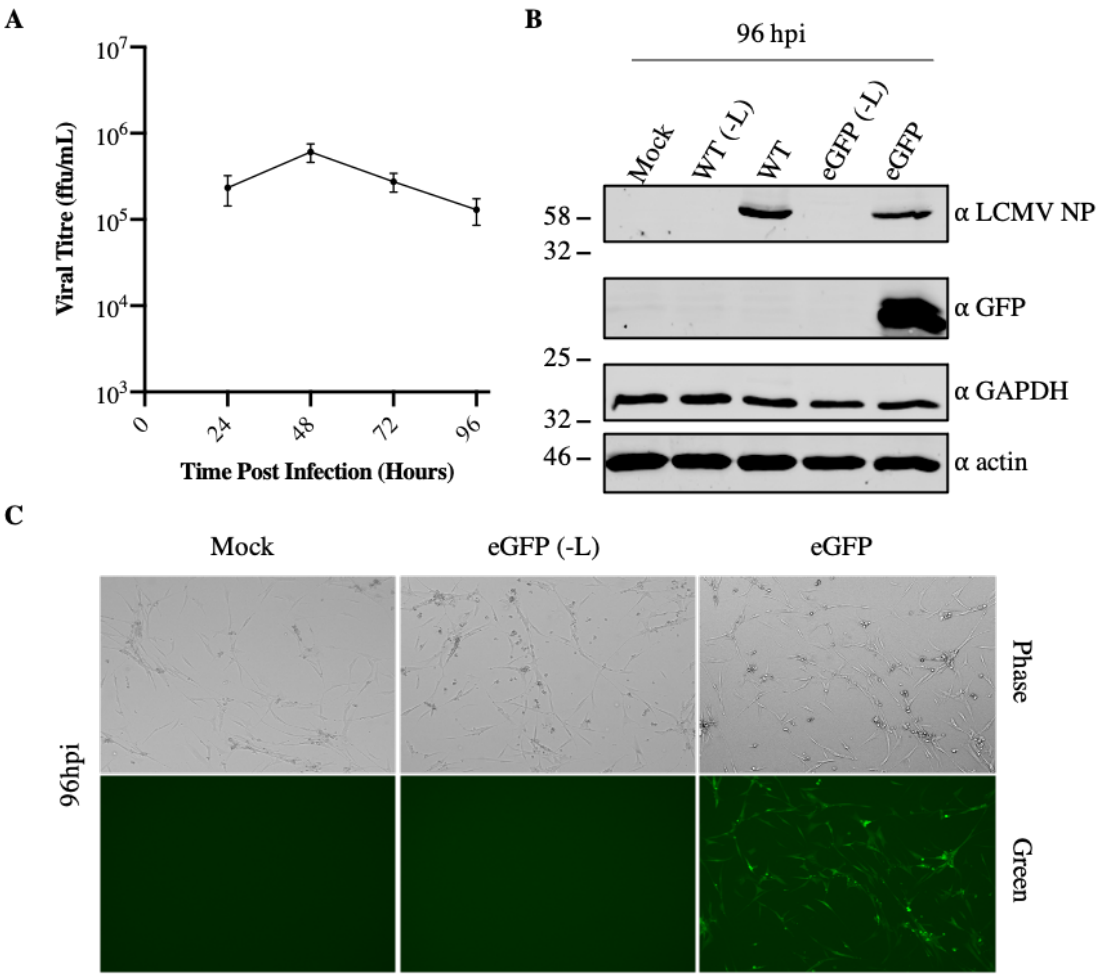

Figure 4.10: Generation of Infectious Recombinant LCMV expressing eGFP
The supernatants from the BSR-T7 cells that were transfected in figure 4.9 (including mock, WT(-L), WT, eGFP(-L) and eGFP) were harvested and used to infect BHK-21 cells. The BHK-21 cells were incubated for a total of 96 hours and supernatant was collected every 24 hours and stored at -80 ℃. At 96 hours post infection (hpi), phase-contrast and green fluorescent images of the cells were collected on the EVOS FL 2 automated microscope (**A**). Lysates were also collected at this timepoint for SDS-PAGE and western blot analysis, whereby the western blots were stained with antibodies against LCMV NP (α-LCMV NP) or GFP (α-GFP) and loading controls GAPDH (α-GAPDH) or actin (α-actin) (**B**). The position of relevant size marker bands have been indicated and the un-cropped western blots have been shown in chapter 7, in figure 7.6. The titres of the supernatants collected every 24 hours were determined through the focus forming assay, which was performed in triplicate (**C**).

4.2.8 Determining the Influence of eGFP Expression on rLCMV Growth

The data collected for the titres at 24 hour timepoints following transfection and subsequent infection for both rLCMV-WT and rLCMV-eGFP rescues were then compared to determine whether the growth efficiency was affected by inclusion of the eGFP ORF (figure 4.11A and B). The first detectable titres of rLCMV-WT

and rLCMV-eGFP, at 48 hpt, were very similar, suggesting that the corresponding transfections were equally effective. The titres of the supernatants collected at the later timepoints post transfection, where the titre increases are most likely due to subsequent infection of the BSR-T7 cells, was where the titres of rLCMV-WT and rLCMV-eGFP become discrepant, with a 1-log reduction in rLCMV-eGFP titre (figure 4.11A).

After infection of BHK-21 cells with the 120 hpt supernatant from the transfected BSR-T7 cells, the rLCMV-WT and rLCMV-eGFP supernatants were harvested and titred every 24 hpi (figure 4.11B). Interestingly the 24 hpi timepoint was the only timepoint where the titre of rLCMV-eGFP was higher than rLCMV-WT, by approximately 1-log-fold. The following timepoints all show that the titre of rLCMV-eGFP has returned to being 1-log-fold lower than the rLCMV-WT titre. The titre of rLCMV-eGFP at 24 hpi could be higher than that of rLCMV-WT because the titre of rLCMV-eGFP at 120 hpt was lower than rLCMV-WT, meaning fewer viruses were used for the subsequent infection, which could potentially reduce the effect of homologous interference. Homologous interference is the mechanism by which viruses, including arenaviruses, restrict their own growth through the production of defective interfering viruses (DIs) (Ziegler and Botten, 2020). DIs are thought to be generated through viral polymerase-directed mutation or deletion of the viral genome; these viruses then co-infect cells alongside competent virus and out-compete the competent virus for access to the viral replication machinery (Ziegler and Botten, 2020). Homologous interference is thought to be beneficial for the establishment of persistent infections in the host, but can limit growth *in vitro*, which means that infection at lower MOIs produces higher titres of competent virus because the effect of homologous interference is reduced (Ziegler and Botten, 2020).

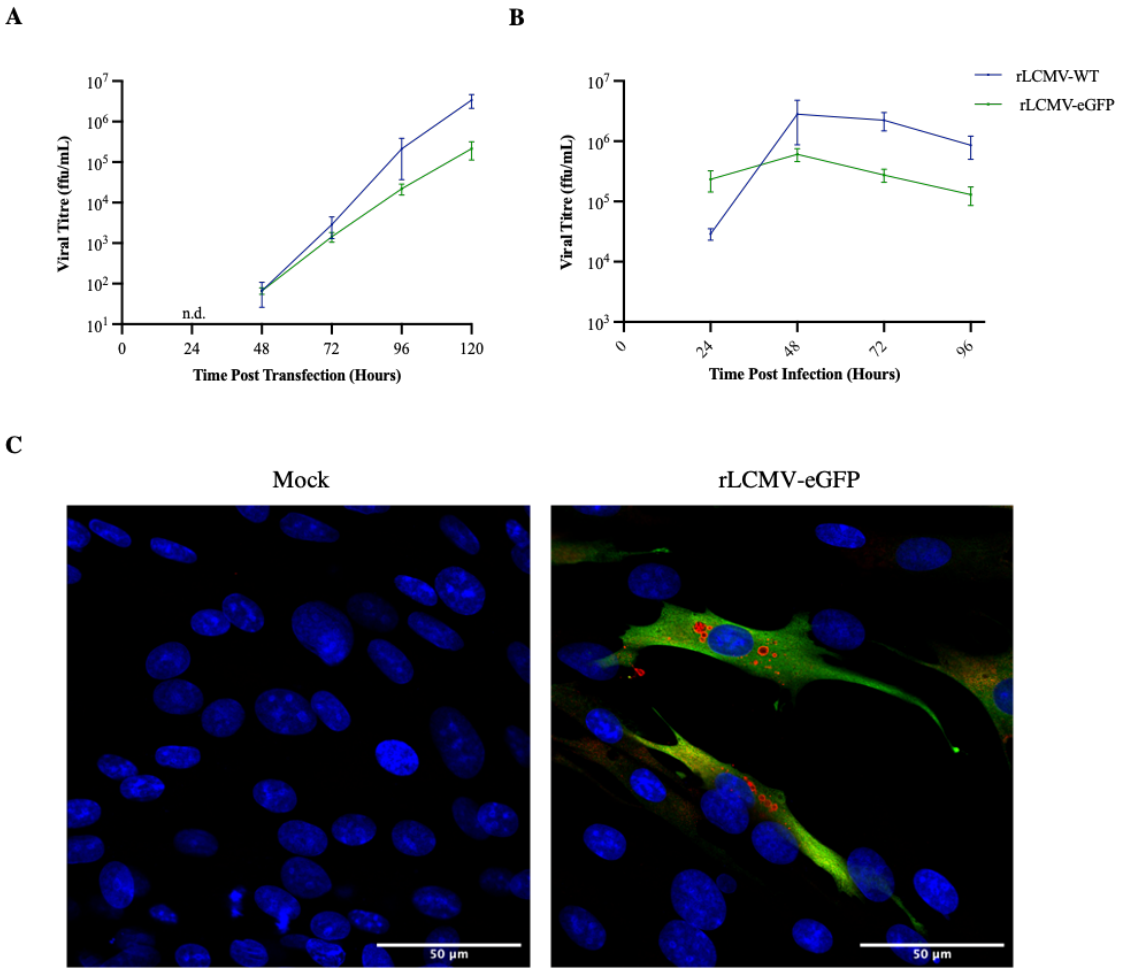

Figure 4.11: Comparison of Recombinant Wildtype LCMV and Recombinant LCMV expressing eGFP BSR-T7 cells were transfected with pUC57-L, pUC57-LP, pUC57-NP, pUC57-T7 and pUC57-S-eGFP. The cells were incubated for a total of 120 hours and supernatant was collected every 24 hours and stored at -80 ℃. The titres of the supernatants collected every 24 hours were determined through the focus forming assay, which was performed in triplicate (**A**). The supernatants from the transfected BSR-T7 cells were harvested and used to infect BHK-21 cells. The BHK-21 cells were incubated for a total of 96 hours and supernatant was collected every 24 hours and stored at -80 ℃. The titres of the supernatants collected every 24 hours were determined through the focus forming assay, which was performed in triplicate (**B**). BHK-21 cells were mock-infected or infected with rLCMV-eGFP at an MOI of 0.01 and incubated for 24 hours. The BHK-21 cells were fixed, permeabilised and stained with LCMV NP antibodies (subsequently stained with 594 nm flurophore-conjugated secondary antibody; red), GFP antibodies (subsequently stained with 488 nm flurophore-conjugated secondary antibody; green) and DAPI (blue) (**C**).

4.2.9 Determining the Influence of eGFP Expression on LCMV NP Localisation

In order to confirm that the presence of eGFP did not affect the cellular localisation of NP, and to ensure that the eGFP ORF was retained by the rLCMV-eGFP viruses, BHK-21 cells were mock-infected or infected with rLCMV-eGFP at an

MOI of 0.01. At 24 hpi, the BHK-21 cells were fixed, permeablised and stained with LCMV NP antibodies, which were stained with 594 nm flurophore-conjugated secondary antibody (red), and GFP antibodies, which were stained with 488 nm flurophore-conjugated secondary antibody (green). The cells were then imaged using confocal microscopy (figure 4.11C). This revealed that the cellular distribution of LCMV NP was not altered when compared to the previous immunofluorescence analysis (figure 3.12C), and the perinuclear puncta were still present. The eGFP distribution was throughout the cytoplasm and was not associated with the LCMV NP-puncta, which was concurrent with the eGFP being expressed as an individual ORF. There was no fluorescence corresponding to the LCMV NP or eGFP in the mock-infected cells, confirming there was no cross-reactivity with the antibodies and a host cellular protein.

4.2.10 Development of rLCMV Expressing the 6xHis Tag

For further development of the LCMV reverse genetics system, we attempted to rescue LCMV containing a 6xHis affinity tag at the C-terminus of the NP to allow for concentration and purification of whole RNPs from virus. Previous studies have shown that a HA tag can be introduced at the C-terminus of the NP, without affecting its functions within a mini-genome system (Martínez-Sobrido et al., 2007). Another study has shown that a Strep-tag can successfully be introduced to the N-terminus of the LCMV NP in a reverse genetics system (Iwasaki et al., 2018). It therefore appears that tags can be introduced to either termini of the LCMV NP without disrupting its activities within the lifecycle.

We mutated the pUC57-S-eGFP plasmid to encode a 6xHis tag at the C terminus of the NP, just prior to the stop codon (pUC57-S-eGFP-6xHis) (figure 4.12A). Transfection was carried out as before, where pUC57-S was replaced with pUC57-S-eGFP-6xHis. After 120 hours, the supernatant was then collected and used to infect BHK-21 cells, whilst the lysate was collected for western blot analysis. After 96 hours, the BHK-21 cell lysates were collected and the supernatant was used to infect fresh BHK-21 cells again and incubated for a further 96 hours, at which point the BHK-21 cell lysates were once again collected and the supernatant was harvested and stored at -80 ℃. The cell lysates from transfected BSR-T7 cells

and subsequently infected BHK-21 cells were examined by western blot analysis, after staining with antibodies raised against the LCMV NP (α-LCMV NP) or 6xHis (α-6xHis) (figure 4.12B). Mock-transfected and mock-infected BSR-T7 and BHK-21 cell lysates were included to ensure the bands were not the result of cross-reactivity with a host protein. Loading controls were also included by staining with either GAPDH (α-GAPDH) or actin (α-actin). LCMV NP was not present in the mock-transfected or mock-infected lysates but was present in the transfected and rLCMV-6xHis-infected lysates. The same lysates also demonstrated that a similarly sized band was reactive with the α-6xHis antibody in the same lysates as the LCMV NP band, strongly suggesting that the NP was successfully tagged with the 6xHis tag. To our knowledge, this is the first report of the generation of infectious rLCMV expressing a C-terminally 6xHis-tagged NP.

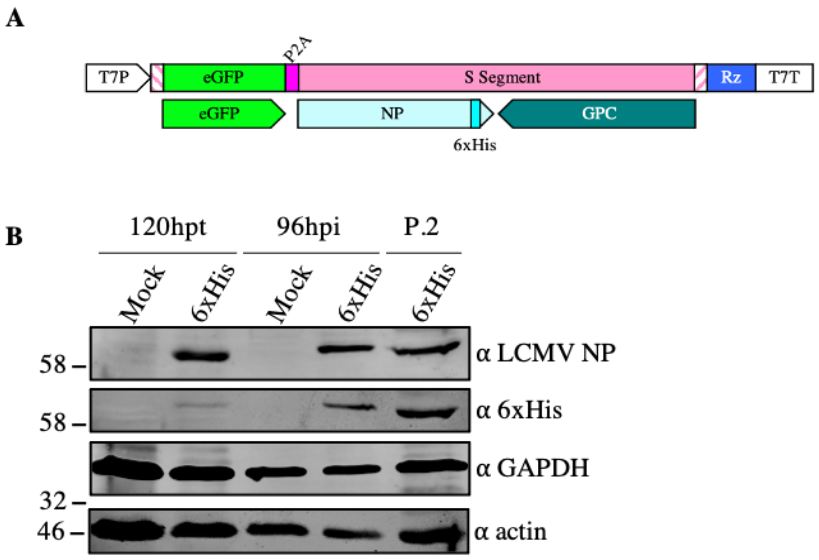

Figure 4.12: Generation of Recombinant LCMV expressing a 6xHis tag on the C-terminus of the Nucleocapsid Protein A 6xHis tag was introduced into the C terminus of the nucleocapsid protein (NP) within the S segment to generate plasmid pUC57-S-eGFP-6xHis, the open reading frames of which have been shown schematically in (**A**). BSR-T7 cells were either mock-transfected or transfected with pUC57-L, pUC57-LP, pUC57-NP, pUC57-T7 and pUC57-S-6xHis (6xHis). The cells were incubated for a total of 120 hours (120 hpt), at which point the BSR-T7 cell lysates were collected for western blot analysis and the supernatant was used to infect BHK-21 cells, which were incubated for 96 hours (96 hpi). The supernatant from the BHK-21 cells was then used to infect fresh BHK-21 cells, which were incubated for another 96 hours, as a second passage of the virus (P.2). Lysates were collected at 96 hours post infection from the first infection (96 hpi) and the second passage (P.2). All lysates were then examined by SDS-PAGE and western blot analysis, whereby the western blots were stained with antibodies against LCMV NP (α-LCMV NP) or 6xHis (α-6xHis) and loading controls GAPDH (α-GAPDH) or actin (α-actin) (**B**). The position of relevant size marker bands have been indicated and the un-cropped western blots have been shown in chapter 7, in figure 7.7.

4.2.11 Comparison of Recombinant Wildtype LCMV and Recombinant LCMV Expressing Genetic Tags

The development of this reverse genetics system provided a source of infectious recombinant LCMV with a consistent genotype that exhibited stable growth properties and high viral titres. It was previously discovered that our current WT LCMV stock had issues with repeated stock passaging, reduced titres and difficulty with titration (prior to the development of the focus-forming assay). The lack of a stable, titred stock of infectious WT LCMV meant that we were unable to compare growth properties and protein expression of recombinant LCMV with WT LCMV, as a control.

In order to determine whether the insertion of eGFP or C-terminal NP 6xHis tag into the S segment had any detrimental effects on the viral lifecycle, a direct comparison was made between the replication efficiencies of rLCMV-WT, rLCMV-eGFP and rLCMV-6xHis. This was distinct from section 4.2.8 because the experiments here were carried out at a defined MOI, whereas the experiments performed in section 4.2.8 used the supernatant harvested from cells at 120 hpt, without titration. The difference in titre at 120 hpt between rLCMV-WT and rLCMV-eGFP in figure 4.11A suggest the subsequent infection was performed at different MOIs. Therefore, BHK-21 cells were infected in triplicate with either rLCMV-WT, rLCMV-eGFP or rLCMV-6xHis at an MOI of 0.1. Supernatant was harvested at every 24 hours and the titre was determined by focus forming assay. This revealed that introducing the eGFP tag reduced the titre of rLCMV-eGFP by approximately one-log at every collected timepoint, when compared to rLCMV-WT (figure 4.13). Introducing the 6xHis tag resulted in a greater reduction of the titre of rLCMV-6xHis, whereby the highest titre measured was $3.8\text{x}10^4$, which was approximately 3 logs lower than rLCMV-WT. Despite the reduction in titre of the tagged LCMV variants, the growth pattern was similar between WT and the variants, whereby the titre was lowest at 24 hours and rapidly increases to its highest titre at 48 hours. The titres then plateau between 48 hours and 72 hours before experiencing a decrease at 96 hours.

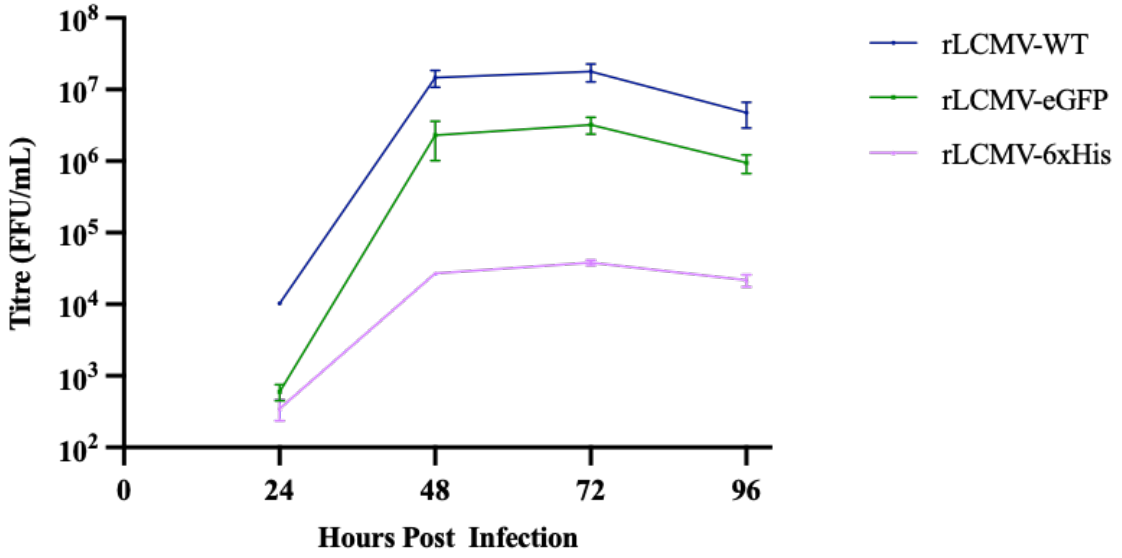

Figure 4.13: Comparison of Replication Efficiency between rLCMV WT and rLCMV Tagged Variants To determine whether incorporation of the eGFP ORF or the C-terminal NP His tag affected the growth efficiency of rLCMV, BHK-21 cells were infected in triplicate with either rLCMV-WT rLCMV-eGFP or rLCMV-6xHis at a MOI of 0.001 (both virus passage 2). Supernatant was collected from the cells every 24 hours and was stored at -80 ℃. The supernatants were then titred by focus forming assay and compared.

4.2.12 Purification of rLCMV-6xHis Ribonucleoprotein Complexes

The 6xHis tag was introduced to the C-terminus of the LCMV NP in order to permit purification of LCMV RNPs using immobilised metal-affinity chromatography. By exploiting interactions between nickel ions on the chromatographic resin and the histidine residues in the 6xHis tag, which would be present in multiple copies of NP throughout the RNP, purification of the RNPs for further structural investigation was attempted. In order to do this, BHK-21 cells were infected with rLCMV-6xHis at an MOI of 0.001 and incubated for approximately 67 hours. After incubation, the infected BHK-21 cells were lysed and the lysate was centrifuged. The supernatant was collected and the pellet was resuspended in an equal volume of buffer. Samples of the supernatant (soluble fraction) and the resuspended pellet (insoluble fraction) were collected. The supernatant was then diluted 1:5 with 20 mM imidazole binding buffer and passed over nickel resin. The flowthrough was collected and the resin was then washed with the 20 mM imidazole binding buffer and a 40 mM imidazole wash buffer. The sample was eluted with 300 mM imidazole elution

buffer and the elutions were collected in 1 mL fractions. Samples of all the washes, elution fractions and the resin were collected for SDS-PAGE analysis, followed by Coomassie staining (figure 4.14A) or western blot analysis and staining with LCMV NP antibodies (figure 4.14B). Both of these showed the presence of a band, corresponding to LCMV NP, in the soluble fraction, which was subsequently eluted in elution fractions 3-6. This shows that the LCMV NP was successfully expressed with the C-terminal 6xHis tag. The 6xHis tag was also sufficiently exposed to allow interaction with the nickel resin and purification of the LCMV NP from infected cell lysates. However, the concentration was too low to determine the presence of RNA using spectrophotometry. To determine whether LCMV RNP complexes had been successfully purified from infected cell lysates, the eluted samples (3-6) were individually examined using negative-stain electron microscopy. No RNP complexes could be identified (data not shown). Whether this was due to the low concentration of the RNP complexes, degradation or aggregation remains to be determined.

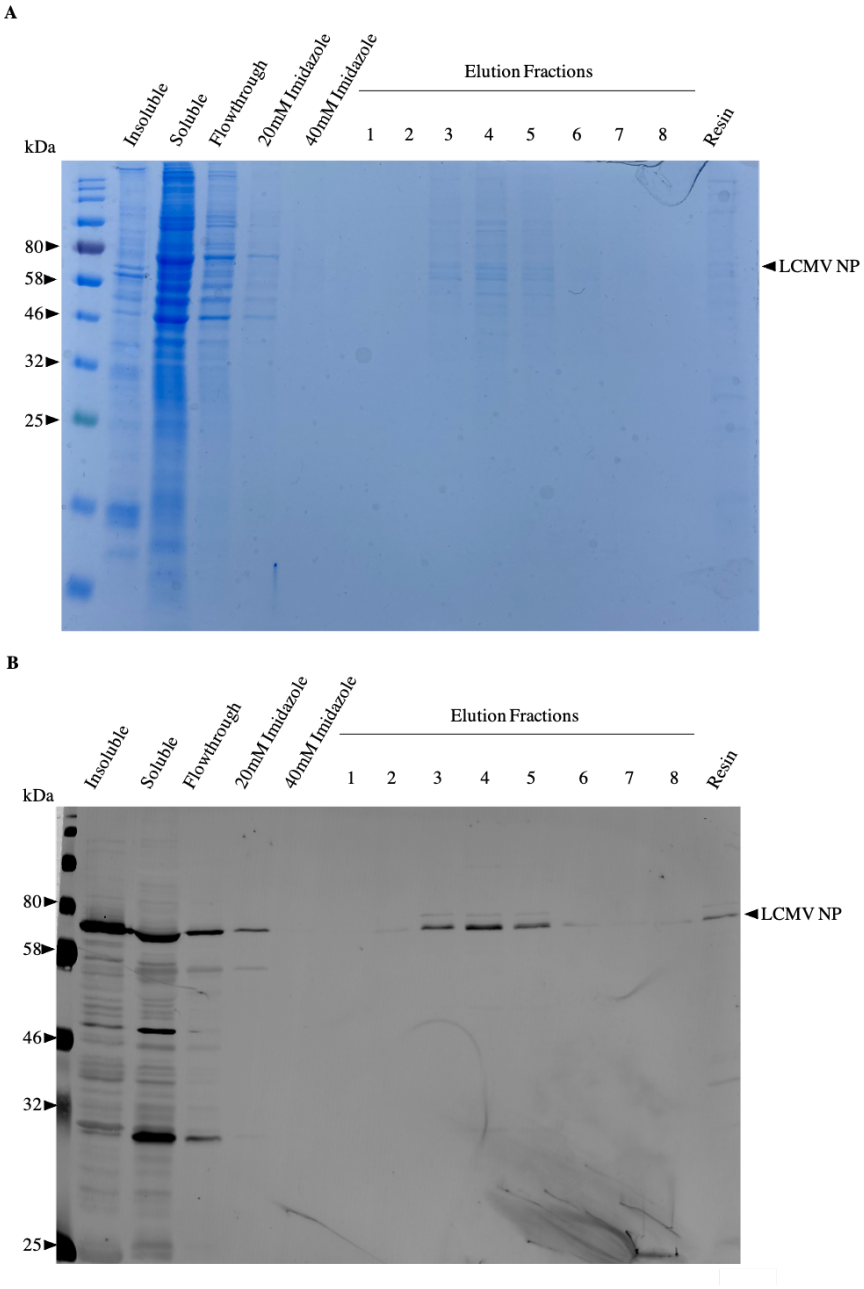

Figure 4.14: Purification of rLCMV-6xHis Ribonucleoprotein Complexes By Immobilised Metal Affinity Chromatography BHK-21 cells were infected with rLCMV-6xHis at an MOI of 0.001 and incubated for approximately 67 hours at which point the cell lysate was harvested and centrifuged. The pellet was resuspended in buffer and a sample was taken (insoluble). A sample of the supernatant was also taken (soluble) before the supernatant was diluted with 20 mM imidazole binding buffer and passed over nickel resin. The flowthrough was collected and the resin was then washed with the 20 mM imidazole binding buffer and a 40 mM imidazole wash buffer. The sample was then eluted with 300 mM imidazole elution buffer and the elutions were collected in 1 mL fractions. Samples of all the washes, elution fractions and the resin were collected for SDS-PAGE analysis, followed by Coomassie staining (**A**) or western blot analysis and staining with LCMV NP antibodies (**B**).

4.3 Chapter Summary and Discussion

This chapter describes the successful creation of a reverse genetics system, designed to recover recombinant LCMV (rLCMV). Supernatant and cellular lysates were collected at 24 hour intervals, post transfection and post infection, in order to determine the optimal harvest time. This system enabled the generation of rLCMV-WT, reaching titres of 10^7 ffu/mL. It was confirmed that the source of rLCMV derived from the reverse genetic system plasmids, using mutational analysis and RT-PCR. The reverse genetics system was modified to incorporate an eGFP ORF into the S segment, which permitted the live-cell monitoring of successful rLCMV-eGFP infection. The development of the rLCMV-eGFP reverse genetics system also provided a system that could be exploited as a quick and simple screening platform for the evaluation of anti-arenaviral drugs. The reverse genetics system was also modified to introduce a C-terminal NP 6xHis tag. rLCMV-6xHis was successfully rescued but the titre was significantly reduced compared to rLCMV-WT. The differences in titres between the recovered recombinant viruses suggest the introduced tags may be interfering with the functions of the NP. To investigate this, monitoring of the other viral proteins, including the GPC, ZP and the LP, could confirm that expression of these proteins is not reduced or their subcellular localisation is not altered through the addition of the tag, which would subsequently affect titre. This could be investigated through purchase or generation of antibodies against each of the arenaviral proteins.

Stocks of rLCMV-6xHis were successfully generated that were used to infect BHK-21 cells and purification of RNP complexes was attempted. Whilst the purification of the RNP complexes using IMAC was somewhat successful, further optimisation is required in order to concentrate the RNP complexes without aggregation and enable structural examination by electron microscopy. Steps to improve the concentration of RNP complexes could firstly involve the optimisation of the growth of rLCMV-6xHis to increase the titre; this would increase the number of infected cells or the number of virions from which to purify the RNPs. Alternatively, trials could be performed to determine whether changing the location of the 6xHis tag from the C-terminus to the N-terminus of the NP may be less disruptive to the NP's functions, permitting higher titres and potentially allowing better exposure of the 6xHis tag.

Figure 4.14 suggests that approximately half of the RNPs (as indicated by the NP band) are collected in the flowthrough and 20 mM imidazole wash and therefore are lost before purification. This indicates the 6xHis tag is inadequately exposed or the sample is becoming insoluble. Attempting different purification buffers to improve stability of the sample could be trialled, such as including glycerol or charged amino acids L-Arg and L-Glu (Golovanov et al., 2004), or resins charged with alternative ions, such as cobalt, which offers stronger interactions between the resin and 6xHis tag.

We had also designed the rLCMV reverse genetics system to rescue other tagged variants of rLCMV, including the addition of a split GFP tag onto the C-terminus of the NP (rLCMV-GFP11) and the addition of a FLAG tag onto the C-terminus of the GPC (rLCMV-FLAG). We successfully introduced the split GFP tag into the C terminus of the NP (pUC57-S-GFP11) and a FLAG tag into the C terminus of the GPC (pUC57-S-FLAG) but the rescues of rLCMV-GFP11 and rLCMV-FLAG were unsuccessful.

First developed by Cabantous et al., the split GFP tag comprises the eleventh strand of the GFP beta barrel and is only 16-amino acids long (Cabantous et al., 2005). Its smaller size allows its incorporation into proteins with a reduced disruption of the structure and function (Kamiyama et al., 2016). Cells can then be transfected with a plasmid expressing GFP strands 1-10. Both GFP11 and GFP1-10 are independently non-fluorescent but together can self-associate to generate fully-functional, fluorescent GFP. This provides a manner of tagging the NP with GFP without introducing the entire GFP polypeptide sequence and disrupting expression, folding, structure or function. Further optimisation is required in order to rescue rLCMV-GFP11, which would then permit live cell fluorescent tracking of the NP within the cell, and potential further exploration of any viral structures, such as the LCMV NP puncta, within the cell by correlative light and electron microscopy (CLEM).

It has previously been shown that a FLAG tag (and GGGS linker) can be added at the C terminus of the GPC of both LCMV and LASV without affecting processing, trafficking, function or infectivity of a pseudotype retrovirus (Capul et al., 2007). However, its functionality in the reverse genetics system has not been tested. We were unable to rescue rLCMV-FLAG at all, therefore further optimisation of the

system is needed. Introducing the FLAG tag into the GPC would permit further mutational study into motifs required for interactions with cellular host trafficking proteins that were suggested by an siRNA screen, performed as part of a Master's project. This could be further investigated for the mutational analysis of motifs in the GPC, in order to determine which are necessary for trafficking between the ER and the Golgi.

Chapter 5

Structural Determination of the Arenavirus Glycoprotein Complex

5.1 Chapter Introduction

Electron microscopy (EM) has been vital in the research of many viruses, including arenaviruses. For example, this technique was originally used to characterise arenavirus isolates and led to the proposal of arenavirus incorporation of ribosomes into virions (Murphy et al., 1970; Rowe et al., 1970b; Dalton et al., 1968; Wood et al., 1970). Over recent years, there have been many advances in EM to improve the way we can visualise viruses and increase the resolution of viral macromolecular complexes. This has recently allowed the characterisation of the structure of the LASV GPC, using cryo-electron tomography and sub-tomogram averaging (Li et al., 2016). This gave insight into the ultra-structural organisation of the GPC and the underlying ZP matrix layer, as well as the entry process of LASV.

This chapter describes the cryo-electron tomography and sub-tomogram averaging of the glycoprotein complexes of PICV, a New World mammarenavirus, and LCMV, an Old World mammarenavirus. Initially, the growth and purification of both PICV and LCMV was optimised in order to generate highly concentrated and highly pure virion preparations. These samples were analysed by negative-stain EM, cryo-electron microscopy and cryo-electron tomography. Sub-tomogram averaging of the viral spikes was performed in order to improve the resolution, in an attempt to determine high-resolution structures of the PICV and LCMV GPC spikes. These structures were then compared to the published LASV GPC structure to highlight potential differences that can be seen between the Old World and New World arenaviruses.

5.1.1 Introduction to Electron Microscopy

EM offers a significant improvement in resolution compared to light microscopy because the sample is imaged using an electron beam rather than visible light. A beam of electrons possesses a much shorter wavelength than that of photons, meaning the resolution is no longer limited at the wavelength of visible light. However, EM does pose some challenges, particularly when imaging biological samples. 1) The electrons are focused into a beam using a series of electromagnetic lenses and the sample has to be imaged under vacuum conditions in order to prevent gas molecules interacting with the electron beam. However, biological samples are aqueous and therefore cannot withstand the vacuum conditions required (Ohi et al., 2004). 2) There is a very small limit on the amount of the sample that can be used to prepare EM grids, which means that the sample has to be highly concentrated for examination. 3) Many atoms found in biological samples, such as carbon and hydrogen, have a limited capacity for electron scattering, which results in low contrast and reduces the ability to resolve finer detail (Ohi et al., 2004). 4) Biological samples are also very susceptible to radiation damage from the electron beam, limiting the electron dose that can be used for imaging (Ohi et al., 2004; Cheng, 2015). However, there are techniques to counteract these problems that biological samples pose. One such technique is negative-stain EM, which coats the biological sample with a heavy metal (typically a uranyl-based salt). Negative-staining quickly dehydrates the biological sample to allow imaging under the vacuum conditions, and the heavy metal atoms interact with the electron beam to significantly increase the signal-to-noise ratio (SNR) and thus the contrast of the image (Thompson et al., 2016). However, the resulting dehydration in negative-stain EM can cause deformation of the biological sample.

Cryo-electron microscopy (cryo-EM) provides the opportunity to image biological samples in their native aqueous environment, whilst still protecting the sample from the vacuum conditions of the microscope and radiation damage (Orlova and Saibil, 2011). Here, the samples are frozen in a vitreous state, whereby the water surrounding the sample is rapidly frozen, preventing the rearrangement of the water molecules into an ice crystal formation that would damage the sample and reduce image quality due to the ability of ice crystals to diffract electrons (Thompson

et al., 2016). This method of preparation prevents dehydration and potential deformation of the sample, that would typically occur with other methods including negative-stain EM.

Whilst vitreous ice does offer some protection against radiation damage of the biological sample, there is still quite a low limit of the electron dose before the sample is damaged. Furthermore, the electron scattering by the biological atoms, rather than the heavy metal atoms, is significantly reduced, lowering the SNR. Therefore, in order to improve the SNR, several techniques can be combined with cryo-EM (or negative-stain EM) to improve the resolution to such that it rivals other techniques such as X-ray crystallography. Such techniques include single-particle analysis and tomography.

Single-particle analysis (SPA) improves resolution of the structures within cryo-EM images by aligning and averaging together multiple particles throughout the 2-dimensional (2D) plane (Cheng, 2015). A requirement of SPA is that the sample needs to be homogeneous. If a sample is homogeneous then it can be assumed all the particles of interest are the same, but in a different position or orientation. Computationally altering these positions and orientations allows the particles to be aligned and then averaged, improving the resolution. The presence of the particles in different orientations also allows computational 3-dimensional (3D) reconstruction of the particle (Cheng, 2015).

Cryo-electron tomography (cryo-ET) allows the generation of 3-dimensional (3D) information through collecting a series of images of the sample at different angles, which are then computationally combined to form a 3D volume called a tomogram (Cope et al., 2011) (figure 5.1). Cryo-ET is particularly useful for the 3D reconstruction of samples that do not contain regularly arranged particles that could be reconstructed through SPA (Cope et al., 2011). The resolution of irregularly arranged macromolecular complexes in reconstructed tomograms can then be improved using a technique known as sub-tomogram averaging (STA), where multiple individual particles are averaged in order to improve the resolution of the feature of interest (Cope et al., 2011).

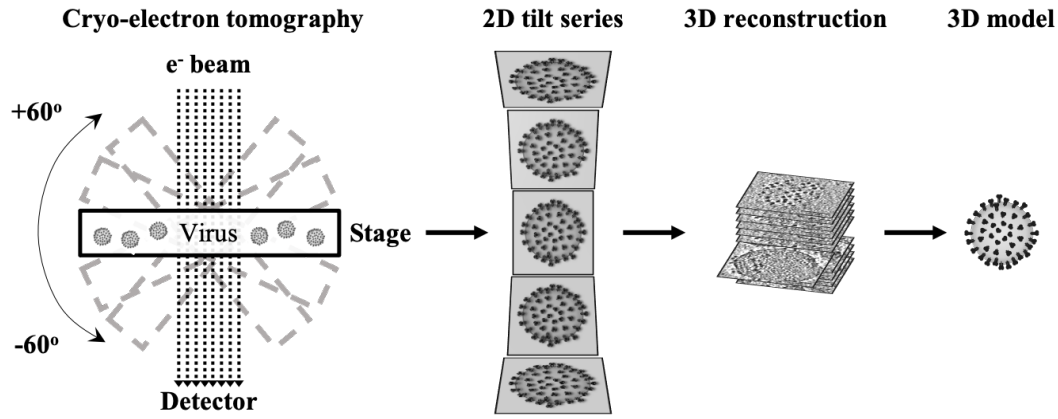

Figure 5.1: Schematic Work Flow for Cryo-Electron Tomography The grid onto which the sample (containing virus) is loaded onto an electron microscope. The stage is then tilted from -60° to +60°, with images acquired every 2° increments. The images acquired form a 2D tilt-series and can be computationally combined to reconstruct a 3D tomogram, which can be used to generate a 3D model of the virus.

Furthermore, there has been significant improvement in the data collected from cryo-EM, due to recent advances in cryo-EM technology. Such advances include the development of direct-electron detectors (DEDs) as opposed to charged coupled device cameras (CCDs) for the detection of the electrons which have passed through, or been scattered by, the sample being imaged. CCDs use scintillators, which, when an electron strikes it, induces photon emission that is transformed into electrical signals. These electrical signals accumulate to build an electrical charge, which is then amplified and an image is formed (Dillard et al., 2018; Thompson et al., 2016). In contrast, DEDs use a very thin semi-conductor wafer that detects the energy deposited by the electrons directly. Noise, created from the electrons being back-scattered from the support matrix of the DED and hitting the semi-conductor again, is reduced by making the support matrix of the DEDs as thin as possible (Mitra, 2019; Thompson et al., 2016). DEDs also have a high frame rate, which offers the benefit to detect the exposure as multiple frames, rather than a single frame. These frames can then be aligned together to correct for any movement that occurs during the exposure, which could be the result of specimen movement, mechanical movement or beam-induced movement (Mitra, 2019; Thompson et al., 2016).

In cryo-EM and cryo-ET, biological samples have to be imaged with a low electron dose to prevent damage to the sample. In cryo-ET, the electron dose has to be even lower because the same region of interest is imaged multiple times in the different

projection angles. Imaging with a low electron dose poses a further challenge to generate sufficient contrast in low contrast biological samples. Therefore, in order to counteract the low electron dose and improve the SNR, several techniques can be used. One conventional way is to apply defocus to the collection to increase the contrast. Another way is to use a Volta phase plate. The phase plate allows imaging to occur closer to focus and improves the SNR to introduce contrast to the specimen by applying a phase shift to the scattered electrons (Danev and Baumeister, 2017; Thompson et al., 2016).

5.1.2 Structural Understanding of the Arenavirus Glycoproteins

In 1968, thin-section negative-stain EM was successfully used to observe the morphology of LCMV (Dalton et al., 1968). This study, and subsequent research, found that the viruses were spherical or pleomorphic, with diameters ranging between 60 nm and 260 nm, and a well-defined membrane with surface projections. The surface projections, which correspond to the arenavirus glycoprotein complexes, were described as randomly distributed and approximately 5-10 nm long (Murphy et al., 1970; Howard and Young, 1984; Murphy and Whitfield, 1975).

The subsequent advances in cryo-EM have allowed for further investigation into the structure of the trimeric arenavirus glycoprotein complexes at higher resolutions.

In 2005, (Neuman et al., 2005) performed cryo-EM on PICV, TCRV and LCMV. They confirmed the viruses were pleomorphic, enveloped and ranged in diameter from 40 nm to 200 nm. They identified the spike projections as distinct stalk and head domains and found them to be spaced approximately 10 nm apart and were about 9 nm long (stalk; 3 nm and head; 6 nm).

Then, in 2013, the causative agent of Boid inclusion body disease (BIBD), a fatal disease of snakes, was identified as a novel arenavirus; University of Helsinki virus (UHV) (Hetzel et al., 2013). This study also performed cryo-ET on UHV and STA on the UHV glycoproteins. They identified spikes, which were randomly distributed across the entire virion surface, spaced 11-15 nm apart. The spikes had distinctive stalk and head domains, which were approximately 10 nm long (stalk; 1 nm and head; 9 nm), with the three head domains forming a cup-like structure (Hetzel

et al., 2013). They also identified two groups of virus particles; virions (type 1), which had surface projections, granular density and an additional secondary density approximately 5 nm beneath the viral membrane and virus-like particles (type 2), which were similarly sized and had granular density, but had reduced or no surface projections and no secondary layer beneath the membrane (Neuman et al., 2005).

In 2016, the structure of the LASV GPC spike was solved through cryo-ET and STA (Li et al., 2016) (figure 1.15A). The 3D tomographic reconstruction of fixed LASV agreed with previous observations, whereby the virions were roughly spherical and ranged in diameter from 110 nm to 150 nm (Li et al., 2016). These researchers performed subtomogram averaging on the trimeric GPC spikes and they identified the distinct head, stalk and tail domains (Li et al., 2016) (figure 1.15A). The head/stalk was found to be 9 nm long and 10 nm wide and the three stalk domains, which they assigned to the GP2 domain, were spaced 4 nm apart (Li et al., 2016). They further identified densities attributed to the membrane bilayer, in addition to two layers on the inner side of the membrane, one attributed to the GPC tails and the other to the ZP matrix layer (Li et al., 2016) (figure 1.15A). Li et al. also performed analysis on the structure of the LASV GPC in comparison to the structure of the UHV GPC, which was actually found to have higher structural homology with EBOV GPs than the LASV GPC (Li et al., 2016). Furthermore, the tomographic structure of the LASV GPC was solved at pH 5 and in complex with its secondary receptor, lysosomal-associated membrane protein 1 (LAMP1) (figure 1.15B). This showed that the reduction in pH induced structural changes in the LASV GPC, which allowed the GPC to interact with LAMP1 (Li et al., 2016).

The crystal structures of the prefusion GPCs of LCMV (Hastie et al., 2016a) and LASV (Hastie et al., 2017) have been solved (figure 1.16), although the transmembrane domain was omitted and mutations were introduced in order to stabilise the proteins for x-ray crystallography. These structures added to the numerous crystal structures available for independent GP1 and GP2 domains from a range of arenaviruses (Bowden et al., 2009; Cohen-Dvashi et al., 2015, 2018; Israeli et al., 2017; Shimon et al., 2017; Pryce et al., 2018; Hastie et al., 2017). High structural homology is shared between the arenavirus GP1 domains and the crystal structure of the LASV GPC aligned well with the tomographic reconstruction of the LASV GPC (Li et al., 2016; Hastie et al., 2017; Hastie and Saphire, 2018) (figure

1.15C). This provided information for the positioning of the histidine triad in the crystallographic reconstruction of LASV GPC for its interaction with LAMP1 (figure 1.15D). The histidine triad is also conserved in the LCMV GPC, but LAMP1 has not been shown to be required for LCMV infection (Jae et al., 2014). However, mutations of the histidine triad residues are lethal, suggesting it performs a critical function, perhaps for stability or for interaction with an additional, as of yet unidentified, receptor for LCMV (Hastie et al., 2016a).

Old World mammarenaviruses such as LCMV and LASV require α-dystroglycan as an entry receptor, and enter cells in a macropinocytosis-like manner (figure 1.20). Alternatively, New World mammarenaviruses, classified within clade B, require transferrin receptor 1 and enter cells through clathrin-mediated endocytosis (figure 1.20). PICV is a New World mammarenavirus classified within clade A, and the cellular entry receptor and pathway have not yet been identified. The requirement of a different entry receptor by PICV indicates that the GPC of the New World clade A mammarenaviruses could be structurally different to the structures of the GPC and GP1 from mammarenaviruses classified within the Old World group and the New World group, clades B and D.

5.1.3 Chapter Aims

In this chapter, the first aim was to successfully optimise the propagation and purification of two mammarenaviruses, PICV and LCMV, resulting in viral titres reaching 10^7 plaque forming units per mL (pfu/mL) or ffu/mL. Once this was achieved, the following aims were to investigate the ultra-structure of the viruses using cryo-ET and to resolve the structure of the GPCs using STA. This would allow for a structural comparison of the GPCs from Old World and New World mammarenaviruses.

5.2 Results

5.2.1 Optimisation of PICV Propagation

In order to generate a highly concentrated sample of PICV virions, it was first necessary to determine the optimal protocol for the production of high titre stocks. Initially, to determine the optimal initial MOI that resulted in the highest titre of released virus, BHK-21 cells were infected with PICV at MOIs that ranged from 0.1 to 0.0001. Every 24 hours, until 72 hpi, a sample of the supernatant was collected. The supernatants were then diluted ten-fold and used to infect vero cells, which were overlaid with 1.6 % methylcellulose and incubated for six days, prior to crystal violet staining to identify formation of plaques. This revealed that infection with PICV at an MOI of 0.1 resulted in a higher titre (0.1; $4x10^5$ pfu/mL) at 24 hours, when compared to the titres after infection with PICV MOIs of 0.01, 0.001 or 0.0001 (respectively, $9x10^4$ pfu/mL, $2x10^4$ pfu/mL and 0.0001; $1x10^3$ pfu/mL) (figure 5.2A). However, the later timepoints after infection with PICV at MOIs of 0.1 or 0.01 showed little increase in the viral titre; in fact, there was a decrease at 72 hpi (0.1; $2x10^5$ pfu/mL or 0.01; $3.5x10^5$ pfu/mL) (figure 5.2A). This was in contrast to the later timepoints after infection with PICV at an MOI of 0.001 or 0.0001, the titres of which continued increasing and reached the highest titre at 72 hpi (0.001; $1.5x10^7$ pfu/mL or 0.0001; $1.5x10^6$ pfu/mL) (figure 5.2A). This showed that titres reaching 10^7 pfu/mL were achievable by infecting BHK-21 cells with PICV at an MOI of 0.001 and incubating for 72 hpi.

As the aim was to purify PICV for EM, it was reasoned that it would be beneficial to remove any contaminants that could affect imaging prior to propagation, such as foetal bovine serum (FBS). Therefore, BHK-21 cells were infected with PICV at an MOI of 0.001 in either DMEM containing 2 % FBS (+FBS), DMEM containing 2 % FBS for the first 24 hours and then replaced with DMEM only (+FBS (24h)) or DMEM only (-FBS). The infected cells were incubated for a total of 96 hours, with a sample of the supernatant harvested every 24 hours and titred by crystal violet plaque assay as described above. This revealed that the presence of FBS was required throughout the entire infection in order to reach a titre of $1.65x10^7$ pfu/mL (figure 5.2B; +FBS). When FBS was not present throughout the entire infection, the

titre was consistently lower, resulting in a 2-log reduction in titre at 72 and 96 hpi (figure 5.2B; -FBS). Including FBS for the first 24 hours of infection showed similar titres to +FBS, at 24 and 48 hpi, as infections where FBS was present throughout (figure 5.2B; +FBS(24h)), but the titres at 72 and 96 hpi showed approximately a 0.8-log reduction from those achieved by infections with FBS present throughout. Additionally, this experiment showed that incubating the infection for 96 hours instead of 72 hours offered no further increase in titre (figure 5.2B). Therefore, FBS could not be removed from the infection media without significantly reducing the titre of PICV.

Based on these results, propagation of PICV was subsequently performed by infecting BHK-21 cells at an MOI of 0.001 in presence of FBS throughout, and incubating for 72 hpi before the supernatant was harvested. Representative plaques for the 10^{-4} and 10^{-5} dilutions, and the mock-infected control, have been shown in figure 5.2C.

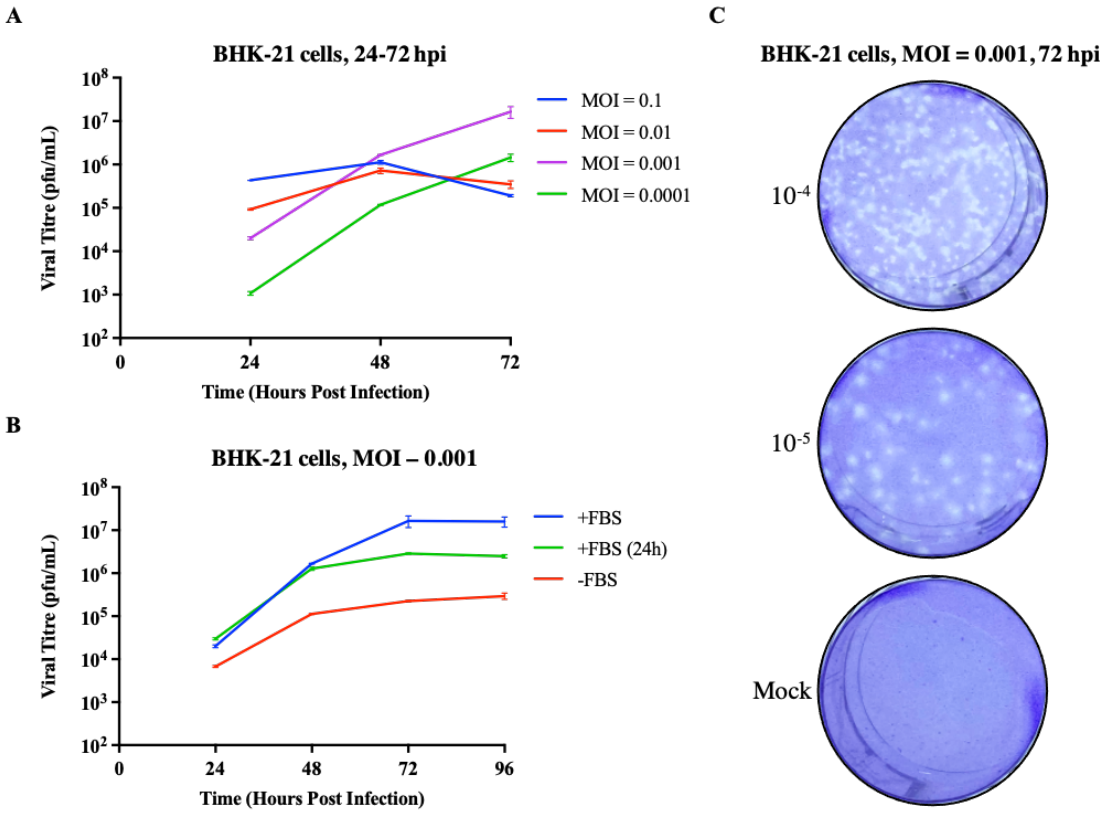

Figure 5.2: Optimisation of PICV Propagation BHK-21 cells were infected with PICV at multiplicity of infections (MOIs) ranging from 0.1 to 0.0001 and incubated at 37 ℃ for a total of 72 hours. The supernatants were sampled every 24 hours and titred in duplicate by crystal violet plaque assay. The titres were then plotted on a graph (**A**) to determine the optimal MOI for infection. BHK-21 cells were then infected with PICV at an MOI of 0.001 and incubated at 37 ℃ for 96 hours. Simultaneous infections were set up whereby the infection was performed in either DMEM containing 2 % FBS (+FBS), DMEM containing 2 % FBS for the first 24 hours and then replaced with DMEM only (+FBS (24h)) or DMEM only (-FBS). Samples of the supernatant were collected every 24 hours and titred in duplicate by crystal violet plaque assay. The titres were then plotted on a graph (**B**) to determine the optimal harvest time. BHK-21 cells were infected with PICV at an MOI of 0.001 and incubated at 37 ℃ for 72 hours. The supernatants were collected for further purification and a sample was serially diluted (10-fold) to determine the titre by crystal violet plaque assay. Representative wells showing countable plaques from the mock-infected control and the 10^{-4} and 10^{-5} dilutions have been shown (**C**).

5.2.2 Purification of PICV for Cryo-Electron Microscopy

For examination by EM, the virus sample must be highly concentrated and relatively free of cellular contaminants. To achieve this, PICV was propagated as described in section 5.2.1. The harvested supernatant was then clarified by centrifugation, before being passed through a 0.45 µm filter and then a second round of centrifugation (figure 5.3A). The clarified supernatant was then purified through a 30 % sucrose cushion by ultracentrifugation at 150,000 x g in order to pellet PICV. The virus pellet was then briefly dried and resuspended overnight at 4℃ in 0.1X PBS, which

was supplemented with 0.1 mM $CaCl_2$ and 0.1 mM $MgCl_2$.

Samples were collected throughout the purification process to monitor concentration and removal of contaminants (figure 5.3A). These samples were analysed by SDS-PAGE through western blotting (using the LCMV NP antibody that was previously shown to be cross-reactive with PICV NP; chapter 3, figure 3.11). The western blot analysis revealed the NP band was only visible in the resuspended pellet (purified PICV), showing successful concentration of PICV (figure 5.3B). The samples were also examined using SDS-PAGE and silver staining to show the total protein present in each sample. The silver stain showed a large band at approximately 65 kDa that was present in the harvested supernatant and throughout the purification. Due to the presence of FBS in the infection media, it was thought that this band could represent bovine serum albumin (BSA), which is the major constituent of FBS and is approximately 66.4 kDa. The majority of the BSA was successfully removed by the sucrose cushion, because the band was drastically smaller in the sucrose and purified PICV samples. The silver stain revealed additional bands, which first become visible in the purified PICV sample, that were a similar molecular weight to the predicted molecular weights of the other structural viral proteins, including the LP (~252 kDa), the NP (~62 kDa), the constituents of the GPC (GP1; ~44 kDa and GP2; ~35 kDa) and the ZP (~11 kDa) (as indicated in figure 5.3C). Additional bands can also be seen, which may be the result of cellular proteins that could be associated with the virus or contaminating proteins that have not been successfully removed by the sucrose cushion.

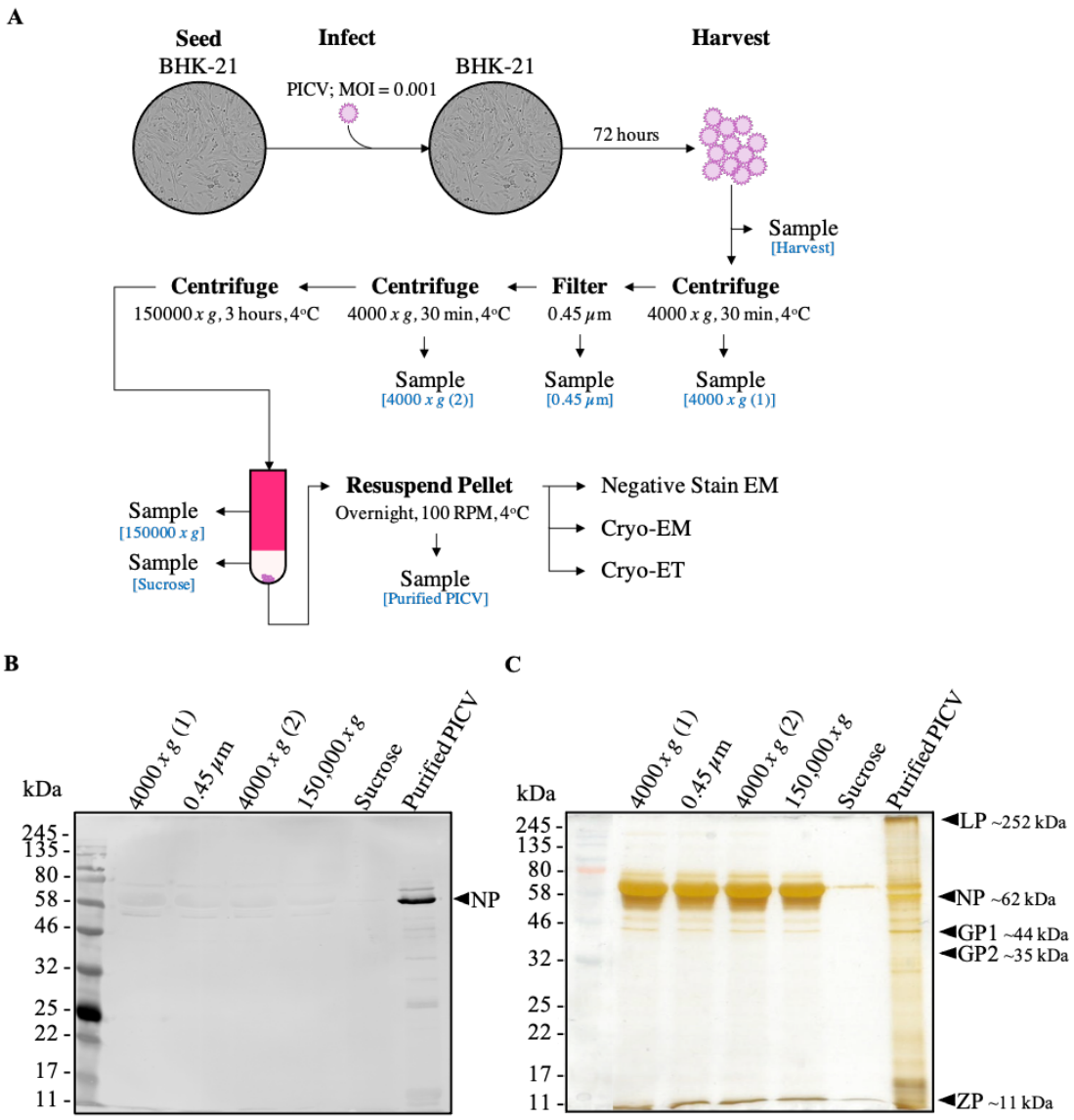

Figure 5.3: Purification of PICV (**A**) shows the process of PICV purification. BHK-21 cells were seeded one day before infection, to reach a confluency of 60-70 %. The BHK-21 cells were infected with PICV at an MOI of 0.001 and incubated at 37 °C for 72 hours. The supernatant was harvested, centrifuged at 4000 *x g* for 30 minutes at 4 °C, filtered through a 0.45 µm filter and finally centrifuged again at 4000 *x g* for 30 minutes at 4 °C. The supernatant was underlayed with an 8 mL 30 % sucrose cushion, which was centrifuged at 150,000 *x g* for 3 hours at 4 °C. The PICV pellet was briefly air-dried and resuspended overnight in 0.1 X PBS buffer supplemented with 0.1 mM $CaCl_2$ and 0.1 mM $MgCl_2$. The resuspended pellet was then examined by negative-stain EM, cryo-EM and tomography. Samples were taken throughout the process, as indicated, for western blotting analysis with the LCMV NP antibody (**B**) and silver stain analysis (**C**). Potential bands in the silver stain that could correspond to viral proteins have been indicated.

5.2.3 Examination of PICV using Negative-Stain Electron Microscopy

In order to further assess the purity, concentration and morphology of purified PICV, the sample was diluted 1:10 and loaded onto glow-discharged carbon-coated grids,

where it was stained with 2 % heavy metal uranyl acetate solution and examined by electron microscopy. Images were taken at 5000 x magnification, to gain an overview of the amount of virus present (figure 5.4A). These images showed there was virus present, which appeared to be undisrupted after the ultracentrifugation process. There was some background that could have been the result of contaminating proteins or erupted viruses, but overall it was easy to identify the virions of interest, which had a predominantly spherical morphology. Images were also collected at 30,000 x magnification to further investigate the size and morphology of the individual virions, which have been indicated by white arrowheads (figure 5.4B). The higher magnification showed a mixture of larger viruses (average diameter 104.6 nm ± 16.9 nm) and smaller viruses (average diameter 59.7 nm ± 8.2 nm). The viruses did not appear to be perfectly spherical, with some viruses presenting as oval-shaped or dented. The viruses showed a speckled appearance, attributed to the GPC spike projections, which suggests that the purification of PICV was successful and the sample could be taken forward to cryo-EM.

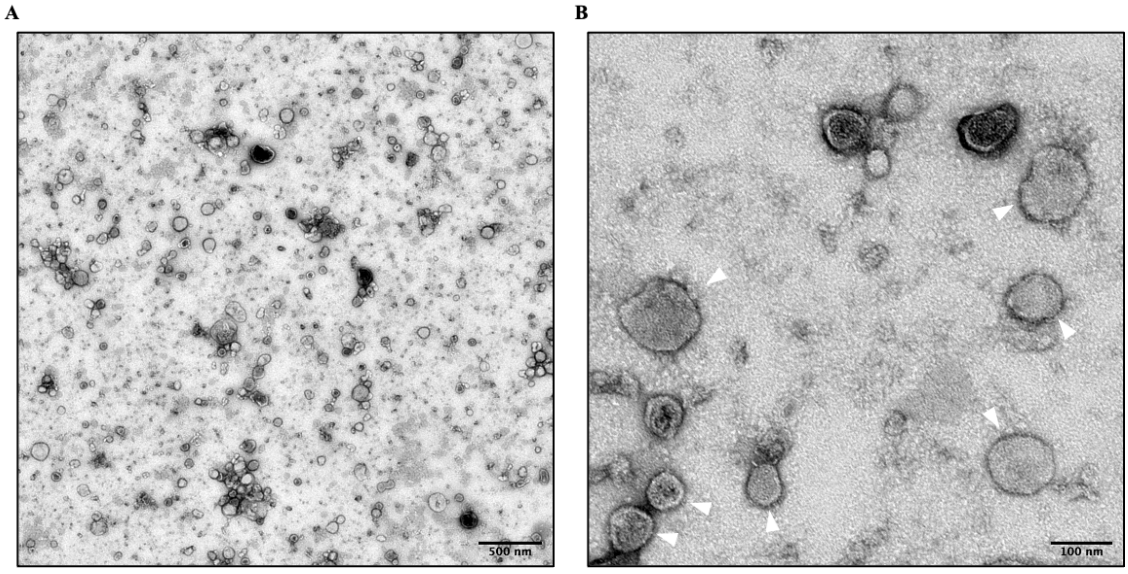

Figure 5.4: Examination of PICV by Negative-Stain Electron Microscopy Purified PICV was diluted 1:10 and examined by negative-stain EM to assess sample concentration and purity. The sample was stained with 2 % uranyl acetate and imaged at 5000 x magnification (**A**) and 30,000 x magnification (**B**) at 120 kV on a JEOL 1400 transmission electron microscope. Scale bars represent 500 nm (**A**) and 100 nm (**B**). Individual virions have been indicated with white arrowheads.

5.2.4 Examination of PICV using Cryo-Electron Microscopy

Cryo-EM was then performed to assess the suitability of the purified PICV sample for cryo-ET and to confirm that the background contamination was sufficiently low. The purified PICV sample was mixed 1:1 with Protein A conjugated with 10 nm colloidal gold (Aurion), which would act as fiducial markers for subsequent tilt series alignment. This was then immediately added to glow-discharged Quantifoil R 2/2 grids and incubated for 1 minute. The grid was then blotted to leave a very thin film of liquid. The grid was subsequently vitrified by immediate submersion into liquid ethane and transferred to liquid nitrogen for all further handling, storage and imaging steps. This method results in virions suspended within the carbon holes in a thin layer of vitreous ice.

QUANTIFOIL R 2/2 (2 µm holes spaced 2 µm apart) 400-mesh (number of squares per inch) grids, which have regularly spaced, circular holes, were chosen for cryo-EM and cryo-ET investigation. Images were taken at 9,000 x magnification, which revealed a lack of ice crystal formation and the majority of viruses in the sample were distributed evenly across the hole in the carbon, although there were some viruses present on the carbon itself too (figure 5.5A). Images taken at higher magnifications (29,000 x and 59,000 x) showed the presence of roughly spherical viruses, which had dense interiors and a membrane bilayer. The viruses also possessed an irregular spiky exterior, which was likely to be the result of projections from the membrane that correspond to the GPC spikes (figure 5.5B, C and D). The cryo-EM images also showed the presence of a low level of background contamination but this was not significant enough to affect cryo-ET. The structure of the GPC could not be resolved at this stage. Overall, cryo-EM confirmed that the sample of purified PICV was suitable for cryo-ET.

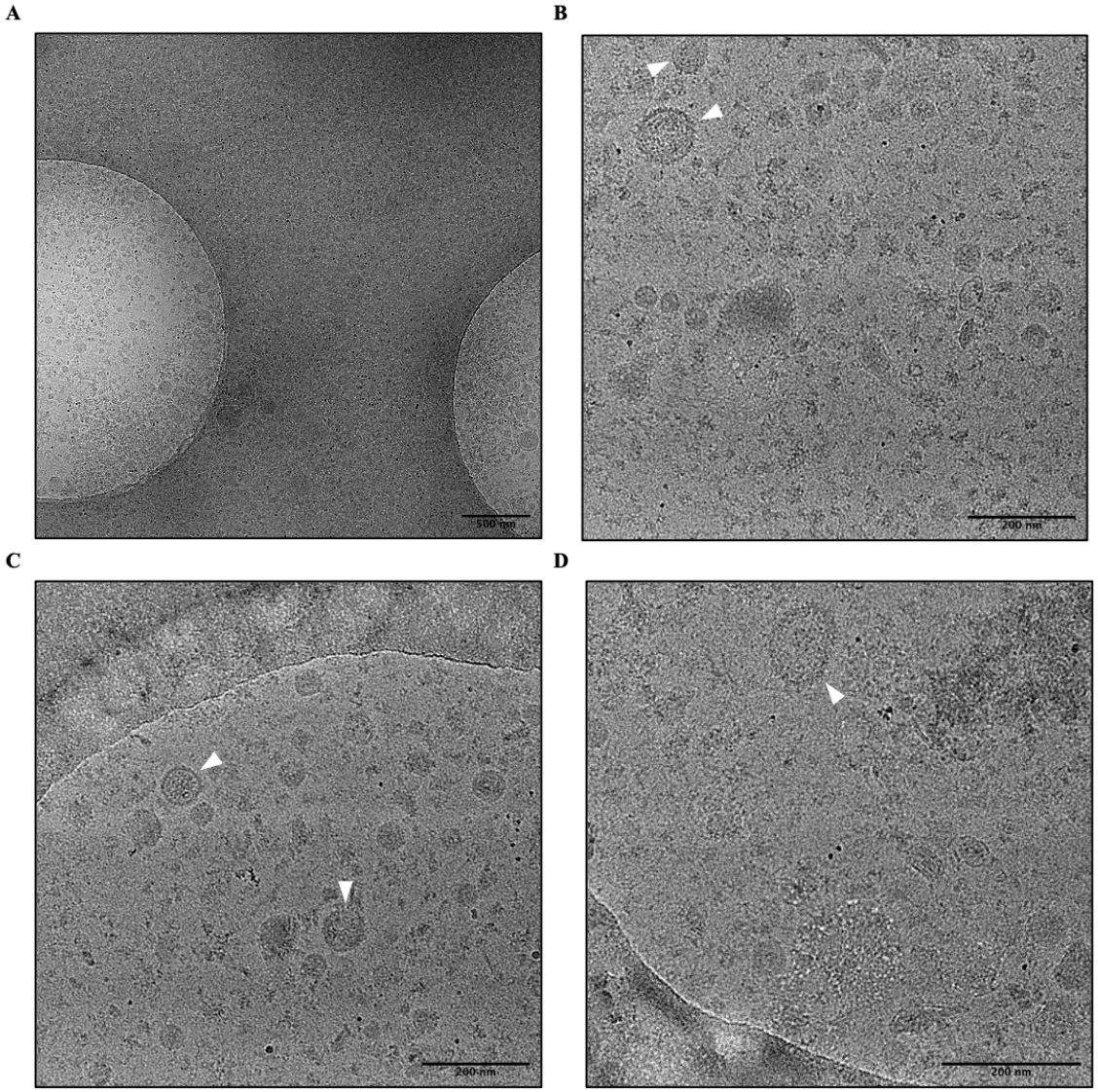

Figure 5.5: Examination of PICV by Cryo-Electron Microscopy The purified PICV sample was mixed 1:1 with Protein A conjugated with 10 nm colloidal gold, added to glow-discharged Quantifoil R 2/2 grids and vitrified. The grid was transferred to liquid nitrogen and imaged using the Titan Krios 2 transmission electron microscope. Images were taken at 9000 x magnification (**A**), 29,000 x magnification (**B** and **C**) 59,000 x magnification (**D**). Scale bars represent 500 nm (**A**) and 200 nm (**B**, **C** and **D**). Individual virions have been indicated with white arrowheads.

5.2.5 Examination of PICV using Cryo-Electron Tomography

To understand the structure of the native GPC spikes on the PICV surface, it was necessary to create 3D reconstructions of the viruses, and then apply STA to average the spikes. Arenaviruses are pleomorphic, enveloped viruses, as seen in the negative-stain EM and cryo-EM examination (figures 5.4 and 5.5). Furthermore, the arenavirus glycoprotein spikes were also not regularly arranged across the virion. This meant that cryo-EM and single-particle analysis could not be used to generate 3D reconstructions of the pleomorphic arenaviruses or the irregularly arranged GPC spikes (Cope et al., 2011).

Cryo-ET allows to generate the 3D reconstructions of pleomorphic, irregular particles, through collecting multiple micrographs of the same feature of interest at different projection angles, forming what is called a tilt-series. Typically in cryo-ET, the holder is physically tilted from -60° to +60° and images are collected at every 1° or 2° increments. For the cryo-ET of PICV, the mesh size of the chosen grid was too small and the grid bars obstructed the electron beam at higher tilts. To account for this, the PICV tilt series were acquired from -50° to +50° with 2° increments (figure 5.1). Due to 51 images being collected from the same region, a low electron dose was used to limit radiation damage of the sample. In order to improve the SNR, a Volta phase plate was used, which introduced contrast to the specimen by applying phase shift to the scattered electrons (Danev and Baumeister, 2017; Thompson et al., 2016). The 2D tilt-series are then computationally combined to form a 3D volume (tomogram) (figure 5.1). STA can then be performed on repeated structures within a tomogram; particles (such as the GPC spikes) are selected and aligned to one another to generate an average, which improves the SNR and resolution.

A total of 24 single-axis tilt-series were collected on PICV, using a Titan Krios transmission electron microscope and Tomography 4 software for an automated data collection. Using the Etomo program from the IMOD package, 3D tomograms were reconstructed from all the tilt-series collected (Kremer et al., 1996). The tilt-series were initially aligned using the gold particles as fiducial markers, which acted as constant reference points in all the images of the tilt-series. Two of the tilt-series were unable to be reconstructed due to either poor contrast or a low number of gold

particles present, affecting the alignment, resulting in 22 reconstructed tomograms. These tomograms were binned by 2, to speed up image processing, giving a final pixel size of 5.44 Å.

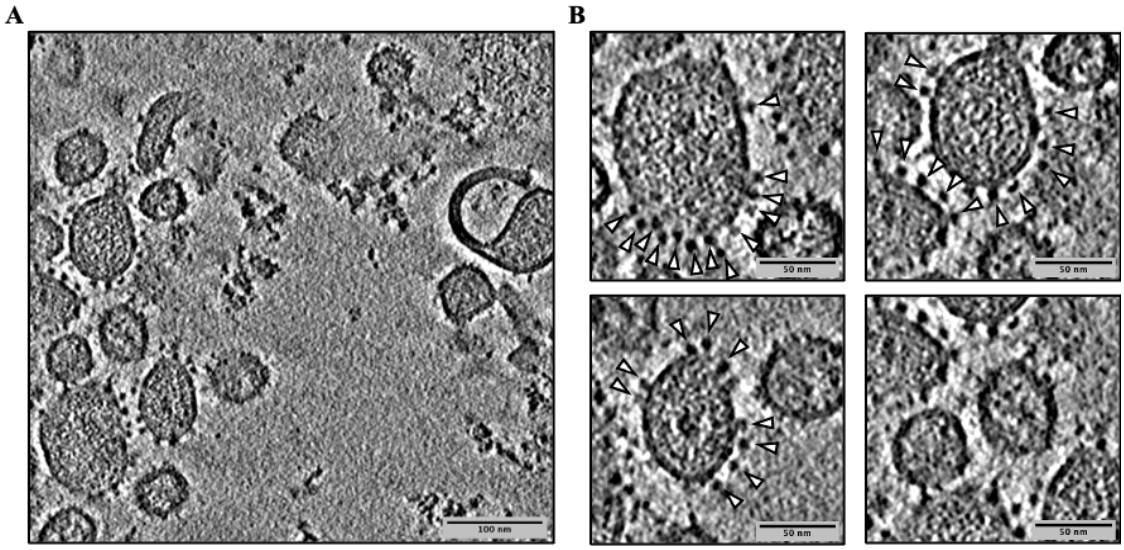

Figure 5.6: Examination of PICV by Cryo-Electron Tomography Cryo-ET was performed following the process depicted in figure 5.1. A series of images were collected at every 2° increment between -50° to +50°. This tilt-series was then used to reconstruct a 3D tomogram (**A**). Virions displaying glycoprotein spikes can be clearly seen in (**A**). Enlarged images of individual virions have been shown in (B), with white arrowheads indicating the positions of the glycoprotein spikes. Scale bars have been included, representing 100 nm (**A**) and 50 nm (**B**). All the images were filtered in ImageJ using Gaussian Blur 3D.

The 3D tomographic reconstruction of PICV allowed visualisation of the lipid bilayer and the GPC spikes present on the virion surface, which have been indicated with white arrowheads (figure 5.6B). The electron density within the virions was too disordered to determine the structural organisation and packing of the viral genomic RNPs (figure 5.6). It was also too disordered to determine whether ribosomes were present in the virions, but there was no clear indication of their presence (figure 5.6).

Figure 5.7A shows multiple sections taken throughout the Z-plane of a PICV virion. The top (1) and bottom (6) slices show the GPC spikes on the exterior of the virion surface. This revealed that the GPC spikes appeared to be randomly distributed. The slices 2, 3, 4 and 5 show the cross-section of the GPC spikes present with the membrane bilayer (figure 5.7A). The GPC spikes were on average approximately 8.7 nm (±1.4 nm) long (measured from the membrane) and 6.6 nm (±0.9 nm) wide (measured at from the top and bottom views). A triangle shape, indicating trimeric organisation, was apparent, with a few GPC spikes in the top and bottom views,

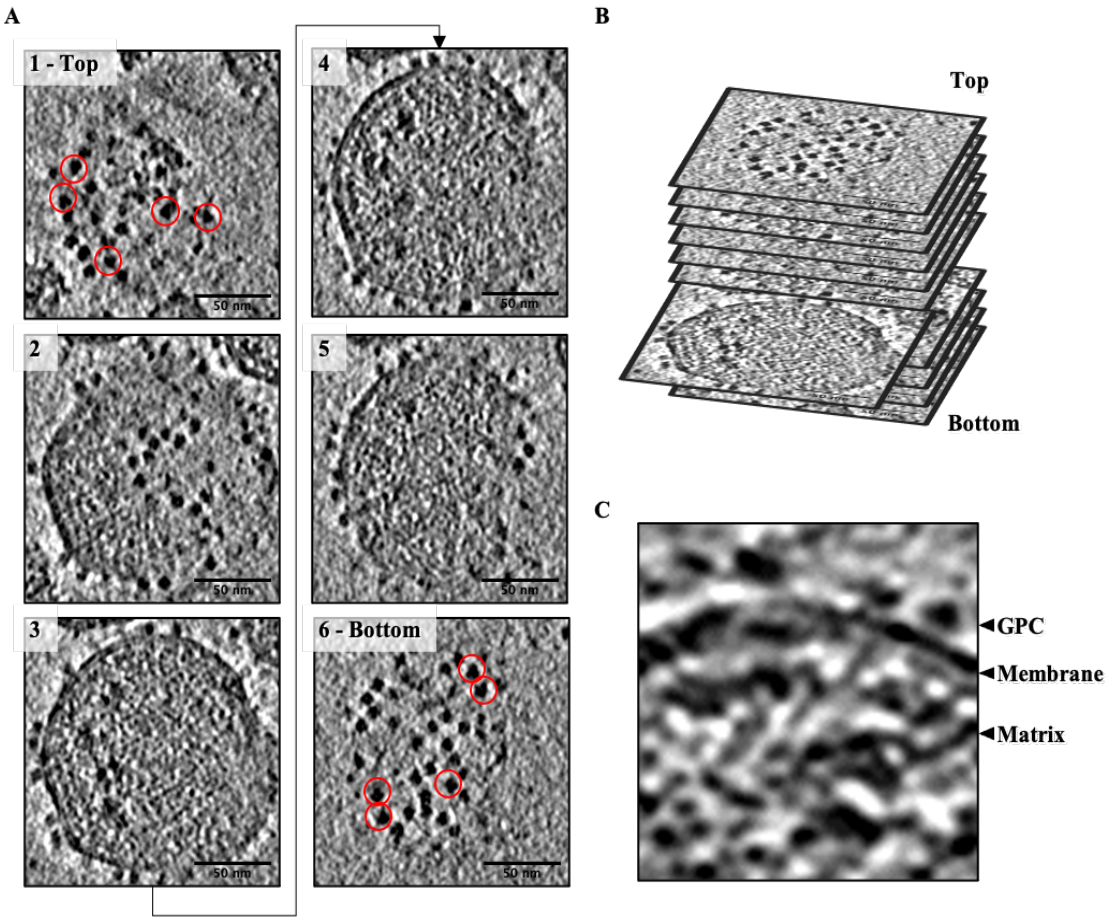

Figure 5.7: Visualisation of PICV in Slices Through the Virus Sections (1-6) throughout the Z-plane of a single virus have been shown, which were taken approximately every 30 slices working from the top of the virus (1) to the bottom of the virus (6) (**A**). There is an additional layer that can be seen in image (4), which could potentially represent the ZP matrix layer. The arrangement of these slices for the reconstruction of a 3D volume is shown schematically in (**B**). Scale bars represent 50 nm. All the images were filtered in ImageJ using Gaussian Blur 3D.

as indicated by red circles (figure 5.7A). Furthermore, slice 4 showed an additional electron density that was running parallel to the membrane bilayer, which may represent the ZP matrix layer, as can be seen in the zoomed-in image (figure 5.7C).

To further resolve the structure of the GPC spikes, STA was performed to generate an average of the structure.

5.2.6 Sub-Tomogram Averaging of the PICV Glycoprotein Complex

The STA of the PICV GPC spikes, which involves several iterations of alignment, averaging and refinement, was performed using the PEET (Particle Estimation for

Electron Tomography) software from the IMOD package (Nicastro, 2006; Heumann et al., 2011; Li et al., 2016; Cope et al., 2011; Punch et al., 2018). Approximately 2,800 spikes were selected manually and an initial orientation perpendicular to the viral membrane was provided. The spikes were then subject to alignment and averaging, which involved iterative refinements whereby PEET searched for the position (the position of the spike on the membrane) and orientation (the rotation of the spike) of the particles in order to include them in the final average.

The spikes were initially averaged without any alignment to generate an initial reference (figure 5.8A). The average generated from this first stage, had C120 symmetry applied (using the Bsoft programme; bsym) to remove any features that the reference could have. This C120-symmetrised average was used as the initial reference in the next stage of refinement.

The first stage of refinement (figure 5.8B) allowed for a wide search around the particle position and orientation in order to allow the program to correct the position of particles that were not properly centred during manual picking, and the orientation of particles that was not correctly estimated (e.g. because they were not perpendicular to the membrane). Spherical masking, which was centred on the spike, was applied to focus the programme on aligning the electron densities that correspond to the spike. The reference spike was allowed to improve with the iterations to drive improvement of subsequent averages. PEET was also set to remove particles that were identified as duplicates, which were any particles that were within 5.44 nm of another particle.

In the second stage of refinement (figure 5.8C), there were several iterative steps where the angular searches to improve the spike positioning were increasingly restricted. The final average of this run was band pass filtered (to remove high and/or low spatial frequencies) and used for the reference in the next stage.

In the third stage of refinement (figure 5.8D), the GPC spikes displayed C3 symmetry. The C3 symmetry was further confirmed by masking only glycoprotein base, where C3 symmetry would be most evident, and searches were limited to the twist orientation of the particles around the Y-axis. The averages from this run confirmed C3 symmetry and therefore C3 symmetry was applied to the average to form the reference for the next stage of refinement.

In the final stage of refinement (figure 5.8E), the C3 symmetrised average from the previous run was used as the reference and the mask, which was still centred on the GPC spike, was increased to 20 pixels to focus on gaining high resolution information from the spike only. The initial iterations only refined the angle around the Y-axis, but the final iterations refined all the angles to very small searches.

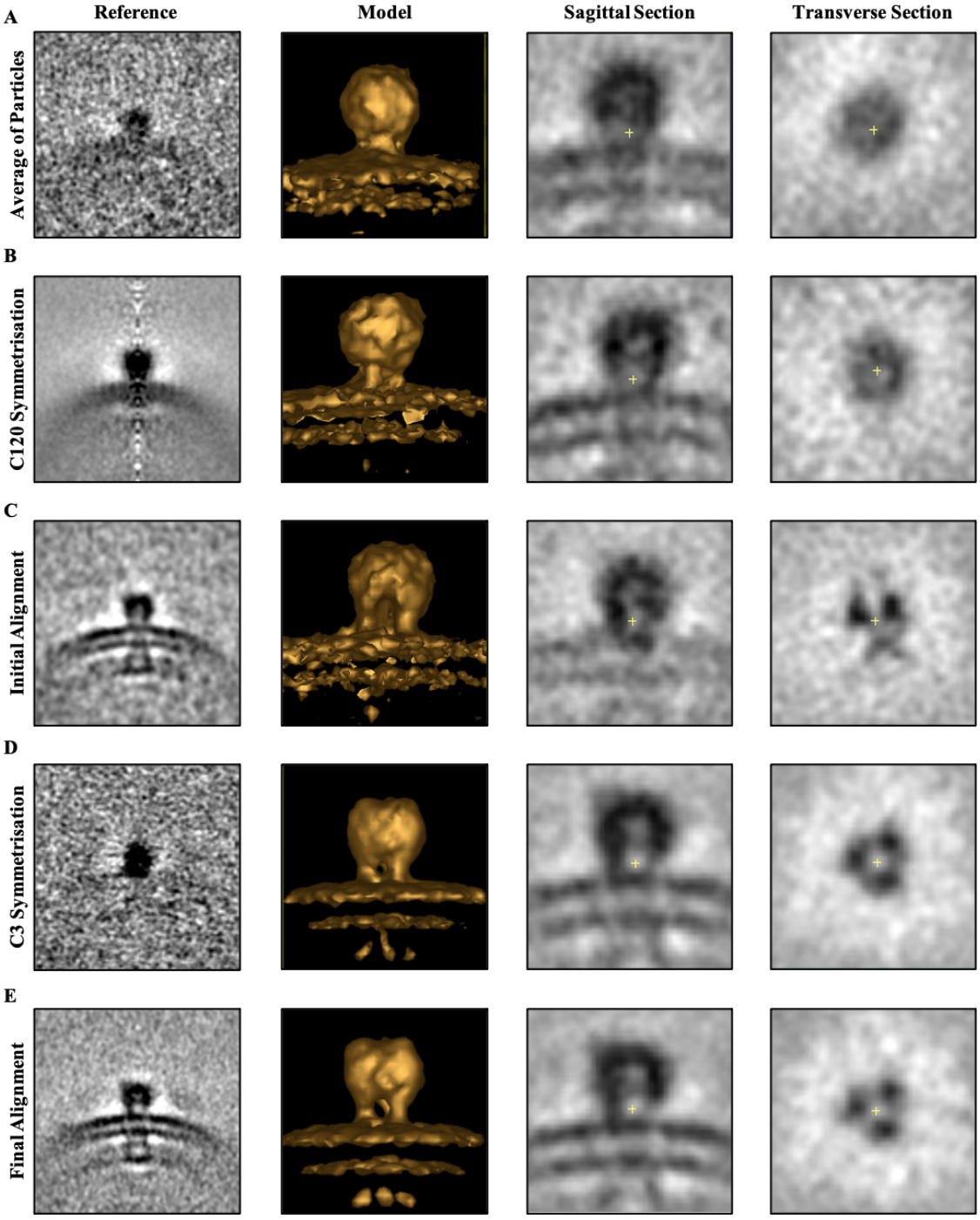

Figure 5.8: Stages of Sub-Tomogram Averaging of PICV GPC In each stage, the following has been shown; the reference particle used as the template particle for that stage (reference), the isosurface rendering of the average generated in that stage (model) and sagittal and transverse sections of the average generated in that stage (sagittal section and transverse section). The STA performed with the PICV GPC began with the averaging of all the manually selected particles (**A**), followed by averaging using a C120 symmetrised reference (**B**). The particles were then initially aligned (**C**), where C3 symmetry was identified. C3 symmetrisation of the average provided the reference for the next stage of refinement (**D**) before minute adjustments in the final stage of refinement (**E**).

The final average shows the trimeric organisation of the PICV GPC spike (figure 5.9). Figure 5.9A shows the electron densities of the average derived from the final round of refinement, whereby the black indicates the regions of high electron density. Image 1 shows a sagittal sections of the GPC spike, image 2 shows another sagittal section of the GPC spike (from the position indicated by "2" in image 1) and image 3 shows a transverse section of the GPC spike (from the position indicated by "3" in image 1). The membrane bilayer can be clearly defined and the GPC spike on one side of the bilayer and the GPC cytoplasmic tails can also be seen (figure 5.9A). The GPC spike measures approximately 9.6 nm across and 9 nm long (from the membrane) whereas the GPC tail measures approximately 4 nm long (figure 5.9A). Image 3 shows the trimeric organisation of the GPC spike, where the three stalks of each monomer were clearly visible. The isosurface rendering of the spike (figure 5.9B) shows the GPC head, stalk and tail from each monomer, in addition to the membrane bilayer. The trimeric organisation was easily identified throughout the model, but becomes more evident in the head region when the model has been tilted 45° toward the viewer and then again when the transverse plane has been shown at 90°, which was sectioned at the stalk region. The resolution of our electron density was calculated by Fourier shell correlation (FSC), using a 0.5 cut-off (black line), and was estimated to be ~22.7 Å (figure 5.9C). The other lines (blue, orange, yellow, purple) were the FSC plots calculated for averages generated from fewer sub-tomograms, which show that the resolution was not significantly improved through addition of more particles, suggesting the resolution was not limited by the number of particles. This may be due to an error during the data collection, where only one frame for each angle projection was collected, in contrast to the usual four, which are then averaged together. To improve the resolution therefore, this work has been repeated and is ongoing.

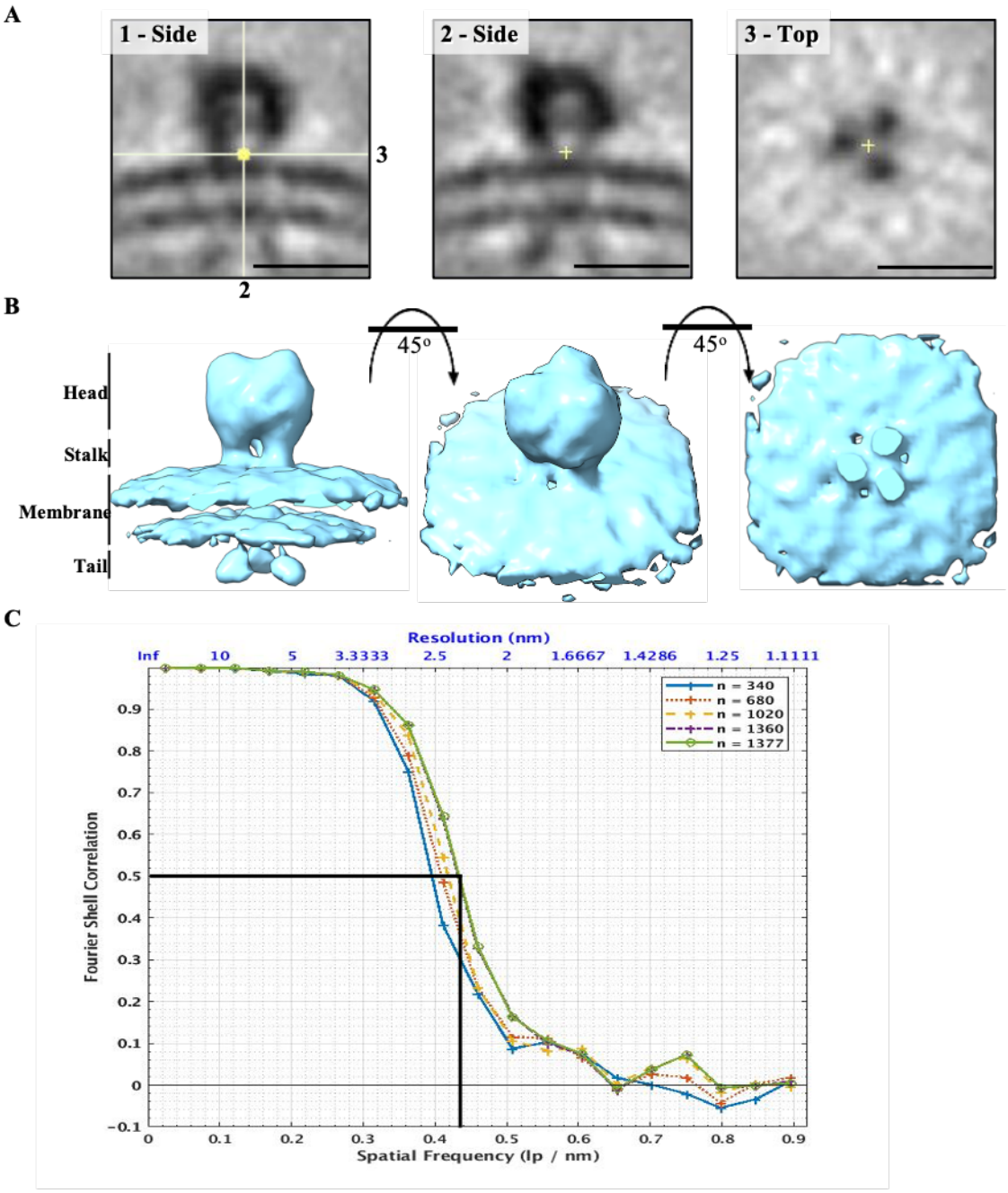

Figure 5.9: Sub-Tomogram Averaging of the PICV Glycoprotein Complex STA on the reconstructed PICV tomograms was performed on 2,754 manually-picked PICV GPC spikes, which were averaged and subject to refinement through several iterations using the IMOD PEET software. The sagittal planes (1 and 2) and the transverse plane (3) of the electron density averages of the GPC spikes have been shown (**A**). The crossed lines on image 1 correspond to the sections used for images 2 and 3. Scale bars depict 10 nm. The isosurface rendered model of the GPC spike reveals three regions; head, stalk and tail and a trimeric organisation (**B**). The GPC spike model has also been tilted forward in the X-plane by 45° to show the top of the head domain (central panel). The GPC spike model has been further tilted forward in the X-plane by a total of 90° to show the transverse section of the GPC spike and the trimeric organisation (right panel). This model was visualised using UCSF Chimera X. To determine the resolution, an FSC plot was used and the resolution was found to be ~22.8 Å at the 0.5 cut-off (black line) (**C**). "n" represents the number of particles included in the averaging and the green line represents the maximum number of particles included (1,377).

5.2.7 Optimisation of LCMV Propagation

At this point, it had been determined that a titre of 10^7 pfu/mL was achievable for PICV after infection of BHK-21 cells with an MOI of 0.001 (figure 5.2). It had also been determined that a titre of 10^7 ffu/mL was achievable for rLCMV after infection of BHK-21 cells with an MOI of 0.001 (figure 4.13). To see whether the titre could be increased further, and to limit the introduction of mutations into the viral genome through repeated passaging, BHK-21 cells were infected, at an MOI of 0.001, with rLCMV-WT harvested directly from the transfection of BSR-T7 cells with the reverse genetics plasmids (at 120 hpt). The infected cells were incubated for a total of 96 hours, with samples of the supernatant taken every 24 hours and titred by focus forming assay. There was a steep 3-log-fold increase in titre between 24 ($1.6\text{x}10^3$ ffu/mL) and 48 hours ($5\text{x}10^6$ ffu/mL) (figure 5.10A). The titre then increased further at 72 hours, reaching $1.6\text{x}10^7$ ffu/mL, before decreasing again at 96 hours ($6\text{x}10^6$ ffu/mL; figure 5.10A). The titre harvested here was not significantly different to the titre collected in figure 4.13. However, it was thought that viruses harvested from an earlier passage would have fewer mutations and fewer defective interfering particles. Therefore, in order to generate the stock of rLCMV-WT (hereby referred to as LCMV) for further purification and cryo-ET, BHK-21 cells were infected with LCMV (which had been generated from the transfected BSR-T7 cells) at an MOI of 0.001 and incubated for 72 hours. The supernatant was collected and a sample was taken for the titre to be determined by focus forming assay (figure 5.11B; Harvest). Unfortunately, on this occasion, the titre was one-log lower than was previously achieved ($1.5\text{x}10^6$ ffu/mL), but purification was continued anyway.

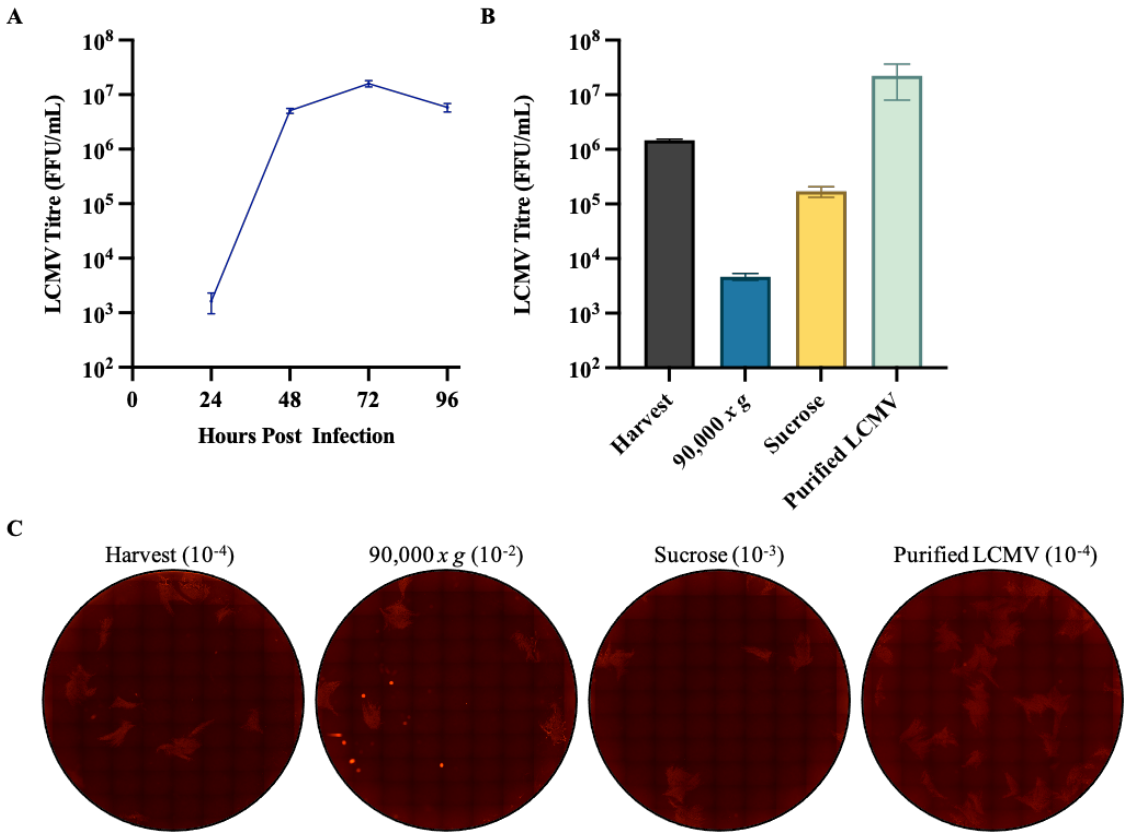

Figure 5.10: Optimisation of LCMV Propagation BHK-21 cells were infected with LCMV at MOI of 0.001 and incubated at 37 ℃ for 96 hours. Samples of the supernatant were collected every 24 hours and titred in triplicate by focus forming assay. The titres were then plotted on a graph (**A**) to determine the optimal harvest time. BHK-21 cells were then infected with LCMV at an MOI of 0.001 and incubated at 37 ℃ for 72 hours. The supernatants were collected for further purification as detailed in figure 5.11. Samples were collected throughout the purification process; the supernatant prior to purification (harvest), the supernatant after centrifugation at 90,000 *x g* for 3 hours (90,000 *x g*), the sucrose cushion used for purification (sucrose) and the resuspended LCMV pellet (purified LCMV) (**B**). The titres of these samples were determined by focus forming assay and were plotted on a graph (**B**). Representative wells of each of the purification samples showing countable plaques have been shown, and the dilution specified in brackets (**C**).

5.2.8 Purification of LCMV for Cryo-Electron Microscopy

In order to purify LCMV for electron microscopy, a similar propagation and purification protocol as was performed for PICV was carried out, although with a reduced sucrose concentration (20 % instead of 30 %) and with ultracentrifugation performed at 90,000 *x g* (instead of 150,000 *x g*) (figure 5.11A). Following resuspension, the resuspended LCMV pellet was flash frozen in liquid nitrogen and stored at -80 ℃.

Samples were collected throughout the purification process to monitor the titre of infectious LCMV. The harvested supernatant (180 mL) had a titre of 1.5x10^6

ffu/mL and the purified LCMV pellet was resuspended in 90 µL, suggesting a 2000-fold concentration of the harvested supernatant, which would result in a titre of $3x10^9$ ffu/mL. However, the titre of the purified LCMV pellet was calculated to be $2.2x10^7$ ffu/mL (figure 5.10B). The titre of the remaining supernatant after the ultra-centrifuge spin (90,000 *x g*; 180 mL) was $5x10^3$ ffu/mL whilst the titre of the sucrose cushion (sucrose; 48 mL) was $1.7x10^5$ ffu/mL (figure 5.10B). It was evident that a proportion of infectious LCMV does not pellet through the supernatant and the sucrose, suggesting that the samples may need to be centrifuged at a higher speed or for longer. However, the loss of infectious virus in the supernatant and sucrose does not account for the lack of appropriate increase in the titre of the purified LCMV pellet. This may be due to inactivation of the virions occuring at any number of stages, including the 90,000 *x g* centrifuge, the pellet drying out process, the overnight resuspension, the liquid nitrogen flash freeze of the resuspended pellet or the subsequent defrost. Further optimisation of the purification protocol of LCMV may be required, in order to understand where this loss of infectious LCMV happened and to recover the highest possible amount of infectious LCMV for subsequent examination.

Samples were also collected throughout the purification process to monitor the concentration of LCMV and the successful removal of contaminants. These samples were analysed by western blotting (stained with the LCMV NP antibody), which revealed the NP band was visible in the samples prior to ultracentrifugation, but the band was more abundant in the purified LCMV sample, confirming LCMV had been successfully concentrated (figure 5.11B). The samples were also examined using SDS-PAGE and silver staining. The silver stain showed that the large band at approximately 65 kDa, which was thought to represent BSA from the FBS in the PICV purification, was similarly removed by the 20 % sucrose barrier as the band was less abundant in the sucrose and purified LCMV samples. The silver stain revealed additional bands in the purified LCMV sample that had comparable molecular weights to those seen in the PICV purification (figure 5.3) and could represent the other viral proteins (figure 5.11C). Additional bands could also be seen but may have resulted from associated cellular proteins or contaminating proteins that purified through the sucrose cushion.

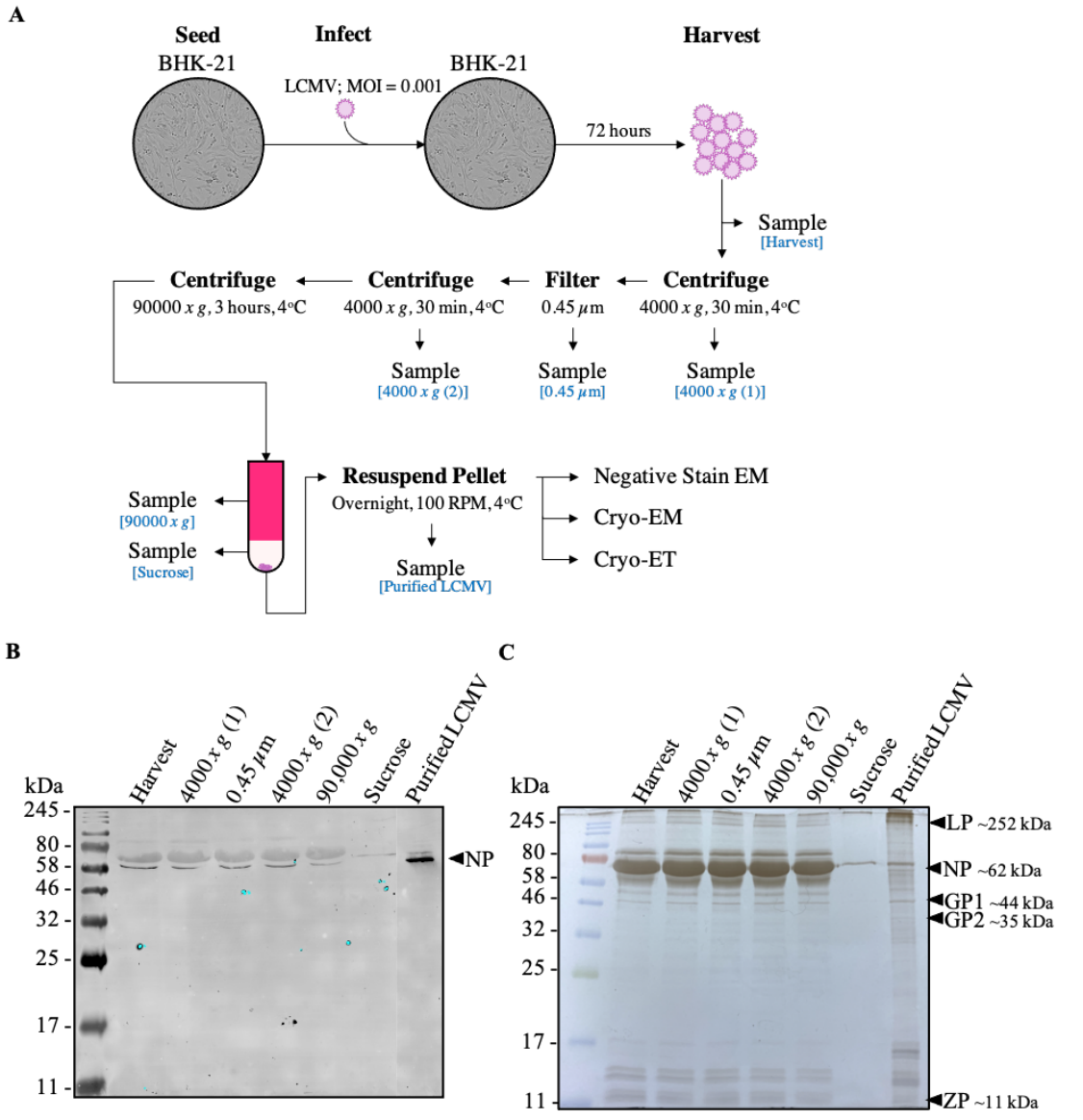

Figure 5.11: Purification of LCMV LCMV was purified following the process depicted in (**A**). BHK-21 cells were seeded one day before infection, to reach a confluency of 60-70 %. The BHK-21 cells were then infected with LCMV at an MOI of 0.001 and incubated at 37 ℃ for 72 hours, at which point the supernatant was harvested and centrifuged at 4000 *x g* for 30 minutes at 4 ℃. The supernatant was filtered through a 0.45 µm filter before it was centrifuged again at 4000 *x g* for 30 minutes at 4 ℃. The supernatant was then underlayed with an 8 mL 20 % sucrose cushion and centrifuged at 90,000 *x g* for 3 hours at 4 ℃. The supernatant and sucrose cushion were removed and the LCMV pellet was briefly air-dried and resuspended overnight in 0.1 X PBS buffer supplemented with 0.1 mM $CaCl_2$ and 0.1 mM $MgCl_2$. The resuspended pellet was flash frozen in liquid nitrogen and stored at -80 ℃. Purified LCMV was then defrosted once for examination by negative-stain EM, cryo-EM and cryo-ET. Samples were taken throughout the process, as indicated, for SDS-PAGE analysis through western blotting with the LCMV NP antibody (**B**) and silver stain (**C**). Bands in the silver stain that could correspond to viral proteins have been indicated.

5.2.9 Examination of LCMV using Negative-Stain Electron Microscopy

To characterise the purity, concentration and morphology of purified LCMV, the sample was diluted 1:10, loaded onto glow-discharged carbon-coated grids, and stained with 2 % uranyl acetate solution. Images were taken at 10,000 x magnification (figure 5.12A) and 20,000 x magnification (figure 5.12B). Individual virions have been indicated by white arrowheads. There was very little background and the majority of the viruses appear whole (figure 5.12A). However, there were a few virions which had stain present on the inside of the virion, suggesting a breach of membrane integrity. Figure 5.12B revealed a mixture of larger viruses (average diameter 110.6 nm ± 32.4 nm) and smaller viruses (average diameter 66.9 nm ± 10.9 nm). Similarly to PICV, the viruses had a predominantly spherical morphology and showed the speckled appearance, consistent with the presence of the GPC spikes. The negative-stain EM confirmed that the sample was suitably concentrated and purified for cryo-EM. The purified LCMV sample (figure 5.12) appeared to have a lower level of background contamination and an increased concentration of virions, when compared to the purified PICV sample (figure 5.4).

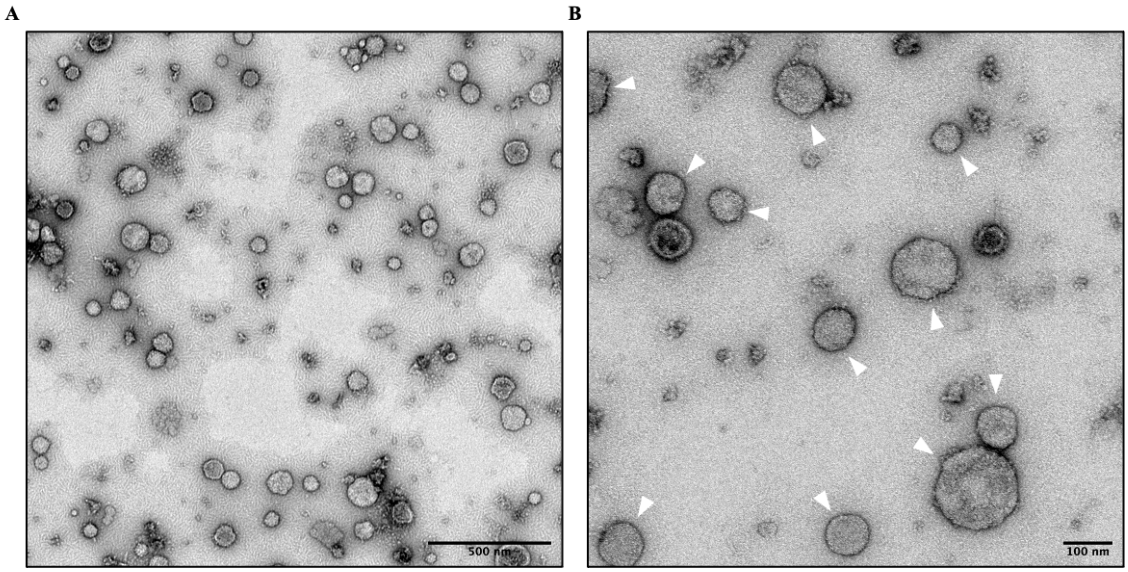

Figure 5.12: Examination of LCMV by Negative-Stain Electron Microscopy A sample of the resuspended LCMV pellet was examined by negative-stain EM to assess sample concentration and purity. The sample was stained with 2 % uranyl acetate and was imaged at 10,000 x magnification (**A**) and 20,000 x magnification (**B**) on a JEOL 1400 transmission electron microscope. Scale bars represent 500 nm (**A**) and 100 nm (**B**). Individual virions have been indicated with white arrowheads.

5.2.10 Examination of LCMV using Cryo-Electron Microscopy

The purified LCMV sample was screened using cryo-EM, as described for PICV, although the mesh size of the grids was increased (to 200-mesh) to minimise the metallic mesh obstructing the electron beam. Furthermore, the purified LCMV sample was mixed 1:1 with a different brand of colloidal gold labelled Protein A (Boster Bio), which had to be centrifuged (16,000 x g, 30 minutes) and resuspended in an equal volume of 0.1X PBS to remove the buffer components. The grid was then screened, confirming a lack of ice crystal formation and the presence of viruses spread evenly across the hole in the carbon (figure 5.13A). Images taken at higher magnifications (53,000 x) showed spherical viruses with dense interiors, a membrane layer and membrane projections (figure 5.13B, C and D). The cryo-EM images showed a low level of background contamination, which would not affect cryo-ET. This sample of purified LCMV was suitable for continuation to cryo-ET.

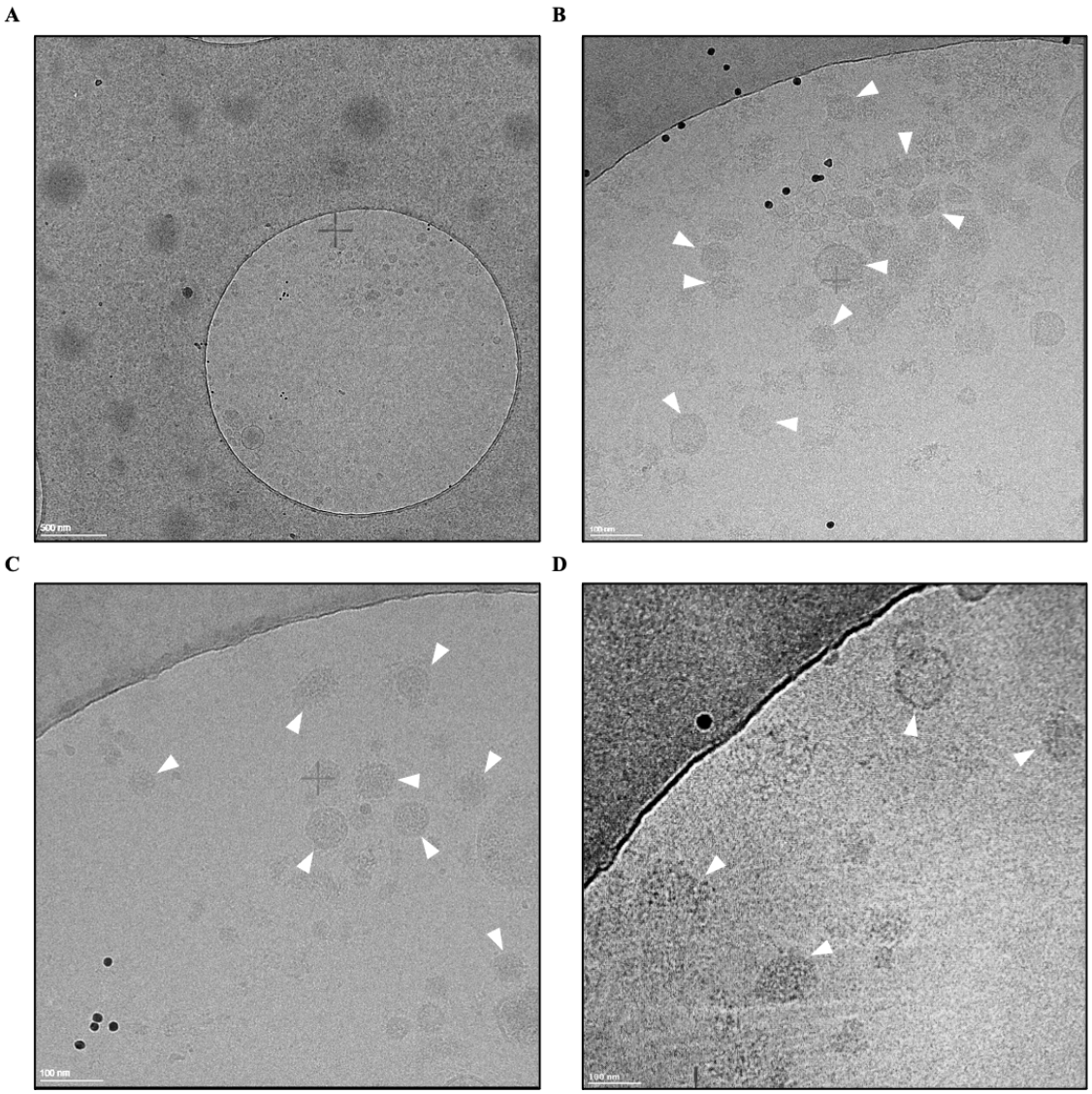

Figure 5.13: Examination of LCMV by Cryo-Electron Microscopy The purified LCMV sample was added to glow-discharged Quantifoil R 2/2 grids and incubated at room temperature for 1 minute, before the sample was blotted and the grid was immediately frozen by submersion into liquid ethane. The grid was transferred to liquid nitrogen and imaged using the Titan Krios 2 transmission electron microscope. Images were taken at 9000 x magnification (**A**) and 53,000 x magnification (**B**, **C** and **D**). Scale bars represent 500 nm (**A**) and 100 nm (**B**, **C** and **D**) Individual virions have been indicated with white arrowheads.

5.2.11 Examination of LCMV using Cryo-Electron Tomography

Cryo-ET was performed on LCMV, as described for PICV, although images were collected from -60° to +60°, every 2° increments. 3D tomograms were reconstructed for all the tilt-series collected using batchtomo (Etomo; IMOD). The gold particles were not well distributed across the image, potentially due to the centrifugation step

and poor resuspension of the gold pellet, therefore any of the tilt-series that were unable to be reconstructed using batchtomo were manually reconstructed. After reconstruction, the tomograms were binned by 2, resulting in a final pixel size of 5.44 Å.

The 3D tomographic reconstruction of LCMV, allowed clear visualisation of the GPC spikes present on the virion surface, which have been indicated with white arrowheads (figure 5.14B). However, whilst the viral membrane was visible, the membrane bilayer was not well resolved, suggesting some issues with the image acquisition. Again, there was no clear electron density within the virions that would reveal the structural organisation of the viral genomic RNPs or the inclusion of ribosomes in the virions (figure 5.14B).

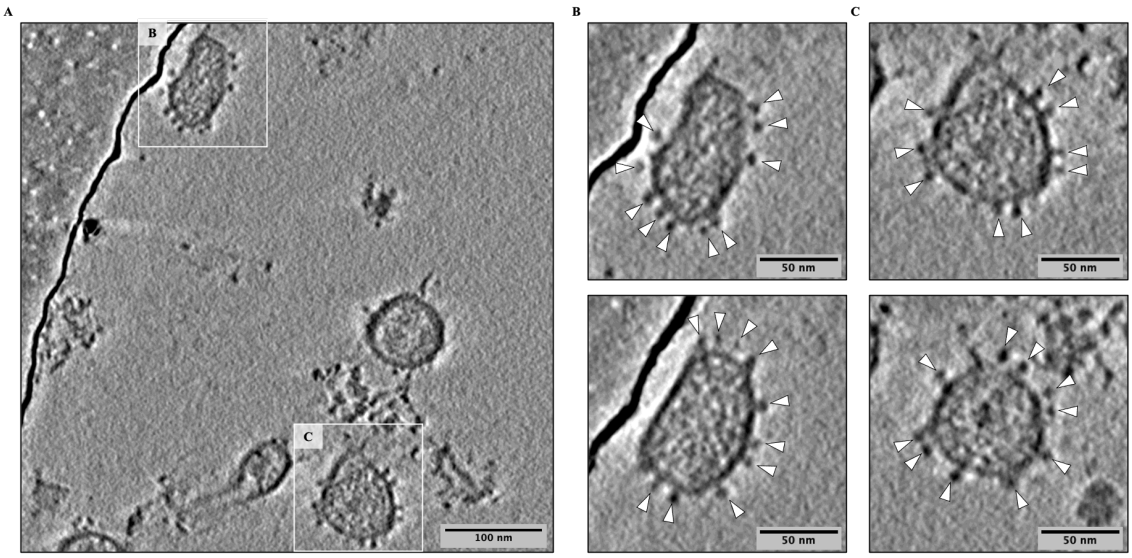

Figure 5.14: Examination of LCMV by Cryo-Electron Tomography Cryo-ET of purified LCMV (**A**). Virions displaying glycoprotein spikes can be clearly seen in (**A**) and larger images of two individual virions, in different Z-frames, have been shown in (**B** and **C**), with white arrowheads indicating the positions of the glycoprotein spikes. Scale bars represent 100 nm (**A**) and 50 nm (**B** and **C**). All the images were filtered in ImageJ using Gaussian Blur 3D.

Figure 5.15A shows sagittal sections that were collected throughout the Z-plane of the LCMV virion. Top (1) and bottom (6) slices revealed the GPC spikes on the exterior of the virion surface. Similarly to PICV, the GPC spikes seemed to be randomly distributed. The slices 2, 3, 4 and 5 showed the cross-section of the GPC spikes present with the membrane bilayer (figure 5.15A). In particular, slice 4 showed an additional electron density that was running parallel to the membrane bilayer, which may represent the ZP matrix layer, as has been indicated in the zoomed-in image (figure 5.15C).

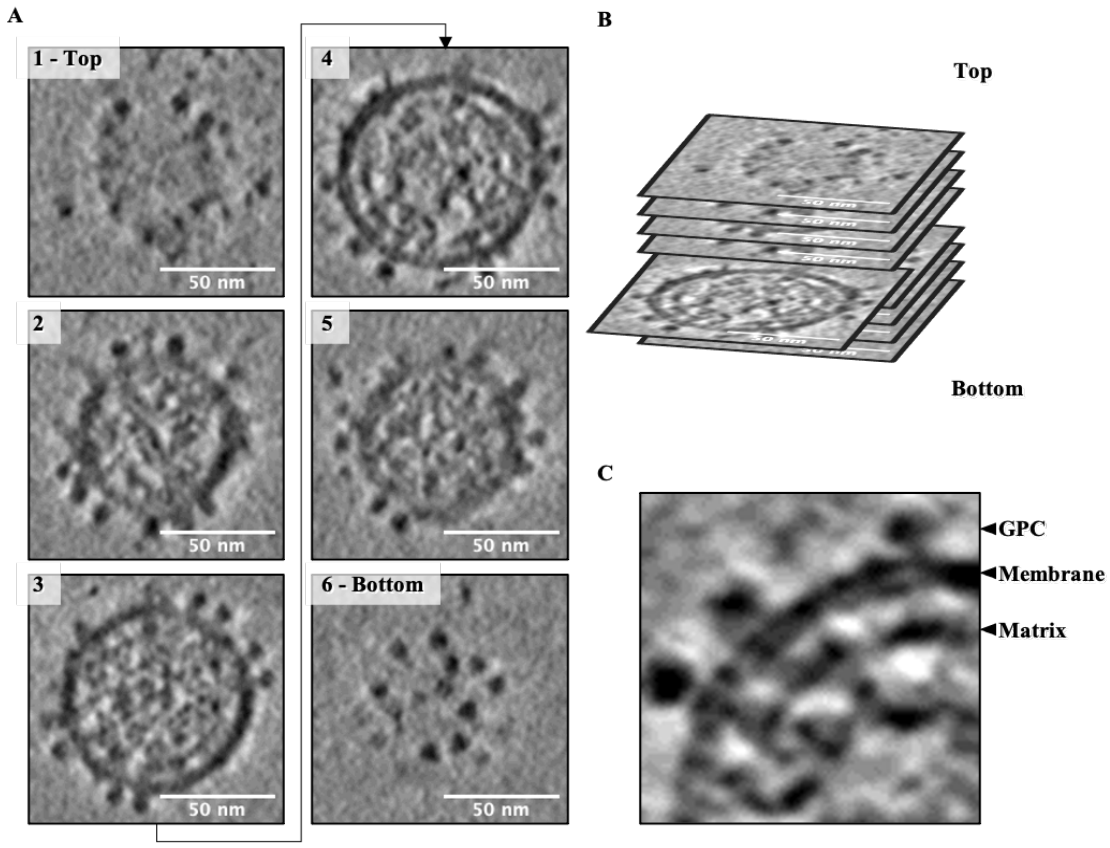

Figure 5.15: Visualisation of LCMV in Slices Through the Virus Sections (1-6) throughout the Z-plane of a single virus have been shown, which were taken approximately every 30 slices working from the top of the virus (1) to the bottom of the virus (6) (**A**). There is an additional layer that can be seen in image (4), which could potentially represent the ZP matrix layer. The arrangement of these slices for the reconstruction of a 3D volume is shown schematically in (**B**). Scale bars represent 50 nm. All the images were filtered in ImageJ using Gaussian Blur 3D.

The 3D tomographic reconstructions also revealed the presence of two distinct variants of LCMV GPC; GPC spikes that closely resembled what had been seen before with PICV and LASV (Li et al., 2016) (termed "compact") (figure 5.16B; "compact" GPC spikes indicated by white arrowheads), as described above. However, there were GPC spikes that did not show the typical morphology as the "compact" GPC spikes (termed "extended") (figure 5.16C; "extended" GPC spikes indicated by black arrowheads). Occasionally, virions that had predominantly "compact" GPC spikes also displayed a few "extended" spikes, as seen in figure 5.16B ("compact" GPC spikes indicated by white arrowheads and "extended" GPC spikes indicated by black arrowheads). A rough estimation of the virions present was performed and approximately 60 % of virions displayed "compact" GPC spikes, 30 % of virions displayed "extended" GPC spikes and 10 % of virions displayed a mixture of "compact" and "extended" spikes. These "extended" spikes were on average 13.16

nm ± 3.0 nm long (as measured from the membrane), which was almost double the length of the "compact" spikes (7.6 nm ± 1.0 nm). Some "extended" spikes appeared to retain the globular head, of a similar size to the "compact" spikes, whilst other "extended" spikes appeared to just have the stalk domain. Attempts were then made to resolve the structure of the "compact" LCMV GPC spikes using STA.

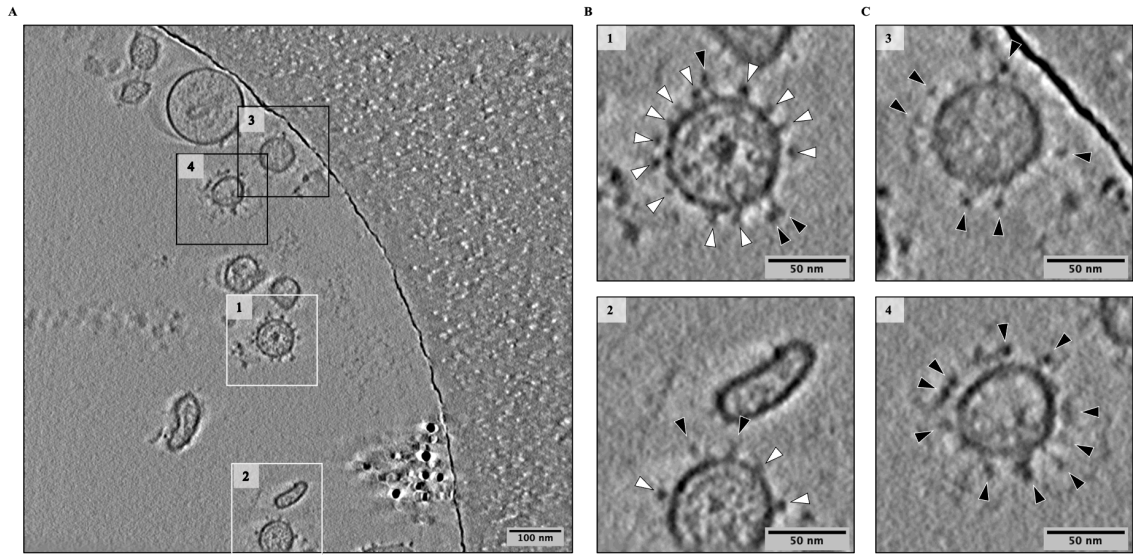

Figure 5.16: Comparison of LCMV Virions Displaying "Compact" Versus "Extended" GPC Spikes After tomogram reconstruction, virions displaying two distinct types of GPC spikes ("compact" or "extended") were found. In this tomogram (**A**), two virions displaying "compact" spikes can be seen (white box; 1 and 2) and two virions showing "extended" spikes can also be seen (black box; 3 and 4). These images have been enlarged in (**B**) and (**C**), where (**B**) represents the two virions displaying "compact" GPC spikes, which have been indicated using white arrowheads, and (**C**) represents the two virions displaying "extended" GPC spikes, which have been indicated using black arrowheads. A few "extended" GPC spikes (indicated by black arrowheads) were seen on the virions predominantly displaying "compact" GPC spikes in (B). Scale bars represent 50 nm. All the images were filtered in ImageJ using Gaussian Blur 3D.

5.2.12 Sub-Tomogram Averaging of the LCMV Glycoprotein Complex

The STA of the LCMV GPC spikes was performed as for PICV. From 15 tomograms, 1,765 spikes were manually selected and an initial orientation perpendicular to the viral membrane was provided. The spikes were then aligned and averaged, following the iterations used in the initial averaging and the first refinement stage of the PICV GPC (figure 5.8A-C). At this point, it was becoming evident that the averages were not improving and the membrane bilayer was not being resolved (figure 5.17A). Figure 5.17B shows the isosurface rendering of the spike average from figure 5.17A,

which had C3 symmetry applied. The resolution was calculated to be 26.3 Å using calcFSC (figure 5.17C).

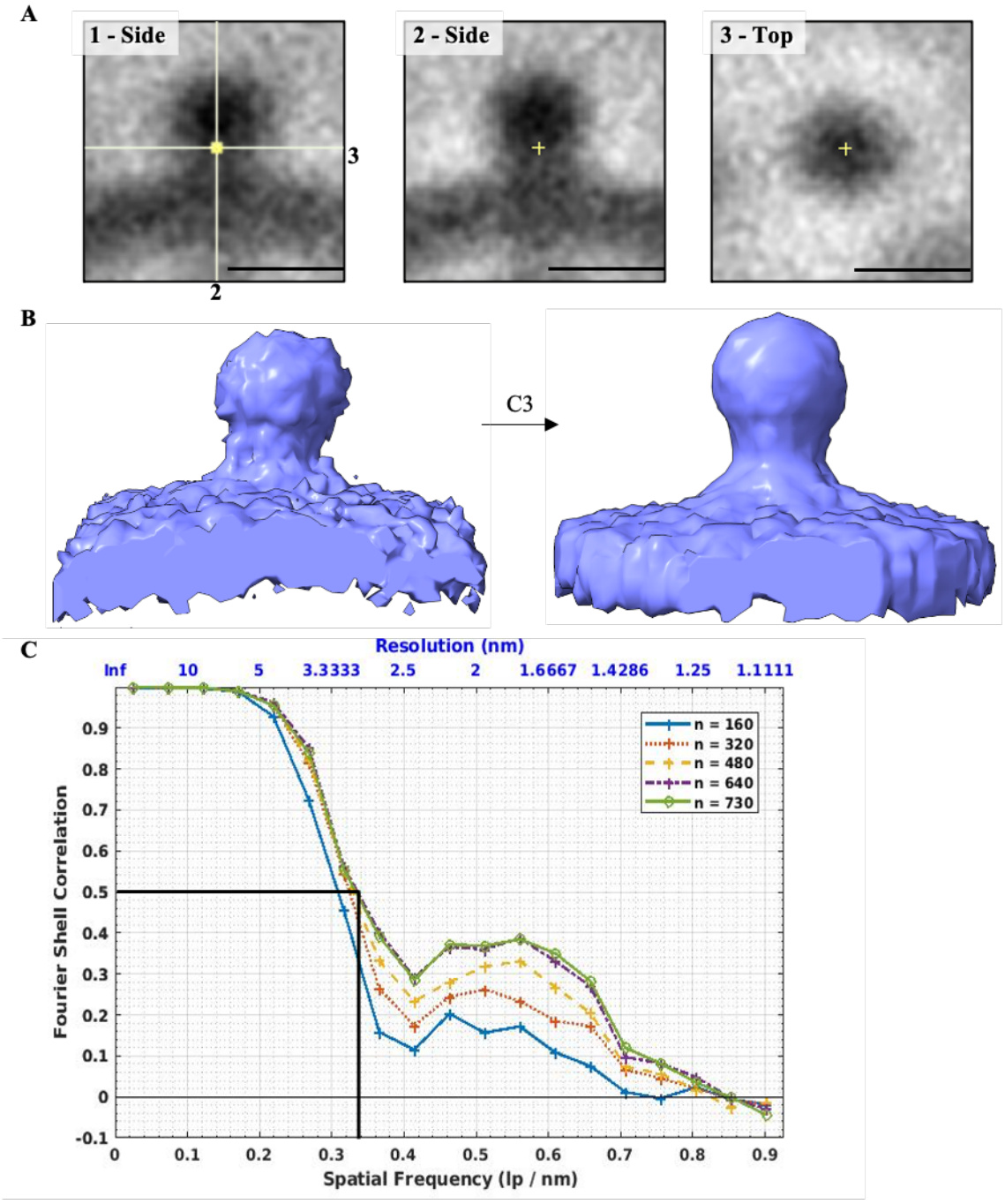

Figure 5.17: Sub-Tomogram Averaging of the LCMV Glycoprotein Complex STA of manually picked LCMV spikes. 1,765 sub-tomograms were averaged and subject to refinement through several iterations using the IMOD PEET software. The sagittal planes (1 and 2) and the transverse plane (3) of the electron density averages of the GPC spikes have been shown (**A**). The crossed lines on image 1 represent the view of image 1 represented in images 2 and 3. Scale bars have been included and depict 10 nm. The isosurface rendering of the GPC spike has also been shown before and after C3-symmetrisation (**B**). This model was visualised using UCSF Chimera X. To determine the resolution, an FSC plot was used and the resolution was found to be ~26.3 Å at the 0.5 cut-off (black line) (**C**). "n" represents the number of particles included in the averaging and the green line represents the maximum number of particles included (730).

5.2.13 CTF-Corrections of the LCMV Tomograms

In an attempt to improve the resolution, the individual projections were corrected for the contrast transfer function (CTF) of the microscope, which is typically calculated from the defocus across a 2D plane. However, CTF-corrections prove more challenging for tilt-series samples because of the low SNR, resulting from the low electron dose in each image and the tilting of the sample, which makes the sample appear thicker. Furthermore, the defocus values within a given projection vary, due to the fact the stage is tilted during acquisition (Turoňová et al., 2017). The reduction in the signal and the changes in defocus makes applying CTF-corrections less reliable. Therefore, we attempted to estimate the CTF in a two stage process: we first calculated the defocus and phase shift per projection without limiting the phase shift; and then we performed a second CTF estimation by using a phase shift minimum of 65 and a phase shift maximum of 115, which were±25 around the initial phase shift average, which was 90. Using this estimates for defocus and phase shift, the projections were CTF-corrected, and new tomograms were then calculated.

It was also thought that excluding some of the extreme tilt angles may improve the resolution of the final tomogram by removing some of the extra noise. However, it also increases the effect of the missing wedge. To determine which angles to include in the reconstruction of the final tomogram, two tomograms were recreated with views from the extreme angles excluded from the reconstruction. The same position was then compared between the non-CTF corrected tomogram, and the CTF-corrected tomograms which had either; included all angles (CTF, -60° to +60°), only included angles from -60° to 0° (CTF, -60° to 0°), only included angles from -30° to +30° (CTF, -30° to +30°), or only included angles from -46° to +46° (CTF, -46° to +46°). The most improvement in resolution appeared to be in the CTF-corrected version, which had only included angles from -30° to +30°, as judged by the presence of a better defined membrane (figure 5.18; CTF, -30° to +30°). Therefore, STA was then performed with these tomograms.

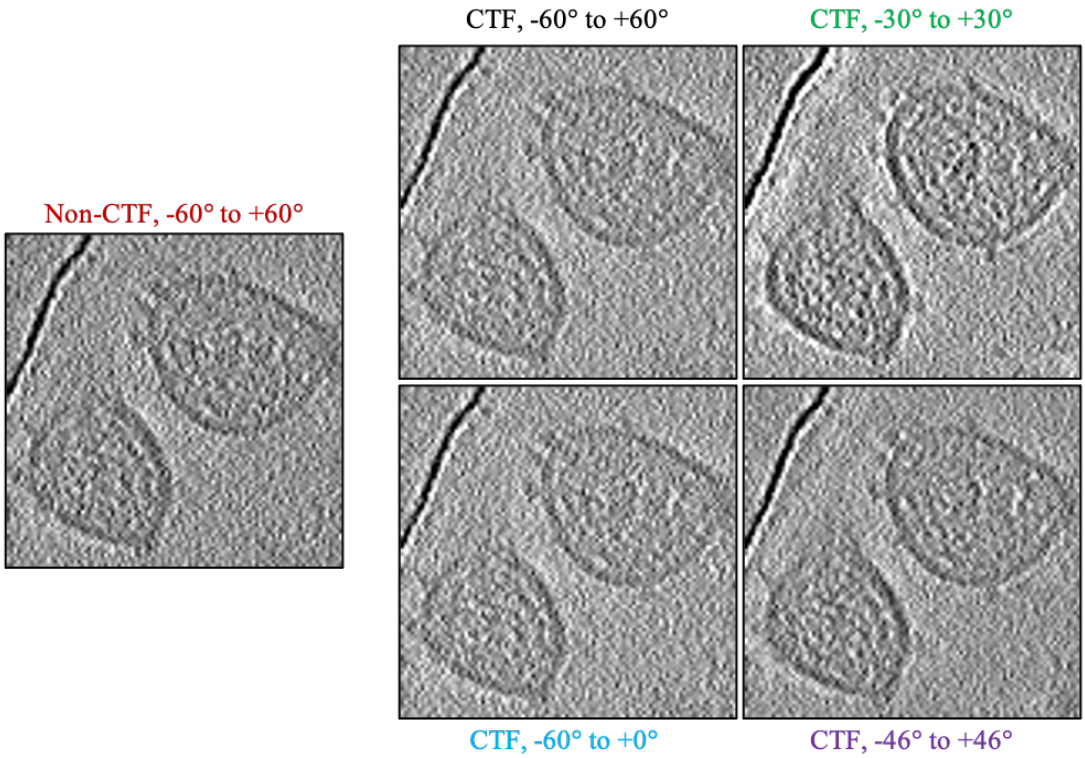

Figure 5.18: CTF Corrections of the LCMV Tomograms CTF-corrections were estimated and applied to the tomograms. The tomograms were then reconstructed, with a range of angles excluded from the tomograms in an attempt to improve resolution. The same position was then compared between the non-CTF corrected tomogram (non-CTF, -60° to +60°) and the CTF-corrected tomograms which had either; included all angles (CTF, -60° to +60°), only included angles from -60° to 0° (CTF, -60° to 0°), only included angles from -30° to +30° (CTF, -30° to +30°), or only included angles from -46° to +46° (CTF, -46° to +46°). To avoid any image distortion due to filtering, these images were not filtered using Gaussian Blur 3D.

5.2.14 Sub-Tomogram Averaging of the CTF-Corrected LCMV Glycoprotein Complex

Once the new CTF-corrected tomograms (CTF, -30° to +30°) were reconstructed, a new STA was calculated. Any manually picked spikes that were on the top or bottom of the virus were excluded, because the omission of the angles increased the missing wedge effect, distorting the information at those positions. Again, the spikes were initially averaged without any angular searches, and C120 symmetry applied, to be used as a reference for the next stage. In order to identify the membrane bilayer and show that it could be resolved, only one iteration was performed, with a wide search in the orientation of the spike (without searching for the rotation along the Y-axis) and a large search distance (figure 5.19). Unfortunately, this did not improve resolution of the membrane bilayer (35.7 Å; figure 5.19C) and it was

assumed that the limit of this tomographic data collection had been reached.

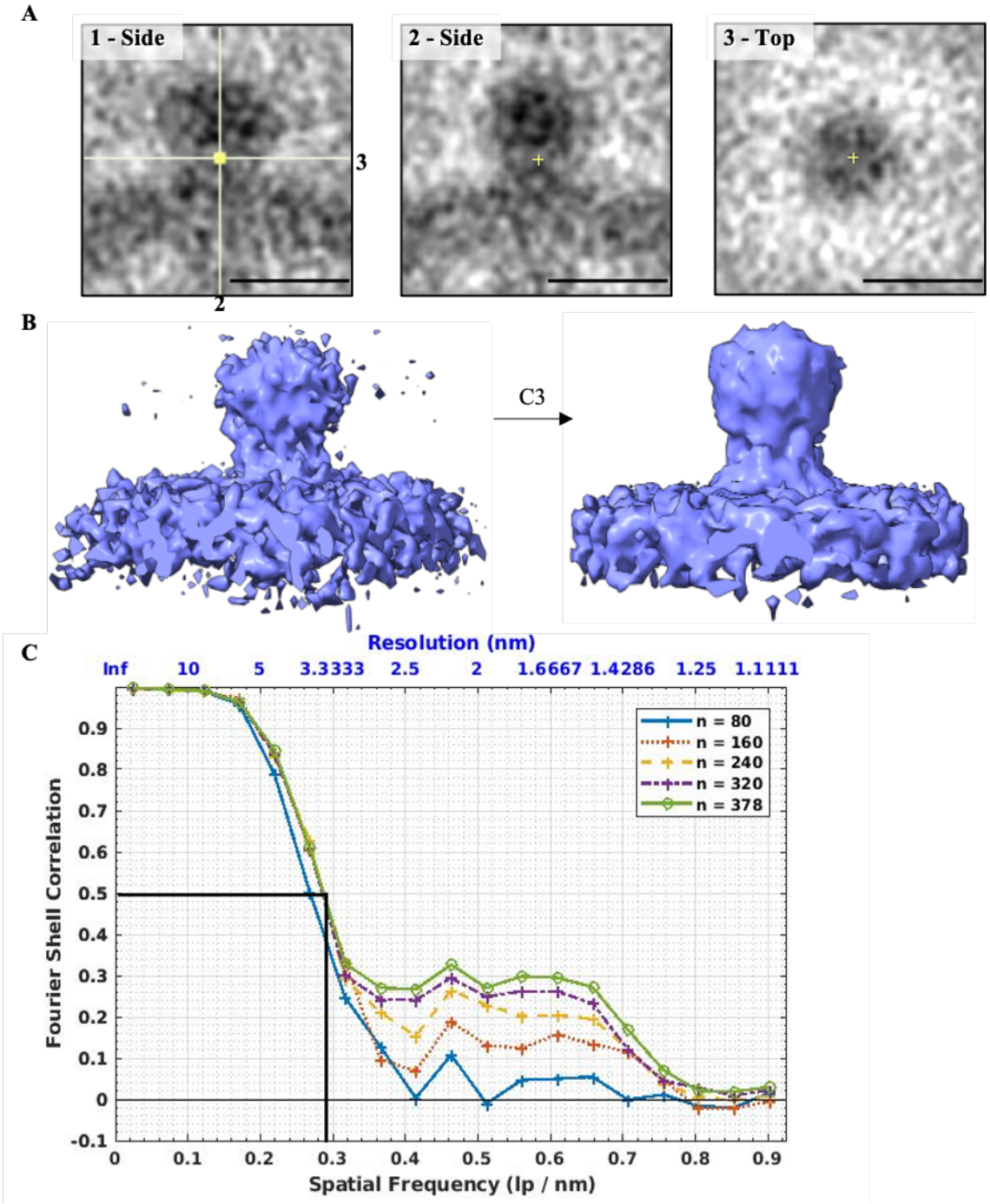

Figure 5.19: Sub-Tomogram Averaging of the CTF-Corrected LCMV Glycoprotein Complex STA of the CTF-corrected reconstructed LCMV tomograms was performed on 865 LCMV GPC spikes, which were averaged and subject to refinement through several iterations using the IMOD PEET software. The sagittal planes (1 and 2) and the transverse plane (3) of the electron density averages of the GPC spikes have been shown (**A**). The crossed lines on image 1 represent the view of image 1 represented in images 2 and 3. Scale bars represent 10 nm. The isosurface rendering of the GPC spike has also been shown before and after C3-symmetrisation (**B**). This model was visualised using UCSF Chimera X. To determine the resolution, an FSC plot was calculated and the resolution was found to be ~35.7 Å at the 0.5 cut-off (black line) (**C**). "n" represents the number of particles included in the averaging and the green line represents the maximum number of particles included (378).

In an attempt to understand why the tomograms were limited at such a low resolution, we collected cryo-EM images of the purified LCMV grid at different defocus levels. By imaging the sample at a range of defocus levels, we aimed to find out the conditions to resolve the lipid bilayer. The same grid used for cryo-ET was re-imaged using a Titan Krios transmission electron microscope. Several positions were automatically selected and imaged at different defocus levels, ranging from -1.7 µm to -4.4 µm, without a phase plate. This was in comparison to the defocus used in the tomographic acquisition, which ranged from -0.5 µm to -1 µm due to the phase plate allowing imaging to take place closer to focus. These images revealed that the membrane bilayer of the virions was distinguishable at all the defocus levels (figure 5.20). This suggests that the tomographic acquisition perhaps should have been performed at a higher defocus to introduce sufficient contrast or that the phase plate during the tomographic acquisition did not function correctly.

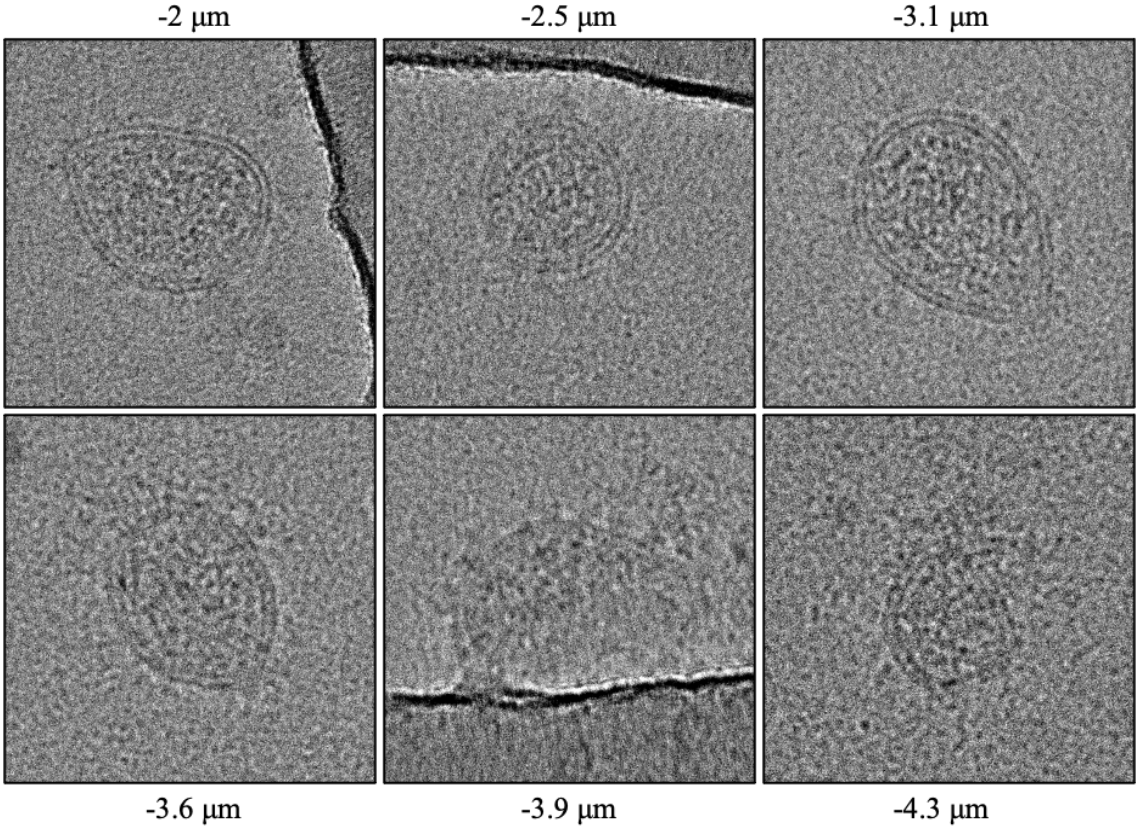

Figure 5.20: Imaging LCMV at Different Defocus Heights Purified LCMV was re-imaged using the Titan Krios transmission electron microscope. Several positions were automatically selected and imaged at different defocus levels, ranging from -1.7 µm to -4.4 µm. The images shown here represent defocus values of -2 µm, -2.5 µm, -3.1 µm, -3.6 µm, -3.9 µm and -4.3 µm. The membrane bilayer is clearly distinguishable at all these defocus levels.

5.2.15 Comparison of Arenavirus Glycoprotein Complexes

Despite not achieving the expected level of resolution, the final PICV and LCMV virion surface models allowed a comparative analysis of the corresponding spikes with previously published spike structures from LASV and UHV (Li et al., 2016; Hetzel et al., 2013).

The isosurface rendered averages of the PICV (light blue) and LCMV GPC (purple) spikes were compared with those of LASV (EMD-3290; dark blue; Li et al., 2016) and University of Helsinki Virus (UHV; EMD-2424; teal; Hetzel et al., 2013). Similarities in size and trimeric organisation were seen between PICV, LCMV and LASV, which were significantly different to the cup-like structure exhibited by the UHV GPC spike. The LCMV GPC spike, even at the low resolution of 26.3 Å, was very similar to the LASV GPC spike in both size and shape, but the cryo-ET data will have to be collected again in order to improve the resolution and have a thorough comparison of the two structures.

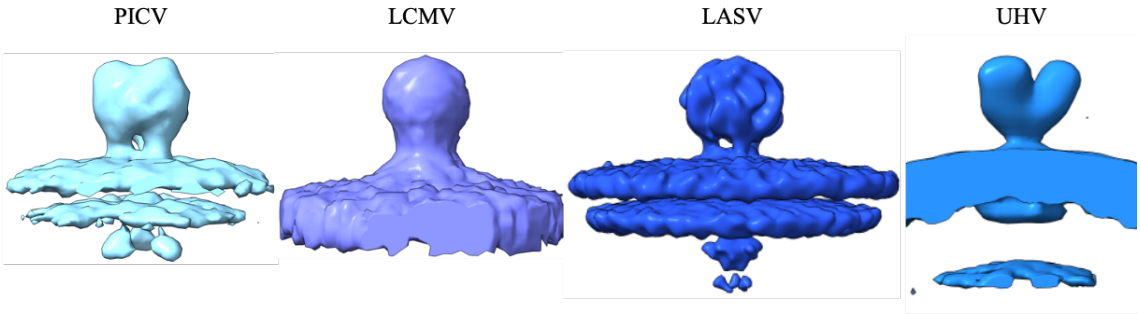

Figure 5.21: Comparison of Arenavirus Glycoprotein Complex Models Isosurface rendering averages of the GPC spikes from PICV (this study; light blue), LCMV (this study; purple), Lassa virus (LASV; EMD-3290; dark blue; Li et al., 2016) and University of Helsinki Virus (UHV; EMD-2424; teal; Hetzel et al., 2013). The averages are at the same scale for comparison. These model were visualised using UCSF Chimera X.

Next, it was attempted to fit the electron density of the PICV GPC spike (light blue) into the electron density of the LASV GPC spike (figure 5.22A; EMD-3290; dark blue). The LASV GPC spike, which was also the result of cryo-ET and STA, reached a resolution of 14 Å (Li et al., 2016). The PICV and LASV GPC spikes aligned quite well (correlation value: 0.9228; membrane was included in the correlation score), in particular the stalk domains and the head domains. However, there were some differences at the very top of the head domain, where the tips of each PICV

GPC monomer have twisted slightly and do not align with the tips of each LASV GPC monomer (figure 5.22A; second row). Furthermore, each of the GPC spike cytoplasmic tails of PICV were present in the area surrounding the LASV GPC spike cytoplasmic tail density (figure 5.22A; third row). Whilst this could be the result of the lower resolution that the PICV spike reached, it could also be that the New World (clade A) mammarenaviruses adopt a slightly different GPC structure.

It was then attempted to fit the electron density of the PICV GPC spike (light blue) into the electron density of the University of Helsinki Virus (UHV) GPC spike (figure 5.22B; EMD-2424; teal). The UHV GPC spike, which was solved by cryo-ET and STA to a resolution of 32 Å (Hetzel et al., 2013). The PICV and UHV GPC spikes did not align as well as the PICV and LASV GPC spikes (correlation value: 0.7219; membrane was included in the correlation score). However, the head domains of the PICV GPC spike, whilst not as long as those of the UHV GPC spike, had the same positioning of each of the monomers at the tip of the head domains (figure 5.22B; second row), unlike what was seen in the comparison of the PICV and LASV GPC spikes (figure 5.22A; second row). The electron density of the GPC tails of PICV and UHV, despite the low resolution, also appeared to be arranged similarly (figure 5.22B; third row), more so than that of the LASV and PICV GPC tails (figure 5.22A; third row). The resolution of the PICV GPC spike would need to be improved further in order to investigate these structural differences, and therefore the cryo-ET data will have to be collected again. However, the data collected here does suggest that there were small structural differences between the PICV (New World) and LASV (Old World) GPCs, and large structural differences between the PICV and UHV GPCs.

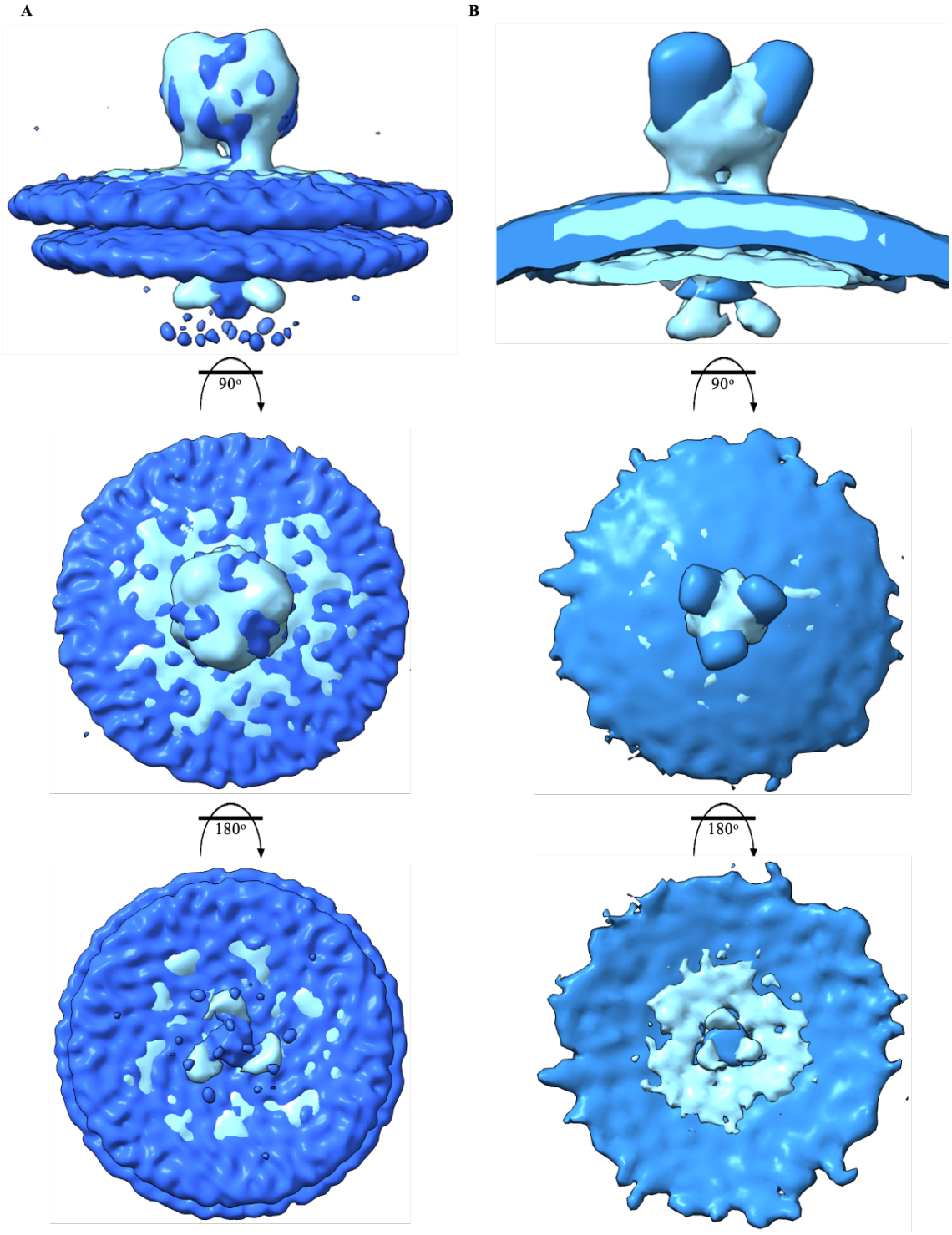

Figure 5.22: Overlay of PICV GPC with LASV GPC and UHV GPC The electron density of the PICV GPC spike (this study; light blue) was fitted into electron densities of the Lassa virus GPC spike (**A**; EMD-3290; dark blue; Li et al., 2016) and University of Helsinki Virus (**B**; EMD-2424; teal; Hetzel et al., 2013), all of which were derived from cryo-ET and STA. The models have been tilted forward in the X-plane by 90° to show the head domains of the GPC spikes. The models have then been flipped 180° in the X-plane to show the tail domains the GPC spikes. These model were visualised using UCSF Chimera X.

5.3 Chapter Summary and Discussion

This chapter has described the successful purification of highly concentrated preparations of PICV and LCMV for their subsequent examination using cryo-ET. Furthermore, this chapter has used STA to determine the structure of the PICV and LCMV GPC spikes. Initially, the growth of PICV and LCMV was optimised in order to reach titres of 10^7 pfu/mL (for PICV) and 10^7 ffu/mL (for LCMV). The virions were then successfully concentrated and purified using ultracentrifugation and a sucrose cushion. Negative-stain EM was used to examine the purified virus samples, which showed the virions were generally spherical, with some that were pleomorphic, and had diameters that ranged from 50 nm to 140 nm for PICV and from 40 nm to 130 nm for LCMV. The purified virus samples were shown to be suitably concentrated and pure for vitrification and cryo-EM examination. Cryo-EM confirmed that the viruses and the fiducial markers were suitably dispersed within vitreous ice for continuation onto cryo-ET.

The cryo-ET performed on PICV was successful and 3D tomograms showed viruses displaying a membrane bilayer and GPC spikes that were approximately 8.7 nm long and 6.6 nm wide. STA was performed on the GPC spikes and the PICV GPC spike structure was successfully solved to a resolution of 22.7 Å. The resolution was limited due to only one frame (out of four used for standard tomographic collections at Leeds) being collected for each tilt angle of the cryo-ET session. Despite the low resolution, the PICV GPC model generated was compared to that of the LASV GPC, showing slight differences in the orientation of the tops of the head domains and the GPC tails. These differences in the PICV GPC appeared to match the protomer arrangement seen in the UHV GPC, suggesting a different arenavirus GPC structure, which shows similarities to both the Old World mammarenaviruses and the reptarenaviruses. Further investigation into this is required, which would be assisted through gaining a higher resolution structure of the PICV GPC. This could be achieved by attempting CTF corrections on the PICV dataset collected here. However, it would be more successful to repeat the cryo-ET collection on purified PICV. This would involve repeating the growth and purification of PICV, in the same manner as described in this chapter, but instead purifying through a 20 % sucrose cushion at 90,000 $x\ g$ in order to limit virion damage. Following this, prior

to vitrification, PICV would be loaded onto 200-mesh grids instead of 400-mesh, allowing collection of the full tilt range. Finally, collection of tomographic data on vitrified virions should also ensure all four frames are collected to attain the best resolution possible. To our knowledge, this is the first structure of the GPC from a New World clade A mammarenavirus.

The cryo-ET performed on LCMV was somewhat successful because the 3D tomograms showed viruses that had GPC spikes, but the membrane bilayer was not resolved, which may be the result of phase plate misalignment or insufficient charging, or the session needed to be performed at a different defocus level. Despite STA being performed on the LCMV GPC spikes, the resolution was limited at 26.3 Å and the membrane bilayer could not be resolved. CTF-corrections were applied to the tomograms, but these did not increase the resolution. In order to improve the dataset collected on LCMV, the cryo-ET will have to be repeated. LCMV purified in this chapter was flash-frozen in liquid nitrogen, which means there is no need to repeat the growth and purification of LCMV. However, new vitrified grids will have to be made using gold fiducial markers from another manufacturer (Aurion) in order to ensure a better fiducial marker distribution, which would improve subsequent alignments in the tomographic reconstruction. When cryo-ET on LCMV is repeated, several tests will have to be performed to assess the functioning of the phase plate and determine that it is charging and functioning properly. Alternatively results may be improved by not using the phase plate and collecting the data at a specified defocus.

One thing that did become apparent during the tomogram reconstruction of LCMV was the presence of two types of GPC spikes; "compact" and "extended". "Compact" GPC spikes were similar in size to PICV GPC spikes, approximately 7.6 nm in length. "Extended" GPC spikes however were found to be on average 13.16 nm long, which was almost double the length of the "compact" GPC spikes. This is of particular interest because the "extended" GPC spikes could potentially represent a post-fusion conformation or an intermediate conformation between pre- and post-fusion. However, the "extended" GPC spikes seen here were not similar to the LASV spikes at pH 5 (figure 1.15B) or pH 3 (Li et al., 2016), which mimicked conditions experienced by the viral GPC during entry through the endocytic pathway, where it mediates viral and host membrane fusion. Therefore, these

"extended" GPC spikes could represent a fusion intermediate conformation that has not been previously documented for the arenaviruses. Recently, cryo-EM was used to determine the structure of the S glycoprotein trimers from SARS-CoV-2, and they identified two distinct conformations of S trimers on the virion surface, which represented the pre-fusion (majority) and post-fusion (minority) forms of S (Ke et al., 2020). This may be similar to what we have seen with the LCMV GPC spikes here. It is not known why "compact" and "extended" GPC spikes were not seen in the purified PICV dataset; it could suggest that the two viruses have slightly different fusion triggers, it could be related to the changes in sucrose concentration and centrifugation speed that were performed with the LCMV purification or it could be an effect of the improper functioning of the phase plate. The cryo-ET of LCMV will have to be repeated in order to gain a higher resolution of the LCMV GPC spike and to further investigate this. A higher resolution will allow for better comparison between the LCMV GPC, the LCMV pre-fusion GPC crystal structure and the LASV GPC spike and identification of any structural changes, which could be attributed to differences in LAMP1 affinities. A repeat of cryo-ET will also allow further investigation into the nature of these "extended" GPC spikes, to determine whether they represent a fusion intermediate structure or the post-fusion conformation. The availability of a post-fusion crystal structure of LCMV GP2 will help reveal whether these "extended" GPC spikes represent a post-fusion GPC structure on the virion.

Interestingly, at no point throughout this chapter did any electron microscopic investigation reveal the suggestion of ribosomes or granules present in the arenavirus virions. Previously, electron microscopy studies suggested that arenavirus particles contained electron-dense granules that were sensitive to ribonuclease and measured 20 to 30 nm in diameter (Dalton et al., 1968). Ribosomal RNA had also been isolated from purified virus samples, leading to the suggestion that the electron dense granules in arenavirus particles were ribosomes (Murphy et al., 1970; Pedersen and Konigshofer, 1976). However, the granules were slightly bigger and more electron-dense than cytoplasmic ribosomes, in addition to requiring a longer incubation in ribonuclease for their disappearance (Dalton et al., 1968; Mannweiler and Lehmann-Grube, 1973). Therefore, it could be that these granules represented RNP complexes instead, although the variation in number of granules between

virions added doubt to this theory (Dalton et al., 1968). Electron-dense granules within virion particles were not seen during this project, although the sample preparation differs from previous investigations. Firstly, the cryo-EM performed here does not utilise heavy metal staining, reducing the electron density of the sample. Secondly, the negative-stain EM performed here was on whole virions, as opposed to thin sections. The cryo-ET performed here showed that the technique was unable to offer insight into the internal organisation of the virions. Therefore, whilst electron-dense granules were not able to be seen, it could be because the techniques used did not permit resolution of the internal organisation. To further reveal whether the electron-dense granules are present, and whether they represent host-derived ribosomes or RNP complexes, negative-stain EM, cryo-EM and cryo-ET could be performed on thin-sections of the virion sample instead, permitting visualisation of the virion interior. This could be achieved through ultramicrotomy or cryo-ultramicrotomy.

Chapter 6

Concluding Remarks

The main goal of this project was to investigate the structural architecture of the arenavirus GPC spikes, but in order to achieve this, several molecular tools had to be developed. Three main objectives, which were previously described in section 1.6, were established for the completion of this goal. These objectives were successfully fulfilled during this project, which has been briefly discussed below.

Generation of LCMV NP antisera for its use as an arenavirus detection tool

Arenavirus NPs are an integral and essential component in the arenavirus lifecycle; it provides the structural backbone by which the genome is supported and protected, it assists the LP in genome replication and it counteracts multiple host defences to ensure successful viral infection. The NP is also the most abundant viral protein synthesised during arenavirus infection. Preparations of concentrated and highly pure NP can be used for structural determination, functional assays or it can be used for the generation of specific antibodies.

Using a bacterial expression system and a combination of chromatographic techniques, LCMV NP was successfully purified and concentrated to be used as the priming agent for the generation of a polyclonal antibody. It was then demonstrated that the antibody was specifically reactive with the LCMV NP from infected BHK-21 and SHSY5Y cells and did not react with unpurified mock-infected cell lysates. The LCMV NP antisera was also cross-reactive with PICV, which is classified within the New World group of the *Mammarenavirus* genus, but it was not cross-reactive with HAZV, which is classified in the *Nairoviridae* family of the *Bunyavirales* order.

The confirmation of the LCMV NP antibody specificity permitted investigation into the intracellular localisation of NP during LCMV infection, through immunofluorescence analysis. This study showed that both the LCMV and PICV

NPs had a cytoplasmic localisation, which presented either as a diffuse distribution or a puncta formation, in agreement with previous research which attributed puncta formation to a single phosphorylated residue (T206) (Baird et al., 2013; Knopp et al., 2015). This residue is conserved in both LCMV and PICV NPs. This could be further investigated, using the reverse genetics system developed here, to determine whether this residue, and the ability to switch between diffused and puncta formation, is essential for the successful viral infection.

Certain strains of LCMV establish persistent, non-cytolytic infections in cell culture (Abdel-Hakeem, 2019). Previous studies were able to perform crystal violet-based plaque assays, which rely on cytolysis, for the titration of LCMV-ARM strain (Ziegler et al., 2016). However, the experiments performed here showed that cytolysis did not occur with the LCMV-Cl13 derivative, suggesting interesting differences in cytopathic effect between the LCMV-Cl13 derivative and the LCMV-ARM parent strain. Nevertheless, this necessitated the development of a titration method for LCMV-Cl13. Using the LCMV-NP antibody, a focus-forming assay was successfully developed, using fluorescence microscopy to detect regions of infected cells (foci) that had originated from a single infected cell. This method was quicker and easier because the fluorescent foci were visible at an earlier timepoint and were imaged at a higher magnification using the microscope, making the foci more detectable. The major benefit of this focus-forming assay was that the titre of LCMV-Cl13 could now be determined, allowing optimisation of the reverse genetics system and investigation into the propagation of engineered LCMV strains.

The future directions of work performed in this chapter could either focus on further optimisation of recombinant LCMV NP expression and purification or it could focus on development of detection assays using the antibody that was generated here. Further optimisation of recombinant LCMV NP expression would involve attempting LCMV NP expression in an alternative expression system, one more suited to expression of eukaryotic proteins, utilising a different solubility tag, expressing the LCMV NP in the periplasm of bacteria to enable disulphide bond formation or codon optimising the LCMV NP gene to be more suited for bacterial expression. Further work on the development of detection assays which would utilise the antibody would involve determining the cross-reactivity of the antibody between other members of the *Arenaviridae* family, as well as its reactivity with

other bunyaviruses. Understanding the cross-reactivity of this antibody with other viruses would reveal whether it reacted against pathogenic arenaviruses, including LASV, JUNV, SBAV, GTOV, CHAPV and MACV. If the antibody was reactive against these viruses, diagnostic tools, such as ELISAs and lateral flow assays, could be created to assist in early diagnosis and therapeutic intervention of these diseases.

Development of a reverse genetics system designed to recover infectious LCMV

Reverse genetics systems are extremely versatile tools, permitting further investigation into the viral genome and proteins in the context of the viral lifecycle to understand cellular interactions, cellular localisation, lethality and pathogenesis. This investigation takes place through mutational analysis of the viral genome and proteins or the introduction of specific epitope tags or fluorescent molecules.

The design of plasmids expressing the positive-sense copies of S and L segments, in addition to NP and LP support plasmids, were transfected into BSR-T7 cells to successfully recover infectious recombinant LCMV. Using the focus-forming assay developed with the LCMV NP antibody, the optimal harvest times post-transfection and post-infection were determined, permitting the generation of a high titre stock of rLCMV. This was extremely important for subsequent structural examination of LCMV by cryo-ET, as discussed shortly.

This LCMV reverse genetics system was engineered to incorporate the eGFP ORF into the S segment, which generated infectious rLCMV stably expressing eGFP (rLCMV-eGFP). This permitted the live-cell fluorescent monitoring of successful rLCMV-eGFP infection, which could be used to better understand the replication kinetics of rLCMV. rLCMV-eGFP was also used to further develop and optimise the focus-forming assay, allowing live-cell monitoring of the foci development and confirming the foci were not the result of cross-reactivity with host cell proteins. Future work could employ rLCMV-eGFP in the development of a quick, easy and high-throughput screening platform for the evaluation of anti-arenaviral drugs and siRNA targets. Through measuring the fluorescent signal, large libraries of anti-viral inhibitors, small-molecule compounds and siRNA targets can be screened for anti-viral activity against the arenaviruses. Development of this assay will allow easier identification of drugs and could potentially lead to the identification of treatment for LCMV infections. Drugs identified using this assay may also have

anti-viral activity against other pathogenic arenaviruses. Furthermore, the ability that this reverse genetics system offers to introduce mutations into the viral proteins could help identify the specific viral targets of the anti-viral drugs.

This reverse genetics system was also engineered to fuse a 6xHis tag onto the C-terminus of the NP, successfully generating infectious rLCMV that stably expressed 6xHis-tagged NP (rLCMV-6xHis). This permitted the chromatographic purification of RNP complexes from BHK-21 cells infected with rLCMV-6xHis. Further optimisation is still required to increase the concentration and to reduce potential aggregation or degradation. However, the ability to extract and purify RNP complexes from infected cells offers huge opportunity to further resolve the RNP structure, using cryo-electron microscopy, and add to research of arenavirus RNPs that was last performed in the 1980s (Young and Howard, 1983). The creation of rLCMV-6xHis offers huge advantages to the arenavirus field, through permitting structural analysis of RNP complexes that could further the understanding of the interactions between the NP and the RNA genome and between NP monomers. These interactions could then be exploited for the development of small molecule inhibitors that would target and interrupt the interactions.

In this project, it was also attempted to recover other tagged variants of LCMV, including LCMV expressing NP that was C-terminally tagged with GFP11 (rLCMV-GFP11) and LCMV expressing GPC that was C-terminally tagged with a FLAG tag (rLCMV-FLAG). The plasmids were successfully sub-cloned but the recoveries of infectious virus were unsuccessful. Recovery of rLCMV-GFP11 was attempted because it would have permitted live cell fluorescent tracking of the NP within the cell during viral infection. This could have provided further information on the temporal dynamics of the RTCs and structural investigation into the RTCs, using techniques such as correlative light and electron microscopy (CLEM). The future directions for successful recovery of the rLCMV-GFP11 variant would involve altering the position of the GFP11 tag within the NP, potentially at the N terminus. This tag placement could reduce interference with the NP's functions and allow rescue of infectious rLCMV-GFP11. Recovery of rLCMV-FLAG was also attempted to have a manner by which to detect the cellular localisation of the GPC, through staining with FLAG antibodies. This would allow mutational analysis of motifs in the GPC, in order to determine which are necessary for trafficking between the ER

and the Golgi. Through co-staining host factors and the GPC, it could also allow the identification of potential secondary entry receptors for LCMV, which could then be structurally investigated using cryo-ET. The future directions for this would also be to try a different position of the tag, potentially on the GPC SSP, or to produce highly-specific LCMV GPC antibodies.

Structural examination of the PICV and LCMV GPCs by cryo-electron tomography

Recent technological advances in EM have significantly improved the resolution at which macromolecular structures can be solved. This has allowed the structural determination of native GPC spikes on the virion surface, which, for the arenaviruses, has been performed on LASV and reptarenavirus UHV.

Here, high titre preparations of PICV (as a representative of the New World mammarenaviruses) and LCMV (as a representative of the Old World mammarenaviruses) were successfully concentrated and purified for examination using cryo-ET. The high titres achieved for LCMV would not have been possible, if not for the development of the molecular tools in the first two objectives. Following the detection of the GPC spikes on the virion surface, STA was performed to align the spike structures to one another, forming an average with an increased resolution.

The 3D tomograms of PICV virions showed GPC spikes that were approximately 8.7 nm long and 6.6 nm wide. Through STA, the PICV GPC spike structure was successfully solved to a resolution of 22.7 Å, providing, to our knowledge, the first structure of the GPC from a New World clade A mammarenavirus. Despite the low resolution, comparison of the PICV GPC model with that of the LASV GPC showed that the tops of the heads of individual protomers appeared to adopt a slightly different position. Furthermore, examination of the PICV GPC cytoplasmic tails presented at a 45° angle as opposed to those of LASV, which were central to the GPC spike. These differences in the PICV GPC appeared to match the protomer arrangement seen in the UHV GPC, suggesting an arenavirus GPC structure that shows similarities to both the Old World mammarenaviruses and the reptarenaviruses.

The 3D tomograms of LCMV virions also displayed GPC spikes, but the membrane bilayer was not resolved. Despite this, STA was performed on the LCMV GPC spikes from the original 3D tomograms and CTF-corrected 3D tomograms, in an

attempt to improve the resolution. However, the resolution was limited at 26.3 Å. Nevertheless, even at this resolution, it was clear that the LCMV GPC spike was showing a similar structure and size to the LASV GPC. The resolution was not high enough to resolve structural differences between the LCMV GPC, the PICV GPC and the LASV GPC.

During the reconstruction of the LCMV 3D tomograms, two types of GPC spikes were seen, termed "compact" and "extended". "Compact" GPC spikes were similar in size to PICV GPC spikes, approximately 7.6 nm in length, whereas "extended" GPC spikes were approximately 13.16 nm long. It was thought that the difference in the appearance of the "extended" GPC spikes, i.e. the increase in length and the occasional loss of the globular head domain, could represent the significant structural change that the GPC undergoes in order to perform fusion of the viral and host membranes. Therefore, the "extended" GPC spikes seen in this study could be the first documentation of post-fusion arenavirus GPC spikes that are present on the virion surface. The significant structural differences that the LCMV GPC encounters through the fusion process have been shown by solving the crystal structures of pre-fusion and post-fusion LCMV GP2, and the extension of the heptad repeats in the alpha-helix bundle of GP2 could account for the increase in length seen in the "extended" GPC spikes here (figure 1.17) (Hastie et al., 2016a). This was not seen in the LASV GPC spikes, which were subjected to lowering pH to induce a post-fusion form (Li et al., 2016). This could be due to different fusion requirements between LCMV and LASV, or because the LASV GPC spikes were present on VLPs rather than native virions. Similarly extended forms have also been seen in cryo-ET of SARS-CoV-2 (Ke et al., 2020). It is interesting to note that "extended" GPC spikes were not seen in the cryo-ET of PICV, which could be related to different fusion triggers of each virus or differences in the protocols.

The repeat of the cryo-ET data collection for both PICV and LCMV is ongoing, in an attempt to improve the resolution of the GPC spike. The work here determined that the future repeats of electron microscopic investigation of LCMV and PICV should purify the viruses through 20 % sucrose at 90,000 $x\ g$ for 3 hours, after which the sample can be flash frozen using liquid nitrogen. The virus samples should then be mixed 1:1 with gold fiducial markers (Aurion) and loaded onto Quantifoil R2/2 grids with a 200-mesh. After plunge-freezing into liquid ethane, these grids can

then be examined by cryo-ET, collecting data every 2° increments from ± 60°. This investigation will further knowledge on the structure of arenavirus glycoproteins and differences in entry receptor requirement and entry pathways. Through working with BSL-2 pathogens, the cryo-ET studies here could be performed on LCMV and PICV, which had not been chemically fixed. This allowed the arenavirus GPC to adopt multiple different intermediate conformations, further investigation of which could offer information into the structural changes that the arenavirus GPC undergoes in order to direct fusion of the host and viral membrane. Understanding these entry requirements and the different structures allow these to be therapeutically targeted to interrupt the entry process of pathogenic arenaviruses. Furthermore, it offers understanding into which sites on the GPC are exposed for recognition by the host antibodies, potentially allowing the development of vaccines to raise antibodies against that susceptible site.

Improving the resolution of the GPC spikes will also allow further investigation into the structural differences between PICV, LCMV, LASV and UHV, providing information on the differences between New World mammarenavirus, Old World mammarenaviruses and reptarenaviruses. The difference in entry receptor requirement between PICV (unknown), LCMV (α-DG) and LASV (α-DG and LAMP1) suggest that there could be structural differences in the GPC spike, which can only be investigated with higher resolution structures. In particular, the histidine triad has been identified for LASV GPC LAMP1 binding, and whilst the mutation of these histidine residues is lethal for LCMV, LCMV infection does not require LAMP1 (Cohen-Dvashi et al., 2015; Jae and Brummelkamp, 2015; Hastie et al., 2016a). Therefore, perhaps the histidine residues adopt a different position, which does not allow their interaction with LAMP1. This could be resolved by docking the crystal structures of the LCMV and LASV GPCs into the tomographic reconstructions of the GPC spikes on the virion surface. This analysis could also support the identification of other residues in GP1 that are positioned for receptor interaction and this could be investigated using the reverse genetics system described here. The rLCMV-eGFP screening platform developed here could also be used to identify potential secondary receptors for LCMV, using siRNA knock-down methods. Cryo-ET could also be performed to identify the interactions mediated between the LCMV GPC and α-DG, by solving the structure of the LCMV GPC in presence of

α-DG.

In conclusion, the results presented here have led to the development of successful molecular tools that allow monitoring and investigation of arenavirus infection. The creation of rLCMV-eGFP can be exploited for the development of a high-throughput screening platform, which could be used to discover novel anti-arenaviral compounds or host cellular components that could be targeted in antiviral therapy. The generation of rLCMV-6xHis allows successful purification of RNPs, which could be investigated to provide a high-resolution structure of an arenavirus RNP complex. Finally, the investigation into the structural organisation of the PICV and LCMV GPC spikes here has indicated some significant structural differences between the New World and Old World GPCs, in addition to the potential presence of post-fusion conformations of the GPC on the LCMV virion surface. Further structural information on the PICV and LCMV GPCs could be exploited for the design of small molecule inhibitors, which target the GPC structure. Any potential for the development of anti-arenaviral compounds is important, in order to identify effective therapy or prophylaxis for the treatment or prevention of arenavirus diseases.

Chapter 7

Appendix

The following chapter includes the un-cropped western blots from figures throughout this thesis in order to depict the size marker (Ma) and reveal the cross-reactivity of the LCMV antisera that was generated here.

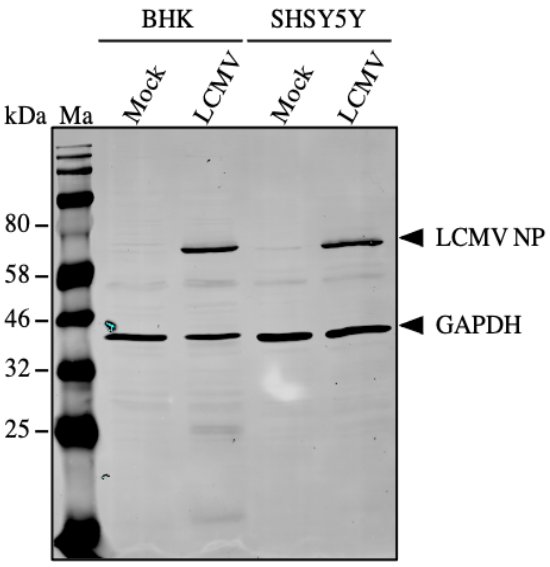

Figure 7.1: Reactivity of LCMV NP Antisera with LCMV-Infected Cell Lysates The un-cropped western blot from figure 3.11B has been shown. The LCMV NP antisera (1:1000) generated in chapter 3 was reactive with LCMV NP from LCMV-infected BHK-21 and SHSY5Y cell lysates. The sizes of relevant size marker bands has also been included and the bands representing LCMV NP and loading control GAPDH have been indicated.

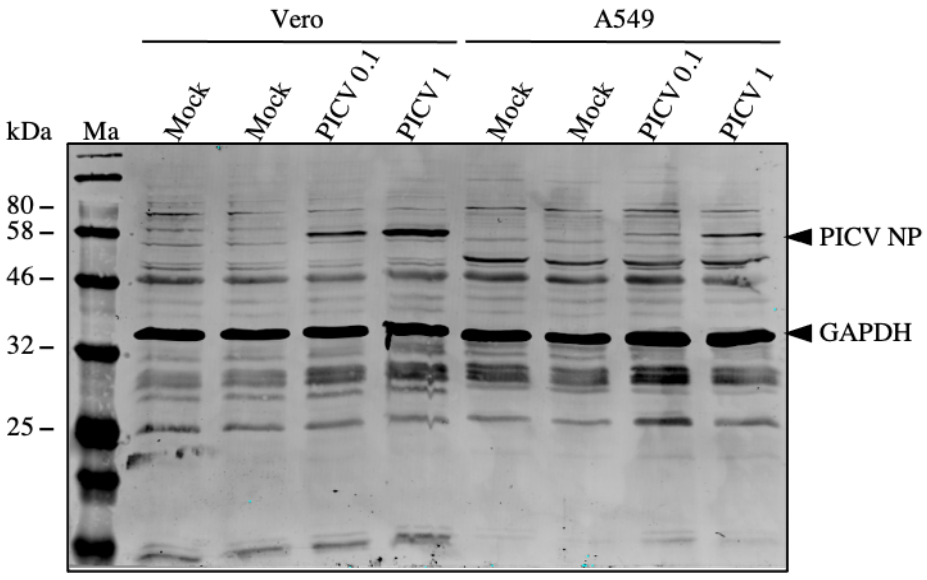

Figure 7.2: Reactivity of LCMV NP Antisera with PICV-Infected Cell Lysates The un-cropped western blot from figure 3.11C has been shown. The LCMV NP antisera (1:1000) generated in chapter 3 was reactive with PICV NP from PICV-infected (either at MOI 0.1 or 1) vero and A549 cell lysates. The sizes of relevant size marker bands has also been included and the bands representing PICV NP and loading control GAPDH have been indicated.

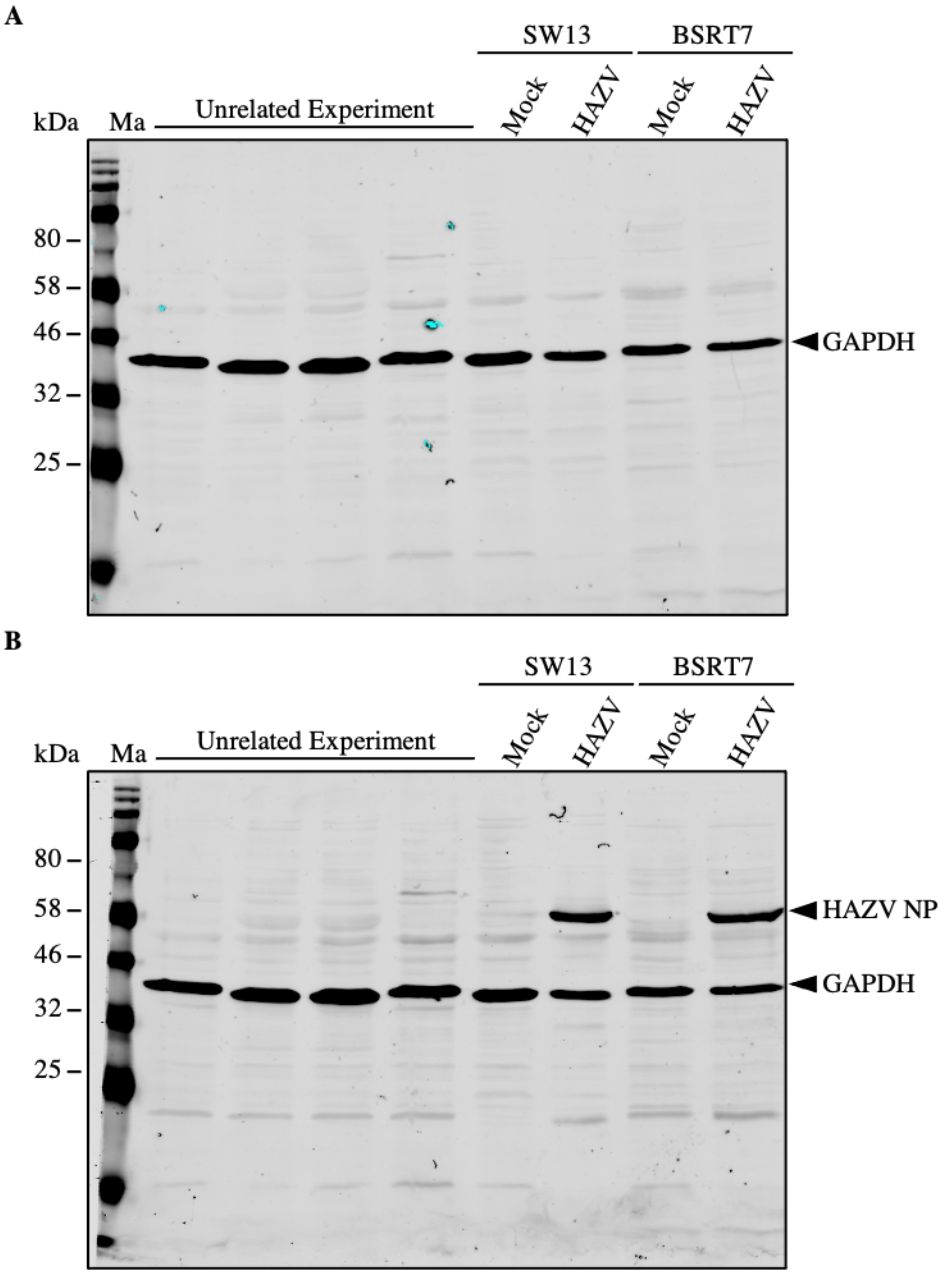

Figure 7.3: Reactivity of LCMV NP Antisera with HAZV-Infected Cell Lysates

The un-cropped western blots from figure 3.11D have been shown. The LCMV NP antisera (1:1000) generated in chapter 3 was not reactive with HAZV NP from HAZV-infected SW13 and BSR-T7 cell lysates (**A**). The same lysates were also probed with HAZV NP antisera to demonstrate successful HAZV infection (**B**). The sizes of relevant size marker bands has also been included and the bands representing HAZV NP and loading control GAPDH have been indicated.

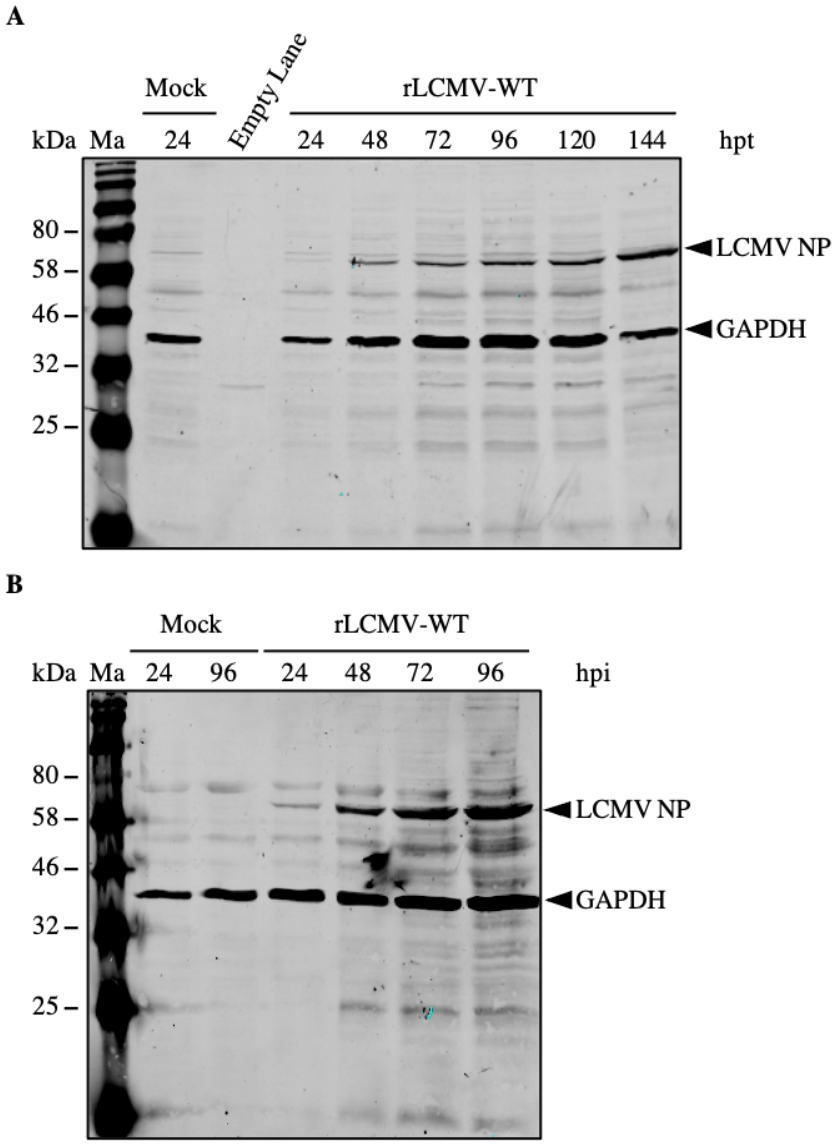

Figure 7.4: Generation of Recombinant LCMV from Transfection and Subsequent Infection

The un-cropped western blots from figures 4.4A (**A**) and 4.5A (**B**) have been shown. BSR-T7 cells were transfected with pUC57-L, pUC57-LP, pUC57-NP, pUC57-T7 and pUC57-S and cell lysates were collected every 24 hours for 144 hours (**A**). Supernatant was collected from the transfected cells at 120 hours post transfection (hpt) and was used to infect BHK-21 cells, after which the cell lysates were collected every 24 hours for 96 hours post infection (hpt) (**B**). The size of relevant size marker bands have been depicted and the bands representing LCMV NP and loading control GAPDH have been indicated.

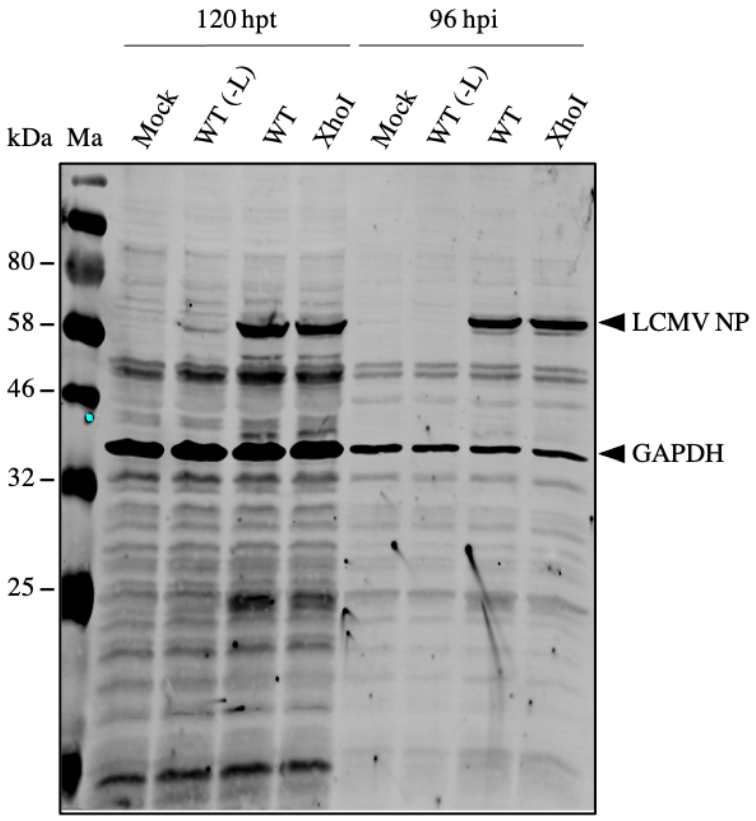

Figure 7.5: Generation of Recombinant LCMV expressing a Silent Mutation The un-cropped western blot from figure 4.6C has been shown. BSR-T7 cells were transfected with pUC57-L, pUC57-LP, pUC57-NP, pUC57-T7 and either pUC57-S (WT) or pUC57-S-XhoI (*Xho*I). The cells were incubated for 120 hours and then the supernatant was used to infect fresh BHK-21 cells. The lysate was collected from both the transfected cells and the infected cells at 120 hours post transfection (hpt) and 96 hours post infection (hpi) respectively and was examined by western blot analysis. The size of relevant size marker bands have been depicted and the bands representing LCMV NP and loading control GAPDH have been indicated.

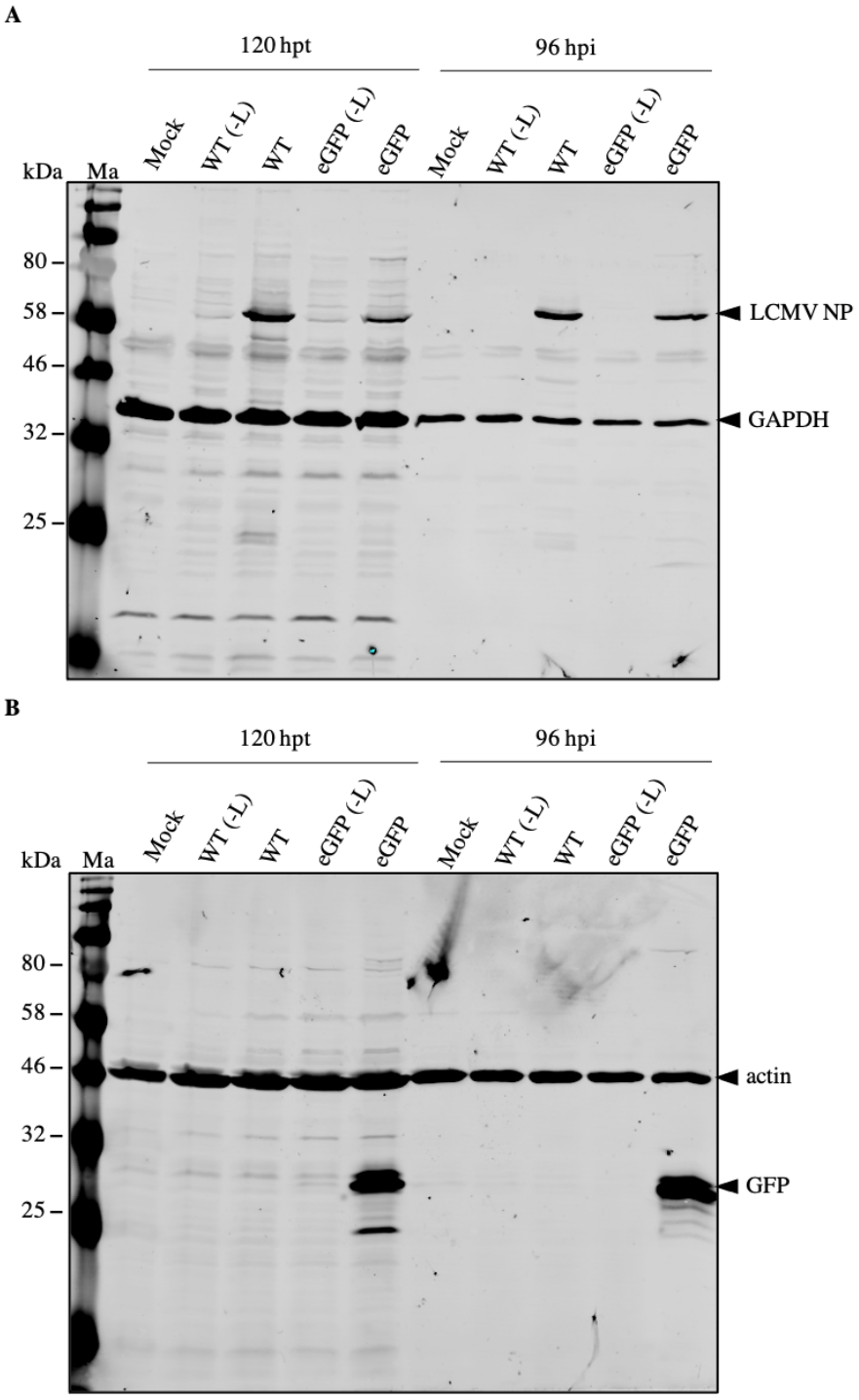

Figure 7.6: Generation of Recombinant LCMV expressing eGFP from Transfection and Subsequent Infection

The un-cropped western blots from figures 4.9B and 4.10B have been shown. BSR-T7 cells were either mock-transfected, transfected with pUC57-NP, pUC57-T7 and pUC57-S-eGFP (eGFP(-L)) or transfected with the pUC57-L, pUC57-LP, pUC57-NP, pUC57-T7 and pUC57-S-eGFP (eGFP). Control transfections were performed alongside substituting pUC57-S-eGFP for pUC57-S (WT(-L) and WT). Lysates were collected at 120 hours post transfection (hpt) (**A**). Supernatant collected from the transfected cells at 120 hpt was used to infect BHK-21 cells, after which the lysates were collected at 96 hours post infection (hpi) (**B**). Western blotting analysis was performed, using either LCMV NP antisera (and loading control GAPDH) (**A**) or GFP antisera (and loading control actin) (**B**). The size of relevant size marker bands have been depicted and the bands representing LCMV NP, eGFP and loading controls GAPDH and actin have been indicated.

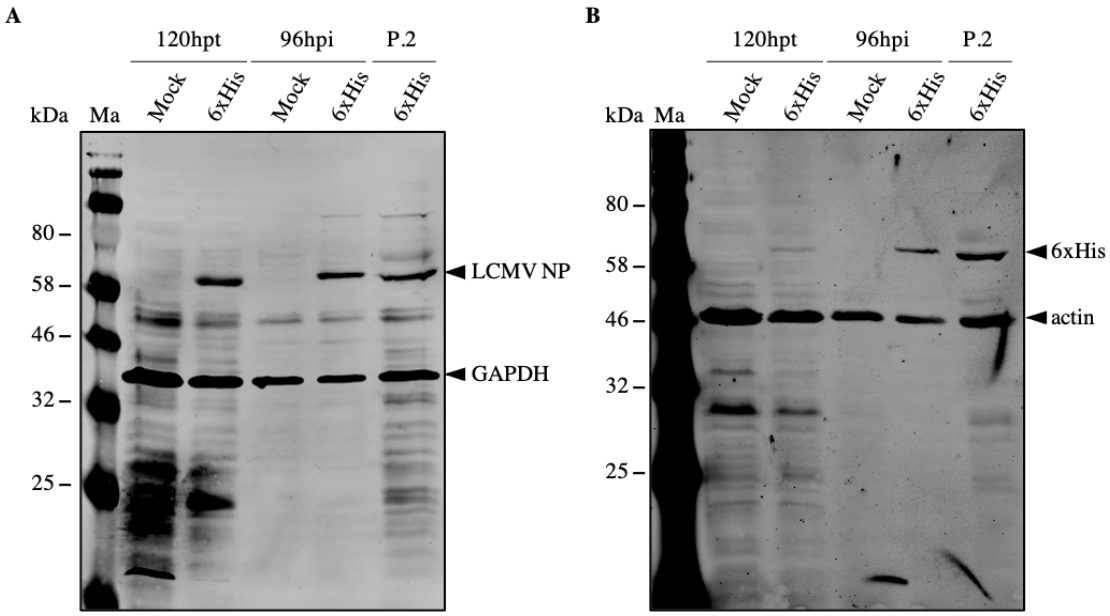

Figure 7.7: Generation of Recombinant LCMV expressing a 6xHis tag on the C-terminus of the Nucleocapsid Protein

The un-cropped western blots from figure 4.12B have been shown. BSR-T7 cells were either mock-transfected or transfected with pUC57-L, pUC57-LP, pUC57-NP, pUC57-T7 and pUC57-S-6xHis (6xHis). The cells were incubated for a total of 120 hours post transfection (120hpt), at which point the BSR-T7 cell lysates were collected for western blot analysis and the supernatant was used to infect BHK-21 cells, which were incubated for 96 hours post infection (96 hpi). The supernatant from the BHK-21 cells was then used to infect fresh BHK-21 cells, which were incubated for another 96 hours, as a second passage of the virus (P.2). Lysates were collected at 96 hpi from the first infection (96 hpi) and the second passage (P.2). Western blotting analysis was performed on these lysates, using either LCMV NP antisera (with GAPDH as a loading control) (**A**) or 6xHis antisera (with actin as a loading control) (**B**). The position of relevant size marker bands have been indicated and the bands representing LCMV NP, 6xHis and loading controls GAPDH and actin have been indicated.

References

Abdel-Hakeem, M. S. (2019). Viruses teaching immunology: Role of LCMV model and human viral infections in immunological discoveries, *Viruses* **11**(2).

Abraham, J., Corbett, K. D., Farzan, M., Choe, H. and Harrison, S. C. (2010). Structural basis for receptor recognition by New World hemorrhagic fever arenaviruses, *Nature Structural & Molecular Biology* **17**(4): 438–444.

Abraham, J., Kwong, J. A., Albariño, C. G., Lu, J. G., Radoshitzky, S. R., Salazar-Bravo, J., Farzan, M., Spiropoulou, C. F. and Choe, H. (2009). Host-Species Transferrin Receptor 1 Orthologs Are Cellular Receptors for Nonpathogenic New World Clade B Arenaviruses, *PLoS Pathogens* **5**(4): e1000358.

Abudurexiti, A., Adkins, S., Alioto, D., Alkhovsky, S. V., Avšič-Županc, T., Ballinger, M. J., Bente, D. A., Beer, M., Bergeron, É., Blair, C. D., Briese, T., Buchmeier, M. J., Burt, F. J., Calisher, C. H., Cháng, C., Charrel, R. N., Choi, I. R., Clegg, J. C. S., de la Torre, J. C., de Lamballerie, X., Dèng, F., Di Serio, F., Digiaro, M., Drebot, M. A., Duàn, X., Ebihara, H., Elbeaino, T., Ergünay, K., Fulhorst, C. F., Garrison, A. R., Gāo, G. F., Gonzalez, J.-P. J., Groschup, M. H., Günther, S., Haenni, A.-L., Hall, R. A., Hepojoki, J., Hewson, R., Hú, Z., Hughes, H. R., Jonson, M. G., Junglen, S., Klempa, B., Klingström, J., Kòu, C., Laenen, L., Lambert, A. J., Langevin, S. A., Liu, D., Lukashevich, I. S., Luò, T., Lò, C., Maes, P., de Souza, W. M., Marklewitz, M., Martelli, G. P., Matsuno, K., Mielke-Ehret, N., Minutolo, M., Mirazimi, A., Moming, A., Mühlbach, H.-P., Naidu, R., Navarro, B., Nunes, M. R. T., Palacios, G., Papa, A., Pauvolid-Corrêa, A., Pawęska, J. T., Qiáo, J., Radoshitzky, S. R., Resende, R. O., Romanowski, V., Sall, A. A., Salvato, M. S., Sasaya, T., Shěn, S., Shí, X., Shirako, Y., Simmonds, P., Sironi, M., Song, J.-W., Spengler, J. R., Stenglein, M. D., Sū, Z., Sūn, S., Táng, S., Turina, M., Wáng, B., Wáng, C., Wáng, H., Wáng, J., Wèi, T., Whitfield, A. E., Zerbini, F. M., Zhāng, J., Zhāng, L., Zhāng, Y., Zhang, Y.-Z., Zhāng, Y., Zhou, X., Zhū, L. and Kuhn, J. H. (2019). Taxonomy of the order Bunyavirales: update 2019, *Archives of Virology* **164**(7): 1949–1965.

Agnihothram, S. S., York, J. and Nunberg, J. H. (2006). Role of the Stable Signal Peptide and Cytoplasmic Domain of G2 in Regulating Intracellular Transport of the Junín Virus Envelope Glycoprotein Complex, *Journal of Virology* **80**(11): 5189–5198.

Agnihothram, S. S., York, J., Trahey, M. and Nunberg, J. H. (2007). Bitopic Membrane Topology of the Stable Signal Peptide in the Tripartite Junín Virus GP-C Envelope Glycoprotein Complex, *Journal of Virology* **81**(8): 4331–4337.

Ahmed, R., Salmi, A., Butler, L. D., Chiller, J. M. and Oldstone, M. B. (1984). Selection of genetic variants of lymphocytic choriomeningitis virus in spleens of persistently infected mice. Role in

suppression of cytotoxic T lymphocyte response and viral persistence., *Journal of Experimental Medicine* **160**(2): 521–540.

Albariño, C. G., Bergeron, É., Erickson, B. R., Khristova, M. L., Rollin, P. E. and Nichol, S. T. (2009). Efficient Reverse Genetics Generation of Infectious Junin Viruses Differing in Glycoprotein Processing, *Journal of Virology* **83**(11): 5606–5614.

Albarino, C. G., Bird, B. H., Chakrabarti, A. K., Dodd, K. A., Erickson, B. R. and Nichol, S. T. (2011). Efficient Rescue of Recombinant Lassa Virus Reveals the Influence of S Segment Noncoding Regions on Virus Replication and Virulence, *Journal of Virology* **85**(8): 4020–4024.

Ammerman, N. C., Beier-Sexton, M. and Azad, A. F. (2008). Growth and Maintenance of Vero Cell Lines, *Current Protocols in Microbiology* **11**(1).

Archer, A. M. and Rico-Hesse, R. (2002). High genetic divergence and recombination in Arenaviruses from the Americas, *Virology* **304**(2): 274–281.

Armstrong, C. and Lillie, R. D. (1934). Experimental Lymphocytic Choriomeningitis of Monkeys and Mice Produced by a Virus Encountered in Studies of the 1933 St. Louis Encephalitis Epidemic, *Public Health Reports (1896-1970)* **49**(35): 1019.

Ashkenazi, A. and Dixit, V. M. (1998). Death Receptors: Signaling and Modulation, *Science* **281**(5381): 1305–1308.

Baird, N. L., York, J. and Nunberg, J. H. (2013). Arenavirus Infection Induces Discrete Cytosolic Structures for RNA Replication, *Journal of Virology* **87**(5): 2983–2983.

Baize, S., Kaplon, J., Faure, C., Pannetier, D., Georges-Courbot, M.-C. and Deubel, V. (2004). Lassa Virus Infection of Human Dendritic Cells and Macrophages Is Productive but Fails to Activate Cells, *The Journal of Immunology* **172**(5): 2861–2869.

Baldridge, J. R. and Buchmeier, M. J. (1992). Mechanisms of antibody-mediated protection against lymphocytic choriomeningitis virus infection: mother-to-baby transfer of humoral protection., *Journal of Virology* **66**(7): 4252–7.

Baldridge, J. R., McGraw, T. S., Paoletti, A. and Buchmeier, M. J. (1997). Antibody prevents the establishment of persistent arenavirus infection in synergy with endogenous T cells., *Journal of Virology* **71**(1): 755–8.

Barry, M., Russi, M., Armstrong, L., Geller, D., Tesh, R., Dembry, L., Gonzalez, J. P., Khan, A. S. and Peters, C. J. (1995). Treatment of a Laboratory-Acquired Sabiá Virus Infection, *New England Journal of Medicine* **333**(5): 294–296.

Barth, H. G., Jackson, C. and Boyes, B. E. (1994). Size Exclusion Chromatography, *Analytical Chemistry* **66**(12): 595–620.

Barton, L. L. and Hyndman, N. J. (2000). Lymphocytic Choriomeningitis Virus: Reemerging Central Nervous System Pathogen, *Pediatrics* **105**(3): e35–e35.

Barton, L. L. and Mets, M. B. (2001). Congenital Lymphocytic Choriomeningitis Virus Infection: Decade of Rediscovery, *Clinical Infectious Diseases* **33**(3): 370–374.

Bausch, D. G., Sesay, S. S. S. S. and Oshin, B. (2004). On the front lines of Lassa fever., *Emerging infectious diseases* **10**(10): 1889–90.

Becares, M., Pascual-Iglesias, A., Nogales, A., Sola, I., Enjuanes, L. and Zuñiga, S. (2016). Mutagenesis of Coronavirus nsp14 Reveals Its Potential Role in Modulation of the Innate Immune Response, *Journal of Virology* **90**(11): 5399–5414.

Bergeron, E., Chakrabarti, A. K., Bird, B. H., Dodd, K. A., McMullan, L. K., Spiropoulou, C. F., Nichol, S. T. and Albarino, C. G. (2012). Reverse Genetics Recovery of Lujo Virus and Role of Virus RNA Secondary Structures in Efficient Virus Growth, *Journal of Virology* **86**(19): 10759–10765.

Beyer, W. R., Pöpplau, D., Garten, W., von Laer, D. and Lenz, O. (2003). Endoproteolytic Processing of the Lymphocytic Choriomeningitis Virus Glycoprotein by the Subtilase SKI-1/S1P, *Journal of Virology* **77**(5): 2866–2872.

Biedler, J. L. and Schachner, M. (1978). Multiple Neurotransmitter Synthesis by Human Neuroblastoma Cell Lines and Clones, *Cancer Research* **38**(November 1972): 3751–3757.

Bodewes, R., Kik, M. J. L., Raj, V. S., Schapendonk, C. M. E., Haagmans, B. L., Smits, S. L. and Osterhaus, A. D. M. E. (2013). Detection of novel divergent arenaviruses in boid snakes with inclusion body disease in The Netherlands, *Journal of General Virology* **94**(6): 1206–1210.

Bonhomme, C. J., Capul, A. A., Lauron, E. J., Bederka, L. H., Knopp, K. A. and Buchmeier, M. J. (2011). Glycosylation modulates arenavirus glycoprotein expression and function, *Virology* **409**(2): 223–233.

Bonthius, D. J. (2012). Lymphocytic Choriomeningitis Virus: An Underrecognized Cause of Neurologic Disease in the Fetus, Child, and Adult, *Seminars in Pediatric Neurology* **19**(3): 89–95.

Borden, K. L. B., Campbell Dwyer, E. J. and Salvato, M. S. (1998a). An Arenavirus RING (Zinc-Binding) Protein Binds the Oncoprotein Promyelocyte Leukemia Protein (PML) and Relocates PML Nuclear Bodies to the Cytoplasm, *Journal of Virology* **72**(1): 758–766.

Borden, K. L. B., CampbellDwyer, E. J., Carlile, G. W., Djavani, M. and Salvato, M. S. (1998b). Two RING Finger Proteins, the Oncoprotein PML and the Arenavirus Z Protein, Colocalize with the Nuclear Fraction of the Ribosomal P Proteins, *Journal of Virology* **72**(5): 3819–3826.

Bornhorst, J. A. and Falke, J. J. (2000). Purification of proteins using polyhistidine affinity tags, *in* J. Thorner, S. D. Emr and J. N. Abelson (eds), *Methods Enzymol*, Vol. 326, Academic Press, pp. 245–254.

Borremans, B., Leirs, H., Gryseels, S., Günther, S., Makundi, R. and de Bellocq, J. G. (2011). Presence of Mopeia Virus, an African Arenavirus, Related to Biotope and Individual Rodent Host Characteristics: Implications for Virus Transmission, *Vector-Borne and Zoonotic Diseases* **11**(8): 1125–1131.

Boulant, S., Stanifer, M. and Lozach, P.-Y. (2015). Dynamics of Virus-Receptor Interactions in Virus Binding, Signaling, and Endocytosis, *Viruses* **7**(6): 2794–2815.

Bouvet, M., Imbert, I., Subissi, L., Gluais, L., Canard, B. and Decroly, E. (2012). RNA 3'-end mismatch excision by the severe acute respiratory syndrome coronavirus nonstructural protein nsp10/nsp14 exoribonuclease complex, *Proceedings of the National Academy of Sciences* **109**(24): 9372–9377.

Bowden, T. A., Crispin, M., Graham, S. C., Harvey, D. J., Grimes, J. M., Jones, E. Y. and Stuart, D. I. (2009). Unusual Molecular Architecture of the Machupo Virus Attachment Glycoprotein, *Journal of Virology* **83**(16): 8259–8265.

Bridgen, A. and Elliott, R. M. (1996). Rescue of a segmented negative-strand RNA virus entirely from cloned complementary DNAs, *Proceedings of the National Academy of Sciences* **93**(26): 15400–15404.

Briese, T., Paweska, J. T., McMullan, L. K., Hutchison, S. K., Street, C., Palacios, G., Khristova, M. L., Weyer, J., Swanepoel, R., Egholm, M., Nichol, S. T. and Lipkin, W. I. (2009). Genetic Detection and Characterization of Lujo Virus, a New Hemorrhagic Fever–Associated Arenavirus from Southern Africa, *PLoS Pathogens* **5**(5): e1000455.

Briknarová, K., Thomas, C. J., York, J. and Nunberg, J. H. (2011). Structure of a Zinc-binding Domain in the Junín Virus Envelope Glycoprotein, *Journal of Biological Chemistry* **286**(2): 1528–1536.

Brunotte, L., Kerber, R., Shang, W., Hauer, F., Hass, M., Gabriel, M., Lelke, M., Busch, C., Stark, H., Svergun, D. I., Betzel, C., Perbandt, M. and Günther, S. (2011a). Structure of the Lassa Virus Nucleoprotein Revealed by X-ray Crystallography, Small-angle X-ray Scattering, and Electron Microscopy, *Journal of Biological Chemistry* **286**(44): 38748–38756.

Brunotte, L., Lelke, M., Hass, M., Kleinsteuber, K., Becker-Ziaja, B. and Günther, S. (2011b). Domain Structure of Lassa Virus L Protein, *Journal of Virology* **85**(1): 324–333.

Buchholz, U. J., Finke, S. and Conzelmann, K.-K. (1999). Generation of Bovine Respiratory Syncytial Virus (BRSV) from cDNA: BRSV NS2 Is Not Essential for Virus Replication in Tissue Culture, and the Human RSV Leader Region Acts as a Functional BRSV Genome Promoter, *Journal of Virology* **73**(1): 251–259.

Buckley, S. M., Casals, J. and Downs, W. G. (1970). Isolation and Antigenic Characterization of Lassa Virus, *Nature* **227**(5254): 174–174.

Burgess, R. R. (2009). Refolding Solubilized Inclusion Body Proteins, *in* R. R. Burgess and M. P. Deutscher (eds), *Methods in Enzymology*, Academic Press, pp. 259–282.

Burri, D. J., da Palma, J. R., Kunz, S. and Pasquato, A. (2012a). Envelope glycoprotein of arenaviruses., *Viruses* **4**(10): 2162–2181.

Burri, D. J., Pasqual, G., Rochat, C., Seidah, N. G., Pasquato, A. and Kunz, S. (2012b). Molecular Characterization of the Processing of Arenavirus Envelope Glycoprotein Precursors by Subtilisin Kexin Isozyme-1/Site-1 Protease, *Journal of Virology* **86**(9): 4935–4946.

Cabantous, S., Terwilliger, T. C. and Waldo, G. S. (2005). Protein tagging and detection with engineered self-assembling fragments of green fluorescent protein, *Nature Biotechnology* **23**(1): 102–107.

Caì, Y., Iwasaki, M., Beitzel, B. F., Yú, S., Postnikova, E. N., Cubitt, B., Dewald, L. E., Radoshitzky, S. R., Bollinger, L., Jahrling, P. B., Palacios, G. F., de la Torre, J. C. and Kuhn, J. H. (2018). Recombinant lassa virus expressing green fluorescent protein as a tool for high-throughput drug screens and neutralizing antibody assays, *Viruses* **10**(11).

Cai, Y., Iwasaki, M., Motooka, D., Liu, D. X., Yu, S., Cooper, K., Hart, R., Adams, R., Burdette, T., Postnikova, E. N., Kurtz, J., St Claire, M., Ye, C., Kuhn, J. H., Martínez-Sobrido, L. and de la Torre, J. C. (2020). A Lassa Virus Live-Attenuated Vaccine Candidate Based on Rearrangement of the Intergenic Region, *mBio* **11**(2): 1–18.

Cao, W. (1998). Identification of -Dystroglycan as a Receptor for Lymphocytic Choriomeningitis Virus and Lassa Fever Virus, *Science* **282**(5396): 2079–2081.

Capul, A. A., de la Torre, J. C. and Buchmeier, M. J. (2011). Conserved Residues in Lassa Fever Virus Z Protein Modulate Viral Infectivity at the Level of the Ribonucleoprotein, *Journal of Virology* **85**(7): 3172–3178.

Capul, A. A., Perez, M., Burke, E., Kunz, S., Buchmeier, M. J. and de la Torre, J. C. (2007). Arenavirus Z-Glycoprotein Association Requires Z Myristoylation but Not Functional RING or Late Domains, *Journal of Virology* **81**(17): 9451–9460.

Carey, D., Kemp, G., White, H., Pinneo, L., Addy, R., Fom, A., Stroh, G., Casals, J. and Henderson, B. (1972). Lassa fever Epidemiological aspects of the 1970 epidemic, Jos, Nigeria, *Transactions of the Royal Society of Tropical Medicine and Hygiene* **66**(3): 402–408.

Carnec, X., Baize, S., Reynard, S., Diancourt, L., Caro, V., Tordo, N. and Bouloy, M. (2011). Lassa Virus Nucleoprotein Mutants Generated by Reverse Genetics Induce a Robust Type I Interferon Response in Human Dendritic Cells and Macrophages, *Journal of Virology* **85**(22): 12093–12097.

Carrion, R., Patterson, J. L., Johnson, C., Gonzales, M., Moreira, C. R., Ticer, A., Brasky, K., Hubbard, G. B., Moshkoff, D., Zapata, J., Salvato, M. S. and Lukashevich, I. S. (2007). A ML29

reassortant virus protects guinea pigs against a distantly related Nigerian strain of Lassa virus and can provide sterilizing immunity, *Vaccine* **25**(20): 4093–4102.

Casabona, J. C., Levingston Macleod, J. M., Loureiro, M. E., Gomez, G. A. and Lopez, N. (2009). The RING Domain and the L79 Residue of Z Protein Are Involved in both the Rescue of Nucleocapsids and the Incorporation of Glycoproteins into Infectious Chimeric Arenavirus-Like Particles, *Journal of Virology* **83**(14): 7029–7039.

Casals, J., Shope, R. E. and Mettler, N. E. (1963). Study of the Antigenic Relationships between Junín Virus, the Etiological Agent of Argentinian Hemorrhagic Fever, and Other Arthropod-Borne Viruses, *The American Journal of Tropical Medicine and Hygiene* **12**(4): 647–652.

Charrel, R. N. and de Lamballerie, X. (2010). Zoonotic aspects of arenavirus infections, *Veterinary Microbiology* **140**(3-4): 213–220.

Charrel, R. N., de Lamballerie, X. and Fulhorst, C. F. (2001). The Whitewater Arroyo Virus: Natural Evidence for Genetic Recombination among Tacaribe Serocomplex Viruses (Family Arenaviridae), *Virology* **283**(2): 161–166.

Charrel, R. N., Feldmann, H., Fulhorst, C. F., Khelifa, R., de Chesse, R. and de Lamballerie, X. (2002). Phylogeny of New World arenaviruses based on the complete coding sequences of the small genomic segment identified an evolutionary lineage produced by intrasegmental recombination, *Biochemical and Biophysical Research Communications* **296**(5): 1118–1124.

Chen, M., Lan, S., Ou, R., Price, G. E., Jiang, H., de la Torre, J. C. and Moskophidis, D. (2008). Genomic and biological characterization of aggressive and docile strains of lymphocytic choriomeningitis virus rescued from a plasmid-based reverse-genetics system, *Journal of General Virology* **89**(6): 1421–1433.

Cheng, Y. (2015). Single-particle Cryo-EM at crystallographic resolution, *Cell* **161**(3): 450–457.

Clark, L. E., Mahmutovic, S., Raymond, D. D., Dilanyan, T., Koma, T., Manning, J. T., Shankar, S., Levis, S. C., Briggiler, A. M., Enria, D. A., Wucherpfennig, K. W., Paessler, S. and Abraham, J. (2018). Vaccine-elicited receptor-binding site antibodies neutralize two New World hemorrhagic fever arenaviruses, *Nature Communications* **9**(1): 1884.

Clegg, J. C. S. and Lloyd, G. (1983). Structural and Cell-associated Proteins of Lassa Virus, *Journal of General Virology* **64**(5): 1127–1136.

Cogswell-Hawkinson, A., Bowen, R., James, S., Gardiner, D., Calisher, C. H., Adams, R. and Schountz, T. (2012). Tacaribe Virus Causes Fatal Infection of An Ostensible Reservoir Host, the Jamaican Fruit Bat, *Journal of Virology* **86**(10): 5791–5799.

Cohen-Dvashi, H., Cohen, N., Israeli, H. and Diskin, R. (2015). Molecular Mechanism for LAMP1 Recognition by Lassa Virus, *Journal of Virology* **89**(15): 7584–7592.

Cohen-Dvashi, H., Kilimnik, I. and Diskin, R. (2018). Structural basis for receptor recognition by Lujo virus, *Nature Microbiology* **3**(10): 1153–1160.

Collins, P. L., Hill, M. G., Camargo, E., Grosfeld, H., Chanock, R. M. and Murphy, B. R. (1995). Production of infectious human respiratory syncytial virus from cloned cDNA confirms an essential role for the transcription elongation factor from the 5' proximal open reading frame of the M2 mRNA in gene expression and provides a capability for vaccine, *Proceedings of the National Academy of Sciences* **92**(25): 11563–11567.

Cope, J., Heumann, J. and Hoenger, A. (2011). Cryo-Electron Tomography for Structural Characterization of Macromolecular Complexes, *Current Protocols in Protein Science*, Vol. 1, John Wiley & Sons, Inc., Hoboken, NJ, USA, chapter 17, pp. 17.13.1–17.13.31.

Cornu, T. I. and de la Torre, J. C. (2001). RING Finger Z Protein of Lymphocytic Choriomeningitis Virus (LCMV) Inhibits Transcription and RNA Replication of an LCMV S-Segment Minigenome, *Journal of Virology* **75**(19): 9415–9426.

Cornu, T. I. and de la Torre, J. C. (2002). Characterization of the Arenavirus RING Finger Z Protein Regions Required for Z-Mediated Inhibition of Viral RNA Synthesis, *Journal of Virology* **76**(13): 6678–6688.

Cornu, T. I., Feldmann, H. and de la Torre, J. C. (2004). Cells Expressing the RING Finger Z Protein Are Resistant to Arenavirus Infection, *Journal of Virology* **78**(6): 2979–2983.

Costa, S., Almeida, A., Castro, A. and Domingues, L. (2014). Fusion tags for protein solubility, purification, and immunogenicity in Escherichia coli: The novel Fh8 system, *Frontiers in Microbiology* **5**(FEB): 1–20.

Cross, R. W., Mire, C. E., Branco, L. M., Geisbert, J. B., Rowland, M. M., Heinrich, M. L., Goba, A., Momoh, M., Grant, D. S., Fullah, M., Khan, S. H., Robinson, J. E., Geisbert, T. W. and Garry, R. F. (2016). Treatment of Lassa virus infection in outbred guinea pigs with first-in-class human monoclonal antibodies, *Antiviral Research* **133**: 218–222.

Cummins, D. (1990). Acute Sensorineural Deafness in Lassa Fever, *JAMA: The Journal of the American Medical Association* **264**(16): 2093.

Daber, R., Stayrook, S., Rosenberg, A. and Lewis, M. (2007). Structural Analysis of Lac Repressor Bound to Allosteric Effectors, *Journal of Molecular Biology* **370**(4): 609–619.

Dalton, A. J., Rowe, W. P., Smith, G. H., Wilsnack, R. E. and Pugh, W. E. (1968). Morphological and Cytochemical Studies on Lymphocytic Choriomeningitis Virus, *Journal of Virology* **2**(12): 1465–1478.

Danev, R. and Baumeister, W. (2017). Expanding the boundaries of cryo-EM with phase plates, *Current Opinion in Structural Biology* **46**: 87–94.

Demain, A. L. and Vaishnav, P. (2009). Production of recombinant proteins by microbes and higher organisms, *Biotechnology Advances* **27**(3): 297–306.

Denison, M. R., Graham, R. L., Donaldson, E. F., Eckerle, L. D. and Baric, R. S. (2011). Coronaviruses: An RNA proofreading machine regulates replication fidelity and diversity, *RNA Biology* **8**(2): 270–279.

Dillard, R. S., Hampton, C. M., Strauss, J. D., Ke, Z., Altomara, D., Guerrero-Ferreira, R. C., Kiss, G. and Wright, E. R. (2018). Biological Applications at the Cutting Edge of Cryo-Electron Microscopy, *Microscopy and Microanalysis* **24**(4): 406–419.

Djavani, M., Topisirovic, I., Zapata, J. C., Sadowska, M., Yang, Y., Rodas, J., Lukashevich, I. S., Bogue, C. W., Pauza, C. D., Borden, K. L. B. and Salvato, M. S. (2005). The Proline-Rich Homeodomain (PRH/HEX) Protein Is Down-Regulated in Liver during Infection with Lymphocytic Choriomeningitis Virus, *Journal of Virology* **79**(4): 2461–2473.

Djomand, G., Quaye, S. and Sullivan, P. S. (2014). HIV epidemic among key populations in west Africa, *Current Opinion in HIV and AIDS* **9**(5): 506–513.

Donnelly, M. L. L., Luke, G., Mehrotra, A., Li, X., Hughes, L. E., Gani, D. and Ryan, M. D. (2001). Analysis of the aphthovirus 2A/2B polyprotein 'cleavage' mechanism indicates not a proteolytic reaction, but a novel translational effect: a putative ribosomal 'skip', *Journal of General Virology* **82**(5): 1013–1025.

Downs, W. G., Anderson, C. R., Spence, L., Aitken, T. H. G. and Greenhall, A. H. (1963). Tacaribe Virus, a New Agent Isolated from Artibeus Bats and Mosquitoes in Trinidad, West Indies *, *The American Journal of Tropical Medicine and Hygiene* **12**(4): 640–646.

Dubendorf, J. W. and Studier, W. F. (1991). Controlling basal expression in an inducible T7 expression system by blocking the target T7 promoter with lac repressor, *Journal of Molecular Biology* **219**(1): 45–59.

Dunn, B. M. and Pennington, M. W. (2003). *Peptide Analysis Protocols*, Humana Press.

Eckerle, L. D., Becker, M. M., Halpin, R. A., Li, K., Venter, E., Lu, X., Scherbakova, S., Graham, R. L., Baric, R. S., Stockwell, T. B., Spiro, D. J. and Denison, M. R. (2010). Infidelity of SARS-CoV Nsp14-Exonuclease Mutant Virus Replication Is Revealed by Complete Genome Sequencing, *PLoS Pathogens* **6**(5): e1000896.

Eddy, G. A., Wagner, F. S., Scott, S. K. and Mahlandt, B. J. (1975). Protection of monkeys against Machupo virus by the passive administration of Bolivian haemorrhagic fever immunoglobulin (human origin)., *Bulletin of the World Health Organization* **52**(4-6): 723–7.

Eichler, R., Lenz, O., Garten, W. and Strecker, T. (2006). The role of single N-glycans in proteolytic processing and cell surface transport of the Lassa virus glycoprotein GP-C, *Virology Journal* **3**: 8–10.

Eichler, R., Lenz, O., Strecker, T. and Garten, W. (2003). Signal peptide of Lassa virus glycoprotein GP-C exhibits an unusual length, *FEBS Letters* **538**(1-3): 203–206.

Emonet, S. F., de la Torre, J. C., Domingo, E. and Sevilla, N. (2009). Arenavirus genetic diversity and its biological implications, *Infection, Genetics and Evolution* **9**(4): 417–429.

Emonet, S. F., Seregin, A. V., Yun, N. E., Poussard, A. L., Walker, A. G., de la Torre, J. C. and Paessler, S. (2011). Rescue from Cloned cDNAs and In Vivo Characterization of Recombinant Pathogenic Romero and Live-Attenuated Candid #1 Strains of Junin Virus, the Causative Agent of Argentine Hemorrhagic Fever Disease, *Journal of Virology* **85**(4): 1473–1483.

Enria, D. A. and Barrera Oro, J. G. (2002). Junin virus vaccines., *Current topics in microbiology and immunology* **263**: 239–61.

Enria, D. A., Briggiler, A. M., Fernandez, N. J., Levis, S. C. and Maiztegui, J. I. (1984). Importance of dose of neutralising antibodies in treatment of Argentine haemorrhagic fever with immune plasma., *Lancet (London, England)* **2**(8397): 255–6.

Enria, D. A. and Maiztegui, J. I. (1994). Antiviral treatment of Argentine hemorrhagic fever., *Antiviral research* **23**(1): 23–31.

Eschli, B., Quirin, K., Wepf, A., Weber, J., Zinkernagel, R. and Hengartner, H. (2006). Identification of an N-Terminal Trimeric Coiled-Coil Core within Arenavirus Glycoprotein 2 Permits Assignment to Class I Viral Fusion Proteins, *Journal of Virology* **80**(12): 5897–5907.

Fan, L., Briese, T. and Lipkin, W. I. (2010). Z Proteins of New World Arenaviruses Bind RIG-I and Interfere with Type I Interferon Induction, *Journal of Virology* **84**(4): 1785–1791.

Fedeli, C., Moreno, H. and Kunz, S. (2018). Novel Insights into Cell Entry of Emerging Human Pathogenic Arenaviruses, *Journal of Molecular Biology* **430**(13): 1839–1852.

Fedeli, C., Torriani, G., Galan-Navarro, C., Moraz, M.-L., Moreno, H., Gerold, G. and Kunz, S. (2017). Axl Can Serve as Entry Factor for Lassa Virus Depending on the Functional Glycosylation of Dystroglycan, *Journal of Virology* **92**(5): 1–22.

Fehling, S. K., Lennartz, F. and Strecker, T. (2012). Multifunctional nature of the arenavirus RING finger protein Z., *Viruses* **4**(11): 2973–3011.

Fenner, F. (1976). Classification and Nomenclature of Viruses. Second Report of the International Committee on Taxonomy of Viruses, *Intervirology* **7**(1-2): 1–3.

Fernandes, J., Guterres, A., de Oliveira, R. C., Chamberlain, J., Lewandowski, K., Teixeira, B. R., Coelho, T. A., Crisóstomo, C. F., Bonvicino, C. R., D'Andrea, P. S., Hewson, R. and de Lemos, E. R. S. (2018). Xapuri virus, a novel mammarenavirus: natural reassortment and increased diversity between New World viruses, *Emerging Microbes & Infections* **7**(1): 1–10.

Ferron, F., Subissi, L., Silveira De Morais, A. T., Le, N. T. T., Sevajol, M., Gluais, L., Decroly, E., Vonrhein, C., Bricogne, G., Canard, B. and Imbert, I. (2018). Structural and molecular basis of mismatch correction and ribavirin excision from coronavirus RNA, *Proceedings of the National Academy of Sciences* **115**(2): E162–E171.

Fischer, S. A., Graham, M. B., Kuehnert, M. J., Kotton, C. N., Srinivasan, A., Marty, F. M., Comer, J. A., Guarner, J., Paddock, C. D., DeMeo, D. L., Shieh, W.-J., Erickson, B. R., Bandy, U., DeMaria, A., Davis, J. P., Delmonico, F. L., Pavlin, B., Likos, A., Vincent, M. J., Sealy, T. K., Goldsmith, C. S., Jernigan, D. B., Rollin, P. E., Packard, M. M., Patel, M., Rowland, C., Helfand, R. F., Nichol, S. T., Fishman, J. A., Ksiazek, T. and Zaki, S. R. (2006). Transmission of Lymphocytic Choriomeningitis Virus by Organ Transplantation, *New England Journal of Medicine* **354**(21): 2235–2249.

Flatz, L., Bergthaler, A., de la Torre, J. C. and Pinschewer, D. D. (2006). Recovery of an arenavirus entirely from RNA polymerase I/II-driven cDNA., *Proceedings of the National Academy of Sciences of the United States of America* **103**(12): 4663–4668.

Fox, B. G. and Blommel, P. G. (2009). Autoinduction of protein expression, *Current Protocols in Protein Science* **Chapter 5**(Unit-5.23).

Frame, J. D., Gocke, D. J., Baldwin, J. M. and Troup, J. M. (1970). Lassa Fever, a New Virus Disease of Man From West Africa. I. Clinical Description and Pathological Findings, *The American Journal of Tropical Medicine and Hygiene* **19**(4): 670–676.

Francis, S. J. and Southern, P. J. (1988). Molecular analysis of viral RNAs in mice persistently infected with lymphocytic choriomeningitis virus., *Journal of Virology* **62**(4): 1251–1257.

Freed, E. O. (2002). Viral Late Domains, *Journal of Virology* **76**(10): 4679–4687.

Froeschke, M., Basler, M., Groettrup, M. and Dobberstein, B. (2003). Long-lived Signal Peptide of Lymphocytic Choriomeningitis Virus Glycoprotein pGP-C, *Journal of Biological Chemistry* **278**(43): 41914–41920.

Fulhorst, C. F., Bennett, S. G., Milazzo, M. L., Murray, H. L., Webb, J. P., Cajimat, M. N. and Bradley, R. D. (2002). Bear Canyon Virus: An Arenavirus Naturally Associated with the California Mouse (Peromyscus californicus), *Emerging Infectious Diseases* **8**(7): 717–721.

Funston, G. M., Kallioinen, S. E., de Felipe, P., Ryan, M. D. and Iggo, R. D. (2008). Expression of heterologous genes in oncolytic adenoviruses using picornaviral 2A sequences that trigger ribosome skipping, *Journal of General Virology* **89**(2): 389–396.

Furuta, Y., Komeno, T. and Nakamura, T. (2017). Favipiravir (T-705), a broad spectrum inhibitor of viral RNA polymerase, *Proceedings of the Japan Academy, Series B* **93**(7): 449–463.

Gaberc-Porekar, V. and Menart, V. (2001). Perspectives of immobilized-metal affinity chromatography, *Journal of Biochemical and Biophysical Methods* **49**(1-3): 335–360.

Gallaher, W. R., DiSimone, C. and Buchmeier, M. J. (2001). The viral transmembrane superfamily: possible divergence of Arenavirus and Filovirus glycoproteins from a common RNA virus ancestor., *BMC microbiology* **1**: 1.

Garcin, D. and Kolakofsky, D. (1990). A novel mechanism for the initiation of Tacaribe arenavirus genome replication., *Journal of Virology* **64**(12): 6196–6203.

Garcin, D. and Kolakofsky, D. (1992). Tacaribe arenavirus RNA synthesis in vitro is primer dependent and suggests an unusual model for the initiation of genome replication., *Journal of Virology* **66**(3): 1370–1376.

Garcin, D., Pelet, T., Calain, P., Roux, L., Curran, J. and Kolakofsky, D. (1995). A highly recombinogenic system for the recovery of infectious Sendai paramyxovirus from cDNA: generation of a novel copy-back nondefective interfering virus., *The EMBO journal* **14**(24): 6087–94.

Garry, C. E. and Garry, R. F. (2019). Proteomics Computational Analyses Suggest that the Antennavirus Glycoprotein Complex Includes a Class I Viral Fusion Protein (α-Penetrene) with an Internal Zinc-Binding Domain and a Stable Signal Peptide, *Viruses* **11**(8): 750.

Gary, J. M., Welch, S. R., Ritter, J. M., Coleman-McCray, J., Huynh, T., Kainulainen, M. H., Bollweg, B. C., Parihar, V., Nichol, S. T., Zaki, S. R., Spiropoulou, C. F. and Spengler, J. R. (2019). Lassa Virus Targeting of Anterior Uvea and Endothelium of Cornea and Conjunctiva in Eye of Guinea Pig Model, *Emerging Infectious Diseases* **25**(5): 865–874.

Gasteiger, E., Hoogland, C., Gattiker, A., Duvaud, S., Wilkins, M. R., Appel, R. D. and Bairoch, A. (2005). *The Proteomics Protocols Handbook*, Humana Press, Totowa, NJ.

Geisbert, T. W., Jones, S., Fritz, E. A., Shurtleff, A. C., Geisbert, J. B., Liebscher, R., Grolla, A., Ströher, U., Fernando, L., Daddario, K. M., Guttieri, M. C., Mothé, B. R., Larsen, T., Hensley, L. E., Jahrling, P. B. and Feldmann, H. (2005). Development of a New Vaccine for the Prevention of Lassa Fever, *PLoS Medicine* **2**(6): e183.

Giard, D. J., Aaronson, S. A., Todaro, G. J., Arnstein, P., Kersey, J. H., Dosik, H. and Parks, W. P. (1973). In Vitro Cultivation of Human Tumors: Establishment of Cell Lines Derived From a Series of Solid Tumors2, *JNCI: Journal of the National Cancer Institute* **51**(5): 1417–1423.

Goddard, T. D., Huang, C. C. and Ferrin, T. E. (2007). Visualizing density maps with UCSF Chimera, *Journal of Structural Biology* **157**(1): 281–287.

Goff, S. P. and Berg, P. (1976). Construction of hybrid viruses containing SV40 and $lambda$; phage DNA segments and their propagation in cultured monkey cells, *Cell* **9**(4): 695–705.

Goldsmith, C. S., Ksiazek, T. G., Rollin, P. E., Comer, J. A., Nicholson, W. L., Peret, T. C., Erdman, D. D., Bellini, W. J., Harcourt, B. H., Rota, P. A., Bhatnagar, J., Bowen, M. D., Erickson, B. R., McMullan, L. K., Nichol, S. T., Shieh, W.-J., Paddock, C. D. and Zaki, S. R.

(2013). Cell Culture and Electron Microscopy for Identifying Viruses in Diseases of Unknown Cause, *Emerging Infectious Diseases* **19**(6): 864–869.

Golovanov, A. P., Hautbergue, G. M., Wilson, S. A. and Lian, L.-Y. (2004). A Simple Method for Improving Protein Solubility and Long-Term Stability, *Journal of the American Chemical Society* **126**(29): 8933–8939.

Goncalves, A.-R., Moraz, M.-L., Pasquato, A., Helenius, A., Lozach, P.-Y. and Kunz, S. (2013). Role of DC-SIGN in Lassa Virus Entry into Human Dendritic Cells, *Journal of Virology* **87**(21): 11504–11515.

Gowen, B. B., Juelich, T. L., Sefing, E. J., Brasel, T., Smith, J. K., Zhang, L., Tigabu, B., Hill, T. E., Yun, T., Pietzsch, C., Furuta, Y. and Freiberg, A. N. (2013). Favipiravir (T-705) Inhibits Junín Virus Infection and Reduces Mortality in a Guinea Pig Model of Argentine Hemorrhagic Fever, *PLoS Neglected Tropical Diseases* **7**(12): e2614.

Grande-Pérez, A., Martin, V., Moreno, H. and de la Torre, J. C. (2016). Arenavirus Quasispecies and Their Biological Implications., *Current topics in microbiology and immunology* **392**: 231–76.

Granville, D. J. and Gottlieb, R. A. (2002). Mitochondria: Regulators of Cell Death and Survival, *The Scientific World JOURNAL* **2**: 1569–1578.

Griffiths, A. J., Miller, J. H., Suzuki, D. T., Lewontin, R. C. and Gelbart, W. M. (2000). *An Introduction to Genetic Analysis, 7th edition*, 7th edn, W.H.Freeman & Co Ltd.

Groseth, A., Wolff, S., Strecker, T., Hoenen, T. and Becker, S. (2010). Efficient Budding of the Tacaribe Virus Matrix Protein Z Requires the Nucleoprotein, *Journal of Virology* **84**(7): 3603–3611.

Gryseels, S., Baird, S. J. E., Borremans, B., Makundi, R., Leirs, H. and Goüy de Bellocq, J. (2017). When Viruses Don't Go Viral: The Importance of Host Phylogeographic Structure in the Spatial Spread of Arenaviruses, *PLOS Pathogens* **13**(1): e1006073.

Habjan, M., Penski, N., Spiegel, M. and Weber, F. (2008). T7 RNA polymerase-dependent and -independent systems for cDNA-based rescue of Rift Valley fever virus, *Journal of General Virology* **89**(9): 2157–2166.

Harnish, D. G., Leung, W. C. and Rawls, W. E. (1981). Characterization of polypeptides immunoprecipitable from Pichinde virus-infected BHK-21 cells., *Journal of Virology* **38**(3): 840–8.

Hass, M., Gölnitz, U., Müller, S., Becker-Ziaja, B. and Günther, S. (2004). Replicon System for Lassa Virus, *Journal of Virology* **78**(24): 13793–13803.

Hass, M., Lelke, M., Busch, C., Becker-Ziaja, B. and Günther, S. (2008). Mutational Evidence for a Structural Model of the Lassa Virus RNA Polymerase Domain and Identification of Two

Residues, Gly1394 and Asp1395, That Are Critical for Transcription but Not Replication of the Genome, *Journal of Virology* **82**(20): 10207–10217.

Hass, M., Westerkofsky, M., Müller, S., Becker-Ziaja, B., Busch, C. and Günther, S. (2006). Mutational Analysis of the Lassa Virus Promoter, *Journal of Virology* **80**(24): 12414–12419.

Hastie, K. M., Igonet, S., Sullivan, B. M., Legrand, P., Zandonatti, M. A., Robinson, J. E., Garry, R. F., Rey, F. A., Oldstone, M. B. and Saphire, E. O. (2016a). Crystal structure of the prefusion surface glycoprotein of the prototypic arenavirus LCMV, *Nature Structural & Molecular Biology* **23**(6): 513–521.

Hastie, K. M., Kimberlin, C. R., Zandonatti, M. A., MacRae, I. J. and Saphire, E. O. (2011a). Structure of the Lassa virus nucleoprotein reveals a dsRNA-specific 3' to 5' exonuclease activity essential for immune suppression, *Proceedings of the National Academy of Sciences* **108**(6): 2396–2401.

Hastie, K. M., Liu, T., Li, S., King, L. B., Ngo, N., Zandonatti, M. A., Woods, V. L., de la Torre, J. C. and Saphire, E. O. (2011b). Crystal structure of the Lassa virus nucleoprotein-RNA complex reveals a gating mechanism for RNA binding, *Proceedings of the National Academy of Sciences* **108**(48): 19365–19370.

Hastie, K. M. and Saphire, E. O. (2018). Lassa virus glycoprotein: stopping a moving target, *Current Opinion in Virology* **31**: 52–58.

Hastie, K. M., Zandonatti, M. A., Kleinfelter, L. M., Heinrich, M. L., Rowland, M. M., Chandran, K., Branco, L. M., Robinson, J. E., Garry, R. F. and Saphire, E. O. (2017). Structural basis for antibody-mediated neutralization of Lassa virus, *Science* **356**(6341): 923–928.

Hastie, K. M., Zandonatti, M., Liu, T., Li, S., Woods, V. L. and Saphire, E. O. (2016b). Crystal Structure of the Oligomeric Form of Lassa Virus Matrix Protein Z, *Journal of Virology* **90**(9): 4556–4562.

Hedhammar, M., Karlstrom, A. and Hober, S. (2006). Chromatographic methods for protein purification, *Stockholm: Royal Institute of Technology* pp. 1–31.

Hepojoki, J., Hepojoki, S., Smura, T., Szirovicza, L., Dervas, E., Prähauser, B., Nufer, L., Schraner, E. M., Vapalahti, O., Kipar, A. and Hetzel, U. (2018). Characterization of Haartman Institute snake virus-1 (HISV-1) and HISV-like viruses—The representatives of genus Hartmanivirus, family Arenaviridae, *PLOS Pathogens* **14**(11): e1007415.

Hepojoki, J., Salmenperä, P., Sironen, T., Hetzel, U., Korzyukov, Y., Kipar, A. and Vapalahti, O. (2015). Arenavirus Coinfections Are Common in Snakes with Boid Inclusion Body Disease, *Journal of Virology* **89**(16): 8657–8660.

Herrador, A., Fedeli, C., Radulovic, E., Campbell, K. P., Moreno, H., Gerold, G. and Kunz, S. (2019). Dynamic dystroglycan complexes mediate cell entry of lassa virus, *mBio* **10**(2): 1–20.

Hetzel, U., Sironen, T., Laurinmaki, P., Liljeroos, L., Patjas, A., Henttonen, H., Vaheri, A., Artelt, A., Kipar, A., Butcher, S. J., Vapalahti, O. and Hepojoki, J. (2013). Isolation, Identification, and Characterization of Novel Arenaviruses, the Etiological Agents of Boid Inclusion Body Disease, *Journal of Virology* **87**(20): 10918–10935.

Heumann, J. M., Hoenger, A. and Mastronarde, D. N. (2011). Clustering and variance maps for cryo-electron tomography using wedge-masked differences, *Journal of Structural Biology* **175**(3): 288–299.

Hornung, V., Ellegast, J., Kim, S., Brzozka, K., Jung, A., Kato, H., Poeck, H., Akira, S., Conzelmann, K.-K., Schlee, M., Endres, S. and Hartmann, G. (2006). 5'-Triphosphate RNA Is the Ligand for RIG-I, *Science* **314**(5801): 994–997.

Howard, C. and Young, P. (1984). Structure and variation among arenaviruses, *in* E. Kurstak (ed.), *Applied Virology*, Academic Press, Orlando, Fla., pp. 327–341.

Howley, P. M. and Knipe, D. M. (2020). *Fields Virology: Emerging Viruses 7th Edition*, Wolters Kluwer Health.

Huang, Q., Shao, J., Lan, S., Zhou, Y., Xing, J., Dong, C., Liang, Y. and Ly, H. (2015). In Vitro and In Vivo Characterizations of Pichinde Viral Nucleoprotein Exoribonuclease Functions, *Journal of Virology* **89**(13): 6595–6607.

Hulseberg, C. E., Fénéant, L., Szymańska, K. M. and White, J. M. (2018). Lamp1 Increases the Efficiency of Lassa Virus Infection by Promoting Fusion in Less Acidic Endosomal Compartments, *mBio* **9**(1): 1–14.

Huttner, A., Combescure, C., Grillet, S., Haks, M. C., Quinten, E., Modoux, C., Agnandji, S. T., Brosnahan, J., Dayer, J.-A., Harandi, A. M., Kaiser, L., Medaglini, D., Monath, T., VEBCON and VSV-EBOVAC Consortia, Roux-Lombard, P., Kremsner, P. G., Ottenhoff, T. H. M. and Siegrist, C.-A. (2017). A dose-dependent plasma signature of the safety and immunogenicity of the rVSV-Ebola vaccine in Europe and Africa., *Science translational medicine* **9**(385).

Igonet, S., Vaney, M. C., Vonhrein, C., Bricogne, G., Stura, E. A., Hengartner, H., Eschli, B. and Rey, F. A. (2011). X-ray structure of the arenavirus glycoprotein GP2 in its postfusion hairpin conformation, *Proceedings of the National Academy of Sciences of the United States of America* **108**(50): 19967–19972.

Israeli, H., Cohen-Dvashi, H., Shulman, A., Shimon, A. and Diskin, R. (2017). Mapping of the Lassa virus LAMP1 binding site reveals unique determinants not shared by other old world arenaviruses, *PLOS Pathogens* **13**(4): e1006337.

Iwasaki, M., Minder, P., Caì, Y., Kuhn, J. H., Yates, J. R., Torbett, B. E. and de la Torre, J. C. (2018). Interactome analysis of the lymphocytic choriomeningitis virus nucleoprotein in infected cells reveals ATPase Na+/K+ transporting subunit Alpha 1 and prohibitin as host-cell factors involved in the life cycle of mammarenaviruses, *PLOS Pathogens* **14**(2): e1006892.

Iwasaki, M., Ngo, N., Cubitt, B. and de la Torre, J. C. (2015). Efficient Interaction between Arenavirus Nucleoprotein (NP) and RNA-Dependent RNA Polymerase (L) Is Mediated by the Virus Nucleocapsid (NP-RNA) Template, *Journal of Virology* **89**(10): 5734–5738.

Iwasaki, M., Ngo, N. and de la Torre, J. C. (2014). Sodium Hydrogen Exchangers Contribute to Arenavirus Cell Entry, *Journal of Virology* **88**(1): 643–654.

Jacob, F. and Monod, J. (1961). Genetic regulatory mechanisms in the synthesis of proteins, *Journal of Molecular Biology* **3**(3): 318–356.

Jae, L. T. and Brummelkamp, T. R. (2015). Emerging intracellular receptors for hemorrhagic fever viruses, *Trends in Microbiology* **23**(7): 392–400.

Jae, L. T., Raaben, M., Herbert, A. S., Kuehne, A. I., Wirchnianski, A. S., Soh, T. K., Stubbs, S. H., Janssen, H., Damme, M., Saftig, P., Whelan, S. P., Dye, J. M. and Brummelkamp, T. R. (2014). Lassa virus entry requires a trigger-induced receptor switch, *Science* **344**(6191): 1506–1510.

Jahrling, P. B., Hesse, R. A., Eddy, G. A., Johnson, K. M., Callis, R. T. and Stephen, E. L. (1980). Lassa Virus Infection of Rhesus Monkeys: Pathogenesis and Treatment with Ribavirin, *Journal of Infectious Diseases* **141**(5): 580–589.

Jahrling, P. B., Peters, C. J. and Stephen, E. L. (1984). Enhanced Treatment of Lassa Fever by Immune Plasma Combined with Ribavirin in Cynomolgus Monkeys, *Journal of Infectious Diseases* **149**(3): 420–427.

Jahrling, P. B., Peters, C. J. and Stephen, E. L. (1984b). Enhanced Treatment of Lassa Fever by Immune Plasma Combined with Ribavirin in Cynomolgus Monkeys, *Journal of Infectious Diseases* **149**(3): 420–427.

Jaòcamo, R., Loòpez, N., Wilda, M. and Franze-Fernaòndez, M. T. (2003). Tacaribe Virus Z Protein Interacts with the L Polymerase Protein To Inhibit Viral RNA Synthesis, *Journal of Virology* **77**(19): 10383–10393.

Jiang, X., Huang, Q., Wang, W., Dong, H., Ly, H., Liang, Y. and Dong, C. (2013). Structures of Arenaviral Nucleoproteins with Triphosphate dsRNA Reveal a Unique Mechanism of Immune Suppression, *Journal of Biological Chemistry* **288**(23): 16949–16959.

Johnson, K. M., Wiebenga, N. H., Mackenzie, R. B., Kuns, M. L., Tauraso, N. M., Shelokov, A., Webb, P. A., Justines, G. and Beye, H. K. (1965). Virus Isolations from Human Cases of Hemorrhagic Fever in Bolivia, *Experimental Biology and Medicine* **118**(1): 113–118.

Kamiyama, D., Sekine, S., Barsi-Rhyne, B., Hu, J., Chen, B., Gilbert, L. A., Ishikawa, H., Leonetti, M. D., Marshall, W. F., Weissman, J. S. and Huang, B. (2016). Versatile protein tagging in cells with split fluorescent protein, *Nature Communications* **7**(1): 11046.

Kaur, J., Kumar, A. and Kaur, J. (2018). Strategies for optimization of heterologous protein expression in E. coli: Roadblocks and reinforcements, *International Journal of Biological Macromolecules* **106**: 803–822.

Ke, A., Zhou, K., Ding, F., Cate, J. H. D. D. and Doudna, J. A. (2004). A conformational switch controls hepatitis delta virus ribozyme catalysis, *Nature* **429**(6988): 201–205.

Ke, Z., Oton, J., Qu, K., Cortese, M., Zila, V., McKeane, L., Nakane, T., Zivanov, J., Neufeldt, C. J., Cerikan, B., Lu, J. M., Peukes, J., Xiong, X., Kräusslich, H.-G., Scheres, S. H. W., Bartenschlager, R. and Briggs, J. A. G. (2020). Structures and distributions of SARS-CoV-2 spike proteins on intact virions, *Nature* **588**(7838): 498–502.

Kentsis, A., Dwyer, E. C., Perez, J. M., Sharma, M., Chen, A., Pan, Z. Q. and Borden, K. L. (2001). The RING domains of the promyelocytic leukemia protein PML and the arenaviral protein Z repress translation by directly inhibiting translation initiation factor eIF4E, *Journal of Molecular Biology* **312**(4): 609–623.

Kentsis, A., Gordon, R. E. and Borden, K. L. B. (2002a). Self-assembly properties of a model RING domain, *Proceedings of the National Academy of Sciences* **99**(2): 667–672.

Kentsis, A., Gordon, R. E. and Borden, K. L. B. (2002b). Nonlinear partial differential equations and applications: Control of biochemical reactions through supramolecular RING domain self-assembly, *Proceedings of the National Academy of Sciences* **99**(24): 15404–15409.

Kenyon, R. H., Canonico, P. G., Green, D. E. and Peters, C. J. (1986a). Effect of ribavirin and tributylribavirin on argentine hemorrhagic fever (Junin virus) in guinea pigs., *Antimicrobial Agents and Chemotherapy* **29**(3): 521–523.

Kenyon, R. H., Green, D. E., Eddy, G. A. and Peters, C. J. (1986b). Treatment of junin virus-infected guinea pigs with immune serum: development of late neurological disease., *Journal of Virology Virology* **20**(3): 207–18.

Kernéis, S., Koivogui, L., Magassouba, N., Koulemou, K., Lewis, R., Aplogan, A., Grais, R. F., Guerin, P. J. and Fichet-Calvet, E. (2009). Prevalence and Risk Factors of Lassa Seropositivity in Inhabitants of the Forest Region of Guinea: A Cross-Sectional Study, *PLoS Neglected Tropical Diseases* **3**(11): e548.

Kilgore, P. E., Ksiazek, T. G., Rollin, P. E., Mills, J. N., Villagra, M. R., Montenegro, M. J., Costales, M. A., Paredes, L. C. and Peters, C. J. (1997). Treatment of Bolivian Hemorrhagic Fever with Intravenous Ribavirin, *Clinical Infectious Diseases* **24**(4): 718–722.

Kim, D.-H., Longo, M., Han, Y., Lundberg, P., Cantin, E. and Rossi, J. J. (2004). Interferon induction by siRNAs and ssRNAs synthesized by phage polymerase, *Nature Biotechnology* **22**(3): 321–325.

Kim, J. H., Lee, S.-R., Li, L.-H., Park, H.-J., Park, J.-H., Lee, K. Y., Kim, M.-K., Shin, B. A. and Choi, S.-Y. (2011). High Cleavage Efficiency of a 2A Peptide Derived from Porcine Teschovirus-1 in Human Cell Lines, Zebrafish and Mice, *PLoS ONE* **6**(4): e18556.

Kimata, K., Takahashi, H., Inada, T., Postma, P. and Aiba, H. (1997). cAMP receptor protein-cAMP plays a crucial role in glucose-lactose diauxie by activating the major glucose transporter gene in Escherichia coli, *Proceedings of the National Academy of Sciences* **94**(24): 12914–12919.

King, B. R., Hershkowitz, D., Eisenhauer, P. L., Weir, M. E., Ziegler, C. M., Russo, J., Bruce, E. A., Ballif, B. A. and Botten, J. (2017). A Map of the Arenavirus Nucleoprotein-Host Protein Interactome Reveals that Junín Virus Selectively Impairs the Antiviral Activity of Double-Stranded RNA-Activated Protein Kinase (PKR), *Journal of Virology* **91**(15).

King, B. R., Samacoits, A., Eisenhauer, P. L., Ziegler, C. M., Bruce, E. A., Zenklusen, D., Zimmer, C., Mueller, F. and Botten, J. (2018). Visualization of Arenavirus RNA Species in Individual Cells by Single-Molecule Fluorescence In Situ Hybridization Suggests a Model of Cyclical Infection and Clearance during Persistence, *Journal of Virology* **92**(12).

Klaus, J. P., Eisenhauer, P., Russo, J., Mason, A. B., Do, D., King, B., Taatjes, D., Cornillez-Ty, C., Boyson, J. E., Thali, M., Zheng, C., Liao, L., Yates, J. R., Zhang, B., Ballif, B. A. and Botten, J. W. (2013). The Intracellular Cargo Receptor ERGIC-53 Is Required for the Production of Infectious Arenavirus, Coronavirus, and Filovirus Particles, *Cell Host & Microbe* **14**(5): 522–534.

Klewitz, C., Klenk, H.-D. and ter Meulen, J. (2007). Amino acids from both N-terminal hydrophobic regions of the Lassa virus envelope glycoprotein GP-2 are critical for pH-dependent membrane fusion and infectivity, *Journal of General Virology* **88**(8): 2320–2328.

Knopp, K. A., Ngo, T., Gershon, P. D. and Buchmeier, M. J. (2015). Single Nucleoprotein Residue Modulates Arenavirus Replication Complex Formation, *mBio* **6**(3): 1–11.

Koellhoffer, J. F., Dai, Z., Malashkevich, V. N., Stenglein, M. D., Liu, Y., Toro, R., S. Harrison, J., Chandran, K., DeRisi, J. L., Almo, S. C. and Lai, J. R. (2014). Structural Characterization of the Glycoprotein GP2 Core Domain from the CAS Virus, a Novel Arenavirus-Like Species, *Journal of Molecular Biology* **426**(7): 1452–1468.

Kolokoltsova, O. A., Grant, A. M., Huang, C., Smith, J. K., Poussard, A. L., Tian, B., Brasier, A. R., Peters, C. J., Tseng, C.-T. K., de la Torre, J. C. and Paessler, S. (2014). RIG-I Enhanced Interferon Independent Apoptosis upon Junin Virus Infection, *PLoS ONE* **9**(6): e99610.

Kranzusch, P. J., Schenk, A. D., Rahmeh, A. A., Radoshitzky, S. R., Bavari, S., Walz, T. and Whelan, S. P. (2010). Assembly of a functional Machupo virus polymerase complex, *Proceedings of the National Academy of Sciences of the United States of America* **107**(46): 20069–20074.

Kranzusch, P. J. and Whelan, S. P. (2012). Architecture and regulation of negative-strand viral enzymatic machinery, *RNA Biology* **9**(7): 941–948.

Kranzusch, P. J. and Whelan, S. P. J. (2011). Arenavirus Z protein controls viral RNA synthesis by locking a polymerase-promoter complex, *Proceedings of the National Academy of Sciences* **108**(49): 19743–19748.

Kremer, J. R., Mastronarde, D. N. and McIntosh, J. R. (1996). Computer Visualization of Three-Dimensional Image Data Using IMOD, *Journal of Structural Biology* **116**(1): 71–76.

Kunz, S. (2009). Receptor binding and cell entry of Old World arenaviruses reveal novel aspects of virus–host interaction, *Virology* **387**(2): 245–249.

Kunz, S., Borrow, P. and Oldstone, M. B. A. (2002). *Receptor Structure, Binding, and Cell Entry of Arenaviruses*, Springer Berlin Heidelberg, Berlin, Heidelberg, pp. 111–137.

Kunz, S., Rojek, J. M., Perez, M., Spiropoulou, C. F. and Oldstone, M. B. A. (2005). Characterization of the Interaction of Lassa Fever Virus with Its Cellular Receptor {$alpha$}-Dystroglycan, *Journal of Virology* **79**(10): 5979–5987.

Kunz, S., Sevilla, N., McGavern, D. B., Campbell, K. P. and Oldstone, M. B. A. A. (2001). Molecular analysis of the interaction of LCMV with its cellular receptor {$alpha$}-dystroglycan, *Journal of Cell Biology* **155**(2): 301–310.

Labudova, M., Tomaskova, J., Skultety, L., Pastorek, J. and Pastorekova, S. (2009). The Nucleoprotein of Lymphocytic Choriomeningitis Virus Facilitates Spread of Persistent Infection through Stabilization of the Keratin Network, *Journal of Virology* **83**(16): 7842–7849.

Lan, S., McLay Schelde, L., Wang, J., Kumar, N., Ly, H. and Liang, Y. (2009). Development of Infectious Clones for Virulent and Avirulent Pichinde Viruses: a Model Virus To Study Arenavirus-Induced Hemorrhagic Fevers, *Journal of Virology* **83**(13): 6357–6362.

Lapošová, K., Pastoreková, S. and Tomášková, J. (2013). Lymphocytic choriomeningitis virus: invisible but not innocent, *Acta virologica* **57**(02): 160–170.

Larson, R. A., Dai, D., Hosack, V. T., Tan, Y., Bolken, T. C., Hruby, D. E. and Amberg, S. M. (2008). Identification of a Broad-Spectrum Arenavirus Entry Inhibitor, *Journal of Virology* **82**(21): 10768–10775.

Lawson, N. D., Stillman, E. A., Whitt, M. A. and Rose, J. K. (1995). Recombinant vesicular stomatitis viruses from DNA., *Proceedings of the National Academy of Sciences* **92**(10): 4477–4481.

Lee, K. J., Novella, I. S., Teng, M. N., Oldstone, M. B. A. and de la Torre, J. C. (2000). NP and L Proteins of Lymphocytic Choriomeningitis Virus (LCMV) Are Sufficient for Efficient Transcription and Replication of LCMV Genomic RNA Analogs, *Journal of Virology* **74**(8): 3470–3477.

Lehmann, M., Pahlmann, M., Jerome, H., Busch, C., Lelke, M. and Gunther, S. (2014). Role of the C Terminus of Lassa Virus L Protein in Viral mRNA Synthesis, *Journal of Virology* **88**(15): 8713–8717.

Leibovitz, A., McCombs, W. M., Johnston, D., McCoy, C. E. and Stinson, J. C. (1973). New human cancer cell culture lines. I. SW-13, small-cell carcinoma of the adrenal cortex., *Journal of the National Cancer Institute* **51**(2): 691–7.

Lelke, M., Brunotte, L., Busch, C. and Günther, S. (2010). An N-Terminal Region of Lassa Virus L Protein Plays a Critical Role in Transcription but Not Replication of the Virus Genome, *Journal of Virology* **84**(4): 1934–1944.

Lennartz, F., Hoenen, T., Lehmann, M., Groseth, A. and Garten, W. (2013). The role of oligomerization for the biological functions of the arenavirus nucleoprotein, *Archives of Virology* **158**(9): 1895–1905.

Lenz, O., ter Meulen, J., Feldmann, H., Klenk, H.-D. and Garten, W. (2000). Identification of a Novel Consensus Sequence at the Cleavage Site of the Lassa Virus Glycoprotein, *Journal of Virology* **74**(23): 11418–11421.

Lenz, O., ter Meulen, J., Klenk, H.-D., Seidah, N. G. and Garten, W. (2001). The Lassa virus glycoprotein precursor GP-C is proteolytically processed by subtilase SKI-1/S1P, *Proceedings of the National Academy of Sciences* **98**(22): 12701–12705.

Leventhal, S. S., Wilson, D., Feldmann, H. and Hawman, D. W. (2021). A Look into Bunyavirales Genomes: Functions of Non-Structural (NS) Proteins, *Viruses* **13**(2).

Li, A. L., Grant, D., Gbakie, M., Kanneh, L., Mustafa, I., Bond, N., Engel, E., Schieffelin, J., Vandy, M. J., Yeh, S. and Shantha, J. G. (2020). Ophthalmic manifestations and vision impairment in Lassa fever survivors, *PLOS ONE* **15**(12): e0243766.

Li, C. X., Shi, M., Tian, J. H., Lin, X. D., Kang, Y. J., Chen, L. J., Qin, X. C., Xu, J., Holmes, E. C. and Zhang, Y. Z. (2015). Unprecedented genomic diversity of RNA viruses in arthropods reveals the ancestry of negative-sense RNA viruses, *eLife* **2015**(4): 1–26.

Li, S., Sun, Z., Pryce, R., Parsy, M. L., Fehling, S. K., Schlie, K., Siebert, C. A., Garten, W., Bowden, T. A., Strecker, T. and Huiskonen, J. T. (2016). Acidic pH-Induced Conformations and LAMP1 Binding of the Lassa Virus Glycoprotein Spike, *PLoS Pathogens* **12**(2): 1–18.

Liang, Y., Lan, S. and Ly, H. (2009). Molecular Determinants of Pichinde Virus Infection of Guinea Pigs-a Small Animal Model System for Arenaviral Hemorrhagic Fevers, *Annals of the New York Academy of Sciences* **1171**: E65–E74.

Linero, F., Welnowska, E., Carrasco, L. and Scolaro, L. (2013). Participation of eIF4F complex in Junin virus infection: blockage of eIF4E does not impair virus replication, *Cellular Microbiology* pp. n/a–n/a.

López, N., Jácamo, R., Franze-Fernández, M. T., Loòpez, N., Jaòcamo, R. and Franze-Fernaòndez, M. T. (2001). Transcription and RNA Replication of Tacaribe Virus Genome and Antigenome Analogs Require N and L Proteins: Z Protein Is an Inhibitor of These Processes, *Journal of Virology* **75**(24): 12241–12251.

Lord, R. D., Tzianabos, T., Calisher, C. H. and Coleman, P. H. (1970). Tamiami Virus, a New Member of the Tacaribe Group, *The American Journal of Tropical Medicine and Hygiene* **19**(3): 520–526.

Loureiro, M. E., Wilda, M., Levingston Macleod, J. M., D'Antuono, A., Foscaldi, S., Buslje, C. M. and Lopez, N. (2011). Molecular Determinants of Arenavirus Z Protein Homo-Oligomerization and L Polymerase Binding, *Journal of Virology* **85**(23): 12304–12314.

Loureiro, M. E., Zorzetto-Fernandes, A. L., Radoshitzky, S., Chi, X., Dallari, S., Marooki, N., Lèger, P., Foscaldi, S., Harjono, V., Sharma, S., Zid, B. M., López, N., de la Torre, J. C., Bavari, S. and Zúñiga, E. (2018). DDX3 suppresses type I interferons and favors viral replication during Arenavirus infection, *PLOS Pathogens* **14**(7): e1007125.

Lucia, H., Coppenhaver, D. and Baron, S. (1989). Arenavirus infection in the guinea pig model: Antiviral therapy with recombinant interferon-α, the immunomodulator CL246, 738 and ribavirin, *Antiviral Research* **12**(5-6): 279–292.

Lukashevich, I. S., Patterson, J., Carrion, R., Moshkoff, D., Ticer, A., Zapata, J., Brasky, K., Geiger, R., Hubbard, G. B., Bryant, J. and Salvato, M. S. (2005). A live attenuated vaccine for Lassa fever made by reassortment of Lassa and Mopeia viruses., *Journal of Virology* **79**(22): 13934–42.

Lukashevich, I. S., Rodas, J. D., Tikhonov, I. I., Zapata, J. C., Yang, Y., Djavani, M. and Salvato, M. S. (2004). LCMV-mediated hepatitis in rhesus macaques: WE but not ARM strain activates hepatocytes and induces liver regeneration, *Archives of Virology* **149**(12): 2319–2336.

Luytjes, W., Krystal, M., Enami, M., Parvin, J. D. and Palese, P. (1989). Amplification, expression, and packaging of a foreign gene by influenza virus, *Cell* **59**(6): 1107–1113.

Maes, P., Alkhovsky, S. V., Bào, Y., Beer, M., Birkhead, M., Briese, T., Buchmeier, M. J., Calisher, C. H., Charrel, R. N., Choi, I. R., Clegg, C. S., de la Torre, J. C., Delwart, E., DeRisi, J. L., Di Bello, P. L., Di Serio, F., Digiaro, M., Dolja, V. V., Drosten, C., Druciarek, T. Z., Du, J., Ebihara, H., Elbeaino, T., Gergerich, R. C., Gillis, A. N., Gonzalez, J.-P. J., Haenni, A.-L., Hepojoki, J., Hetzel, U., Hồ, T., Hóng, N., Jain, R. K., Jansen van Vuren, P., Jin, Q., Jonson, M. G., Junglen, S., Keller, K. E., Kemp, A., Kipar, A., Kondov, N. O., Koonin, E. V., Kormelink, R., Korzyukov, Y., Krupovic, M., Lambert, A. J., Laney, A. G., LeBreton, M., Lukashevich, I. S., Marklewitz, M., Markotter, W., Martelli, G. P., Martin, R. R., Mielke-Ehret, N., Mühlbach, H.-P., Navarro, B., Ng, T. F. F., Nunes, M. R. T., Palacios, G., Pawęska, J. T., Peters, C. J., Plyusnin, A., Radoshitzky, S. R., Romanowski, V., Salmenperä, P., Salvato, M. S.,

Sanfaçon, H., Sasaya, T., Schmaljohn, C., Schneider, B. S., Shirako, Y., Siddell, S., Sironen, T. A., Stenglein, M. D., Storm, N., Sudini, H., Tesh, R. B., Tzanetakis, I. E., Uppala, M., Vapalahti, O., Vasilakis, N., Walker, P. J., Wáng, G., Wáng, L., Wáng, Y., Wèi, T., Wiley, M. R., Wolf, Y. I., Wolfe, N. D., Wú, Z., Xú, W., Yang, L., Yāng, Z., Yeh, S.-D., Zhāng, Y.-Z., Zhèng, Y., Zhou, X., Zhū, C., Zirkel, F. and Kuhn, J. H. (2018). Taxonomy of the family Arenaviridae and the order Bunyavirales: update 2018, *Archives of Virology* **163**(8): 2295–2310.

Mahmutovic, S., Clark, L., Levis, S. C., Briggiler, A. M., Enria, D. A., Harrison, S. C. and Abraham, J. (2015). Molecular Basis for Antibody-Mediated Neutralization of New World Hemorrhagic Fever Mammarenaviruses, *Cell Host & Microbe* **18**(6): 705–713.

Mairhofer, J., Wittwer, A., Cserjan-Puschmann, M. and Striedner, G. (2015). Preventing T7 RNA polymerase read-through transcription-A synthetic termination signal capable of improving bioprocess stability, *ACS Synthetic Biology* **4**(3): 265–273.

Maiztegui, J. I., Fernandez, N. J. and de Damilano, A. J. (1979). Efficacy of immune plasma in treatment of Argentine haemorrhagic fever and association between treatment and a late neurological syndrome., *Lancet (London, England)* **2**(8154): 1216–7.

Maiztegui, J. I., McKee, K. T., Barrera Oro, J. G., Harrison, L. H., Gibbs, P. H., Feuillade, M. R., Enria, D. A., Briggiler, A. M., Levis, S. C., Ambrosio, A. M., Halsey, N. A. and Peters, C. J. (1998). Protective efficacy of a live attenuated vaccine against Argentine hemorrhagic fever. AHF Study Group., *The Journal of infectious diseases* **177**(2): 277–83.

Malakhov, M., Mattern, M. R., Malakhova, O. A., Drinker, M., Weeks, S. D. and Butt, T. R. (2004). SUMO fusions and SUMO-specific protease for efficient expression and purification of proteins, *Journal of Structural and Functional Genomics* **5**: 75–86.

Malik, A. (2016). Protein fusion tags for efficient expression and purification of recombinant proteins in the periplasmic space of E. coli, *3 Biotech* **6**(1): 1–7.

Malmlov, A., Seetahal, J., Carrington, C., Ramkisson, V., Foster, J., Miazgowicz, K. L., Quackenbush, S., Rovnak, J., Negrete, O., Munster, V. and Schountz, T. (2017). Serological evidence of arenavirus circulation among fruit bats in Trinidad, *PLOS ONE* **12**(9): e0185308.

Mannweiler, K. and Lehmann-Grube, F. (1973). Electron Microscopy of LCM Virus-Infected L Cells, *Lymphocytic Choriomeningitis Virus and Other Arenaviruses*, Springer Berlin Heidelberg, Berlin, Heidelberg, pp. 37–48.

Marbach, A. and Bettenbrock, K. (2012). Lac operon induction in Escherichia coli: Systematic comparison of IPTG and TMG induction and influence of the transacetylase LacA, *Journal of Biotechnology* **157**(1): 82–88.

Marblestone, J. G., Edavettal, S. C., Lim, Y., Lim, P., Zuo, X. and Butt, T. R. (2006). Comparison of SUMO fusion technology with traditional gene fusion systems: Enhanced expression and solubility with SUMO, *Protein Science* **15**: 182–189.

Mariën, J., Borremans, B., Verhaeren, C., Kirkpatrick, L., Gryseels, S., Goüy de Bellocq, J., Günther, S., Sabuni, C. A., Massawe, A. W., Reijniers, J. and Leirs, H. (2020a). Density dependence and persistence of Morogoro arenavirus transmission in a fluctuating population of its reservoir host, *Journal of Animal Ecology* **89**(2): 506–518.

Mariën, J., Lo Iacono, G., Rieger, T., Magassouba, N., Günther, S. and Fichet-Calvet, E. (2020b). Households as hotspots of Lassa fever? Assessing the spatial distribution of Lassa virus-infected rodents in rural villages of Guinea, *Emerging Microbes & Infections* **9**(1): 1055–1064.

Martin-Serrano, J., Zang, T. and Bieniasz, P. D. (2001). HIV-1 and Ebola virus encode small peptide motifs that recruit Tsg101 to sites of particle assembly to facilitate egress, *Nature Medicine* **7**(12): 1313–1319.

Martinez, M., Bialecki, M. A., Belouzard, S., Cordo, S. M., Candurra, N. A. and Whittaker, G. R. (2013). Utilization of human DC-SIGN and L-SIGN for entry and infection of host cells by the New World arenavirus, Junín virus, *Biochemical and Biophysical Research Communications* **441**(3): 612–617.

Martinez, M. G., Cordo, S. M. and Candurra, N. A. (2007). Characterization of Junin arenavirus cell entry, *Journal of General Virology* **88**(6): 1776–1784.

Martínez-Sobrido, L. and de la Torre, J. C. (2016). Reporter-expressing, replicating-competent recombinant arenaviruses, *Viruses* **8**(7): 1–20.

Martínez-Sobrido, L., Emonet, S., Giannakas, P., Cubitt, B., García-Sastre, A. and de la Torre, J. C. (2009). Identification of Amino Acid Residues Critical for the Anti-Interferon Activity of the Nucleoprotein of the Prototypic Arenavirus Lymphocytic Choriomeningitis Virus, *Journal of Virology* **83**(21): 11330–11340.

Martínez-Sobrido, L., Giannakas, P., Cubitt, B., García-Sastre, A. and de la Torre, J. C. (2007). Differential Inhibition of Type I Interferon Induction by Arenavirus Nucleoproteins, *Journal of Virology* **81**(22): 12696–12703.

Martínez-Sobrido, L., Zúñiga, E. I., Rosario, D., García-Sastre, A. and de la Torre, J. C. (2006). Inhibition of the Type I Interferon Response by the Nucleoprotein of the Prototypic Arenavirus Lymphocytic Choriomeningitis Virus, *Journal of Virology* **80**(18): 9192–9199.

Mateer, E. J., Huang, C., Shehu, N. Y. and Paessler, S. (2018b). Lassa fever–induced sensorineural hearing loss: A neglected public health and social burden, *PLOS Neglected Tropical Diseases* **12**(2): e0006187.

Matthews, R. (1979). Third report of the International Com-mittee on Taxonomy of Viruses. Classification and nomenclature of viruses, *Intervirology* **12**(3-5): 129–296.

McCormick, J. B., King, I. J., Webb, P. A., Scribner, C. L., Craven, R. B., Johnson, K. M., Elliott, L. H. and Belmont-Williams, R. (1986b). Lassa Fever, *New England Journal of Medicine* **314**(1): 20–26.

McCormick, J. B., Walker, D. H., King, I. J., Webb, P. A., Elliott, L. H., Whitfield, S. G. and Johnson, K. M. (1986a). Lassa virus hepatitis: A study of fatal Lassa fever in humans, *American Journal of Tropical Medicine and Hygiene* **35**(2): 401–407.

McKee, Jr., K. T., Oro, J. G. B., Kuehne, A. I., Spisso, J. A. and Mahlandt, B. (1992). Candid No. 1 Argentine Hemorrhagic Fever Vaccine Protects against Lethal Junin Virus Challenge in Rhesus Macaques, *Intervirology* **34**(3): 154–163.

McLay, L., Liang, Y. and Ly, H. (2014). Comparative analysis of disease pathogenesis and molecular mechanisms of New World and Old World arenavirus infections, *Journal of General Virology* **95**(1): 1–15.

Mendenhall, M., Russell, A., Smee, D. F., Hall, J. O., Skirpstunas, R., Furuta, Y. and Gowen, B. B. (2011). Effective Oral Favipiravir (T-705) Therapy Initiated after the Onset of Clinical Disease in a Model of Arenavirus Hemorrhagic Fever, *PLoS Neglected Tropical Diseases* **5**(10): e1342.

Meyer, B. and Groseth, A. (2018). Apoptosis during arenavirus infection: mechanisms and evasion strategies, *Microbes and Infection* **20**(2): 65–80.

Meyer, B. J., De La Torre, J. C. and Southern, P. J. (2002). Arenaviruses: Genomic RNAs, Transcription, and Replication, *in* M. Oldstone (ed.), *Arenaviruses I; The Epidemiology, Molecular and Cell Biology of Arenaviruses*, Springer-Verlag Berlin Heidelberg, pp. 139–157.

Meyer, B. J. and Southern, P. J. (1993). Concurrent sequence analysis of 5' and 3' RNA termini by intramolecular circularization reveals 5' nontemplated bases and 3' terminal heterogeneity for lymphocytic choriomeningitis virus mRNAs., *Journal of Virology* **67**(5): 2621–2627.

Meyer, B. and Ly, H. (2016). Inhibition of Innate Immune Responses Is Key to Pathogenesis by Arenaviruses, *Journal of Virology* **90**(8): 3810–3818.

Milazzo, M. L., Cajimat, M. N., Duno, G., Duno, F., Utrera, A. and Fulhorst, C. F. (2011). Transmission of Guanarito and Pirital Viruses among Wild Rodents, Venezuela, *Emerging Infectious Diseases* **17**(12): 2209–2215.

Mills, J. N., Ellis, B. A., Childs, J. E., McKee, K. T., Maiztegui, J. I., Peters, C. J., Ksiazek, T. G. and Jahrling, P. B. (1994). Prevalence of infection with Junin virus in rodent populations in the epidemic area of Argentine hemorrhagic fever., *The American Journal of Tropical Medicine and Hygiene* **51**(5): 554–62.

Minskaia, E., Hertzig, T., Gorbalenya, A. E., Campanacci, V., Cambillau, C., Canard, B. and Ziebuhr, J. (2006). Discovery of an RNA virus 3'->5' exoribonuclease that is critically

involved in coronavirus RNA synthesis, *Proceedings of the National Academy of Sciences* **103**(13): 5108–5113.

Mitra, A. K. (2019). Visualization of biological macromolecules at near-atomic resolution: cryo-electron microscopy comes of age, *Acta Crystallographica Section F Structural Biology Communications* **75**(1): 3–11.

Morin, B., Coutard, B., Lelke, M., Ferron, F., Kerber, R., Jamal, S., Frangeul, A., Baronti, C., Charrel, R., de Lamballerie, X., Vonrhein, C., Lescar, J., Bricogne, G., Günther, S. and Canard, B. (2010). The N-Terminal Domain of the Arenavirus L Protein Is an RNA Endonuclease Essential in mRNA Transcription, *PLoS Pathogens* **6**(9): e1001038.

Müller, G., Bruns, M., Martínez Peralta, L. and Lehmann-Grube, F. (1983). Lymphocytic choriomeningitis virus, *Archives of Virology* **75**(4): 229–242.

Murphy, F. A., Webb, P. A., Johnson, K. M. and Whitfield, S. G. (1969). Morphological Comparison of Machupo with Lymphocytic Choriomeningitis Virus: Basis for a New Taxonomic Group, *Journal of Virology* **4**(4): 535–541.

Murphy, F. A., Webb, P. A., Johnson, K. M., Whitfield, S. G. and Chappell, W. A. (1970). Arenoviruses in Vero Cells: Ultrastructural Studies, *Journal of Virology* **6**(4): 507–518.

Murphy, F. A. and Whitfield, S. G. (1975). Morphology and Morphogenesis of Arenaviruses, *Bull World Health Organ.* **52**(4-6): 409–419.

Neuman, B. W., Adair, B. D., Burns, J. W., Milligan, R. A., Buchmeier, M. J. and Yeager, M. (2005). Complementarity in the Supramolecular Design of Arenaviruses and Retroviruses Revealed by Electron Cryomicroscopy and Image Analysis, *Journal of Virology* **79**(6): 3822–3830.

Ngo, N., Cubitt, B., Iwasaki, M. and de la Torre, J. C. (2015). Identification and Mechanism of Action of a Novel Small-Molecule Inhibitor of Arenavirus Multiplication, *Journal of Virology* **89**(21): 10924–10933.

Nicastro, D. (2006). The Molecular Architecture of Axonemes Revealed by Cryoelectron Tomography, *Science* **313**(5789): 944–948.

Nunberg, J. H. and York, J. (2012). The Curious Case of Arenavirus Entry, and Its Inhibition, *Viruses* **4**(1): 83–101.

Nuñez, G., Benedict, M. A., Hu, Y. and Inohara, N. (1998). Caspases: the proteases of the apoptotic pathway, *Oncogene* **17**(25): 3237–3245.

Ogbu, O., Ajuluchukwu, E. and Uneke, C. J. (2007). Lassa fever in West African sub-region: an overview., *Journal of Vector Borne Diseases* **44**(1): 1–11.

Ohi, M., Li, Y., Cheng, Y. and Walz, T. (2004). Negative staining and image classification — powerful tools in modern electron microscopy, *Biological Procedures Online* **6**(1): 23–34.

Okokhere, P. O., Ibekwe, T. S. and Akpede, G. O. (2009). Sensorineural hearing loss in Lassa fever: two case reports, *Journal of Medical Case Reports* **3**(1): 36.

Olschewski, S., Cusack, S. and Rosenthal, M. (2020). The Cap-Snatching Mechanism of Bunyaviruses, *Trends in Microbiology* **28**(4): 293–303.

Oppliger, J., Torriani, G., Herrador, A. and Kunz, S. (2016). Lassa Virus Cell Entry via Dystroglycan Involves an Unusual Pathway of Macropinocytosis, *Journal of Virology* **90**(14): 6412–6429.

Orlova, E. V. and Saibil, H. R. (2011). Structural Analysis of Macromolecular Assemblies by Electron Microscopy, *Chemical Reviews* **111**(12): 7710–7748.

Ortiz-Riano, E., Cheng, B. Y. H., de la Torre, J. C. and Martinez-Sobrido, L. (2011). The C-Terminal Region of Lymphocytic Choriomeningitis Virus Nucleoprotein Contains Distinct and Segregable Functional Domains Involved in NP-Z Interaction and Counteraction of the Type I Interferon Response, *Journal of Virology* **85**(24): 13038–13048.

Pannetier, D., Faure, C., Georges-Courbot, M.-C., Deubel, V. and Baize, S. (2004). Human Macrophages, but Not Dendritic Cells, Are Activated and Produce Alpha/Beta Interferons in Response to Mopeia Virus Infection, *Journal of Virology* **78**(19): 10516–10524.

Pannetier, D., Reynard, S., Russier, M., Journeaux, A., Tordo, N., Deubel, V. and Baize, S. (2011). Human Dendritic Cells Infected with the Nonpathogenic Mopeia Virus Induce Stronger T-Cell Responses than Those Infected with Lassa Virus, *Journal of Virology* **85**(16): 8293–8306.

Papageorgiou, N., Spiliopoulou, M., Nguyen, T.-H. V., Vaitsopoulou, A., Laban, E. Y., Alvarez, K., Margiolaki, I., Canard, B. and Ferron, F. (2020). Brothers in Arms: Structure, Assembly and Function of Arenaviridae Nucleoprotein, *Viruses* **12**(7): 772.

Parker, W. B. (2005). Metabolism and antiviral activity of ribavirin, *Virus Research* **107**(2): 165–171.

Parodi, A. S., Greenway, D. J., Rugiero, H. R., Frigerio, M., De La Barrera, J. M., Mettler, N., Garzon, F., Boxaca, M., Guerrero, L. and Nota, N. (1958). [Concerning the epidemic outbreak in Junin.], *El Dia Medico* **30**(62): 2300–2301.

Parodi, A. S., Rugiero, H. R., Greenway, D. J., Mettler, N., Martinez, A., Boxaca, M. and Barrera, J. M. D. L. (1959). [Isolation of the Junin Virus (Epidemic Hemorrhagic Fever) From the Mites of the Epidemic Area (Echinolaelaps Echidninus, Barlese)], *Prensa Med Argent* **4**(46): 2242–2244.

Parsy, M.-L., Harlos, K., Huiskonen, J. T. and Bowden, T. A. (2013). Crystal Structure of Venezuelan Hemorrhagic Fever Virus Fusion Glycoprotein Reveals a Class 1 Postfusion Architecture with Extensive Glycosylation, *Journal of Virology* **87**(23): 13070–13075.

Pasqual, G., Rojek, J. M., Masin, M., Chatton, J.-Y. and Kunz, S. (2011). Old World Arenaviruses Enter the Host Cell via the Multivesicular Body and Depend on the Endosomal Sorting Complex Required for Transport, *PLoS Pathogens* **7**(9): e1002232.

Pasquato, A., Cendron, L. and Kunz, S. (2018). *Cleavage of the Glycoprotein of Arenaviruses*, Springer International Publishing, Cham, pp. 47–70.

Pasquato, A., Rochat, C., Burri, D. J., Pasqual, G., de la Torre, J. C. and Kunz, S. (2012). Evaluation of the anti-arenaviral activity of the subtilisin kexin isozyme-1/site-1 protease inhibitor PF-429242, *Virology* **423**(1): 14–22.

Patterson, M., Seregin, A., Huang, C., Kolokoltsova, O., Smith, J., Miller, M., Smith, J., Yun, N., Poussard, A., Grant, A., Tigabu, B., Walker, A. and Paessler, S. (2014). Rescue of a Recombinant Machupo Virus from Cloned cDNAs and In Vivo Characterization in Interferon ($alpha$$beta$/$gamma$) Receptor Double Knockout Mice, *Journal of Virology* **88**(4): 1914–1923.

Pattis, J. G. and May, E. R. (2020). Markov State Model of Lassa Virus Nucleoprotein Reveals Large Structural Changes during the Trimer to Monomer Transition, *Structure* **28**(5): 548–554.e3.

Pattnaik, A. K., Andrew Ball, L., LeGrone, A. W. and Wertz, G. W. (1992). Infectious defective interfering particles of VSV from transcripts of a cDNA clone, *Cell* **69**(6): 1011–1020.

Pedersen, I. R. and Konigshofer, E. P. (1976). Characterization of ribonucleoproteins and ribosomes isolated from lymphocytic choriomeningitis virus., *Journal of Virology* **20**(1): 14–21.

Pekosz, A., He, B. and Lamb, R. A. (1999). Reverse genetics of negative-strand RNA viruses: Closing the circle, *Proceedings of the National Academy of Sciences of the United States of America* **96**(16): 8804–8806.

Peng, R., Xu, X., Jing, J., Wang, M., Peng, Q., Liu, S., Wu, Y., Bao, X., Wang, P., Qi, J., Gao, G. F. and Shi, Y. (2020). Structural insight into arenavirus replication machinery, *Nature* **579**(7800): 615–619.

Peng, R., Xu, X., Peng, Q. and Shi, Y. (2021). Cryo-EM structures of Lassa and Machupo virus polymerases complexed with cognate regulatory Z proteins identify targets for antivirals., *Nat Microbiol* .

Perez, M., Craven, R. C. and de la Torre, J. C. (2003b). The small RING finger protein Z drives arenavirus budding: Implications for antiviral strategies, *Proceedings of the National Academy of Sciences* **100**(22): 12978–12983.

Perez, M. and de la Torre, J. C. (2003a). Characterization of the Genomic Promoter of the Prototypic Arenavirus Lymphocytic Choriomeningitis Virus, *Journal of Virology* **77**(2): 1184–1194.

Perez, M., Greenwald, D. L. and de La Torre, J. C. (2004). Myristoylation of the RING Finger Z Protein Is Essential for Arenavirus Budding, *Journal of Virology* **78**(20): 11443–11448.

Perrotta, A. T. and Been, M. D. (1991). A pseudoknot-like structure required for efficient self-cleavage of hepatitis delta virus RNA, *Nature* **350**(6317): 434–436.

Peters, C. (2006). Lymphocytic Choriomeningitis Virus — An Old Enemy up to New Tricks, *New England Journal of Medicine* **354**(21): 2208–2211.

Pichlmair, A., Schulz, O., Tan, C. P., Naslund, T. I., Liljestrom, P., Weber, F. and Reis e Sousa, C. (2006). RIG-I-Mediated Antiviral Responses to Single-Stranded RNA Bearing 5'-Phosphates, *Science* **314**(5801): 997–1001.

Pinheiro, F. P., Shope, R. E., de Andrade, A. H. P., Bensabath, G., Cacios, G. V. and Casals, J. (1966). Amapari, a New Virus of the Tacaribe Group from Rodents and Mites of Amapa Territory, Brazil., *Experimental Biology and Medicine* **122**(2): 531–535.

Pinschewer, D. D., Perez, M. and de la Torre, J. C. (2005). Dual Role of the Lymphocytic Choriomeningitis Virus Intergenic Region in Transcription Termination and Virus Propagation, *Journal of Virology* **79**(7): 4519–4526.

Pinschewer, D. D., Perez, M., Sanchez, A. B. and de la Torre, J. C. (2003). Recombinant lymphocytic choriomeningitis virus expressing vesicular stomatitis virus glycoprotein, *Proceedings of the National Academy of Sciences* **100**(13): 7895–7900.

Plumet, S., Herschke, F., Bourhis, J.-M., Valentin, H., Longhi, S. and Gerlier, D. (2007). Cytosolic 5'-Triphosphate Ended Viral Leader Transcript of Measles Virus as Activator of the RIG I-Mediated Interferon Response, *PLoS ONE* **2**(3): e279.

Poch, O., Sauvaget, I., Delarue, M. and Tordo, N. (1989). Identification of four conserved motifs among the RNA-dependent polymerase encoding elements., *The EMBO journal* **8**(12): 3867–74.

Polyak, S. J., Zheng, S. and Harnish, D. G. (1995). 5' termini of Pichinde arenavirus S RNAs and mRNAs contain nontemplated nucleotides., *Journal of Virology* **69**(5): 3211–3215.

Pontremoli, C., Forni, D. and Sironi, M. (2019). Arenavirus genomics: novel insights into viral diversity, origin, and evolution, *Current Opinion in Virology* **34**: 18–28.

Price, M. E., Fisher-Hoch, S. P., Craven, R. B. and McCormick, J. B. (1988). A prospective study of maternal and fetal outcome in acute Lassa fever infection during pregnancy., *BMJ* **297**(6648): 584–587.

Pryce, R., Ng, W. M., Zeltina, A., Watanabe, Y., El Omari, K., Wagner, A. and Bowden, T. A. (2018). Structure-Based Classification Defines the Discrete Conformational Classes Adopted by the Arenaviral GP1, *Journal of Virology* **93**(1): 1–11.

Punch, E. K., Hover, S., Blest, H. T. W., Fuller, J., Hewson, R., Fontana, J., Mankouri, J. and Barr, J. N. (2018). Potassium is a trigger for conformational change in the fusion spike of an enveloped RNA virus, *Journal of Biological Chemistry* **293**(26): 9937–9944.

Pyle, J. D. and Whelan, S. P. (2019). RNA ligands activate the Machupo virus polymerase and guide promoter usage, *Proceedings of the National Academy of Sciences of the United States of America* **116**(21): 10518–10524.

Pythoud, C., Rodrigo, W. W. S. I., Pasqual, G., Rothenberger, S., Martinez-Sobrido, L., de la Torre, J. C. and Kunz, S. (2012). Arenavirus Nucleoprotein Targets Interferon Regulatory Factor-Activating Kinase IKK, *Journal of Virology* **86**(15): 7728–7738.

Qi, X., Lan, S., Wang, W., Schelde, L. M., Dong, H., Wallat, G. D., Ly, H., Liang, Y. and Dong, C. (2010). Cap binding and immune evasion revealed by Lassa nucleoprotein structure, *Nature* **468**(7325): 779–783.

Quirin, K., Eschli, B., Scheu, I., Poort, L., Kartenbeck, J. and Helenius, A. (2008). Lymphocytic choriomeningitis virus uses a novel endocytic pathway for infectious entry via late endosomes, *Virology* **378**(1): 21–33.

Raabe, V. and Koehler, J. (2017b). Laboratory Diagnosis of Lassa Fever, *Journal of Clinical Microbiology* **55**(6): 1629–1637.

Raabe, V. N., Kann, G., Ribner, B. S., Morales, A., Varkey, J. B., Mehta, A. K., Lyon, G. M., Vanairsdale, S., Faber, K., Becker, S., Eickmann, M., Strecker, T., Brown, S., Patel, K., De Leuw, P., Schuettfort, G., Stephan, C., Rabenau, H., Klena, J. D., Rollin, P. E., McElroy, A., Ströher, U., Nichol, S., Kraft, C. S., Wolf, T., Bell, S., Maloney, C., Cosper, P., Feistritzer, N., Lewin, J., Gartland, B., Horowitz, I., Pugh, D., Ritenour, C., Lewis, J., Hatcher, D., Scott-Harris, L., Ometer, L., Hardy, K., Broughton, J., Jackson, R., Thomas, S., Ash, T., Barnes, C., Breedlove, J., Bridgman, B., Darragh, L., Daye, T., Hillis, D., Johnson, C., Johnson, J.-A., LaFond, D., Lyons, C., Mamora, J., McCord, A., McDaniel, S., Morgan, H., Morgan, J., Sanchez, A., Simon, M., Slabach, J., Tirado, K., Watkins, S., Wilson, T., Logan, K., Buchanan, J., Burd, E., Cardella, J., Eaves, B., Evans, C., Hill, C., Igwe, D., Jenkins, K., Lindsey, M., Magee, J., McCarthy, S., Powers, R., Ritchie, J., Pack, J., Rogers, S., Olinger, P., Rengarajan, K., Thomaston, S., Meyer, E., Beck, E., Desroches, P., Hall, C., Walker, C., Baker, E., Hackman, B., Broughton, J., Jackson, R., Lewis, J., Brown-Haithco, R., Richardson, F., Krasilovsky, A., Jordan, C. K., Matthews, S., Lineberger, M. H., Gomes, P. G., McGee, G., Jones, P., Scott-Harris, L., Cain, J., Davis, R., Johnson, T., Pickett, T., Shaw, A., Truesdale, T., Isakov, A., Shartar, S., Miles, W., Jamison, A., Arevalo, J., Stallings, G., Christenbury, J., Dollard, V., De Gennaro, M., Korschun, H., Ziegler, T., Griffith, D. P. and Dave, N. (2017a). Favipiravir and Ribavirin Treatment of Epidemiologically Linked Cases of Lassa Fever, *Clinical Infectious Diseases* **65**(5): 855–859.

Raaben, M., Jae, L. T., Herbert, A. S., Kuehne, A. I., Stubbs, S. H., Chou, Y.-y., Blomen, V. A., Kirchhausen, T., Dye, J. M., Brummelkamp, T. R. and Whelan, S. P. (2017). NRP2 and CD63 Are Host Factors for Lujo Virus Cell Entry, *Cell Host & Microbe* **22**(5): 688–696.e5.

Racaniello, V. and Baltimore, D. (1981). Cloned poliovirus complementary DNA is infectious in mammalian cells, *Science* **214**(4523): 916–919.

Radecke, F., Spielhofer, P., Schneider, H., Kaelin, K., Huber, M., Dötsch, C., Christiansen, G. and Billeter, M. A. (1995). Rescue of measles viruses from cloned DNA., *The EMBO journal* **14**(23): 5773–84.

Radoshitzky, S. R., Abraham, J., Spiropoulou, C. F., Kuhn, J. H., Nguyen, D., Li, W., Nagel, J., Schmidt, P. J., Nunberg, J. H., Andrews, N. C., Farzan, M. and Choe, H. (2007). Transferrin receptor 1 is a cellular receptor for New World haemorrhagic fever arenaviruses, *Nature* **446**(7131): 92–96.

Radoshitzky, S. R., Bào, Y., Buchmeier, M. J., Charrel, R. N., Clawson, A. N., Clegg, C. S., DeRisi, J. L., Emonet, S., Gonzalez, J. P., Kuhn, J. H., Lukashevich, I. S., Peters, C. J., Romanowski, V., Salvato, M. S., Stenglein, M. D. and de la Torre, J. C. (2015). Past, present, and future of arenavirus taxonomy, *Archives of Virology* **160**(7): 1851–1874.

Radoshitzky, S. R., Buchmeier, M. J., Charrel, R. N., Clegg, J. C. S., Gonzalez, J. P. J., Günther, S., Hepojoki, J., Kuhn, J. H., Lukashevich, I. S., Romanowski, V., Salvato, M. S., Sironi, M., Stenglein, M. D. and De La Torre, J. C. (2019). ICTV virus taxonomy profile: Arenaviridae, *Journal of General Virology* **100**(8): 1200–1201.

Radoshitzky, S. R., Kuhn, J. H., Spiropoulou, C. F., Albarino, C. G., Nguyen, D. P., Salazar-Bravo, J., Dorfman, T., Lee, A. S., Wang, E., Ross, S. R., Choe, H. and Farzan, M. (2008). Receptor determinants of zoonotic transmission of New World hemorrhagic fever arenaviruses, *Proceedings of the National Academy of Sciences* **105**(7): 2664–2669.

Radoshitzky, S. R., Longobardi, L. E., Kuhn, J. H., Retterer, C., Dong, L., Clester, J. C., Kota, K., Carra, J. and Bavari, S. (2011). Machupo Virus Glycoprotein Determinants for Human Transferrin Receptor 1 Binding and Cell Entry, *PLoS ONE* **6**(7): e21398.

Raju, R., Raju, L., Hacker, D., Garcin, D., Compans, R. and Kolakofsky, D. (1990). Nontemplated bases at the 5' ends of tacaribe virus mRNAs, *Virology* **174**(1): 53–59.

Regnier, F. E. (1982). High-Performance Ion-Exchange Chromatography of Proteins: The Current Status, *Analytical Biochemistry*, Elsevier, pp. 1–7.

Reguera, J., Gerlach, P., Rosenthal, M., Gaudon, S., Coscia, F., Günther, S. and Cusack, S. (2016). Comparative Structural and Functional Analysis of Bunyavirus and Arenavirus Cap-Snatching Endonucleases, *PLoS Pathogens* **12**(6): 1–24.

Reynard, S., Russier, M., Fizet, A., Carnec, X. and Baize, S. (2014). Exonuclease Domain of the Lassa Virus Nucleoprotein Is Critical To Avoid RIG-I Signaling and To Inhibit the Innate Immune Response, *Journal of Virology* **88**(23): 13923–13927.

Rivers, T. M. and Scott, T. F. (1936). Meningitis in man caused by a filterable virus: II. Identification of the etiological agent, *The Journal of experimental medicine* **63**(3): 415–432.

Rodrigo, W. W. S. I., Ortiz-Riano, E., Pythoud, C., Kunz, S., de la Torre, J. C. and Martinez-Sobrido, L. (2012). Arenavirus Nucleoproteins Prevent Activation of Nuclear Factor Kappa B, *Journal of Virology* **86**(15): 8185–8197.

Rojek, J. M., Lee, A. M., Nguyen, N., Spiropoulou, C. F. and Kunz, S. (2008a). Site 1 Protease Is Required for Proteolytic Processing of the Glycoproteins of the South American Hemorrhagic Fever Viruses Junin, Machupo, and Guanarito, *Journal of Virology* **82**(12): 6045–6051.

Rojek, J. M., Pasqual, G., Sanchez, A. B., Nguyen, N.-T., de la Torre, J.-C. and Kunz, S. (2010). Targeting the Proteolytic Processing of the Viral Glycoprotein Precursor Is a Promising Novel Antiviral Strategy against Arenaviruses, *Journal of Virology* **84**(1): 573–584.

Rojek, J. M., Sanchez, A. B., Nguyen, N. T., de la Torre, J.-C. and Kunz, S. (2008b). Different Mechanisms of Cell Entry by Human-Pathogenic Old World and New World Arenaviruses, *Journal of Virology* **82**(15): 7677–7687.

Rojek, J. M., Spiropoulou, C. F., Campbell, K. P. and Kunz, S. (2007). Old World and Clade C New World Arenaviruses Mimic the Molecular Mechanism of Receptor Recognition Used by α-Dystroglycan's Host-Derived Ligands, *Journal of Virology* **81**(11): 5685–5695.

Rosano, G. L. and Ceccarelli, E. A. (2014). Recombinant protein expression in Escherichia coli: Advances and challenges, *Frontiers in Microbiology* **5**(APR): 1–17.

Rosenthal, M., Gogrefe, N., Vogel, D., Reguera, J., Rauschenberger, B., Cusack, S., Günther, S. and Reindl, S. (2017). Structural insights into reptarenavirus cap-snatching machinery, *PLoS Pathogens* **13**(5): 1–24.

Rowe, W. P., Murphy, F. A., Bergold, G. H., Casals, J., Hotchin, J., Johnson, K. M., Lehmann-Grube, F., Mims, C. A., Traub, E. and Webb, P. A. (1970b). Arenoviruses: Proposed Name for a Newly Defined Virus Group, *Journal of Virology* **5**(5): 651–652.

Rowe, W. P., Pugh, W. E., Webb, P. A. and Peters, C. J. (1970a). Serological Relationship of the Tacaribe Complex of Viruses to Lymphocytic Choriomeningitis Virus, *Journal of Virology* **5**(3): 289–292.

Safronetz, D., Lopez, J. E., Sogoba, N., Traore', S. F., Raffel, S. J., Fischer, E. R., Ebihara, H., Branco, L., Garry, R. F., Schwan, T. G. and Feldmann, H. (2010). Detection of Lassa virus, Mali., *Emerging infectious diseases* **16**(7): 1123–6.

Safronetz, D., Mire, C., Rosenke, K., Feldmann, F., Haddock, E., Geisbert, T. and Feldmann, H. (2015). A Recombinant Vesicular Stomatitis Virus-Based Lassa Fever Vaccine Protects Guinea Pigs and Macaques against Challenge with Geographically and Genetically Distinct Lassa Viruses, *PLOS Neglected Tropical Diseases* **9**(4): e0003736.

Salazar-Bravo, J., Ruedas, L. A. and Yates, T. L. (2002). Mammalian Reservoirs of Arenaviruses, *in* R. Compans, M. Cooper, H. Koprowski, M. Oldstone, M. Potter and P. Vogt (eds), *Arenaviruses I: The Epidemiology, Molecular and Cell Biology of Arenaviruses*, Vol. 262, Springer Berlin Heidelberg, pp. 25–63.

Salvato, M., Clegg, J. C. S., Buchmeier, M. J., Charrel, R., Gonzalez, J.-P., Lukashevich, I., Peters, C. and Romanowski, V. (2011). *Arenaviridae*, Elsevier-Academic Press, pp. 715–723.

Salvato, M. S. (1993). Molecular Biology of the Prototype Arenavirus, Lymphocytic Choriomeningitis Virus, *The Arenaviridae*, Springer US, Boston, MA, pp. 133–156.

Salvato, M. S., Clegg, J. C. S., Buchmeier, M. J., Charrel, R. N., Gonzalez, J. P. and & Lukashevich, I. S. (2005). Family Arenaviridae., *in* Fauquet CM, Mayo MA, Maniloff J, Desselberger U and Ball LA (eds), *Virus taxonomy: VIIIth report of the International Committee on Taxonomy of Viruses*, Academic Press, Amsterdam, pp. 725–733.

Sánchez, A. B. and de la Torre, J. C. (2005). Genetic and Biochemical Evidence for an Oligomeric Structure of the Functional L Polymerase of the Prototypic Arenavirus Lymphocytic Choriomeningitis Virus, *Journal of Virology* **79**(11): 7262–7268.

Sánchez, A. B. and de la Torre, J. C. (2006). Rescue of the prototypic Arenavirus LCMV entirely from plasmid, *Virology* **350**(2): 370–380.

Sandige, H. (2018). Learning in the Lassa Belt, *The American Journal of Tropical Medicine and Hygiene* **99**(5): 1110–1111.

Sarute, N. and Ross, S. R. (2017). New World Arenavirus Biology, *Annual Review of Virology* **4**(1): 141–158.

Sayler, K. A., Barbet, A. F., Chamberlain, C., Clapp, W. L., Alleman, R., Loeb, J. C. and Lednicky, J. A. (2014). Isolation of Tacaribe Virus, a Caribbean Arenavirus, from Host-Seeking Amblyomma americanum Ticks in Florida, *PLoS ONE* **9**(12): e115769.

Schlegel, S., Löfblom, J., Lee, C., Hjelm, A., Klepsch, M., Strous, M., Drew, D., Slotboom, D. J. and de Gier, J.-W. (2012). Optimizing Membrane Protein Overexpression in the Escherichia coli strain Lemo21(DE3), *Journal of Molecular Biology* **423**(4): 648–659.

Schlie, K., Maisa, A., Freiberg, F., Groseth, A., Strecker, T. and Garten, W. (2010b). Viral Protein Determinants of Lassa Virus Entry and Release from Polarized Epithelial Cells, *Journal of Virology* **84**(7): 3178–3188.

Schlie, K., Maisa, A., Lennartz, F., Ströher, U., Garten, W. and Strecker, T. (2010a). Characterization of Lassa Virus Glycoprotein Oligomerization and Influence of Cholesterol on Virus Replication, *Journal of Virology* **84**(2): 983–992.

Schnell, M. J., Mebatsion, T. and Conzelmann, K. K. (1994). Infectious rabies viruses from cloned cDNA., *The EMBO journal* **13**(18): 4195–203.

Sevilla, N., Kunz, S., Holz, A., Lewicki, H., Homann, D., Yamada, H., Campbell, K. P., de la Torre, J. C. and Oldstone, M. B. (2000). Immunosuppression and Resultant Viral Persistence by Specific Viral Targeting of Dendritic Cells, *Journal of Experimental Medicine* **192**(9): 1249–1260.

Sewlall, N. H., Richards, G., Duse, A., Swanepoel, R., Paweska, J., Blumberg, L., Dinh, T. H. and Bausch, D. (2014). Clinical Features and Patient Management of Lujo Hemorrhagic Fever, *PLoS Neglected Tropical Diseases* **8**(11): e3233.

Shao, J., Huang, Q., Liu, X., Di, D., Dileepan, M., Brisse, M., Ly, H. and Liang, Y. (2019). Biological Characterization of Conserved Residues within the Cytoplasmic Tail of the Pichinde Arenaviral Glycoprotein Subunit 2 (GP2), *Journal of Virology* **93**(22).

Shao, J., Huang, Q., Liu, X., Di, D., Liang, Y. and Ly, H. (2018). Arenaviral Nucleoproteins Suppress PACT-Induced Augmentation of RIG-I Function To Inhibit Type I Interferon Production, *Journal of Virology* **92**(13): e00482–18.

Shao, J., Liang, Y. and Ly, H. (2015). Human Hemorrhagic Fever Causing Arenaviruses: Molecular Mechanisms Contributing to Virus Virulence and Disease Pathogenesis, *Pathogens* **4**(2): 283–306.

Shi, M., Lin, X.-D., Chen, X., Tian, J.-H., Chen, L.-J., Li, K., Wang, W., Eden, J.-S., Shen, J.-J., Liu, L., Holmes, E. C. and Zhang, Y.-Z. (2018). The evolutionary history of vertebrate RNA viruses, *Nature* **556**(7700): 197–202.

Shi, M., Lin, X.-D., Tian, J.-H., Chen, L.-J., Chen, X., Li, C.-X., Qin, X.-C., Li, J., Cao, J.-P., Eden, J.-S., Buchmann, J., Wang, W., Xu, J., Holmes, E. C. and Zhang, Y.-Z. (2016). Redefining the invertebrate RNA virosphere, *Nature* **540**(7634): 539–543.

Shimojima, M., Stroher, U., Ebihara, H., Feldmann, H. and Kawaoka, Y. (2012). Identification of Cell Surface Molecules Involved in Dystroglycan-Independent Lassa Virus Cell Entry, *Journal of Virology* **86**(4): 2067–2078.

Shimon, A., Shani, O. and Diskin, R. (2017). Structural Basis for Receptor Selectivity by the Whitewater Arroyo Mammarenavirus, *Journal of Molecular Biology* **429**(18): 2825–2839.

Shtanko, O., Imai, M., Goto, H., Lukashevich, I. S., Neumann, G., Watanabe, T. and Kawaoka, Y. (2010). A Role for the C Terminus of Mopeia Virus Nucleoprotein in Its Incorporation into Z Protein-Induced Virus-Like Particles, *Journal of Virology* **84**(10): 5415–5422.

Shtanko, O., Watanabe, S., Jasenosky, L. D., Watanabe, T. and Kawaoka, Y. (2011). ALIX/AIP1 Is Required for NP Incorporation into Mopeia Virus Z-Induced Virus-Like Particles, *Journal of Virology* **85**(7): 3631–3641.

Shulman, A., Katz, M., Cohen-Dvashi, H., Greenblatt, H. M., Levy, Y. and Diskin, R. (2019). Variations in Core Packing of GP2 from Old World Mammarenaviruses in their Post-Fusion Conformations Affect Membrane-Fusion Efficiencies, *Journal of Molecular Biology* **431**(11): 2095–2111.

Sizikova, T. E., Lebedev, V. N., Syromyatnikova, S. I. and Borisevich, S. V. (2017). Lujo Haemorrhagic Fever, *Problems of Virology, Russian journal* **62**(4): 149–153.

Skinner, H. H. and Knight, E. H. (1974). Factors influencing pre-natal infection of mice with lymphocytic choriomeningitis virus, *Archiv for die gesamte Virusforschung* **46**(1-2): 1–10.

Smelt, S. C., Borrow, P., Kunz, S., Cao, W., Tishon, A., Lewicki, H., Campbell, K. P. and Oldstone, M. B. A. (2001). Differences in Affinity of Binding of Lymphocytic Choriomeningitis Virus Strains to the Cellular Receptor α-Dystroglycan Correlate with Viral Tropism and Disease Kinetics, *Journal of Virology* **75**(1): 448–457.

Sommerstein, R., Flatz, L., Remy, M. M., Malinge, P., Magistrelli, G., Fischer, N., Sahin, M., Bergthaler, A., Igonet, S., ter Meulen, J., Rigo, D., Meda, P., Rabah, N., Coutard, B., Bowden, T. A., Lambert, P.-H., Siegrist, C.-A. and Pinschewer, D. D. (2015). Arenavirus Glycan Shield Promotes Neutralizing Antibody Evasion and Protracted Infection, *PLOS Pathogens* **11**(11): e1005276.

Stenglein, M. D., Sanders, C., Kistler, A. L., Ruby, J. G., Franco, J. Y., Reavill, D. R., Dunker, F. and DeRisi, J. L. (2012). Identification, Characterization, and In Vitro Culture of Highly Divergent Arenaviruses from Boa Constrictors and Annulated Tree Boas: Candidate Etiological Agents for Snake Inclusion Body Disease, *mBio* **3**(4).

Stinebaugh, B. J., Schloeder, F. X., Johnson, K. M., Mackenzie, R. B., Entwisle, G. and De Alba, E. (1966). Bolivian hemorrhagic fever, *The American Journal of Medicine* **40**(2): 217–230.

Stoker, M. and Macpherson, I. (1964). Syrian Hamster Fibroblast Cell Line BHK21 and its Derivatives, *Nature* **203**(4952): 1355–1357.

Stott, R. J., Strecker, T. and Foster, T. L. (2020). Distinct molecular mechanisms of host immune response modulation by arenavirus NP and Z proteins, *Viruses* **12**(7): 1–29.

Strack, B., Calistri, A., Craig, S., Popova, E. and Göttlinger, H. G. (2003). AIP1/ALIX Is a Binding Partner for HIV-1 p6 and EIAV p9 Functioning in Virus Budding, *Cell* **114**(6): 689–699.

Strandin, T., Hepojoki, J. and Vaheri, A. (2013). Cytoplasmic tails of bunyavirus Gn glycoproteins—Could they act as matrix protein surrogates?, *Virology* **437**(2): 73–80.

Strecker, T., Eichler, R., ter Meulen, J., Weissenhorn, W., Dieter Klenk, H., Garten, W. and Lenz, O. (2003). Lassa Virus Z Protein Is a Matrix Protein Sufficient for the Release of Virus-Like Particles, *Journal of Virology* **77**(19): 10700–10705.

Strecker, T., Maisa, A., Daffis, S., Eichler, R., Lenz, O. and Garten, W. (2006). The role of myristoylation in the membrane association of the Lassa virus matrix protein Z., *Virology* **3**: 93.

Studier, F. W. (1991). Use of bacteriophage T7 lysozyme to improve an inducible T7 expression system, *Journal of Molecular Biology* **219**(1): 37–44.

Studier, F. W. (2005). Protein production by auto-induction in high density shaking cultures., *Protein expression and purification* **41**: 207–234.

Studier, F. W. and Moffatt, B. A. (1986). Use of bacteriophage T7 RNA polymerase to direct selective high-level expression of cloned genes, *Journal of Molecular Biology* **189**(1): 113–130.

Tagliapietra, V., Rosà, R., Hauffe, H. C., Laakkonen, J., Voutilainen, L., Vapalahti, O., Vaheri, A., Henttonen, H. and Rizzoli, A. (2009). Spatial and Temporal Dynamics of Lymphocytic Choriomeningitis Virus in Wild Rodents, Northern Italy, *Emerging Infectious Diseases* **15**(7): 1019–1025.

Takagi, T., Ohsawa, M., Morita, C., Sato, H. and Ohsawa, K. (2012). Genomic analysis and pathogenic characteristics of lymphocytic choriomeningitis virus strains isolated in Japan., *Comparative medicine* **62**(3): 185–92.

Taniguchi, T., Palmieri, M. and Weissmann, C. (1978). Qβ DNA-containing hybrid plasmids giving rise to Qβ phage formation in the bacterial host, *Nature* **274**(5668): 223–228.

Teng, M. N., Borrow, P., Oldstone, M. B. and de la Torre, J. C. (1996). A single amino acid change in the glycoprotein of lymphocytic choriomeningitis virus is associated with the ability to cause growth hormone deficiency syndrome., *Journal of Virology* **70**(12): 8438–43.

Thompson, R. F., Walker, M., Siebert, C. A., Muench, S. P. and Ranson, N. A. (2016). An introduction to sample preparation and imaging by cryo-electron microscopy for structural biology, *Methods* **100**: 3–15.

Topcu, Z., Mack, D. L., Hromas, R. A. and Borden, K. L. (1999). The promyelocytic leukemia protein PML interacts with the proline-rich homeodomain protein PRH: a RING may link hematopoiesis and growth control, *Oncogene* **18**(50): 7091–7100.

Torriani, G., Galan-Navarro, C. and Kunz, S. (2017). Lassa Virus Cell Entry Reveals New Aspects of Virus-Host Cell Interaction, *Journal of Virology* **91**(4).

Trapecar, M., Khan, S., Cohn, B. L., Wu, F. and Sanjabi, S. (2018). B cells are the predominant mediators of early systemic viral dissemination during rectal LCMV infection, *Mucosal Immunology* **11**(4): 1158–1167.

Trapido, H. and Sanmartín, C. (1971). Pichindé Virus, *The American Journal of Tropical Medicine and Hygiene* **20**(4): 631–641.

Traub, E. (1935). A filterable virus recovered from white mice, *Science* **81**(2099): 298–299.

Turoňová, B., Schur, F. K., Wan, W. and Briggs, J. A. (2017). Efficient 3D-CTF correction for cryo-electron tomography using NovaCTF improves subtomogram averaging resolution to 3.4 Å, *Journal of Structural Biology* **199**(3): 187–195.

Urata, S., Noda, T., Kawaoka, Y., Yokosawa, H. and Yasuda, J. (2006). Cellular Factors Required for Lassa Virus Budding, *Journal of Virology* **80**(8): 4191–4195.

Urata, S. and Yasuda, J. (2015). Cis- and cell-type-dependent trans-requirements for Lassa virus-like particle production, *Journal of General Virology* **96**(7): 1626–1635.

Urata, S., Yasuda, J. and de la Torre, J. C. (2009). The Z Protein of the New World Arenavirus Tacaribe Virus Has Bona Fide Budding Activity That Does Not Depend on Known Late Domain Motifs, *Journal of Virology* **83**(23): 12651–12655.

Vieth, S., Torda, A. E., Asper, M., Schmitz, H. and Günther, S. (2004). Sequence analysis of L RNA of Lassa virus, *Virology* **318**(1): 153–168.

Vitullo, A. D. and Merani, M. S. (1988). Is Vertical Transmission Sufficient to Maintain Junin Virus in Nature?, *Journal of General Virology* **69**(6): 1437–1440.

Vitullo, A. D., Merani, M. S. and Hodara, V. L. (1987). Effect of Persistent Infection with Junin Virus on Growth and Reproduction of its Natural Reservoir, Calomys musculinus, *The American Journal of Tropical Medicine and Hygiene* **37**(3): 663–669.

Vogel, D., Rosenthal, M., Gogrefe, N., Reindl, S. and Günther, S. (2019). Biochemical characterization of the Lassa virus L protein, *Journal of Biological Chemistry* **294**(20): 8088–8100.

Volpon, L., Osborne, M. J., Capul, A. A., de la Torre, J. C. and Borden, K. L. B. (2010). Structural characterization of the Z RING-eIF4E complex reveals a distinct mode of control for eIF4E, *Proceedings of the National Academy of Sciences* **107**(12): 5441–5446.

von Heijne, G. (1985). Signal sequences, *Journal of Molecular Biology* **184**(1): 99–105.

Wagner, S., Klepsch, M. M., Schlegel, S., Appel, A., Draheim, R., Tarry, M., Högbom, M., van Wijk, K. J., Slotboom, D. J., Persson, J. O. and de Gier, J.-W. (2008). Tuning Escherichia coli for membrane protein overexpression, *PNAS* **105**(38): 14371–14376.

Walker, P. J., Siddell, S. G., Lefkowitz, E. J., Mushegian, A. R., Dempsey, D. M., Dutilh, B. E., Harrach, B., Harrison, R. L., Hendrickson, R. C., Junglen, S., Knowles, N. J., Kropinski, A. M., Krupovic, M., Kuhn, J. H., Nibert, M., Rubino, L., Sabanadzovic, S., Simmonds, P., Varsani, A., Zerbini, F. M. and Davison, A. J. (2019). Changes to virus taxonomy and the International Code

of Virus Classification and Nomenclature ratified by the International Committee on Taxonomy of Viruses (2019), *Archives of Virology* **164**(9): 2417–2429.

Wallat, G. D., Huang, Q., Wang, W., Dong, H., Ly, H., Liang, Y. and Dong, C. (2014). High-resolution structure of the N-terminal endonuclease domain of the Lassa virus L polymerase in complex with magnesium ions, *PLoS ONE* **9**(2): 1–10.

Welsh, R. M. and Seedhom, M. O. (2008). Lymphocytic choriomeningitis virus (LCMV): propagation, quantitation, and storage., *Current protocols in microbiology* **Chapter 15**: Unit 15A.1.

West, B. R., Hastie, K. M. and Saphire, E. O. (2014). Structure of the LCMV nucleoprotein provides a template for understanding arenavirus replication and immunosuppression, *Acta Crystallographica Section D Biological Crystallography* **70**(6): 1764–1769.

Whelan, S. P., Ball, L. A., Barr, J. N. and Wertz, G. T. (1995). Efficient recovery of infectious vesicular stomatitis virus entirely from cDNA clones., *Proceedings of the National Academy of Sciences* **92**(18): 8388–8392.

Whitmer, S. L., Strecker, T., Cadar, D., Dienes, H.-P., Faber, K., Patel, K., Brown, S. M., Davis, W. G., Klena, J. D., Rollin, P. E., Schmidt-Chanasit, J., Fichet-Calvet, E., Noack, B., Emmerich, P., Rieger, T., Wolff, S., Fehling, S. K., Eickmann, M., Mengel, J. P., Schultze, T., Hain, T., Ampofo, W., Bonney, K., Aryeequaye, J. N. D., Ribner, B., Varkey, J. B., Mehta, A. K., Lyon, G. M., Kann, G., De Leuw, P., Schuettfort, G., Stephan, C., Wieland, U., Fries, J. W., Kochanek, M., Kraft, C. S., Wolf, T., Nichol, S. T., Becker, S., Ströher, U. and Günther, S. (2018). New Lineage of Lassa Virus, Togo, 2016, *Emerging Infectious Diseases* **24**(3): 599–602.

Wilda, M., Lopez, N., Casabona, J. C. and Franze-Fernandez, M. T. (2008). Mapping of the Tacaribe Arenavirus Z-Protein Binding Sites on the L Protein Identified both Amino Acids within the Putative Polymerase Domain and a Region at the N Terminus of L That Are Critically Involved in Binding, *Journal of Virology* **82**(22): 11454–11460.

Wolff, S., Becker, S. and Groseth, A. (2013b). Cleavage of the Junin Virus Nucleoprotein Serves a Decoy Function To Inhibit the Induction of Apoptosis during Infection, *Journal of Virology* **87**(1): 224–233.

Wolff, S., Ebihara, H. and Groseth, A. (2013a). Arenavirus Budding: A Common Pathway with Mechanistic Differences, *Viruses* **5**(2): 528–549.

Wolff, S., Groseth, A., Meyer, B., Jackson, D., Strecker, T., Kaufmann, A. and Becker, S. (2016). The New World arenavirus Tacaribe virus induces caspase-dependent apoptosis in infected cells, *Journal of General Virology* **97**(4): 855–866.

Wollert, T., Wunder, C., Lippincott-Schwartz, J. and Hurley, J. H. (2009). Membrane scission by the ESCRT-III complex, *Nature* **458**(7235): 172–177.

Wood, O., Liebhaber, H., Speir, R. W. and Buckley, S. M. (1970). Lassa Fever, a New Virus Disease of Man from West Africa IV. Electron Microscopy of Vero Cell Cultures Infected with Lassa Virus, *The American Journal of Tropical Medicine and Hygiene* **19**(4): 692–694.

Wright, K. (1990). Post-translational processing of the glycoproteins of lymphocytic choriomeningitis virus, *Virology* **177**(1): 175–183.

Wright, R., Johnson, D., Neumann, M., Ksiazek, T. G., Rollin, P., Keech, R. V., Bonthius, D. J., Hitchon, P., Grose, C. F., Bell, W. E. and Bale Jr, J. F. (1997). Congenital Lymphocytic Choriomeningitis Virus Syndrome: A Disease That Mimics Congenital Toxoplasmosis or Cytomegalovirus Infection, *PEDIATRICS* **100**(1): e9–e9.

Ye, C., de la Torre, J. C. and Martínez-Sobrido, L. (2020). Development of Reverse Genetics for the Prototype New World Mammarenavirus Tacaribe Virus, *Journal of Virology* **94**(19).

Yekwa, E., Aphibanthammakit, C., Carnec, X., Picard, C., Canard, B., Baize, S. and Ferron, F. (2019). Arenaviridae exoribonuclease presents genomic RNA edition capacity., *bioRxiv* p. 541698.

Yekwa, E., Khourieh, J., Canard, B., Papageorgiou, N. and Ferron, F. (2017). Activity inhibition and crystal polymorphism induced by active-site metal swapping, *Acta Crystallographica Section D Structural Biology* **73**(8): 641–649.

York, J. and Nunberg, J. H. (2006). Role of the Stable Signal Peptide of Junín Arenavirus Envelope Glycoprotein in pH-Dependent Membrane Fusion, *Journal of Virology* **80**(15): 7775–7780.

York, J. and Nunberg, J. H. (2007). A Novel Zinc-Binding Domain Is Essential for Formation of the Functional Junín Virus Envelope Glycoprotein Complex, *Journal of Virology* **81**(24): 13385–13391.

York, J. and Nunberg, J. H. (2009). Intersubunit Interactions Modulate pH-Induced Activation of Membrane Fusion by the Junín Virus Envelope Glycoprotein GPC, *Journal of Virology* **83**(9): 4121–4126.

York, J. and Nunberg, J. H. (2016). Myristoylation of the Arenavirus Envelope Glycoprotein Stable Signal Peptide Is Critical for Membrane Fusion but Dispensable for Virion Morphogenesis, *Journal of Virology* **90**(18): 8341–8350.

York, J., Romanowski, V., Lu, M. and Nunberg, J. H. (2004). The Signal Peptide of the Junín Arenavirus Envelope Glycoprotein Is Myristoylated and Forms an Essential Subunit of the Mature G1-G2 Complex, *Journal of Virology* **78**(19): 10783–10792.

Young, P. R., Chanas, A. C., Lee, S. R., Gould, E. A. and Howard, C. R. (1987). Localization of an Arenavirus Protein in the Nuclei of Infected Cells, *Journal of General Virology* **68**(9): 2465–2470.

Young, P. R. and Howard, C. R. (1983). Fine Structure Analysis of Pichinde Virus Nucleocapsids, *Journal of General Virology* **64**(4): 833–842.

Zapata, J. and Salvato, M. (2013). Arenavirus Variations Due to Host-Specific Adaptation, *Viruses* **5**(1): 241–278.

Zeltina, A., Krumm, S. A., Sahin, M., Struwe, W. B., Harlos, K., Nunberg, J. H., Crispin, M., Pinschewer, D. D., Doores, K. J. and Bowden, T. A. (2017). Convergent immunological solutions to Argentine hemorrhagic fever virus neutralization, *Proceedings of the National Academy of Sciences* **114**(27): 7031–7036.

Zhang, X., Wang, C., Chen, B., Wang, Q., Xu, W., Ye, S., Jiang, S., Zhu, Y. and Zhang, R. (2019). Crystal Structure of Refolding Fusion Core of Lassa Virus GP2 and Design of Lassa Virus Fusion Inhibitors, *Frontiers in Microbiology* **10**.

Zhang, Y., Li, L., Liu, X., Dong, S., Wang, W., Huo, T., Guo, Y., Rao, Z. and Yang, C. (2013). Crystal structure of Junin virus nucleoprotein, *Journal of General Virology* **94**(10): 2175–2183.

Zhou, S., Cerny, A. M., Zacharia, A., Fitzgerald, K. A., Kurt-Jones, E. A. and Finberg, R. W. (2010). Induction and Inhibition of Type I Interferon Responses by Distinct Components of Lymphocytic Choriomeningitis Virus, *Journal of Virology* **84**(18): 9452–9462.

Ziegler, C. M. and Botten, J. W. (2020). Defective Interfering Particles of Negative-Strand RNA Viruses, *Trends in Microbiology* **28**(7): 554–565.

Ziegler, C. M., Eisenhauer, P., Bruce, E. A., Weir, M. E., King, B. R., Klaus, J. P., Krementsov, D. N., Shirley, D. J., Ballif, B. A. and Botten, J. (2016). The Lymphocytic Choriomeningitis Virus Matrix Protein PPXY Late Domain Drives the Production of Defective Interfering Particles, *PLOS Pathogens* **12**(3): e1005501.

Zuo, Y. and Deutscher, M. P. (2001). Exoribonuclease superfamilies: structural analysis and phylogenetic distribution., *Nucleic Acids Research* **29**(5): 1017–1026.